NONLINEAR RESPONSES OF HIGH-RISE BUILDINGS IN GIANT SUBDUCTION EARTHQUAKES

Thesis by

Jing Yang

In Partial Fulfillment of the Requirements for the

Degree of

Doctor of Philosophy

CALIFORNIA INSTITUTE OF TECHNOLOGY
Pasadena, California

2009

(Defended Dec.10, 2008)

© 2009

Jing Yang

All Rights Reserved

Acknowledgements

I cannot overstate my deep gratitude to my PhD advisor, Professor Tom Heaton for his full support and great guidance. It is hard to count how many times I came into his office full of confusion or even frustration, and came out of his office with excitement and confidence. Professor Heaton's office is like a magic box and he is more like a loving father. Working with Professor Heaton has been a great and cherished experience in my life.

I also wish to thank the members in my thesis defense committee. Thanks to Professor Jim Beck and Swami Krishnan who had spent much of their time to modify my thesis carefully and gave me many precious suggestions. Thanks to Professor Hiroo Kanamori for his encourage and precious time drawing from his busy schedule. I want to especially thank Professor Hall for providing me the building designs and models. His patient and detailed explanations helped me a lot in understanding the building modeling.

This research was supported by the NSF and the Gordon & Betty Moore Foundation. The teleseismic data used in this study is obtained from IRIS, and strong ground motion recordings are obtained from websites of K-Net and KiK-Net. Data from SHIP02 experiment was generously provided by Professor Thomas Pratt at the University of Washington. High-sample GPS data was provided by Prof Kristine Larson at the University of Colorado. Building responses were calculated at SCEC High Performance Computing Center.

My many thanks go to my fellow graduate students, Anna Olsen, Masumi Yamada, Matt Muto, Case Bradford, Georgia Cua and John Clinton for helping me with research and

candidacy exams. Thank you to Carolina Oseguera and many graduate students from Seismolab for lots of help.

Above all, I would like to express my gratitude to my family. Without the support from my father and my mother-in-law, I would not have finished this thesis. My little son Aaron makes my life busy but enjoyable. Finally, I would like to give my deepest thanks to my husband Ke Wang, for his support and encouragement. I wish that my loving mother would see my achievements in heaven.

Abstract

With the exception of the 2003 Tokachi-Oki earthquake, strong ground recordings from large subduction earthquakes (M_w > 8.0) are meager. Furthermore there are no strong motion recordings of giant earthquakes. However, there is a growing set of high-quality broadband teleseismic recordings of large and giant earthquakes. In this thesis, we use recordings from the 2003 Tokachi-Oki (M_w 8.3) earthquake as empirical Green's functions to simulate the rock and soil ground motions from the 2004 Sumatra-Andaman earthquake and a scenario M_w 9.2 Cascadia subduction earthquake in the frequency band of interest to flexible and tall buildings (0.075 to 1 Hz). The effect of amplification by the Seattle basin is considered by using a basin response transfer function, which is derived from deconvolving the teleseismic waves recorded at rock sites from basin sites at the SHIP02 experiment. These strong ground motion time histories are used to simulate of the fully nonlinear response of 20-story and 6-story steel moment-frame buildings designed according to both the U.S. 1994 Uniform Building Code and the 1987 Japanese building code. We consider several realizations of the hypothetical subduction earthquake. The basin amplification and the down-dip limit of rupture are of particular importance to the simulated ground motions in Seattle. At rock sites, if slip is limited to offshore regions, the building model responses are mostly in the linear range. However, if rupture is extended beyond the Olympic Mountains, large deformations occur in the high-rise buildings models, especially those with brittle welds. At basin sites, our simulations indicate the collapse of all building models for a source model with rupture beyond the Olympic Mountains, whereas buildings with perfect welds avoid collapse for simulations based on a source

model with rupture limited to offshore. The synthetic ground motions all have very long durations (more than 5 minutes at basin sites), and our building simulations should be considered as a low estimate since we the degradation model used in our simulation did not consider local flange buckling.

Contents

List of Figures

List of Tables

CHAPTER 1

Introduction

Great earthquakes ($M_w > 8.0$) are rare but occur on the average about once a year on the planet. If they happen to be close to urban areas, they could be catastrophic. Tremendous loss of life and widespread damage would have a long-lasting impact on the affected areas. The 2004 Sumatra-Andaman earthquake with more than 230,000 dead or missing and the 2008 Wenchuan earthquake with about 90,000 dead or missing surprise and remind us of the great power of earthquakes. Many of the deaths in the earthquakes were caused by the collapse of buildings. And modern designed high-rise buildings did collapse in the past moderate to large earthquakes (1985 Michoacan earthquake, 1995 Kobe earthquake, 1999 Chi-Chi earthquake). With the tremendous rise in world population and the mass human migration to cities, urbanization has been rampant and tall building construction has boomed. Today, there is a great possibility of some of these buildings being shaken by great earthquakes.

1.1 Motivation

In order to limit the stresses encountered in beams and columns during earthquake ground shaking, modern moment-resisting frame tall buildings (midheight 15 to 30 story range） are designed to be quite flexible relative to many other types of building designs (e.g., shear

wall); Steel moment-resisting frame is the most popular type of construction in the areas of high seismicity (FEMA-354, 2000). To date, this strategy has largely been successful in that flexible high-rise buildings have generally performed well in past earthquake ground shaking (Yanev, Gillengerten J.D. *et al.*, 1991), even for ground motions with large accelerations such as those that occurred at tall buildings site during the 1995 Kobe earthquake. The one notable exception (at the time of this thesis) was the catastrophic collapse of many 10- to 20-story buildings in Mexico City during the 1985 Michoacan earthquake (M8.2) (Hall and Beck, 1986; Rosenblueth and Meli, 1986). The Mexico City catastrophe has been attributed to a serious underestimation of the importance of resonances of ground shaking in the ½ Hz band caused by the lacustrian deposits beneath Mexico City (Anderson, Bodin P. *et al.*, 1986; Beck and Hall, 1986). Ironically, the Michoacan rupture was approximately 350 km from Mexico City and consequently tens of thousands of stiff brittle buildings were undamaged by the ground shaking in Mexico City. Thus, while tall flexible buildings may perform well in high-frequency ground motions that are damaging to many types of buildings, their unique dynamic characteristics make them vulnerable to large amplitude long-period ground shaking.

Most great earthquakes occur at subduction zones and seismic waves from these earthquakes are rich in long-period waves that may be especially large in regions with local site amplification. Subduction earthquakes occur at the interface of two converging plates jerk past one another examples include the 2004 Sumatra-Andaman earthquake and the 1985 Michoacan earthquake. In a video taken during the Sumatra event at Banda Aceh, people had difficulty in maintaining their balance while keep standing and some were sitting on the curb swaying back and forth at a slow rate. Nance (1988) also described a similar phenomenon in the giant 1964 Alaskan earthquake (M_w9.3). Hundreds of kilometers of Alaskan coastline was horizontally displaced by 20 meters during the minutes of shaking that occurred in that event (Plafker, 1965). This implies that even if these earthquakes may occur at a large distance, they are rich in long-period seismic waves which attenuate more slowly and can travel long distance as a result. Soft soil sites may further amplify these motions. Unfortunately, there are no strong motion records from giant

subduction earthquakes. So it raises the question: what will happen to the high-rise steel moment frame buildings in a large coastal city if a great subduction earthquake occurs offshore? This question is especially critical in the Cascadia subduction zone of the Pacific Northwest.

In the 1980s, the potential of great subduction earthquakes along Cascadia area was first proposed by Heaton *et.al* (1984). Later Atwater (1987) found geologic evidence of great subduction earthquakes; the most recent one is estimated to have occurred 300 years ago. This earthquake also explained the mysterious tsunami documented in Japanese historical documents (Atwater, Satoko *et al.*, 2005) and in native Indian legend (Heaton and Snavely, 1985). It is now apparent and widely agreed upon that such an earthquake will reoccur, resulting in severe shaking of the modern cities of Seattle, Portland and Vancouver. In this study, we focus on Seattle because a number of sites have been investigated (Frankel, Carver *et al.*, 2002; Pratt, Brocher *et al.*, 2003) in that area. Large site amplification from the Seattle basin was found by these investigations and future great subduction earthquakes would pose a serious threat to the flexible buildings in Seattle.

The M_w8.1 2003 Tokachi-Oki subduction earthquake is the largest event recorded by a wealth of modern networks densely-deployed on Hokkaido Island in Japan. The abundant high-quality strong shaking data can extend our knowledge of ground motions from large earthquakes. Furthermore, these motions constitute a good source of empirical Green's functions to simulate strong ground motions from giant subduction earthquakes.

All of the above issues motivate us to simulate the strong ground motions from a hypothetical Cascadia earthquake and use these motions to check the nonlinear performance of high-rise buildings in the city of Seattle.

1.2 Previous Work

1.2.1 Strong Ground Motions in Earthquakes

Since the first good records of ground shaking in 1880 by Ewing at the University of Tokyo (Agnew, 2002), more and more strong or weak ground motions have been recorded worldwide. It provides a principal research tool for seismologists to analyze earthquake mechanism through interpreting and matching these seismic waves. It is also useful for earthquake engineers to computationally simulate or experimentally test the seismic performance of structures. To date, many dense seismic networks have been deployed in Japan, California and Taiwan. Their recordings can be easily accessed through websites open to the public. These seismic networks, the features of their instruments, and data processing technique are described elsewhere (Clinton, 2004).

Although a lot of progress has been made in installing seismic instruments, strong ground motion from great earthquakes has not been recorded yet due to the rarity of their occurrence, and the difficulty in anticipating the corresponding regions of strong shakings. The 1985 Michoacan earthquake (M8.2) used to be the largest earthquake, strong ground shaking from which was recorded at several stations (Anderson, Bodin P. *et al.*, 1986). Now, the largest well recorded earthquake is the 2003 Tokachi-Oki earthquake with a magnitude 8.1. To date, no strong ground motions from moment magnitude 9 earthquakes have been recorded. In order to estimate these motions, earthquake engineers have been scaling the amplitude of motions from smaller earthquakes (Bolt and Abrahamson, 2002). There are two serious limitations to this approach. First, the frequency content of shaking from large earthquakes is different from that in smaller events. Second, the peak ground accelerations saturate at larger magnitudes (Cua and Heaton, 2007; Yamada, 2007). As a result, scaling of ground accelerations based on attenuation characteristics of ground accelerations may severely underestimate the velocities and displacements in large events.

With an increased understanding of earthquake sources, propagation paths, local geology, site conditions. Seismologists have begun to simulate strong ground motions from historic and hypothetical scenario earthquakes. Examples include the simulation of the 1923 Kanto earthquake (Takeo and Kanamori, 1997; Sato, Graves *et al.*, 1999), the 1906 San Francisco earthquake (Aagaard, Brocher *et al.*, 2008), an 1857-like San Andreas fault earthquake (Krishnan, Ji *et al.*, 2006; Olsen, Day *et al.*, 2006) and others (Saikia and Somerville, 1997; Hartzell, Leeds *et al.*, 2002). However, all of these earthquakes are moderate to large crustal earthquakes. Not many simulations of strong ground motions from giant subduction earthquakes ($M_w > 9.0$) have been performed (except Heaton and Hartzell, 1989) until recently because of the lack of knowledge of the earthquake sources and the non-availability of recordings. The 2004 Sumatra-Andaman earthquake provides a good opportunity for understanding giant earthquakes. Sørensen *et al.* (2007) and Mavroeidis *et al.* (2008) have used hybrid processing in different frequency bands to simulate the strong ground motions for the 2004 Sumatra event $M_w9.3$ and the 1964 Alaskan earthquake $M_w9.2$, respectively. Olsen *et.al*. (2008) have used a 3D finite difference method to simulate the fully synthetic strong motions for a Cascadia earthquake with magnitude 9.0 using a source model from the Sumatra event. These simulated strong ground motions were gradually introduced to earthquake engineers in dynamic analysis of structures.

1.2.2 Performance of Steel Moment-Resisting Frame Buildings in Earthquakes

The performance of structures in earthquakes is known through computational simulation, experimentally tests as well as the experience in past earthquakes. Among these ways, experience in past earthquakes has had the greatest impact. Almost every destructive earthquake would lead to a modification of a current building code in that area and disclose some unknown phenomena. Olsen (2008) gave a detailed description the performance of steel moment frame buildings in historic earthquakes. Although steel buildings performed relatively well in comparison to other types of buildings at first glance in these moderate

earthquakes, the Northridge and the Kobe earthquake revealed the susceptibility of moment connections in steel buildings to fracture. This mode of failure significantly reduced the ductility and strength of the steel moment-resisting frame (SMRF) buildings. Learning lessons from past earthquake and improving structural design is valuable, but rather slow. Most importantly, engineers noticed that "satisfactory building performance in a moderate earthquake does not imply satisfactory performance in a great earthquake" (Olsen, 2008). No high-rise SMRF building has experienced a giant subduction earthquake ($M_w > 9.0$). Instead of waiting for the next giant earthquake to cause another disaster, we should better predict the performance of SMRF and do some retrofits in advance.

Computational simulation is a powerful tool to understand the performance of buildings and reduce the loss in earthquakes. The simplest conceptual method is to use single- or multiple-degree-of-freedom oscillators to model the linear elastic response of buildings. The response spectrum is widely used in earthquake engineering research for this purpose and plays an important role in elastic analysis. Along with the rapid increase of computational power, the finite element method (FEM) was introduced to earthquake engineering field. Many commercial software packages such as ETABS, SAP2000 and Staad pro were developed. The finite element method allowed engineers to include nonlinear plastic behavior of structural members. Frame-2D developed by Hall (1995) is a powerful program to simulate the nonlinear performance of planar SMRF buildings. It includes material and geometric nonlinearities and has the ability to simulate collapse mechanisms. Krishnan (2003) later extended it to three-dimensions.

Using Frame-2D, Hall and others (1995) simulated the nonlinear response of 20-story SMRF buildings to ground motions that would be expected to occur in the near-source area of a M 7.0 blind thrust earthquake. These ground motions were characterized by pulse-like displacements exceeding 1 m and with velocities exceeding 1 m/s. They found that these large directivity pulses caused large plastic strains that were often localized within several stories, and in some instances the simulations indicated the collapse of the buildings due to P-Delta instability. Olsen and others (2008) simulated the responses of 20-story SMRF

buildings to the synthetic ground motion of the 1989 Loma Prieta and the 1906 San Francisco earthquake and also found significant damage occurring in these long-period buildings.

Using Frame-3D, Krishnan and others (2006) simulated the responses of 18-story steel moment frame buildings in Southern California from ground motion simulations for a M 7.9 earthquake on the San Andreas fault along the segment that last ruptured in 1857. They demonstrate that large amplification of the seismic waves occurs as they propagate through the deep sedimentary basins on which much of urban Los Angeles is constructed. These simulated large ground motions cause very large inelastic deformations within many buildings and simulated collapse occurs in some regions more than 30 km from the fault trace.

The studies of Hall *et.al.*(1995), Olsen *et.al.*(2008) and Krishnan *et.al.*(2006) indicate potential problems with flexible tall moment-frame buildings in large crustal earthquakes. However, far larger earthquakes have occurred at subducting boundaries than have occurred in crustal ruptures; the largest crustal earthquakes are approximately M 8.0, whereas giant subduction earthquakes can be as large as M 9.5, which corresponds to a factor of almost 200 in terms of seismic moment (Kanamori, 1977). It is important to simulate the response of SMRF buildings under this type of earthquakes.

1.3 Our Work and Outline of Chapters

In this study, we use the empirical Green's function approach to simulate the strong ground motions for the 2004 Sumatra-Andaman earthquake and a scenario Cascadia earthquake M_w 9.2. These synthetic motions are used to simulate the nonlinear performance of 6- and 20- story steel moment-resisting frame buildings. The Seattle basin amplification is modeled by a transfer function as well.

Steel moment-frame buildings are chosen for our analysis since their material properties and moment-connection mechanism are better understood than for other building types.

Moreover, they are widely used for many of the nation's most important facilities and commercial office buildings. FEMA354 (2000) reported that most high-rise buildings constructed in the U.S. in the last 30 years incorporate this type of construction.

In Chapter 2 of this thesis, we briefly introduce the characteristics and limitations of the finite element model Frame-2D used in our analysis. Then we discuss eight steel moment frame building models used in this study. They are 6- and 20-story buildings designed according to both UBC94 and the 1987 Japanese building code. For each code, we consider buildings with both perfect welds and brittle welds similar to those observed in the 1994 Northridge earthquake (FEMA-354, 2000).

In Chapter 3, we analyze the ground motions recorded at 276 stations from the 2003 Tokachi-Oki earthquake M_w8.1 and simulate the fully nonlinear dynamic performance of SMRF buildings in this event. Although the low-rise buildings in Japanese coastal villages performed well in this earthquake, the inherently rich long-period ground motions would have exposed many high-rise buildings there to a high potential of damage. A new parameter called the "collapse factor" is introduced to describe the collapse safety margin of structures to a certain ground motion.

In Chapter 4, we briefly describe the empirical Green's function (EGF) method and the reasons to choose this method as our tool. and to choose the 2003 Tokachi-Oki event as empirical Green's functions to simulate the strong ground motions for giant earthquakes.

The 2004 Sumatra-Andaman earthquake M_w9.2 was recorded by global broadband seismometers. The source parameters were determined through these recorded data. The tectonic setting of the Sumatra subduction zone and the size of this earthquake are similar with the earthquake that can be expected to occur at the Cascadia subduction zone. Therefore, we use the source model from this event as the source model for our scenario Cascadia earthquake.

In Chapter 5, we use EGF method to simulate the strong ground motions at Banda Aceh from the 2004 Sumatra-Andaman earthquake and estimate the response of SMRF buildings in that event. Rupture models with wide and narrow fault width and motions at rock and site sites are considered. The simulated strong motions are validated by the local damage in Banda Aceh.

In Chapter 6, we use the EGF method to simulate the strong ground motions in Seattle from the scenario giant Cascadia subduction earthquake and estimate the response of SMRF buildings in that event. Rupture models with wide, median and narrow fault width and motions at rock and basin sites are considered. The Seattle basin amplification is modeled by a basin Green's function through deconvolving teleseismic motions at rock sites from basin sites.

In Chapter 7, we develop a data processing method to obtain broad-band displacements by combining inertial seismic records and high-sample rate GPS records. It is found that some important ground motion intensity measures such as peak ground displacements are sensitive to the data processing techniques. We also found that the performance of buildings sometimes is sensitive to certain data-processing schemes. To faithfully reflect the real ground motions is important not only for seismologists but also for earthquake engineers.

CHAPTER 2

Computational Building Models

Steel Moment-Resisting Frame (SMRF) is a very popular structural system for many low- and high-rise buildings in seismic regions. The absence of diagonal braces and structural walls in this type of buildings allows complete freedom for interior space layout and aesthetic exterior expression (FEMA-354, 2000). Their construction is economical and fast. Most importantly, many reports concluded that SMRFs performed well in the 1906 San Francisco earthquake (Himmelwright, 1906) as well as in the 1971 San Fernando earthquake (Steinbrugge, Schader *et al.*, 1971). Therefore, the SMRF system is the most common type of structural system used in tall buildings in the 10-30 story range in regions with high seismic activity, such as Los Angeles, San Francisco, Portland and Seattle.

In this chapter, we first discuss the advantages and limitations of finite element models used in our dynamic time history analysis and then discuss the design of steel moment-resisting frame (SMRF) buildings used in this analysis.

2.1 Computational Method

To assess the potential performance, including collapse of high-rise SMRF buildings to large ground motions, the computational model we used must have the capacity to capture the nonlinear large lateral deformation. Frame-2D, a seismic nonlinear structural simulation program developed by Hall (1997), meets this requirement. This program is based on a

planar-frame fiber-element model that includes both material nonlinearities as well as geometric nonlinearities. Most importantly, Frame-2D updates buildings' configuration for each time step. This automatically accounts for the P-Delta effects (AISC 2005) and allows the analysis to follow a building's response well into collapse. In the following, the main features of this model are briefly described. Hall (1997) contains a thorough discussion of the structural behavior assumptions and other details of this program.

2.1.1 Beam-Column Elements

Beam-column elements are the primary component of a moment-resisting frame system. There are many beam-column mathematical models that could account for material and geometric nonlinearities. These models can be classified into two main categories: plastic hinge model and fiber model. Frame-2D employs fiber model.

The plastic hinge model is the earliest and most widely used method in structural analysis to incorporate material nonlinearity of a frame structure. It concentrates plastic hinges on a discrete cross-section and the rest of the member between hinges is assumed to remain elastic. Although this model is computationally efficient and easy to apply, it includes strain hardening and moment-capacity reduction in a crude way. Moreover, residual stresses can not be included. When residual stress or details of the yielding process become important, plastic hinge model is inadequate (Hall and Challa, 1995).

The fiber model is a distributed plasticity method and could accurately capture the gradual spread of yielding within the cross section and along the member length. In addition, this method can naturally include residual stress, stress hardening and moment-capacity reduction which are important features for modeling cyclic loading. Hall and Challa (1995) gave a detailed comparison of these two methods.

In Frame-2D, beam-column elements are subdivided into eight segments along their length. Their cross sections are divided into eight to ten fibers (figure 2.1). Each fiber has an axial stress-strain hysteretic relation shown in figure 2.2. The parameters that is used to define

the skeleton curve is listed in table 2.1. Notice that in this hysteresis model, the yield stress remains constant until strain reaches a very large value. However, in real experiment, the yield stress would gradually decrease when local flange buckling is developing (figure 5.19).

Table 2.1. The stress-strain parameters of the steel used in this study

	Parameters	English Units (ksi)	Metric (ton/cm^2)
E	Initial elastic Young's modulus	29,000	2040
E_{SH}	Initial modulus at strain hardening	580	40.8
σ_Y	Yield stress	42	2.96
σ_U	Ultimate stress	50	3.52
σ_{RES}	Residual stress	6	0.42
τ_Y	Shear yield stress for panel zone	24.0	1.69
G	Shear modulus for panel zone	11,600	816
ε_{SH}	Strain at strain-hardening	0.012	
ε_U	Strain at ultimate strength	0.160	
ν	Poisson's ratio	0.3	

2.1.2 Panel Zone

Connections are the medium through which moments and forces are transferred from one structural member to another. They are the other essential elements in modeling MRF system besides beam-column elements. Their participation in the cyclic energy dissipation is also important.

In the earlier research, connections are idealized as zero dimensional points. Later, finite rigid joints and finite flexible joints are introduced gradually. In Frame-2D, finite-size panel zones are modeled. They have similar hysteresis model as steel fiber (figure 2.2) (Hall, 1997). Double plates can be modeled in this panel zone element. However, the strength degradation contained in the hysteretic model also is relatively simple.

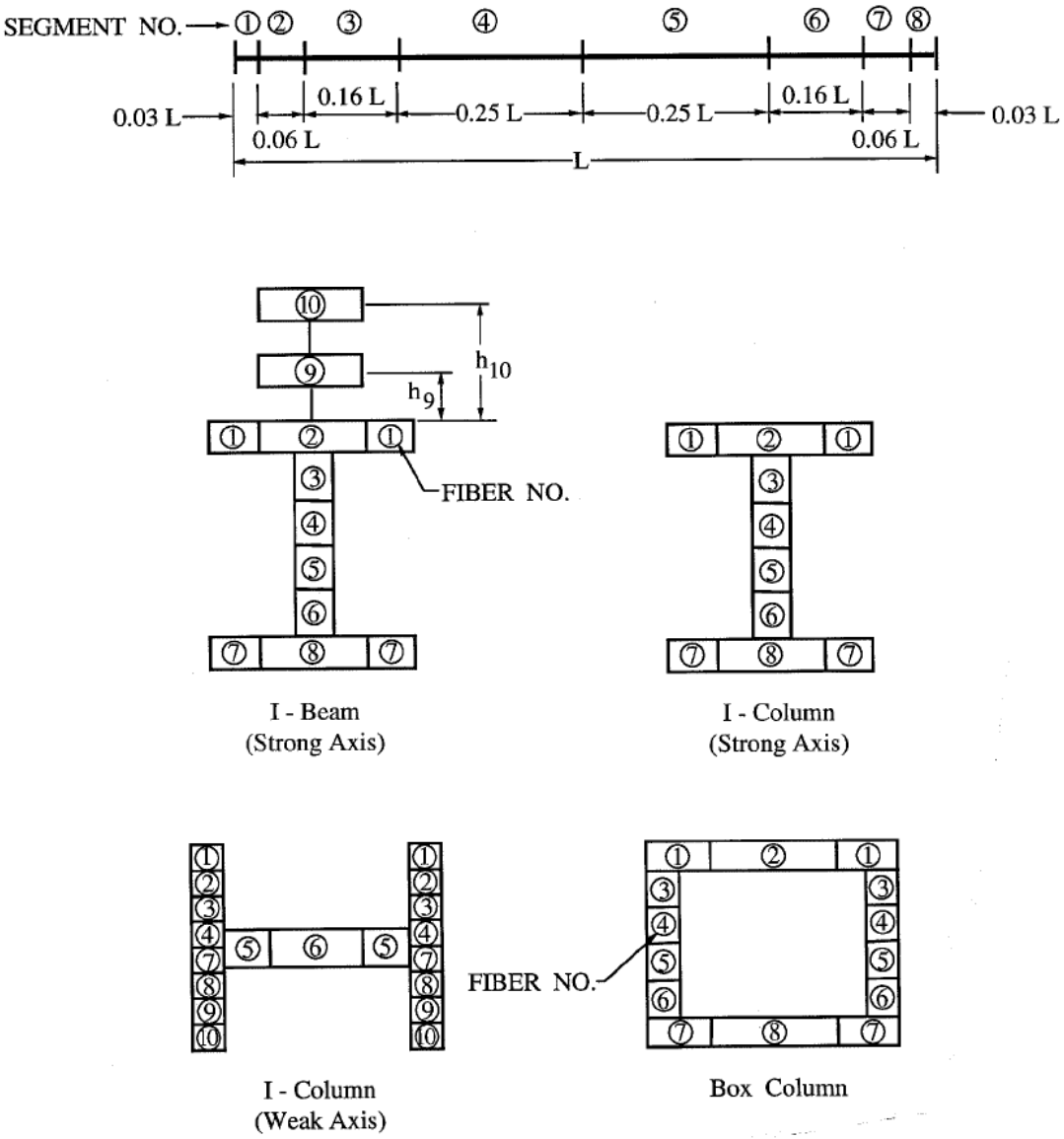

Figure 2.1. Segment layout (top) and fiber layout (bottom) for beams and columns used in this study. Fibers 9 and 10 in the strong axis orientation are used only for beam to represent composite action with a metal deck and concrete slab (Hall, 1997).

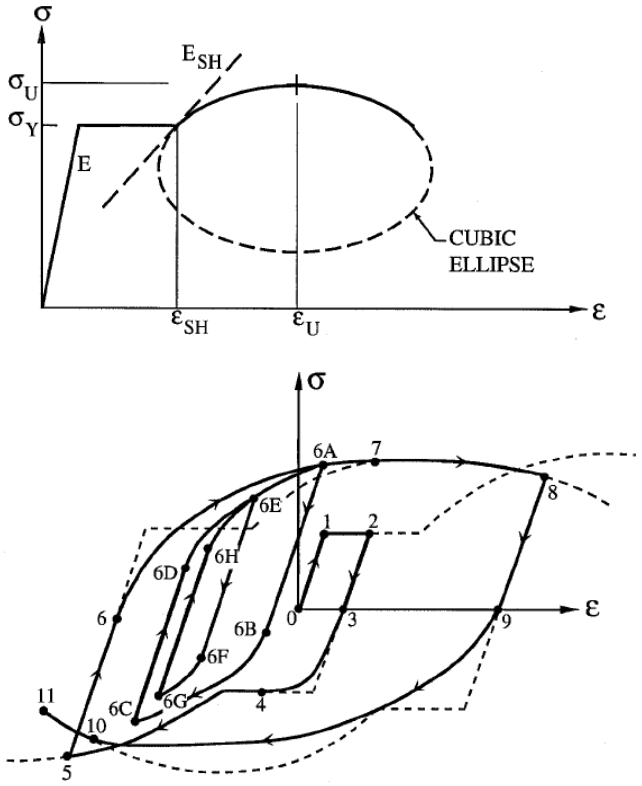

Figure 2.2. The top figure shows the backbone curves for beam or column steel fiber and the bottom figure shows the axial stress-strain hysteresis relation for this fiber. Panel zone hysteresis is similar to that of the fiber. The stress-strain parameters of the steel skeleton curve used in this study are listed in table 2.1 (Hall, 1997).

2.1.3 Weld Fracture

Frame-2D also has the capability to model welds fracturing. Prior to the 1994 Northridge earthquake, it was commonly assumed that welded connections had significantly stronger plastic yield strength than other structural elements and that steel frames would only yield because of plastic deformation of the structural steel. However, numerous welded connections were found to fracture along steel MRF's in the near-source area of the Northridge earthquake (SAC Joint Venture, 1996). Emergency code change was implemented in 1995 to correct this problem in the US. (FEMA, 1995) and in Japan (JASS 1996). However, the vast majority of existing buildings probably have connections

susceptible to fracture which would dramatically lower the lateral force-resisting capacity and the ductility of the building.

In Frame-2D, each fiber in the end-segment of beams and the segment where column splices would be located is assigned a fracture strain ε_f using a randomized process. When the strain in the fiber reaches this fracture strain ε_f, fiber fractures and loses its ability to sustain tension in the future, but it can carry compression when contact is regained. The distribution of fracture strain ε_f is user defined. Figure 2.3 gives the detailed fracture strain probability distribution density used to model our brittle welds building. This distribution is compatible with the observations of welds in the 1994 Northridge earthquake (Hall, 1998). For example, the bottom flange of beams has a median $\varepsilon_f = \varepsilon_y$, while the top flange of beams has a median $\varepsilon_f = 10\ \varepsilon_y$ (Hall, 1997), where ε_y is the yielding strain. This guarantees that the bottom flange of beam is easier to fracture than the top flange. For buildings with perfect welds, fracture strain for all the connections are set to be infinity.

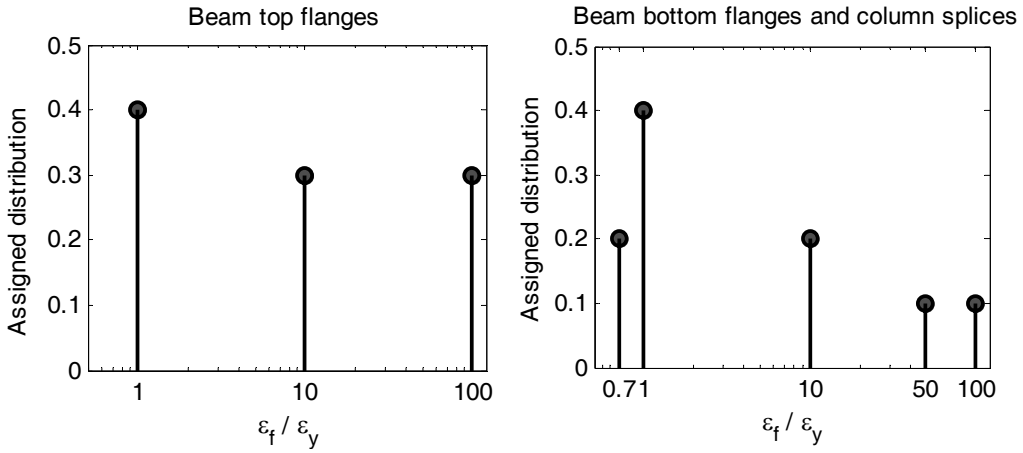

Figure 2.3. Fracture strain distribution of different connections for brittle welds used in this study. The left panel shows the set for top flanges of the beams and the right panel shows the set for bottle flanges of the beams and column splices.

2.1.4 P-Delta Effects

P-Delta effect refers to the 2nd order over-turning moment resulting from the weight of the structure acting through the lateral displaced configuration of the structure (figure 2.4). For low-rise structures with small deflection, this effect is small and can be ignored. However, for high-rise structures experienced large ground motions, this effect can significantly reduce the buildings' lateral force-resisting capacity and trigger collapse (Challa and Hall, 1994; Gupta and Krawinkler, 2000).

In Frame-2D, P-Delta effects are included by geometrically updating the global nodal translation and rotation at each time and satisfying the equations of dynamic equilibrium in the updated configuration of the structure

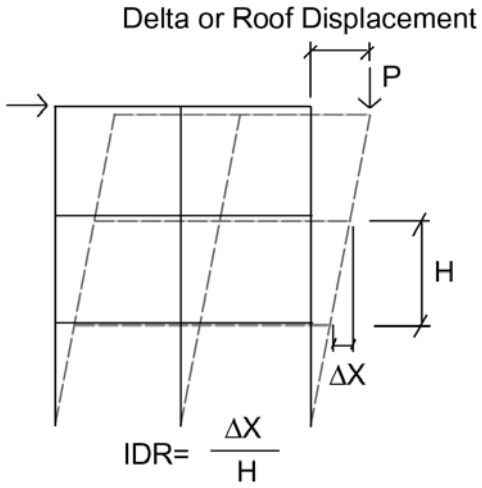

Figure 2.4. Illustration of P-Delta effects on a SMRF and the definition of interstory drift ratio (IDR) and roof displacement (RD).

2.1.5 Limitations of Frame-2D

There are two main limitation of the Frame-2D. The first one is that this is a 2-dimentional model. For regular symmetric buildings, this model is sufficient. Since the center of gravity and rigidity are the same for these buildings, no torsional eccentricity would be generated,

so steel MRF buildings can be simplified as several separated planar frames in the narrow dimension of the building, which has larger stress than the wide dimension of the building due to the smaller stiffness. For simpler irregular SMRFs, this 2-dimensional model can still be used by placing the moment frames in a three dimensional setting with correct location and orientation (Hall, 2002). However when plastic deformation occurs in the building, the stiffness symmetry may break. This may cause discrepancy of results from 2-dimensional and 3-dimensional models. Moreover, for more complicated irregular SMRFs, three-dimensional treatment is necessary. FRAME3D developed recently by Krishnan (http://www.virtualshaker.caltech.edu/), can be used in such cases.

The other limitation is slightly simple strength and stiffness degradation model in Frame-2D for basic elements. Strength degradation can be caused by many factors such as local flange and lateral-torsional buckling, temperature increasing, weld fracture, column tension splice rupture, etc. However, weld fracture is the only degradation mechanism modeled in Frame-2D. In other words, in our simulation, there is no strength degradation for buildings with perfect welds. Many studies have revealed that when the structure members are exposed to repeated reversal inelastic deformation for a long time, accumulated developed damages have a high potential to cause structural collapse (Villaverde, 2007). To incorporate these degradations in the dynamic modeling is a challenge research topic and is out of scope for this thesis. Almost all these modeling limitations indicate that the true behavior of SMRFs could be worse than the simulations undertaken here.

2.2 Buildings Considered

2.2.1 General Characteristics

In this study, we consider four types of SMRF buildings. They are 20- and 6-story buildings designed by Hall according to two codes: the 1994 Uniform Building Code (UBC94) assuming seismic zone 4 and soil site S2 (corresponding to soil type B in UBC97)

and the Japanese building code updated in 1987. Two weld conditions: brittle and perfect (refer section 2.1.3) are considered. The notations of these buildings are listed in table 2.2. For example, U20B represents a 20-story SMRF building designed according to UBC94 with brittle welds. And J6P represents a 6-story SMRF building designed according to Japanese code with perfect welds. Overall there are eight building models. All of these SMRFs are symmetric and their floor plans and planar frames elevations participating in modeling are shown in figure 2.5 to 2.8. Detailed design parameters can be found in Hall (1997).

The main difference between buildings designed according to U.S. and Japanese codes is that Japanese buildings have more moment connections at the middle frame (Frame C in figure 2.6) than U.S. buildings which use simple connections for all joints in the middle frame. As a result, the Japanese model has greater strength and stiffness than the U.S. model, which can be easily seen from the pushover curves in figure 2.10. The reason behind this difference is that the Japanese code prefers stronger buildings while the U.S. code prefers long period buildings which can avoid resonance during moderate earthquakes. The natural period of each model are listed in table 2.3.

The height above the ground is 77.88 m for our 20-story buildings and is 24.54 m for the 6-story buildings. These two models will be assumed to be representative of high-rise and low-rise SMRFs in the US and in Japan. In this study, 20-story building is the main type of building that we are interested in and 6-story building is used mainly for comparison.

Table 2.2. Building types

The 1st letter	U	buildings designed according to the 1994 Uniform Building Code (ICBO 1994).
	J	buildings designed according to the Japanese building provision published at 1987 (IAEE 1992).
The 2nd letter	20	20-story steel moment-frame buildings
	6	6-story steel moment-frame buildings
The 3rd letter	B	buildings with brittle welds at connections
	P	buildings with perfect welds at connections

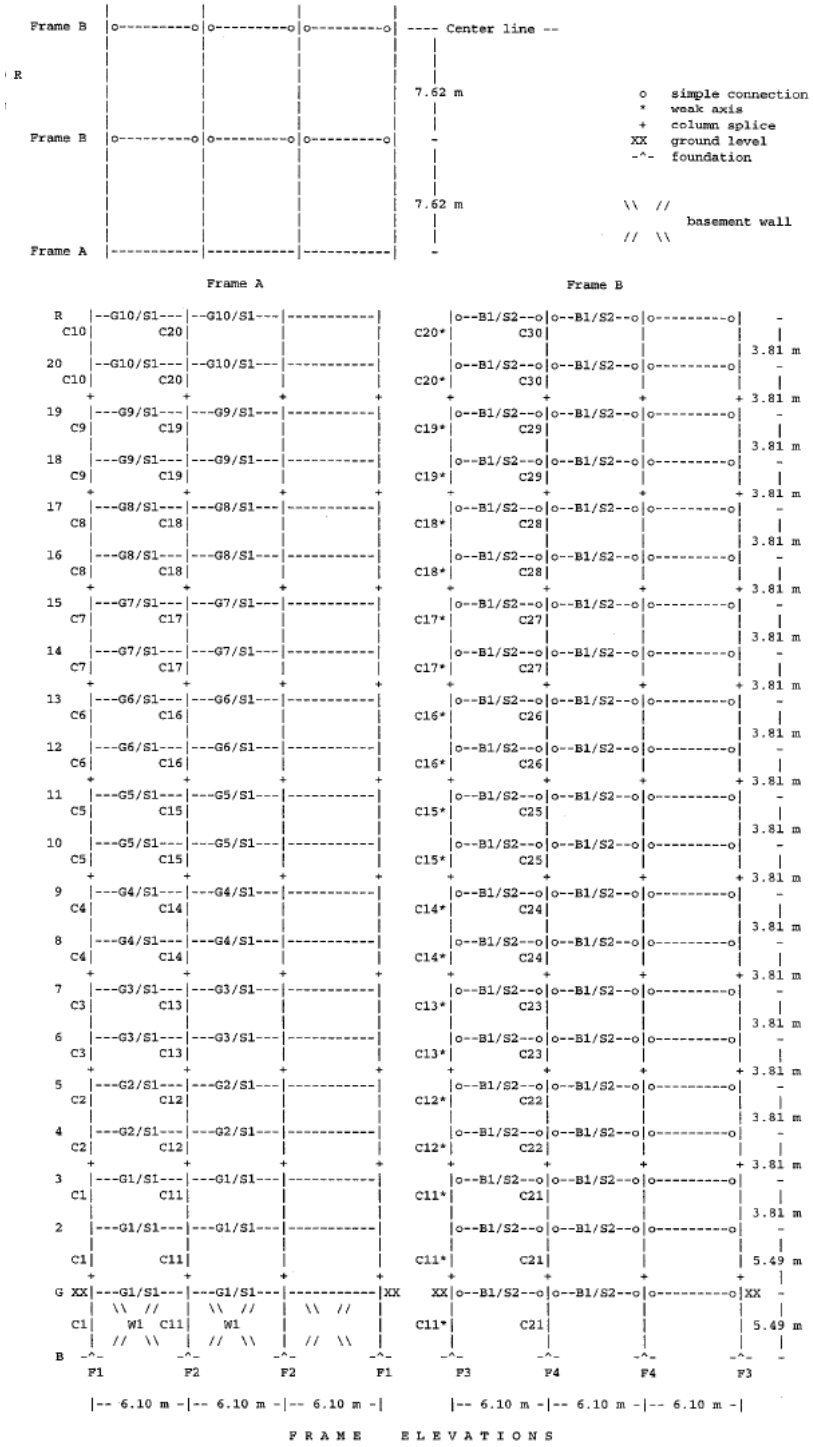

Figure 2.5. Floor plan and frame elevations of the 20-story building designed according to the UBC94 (U20) (Hall, 1997).

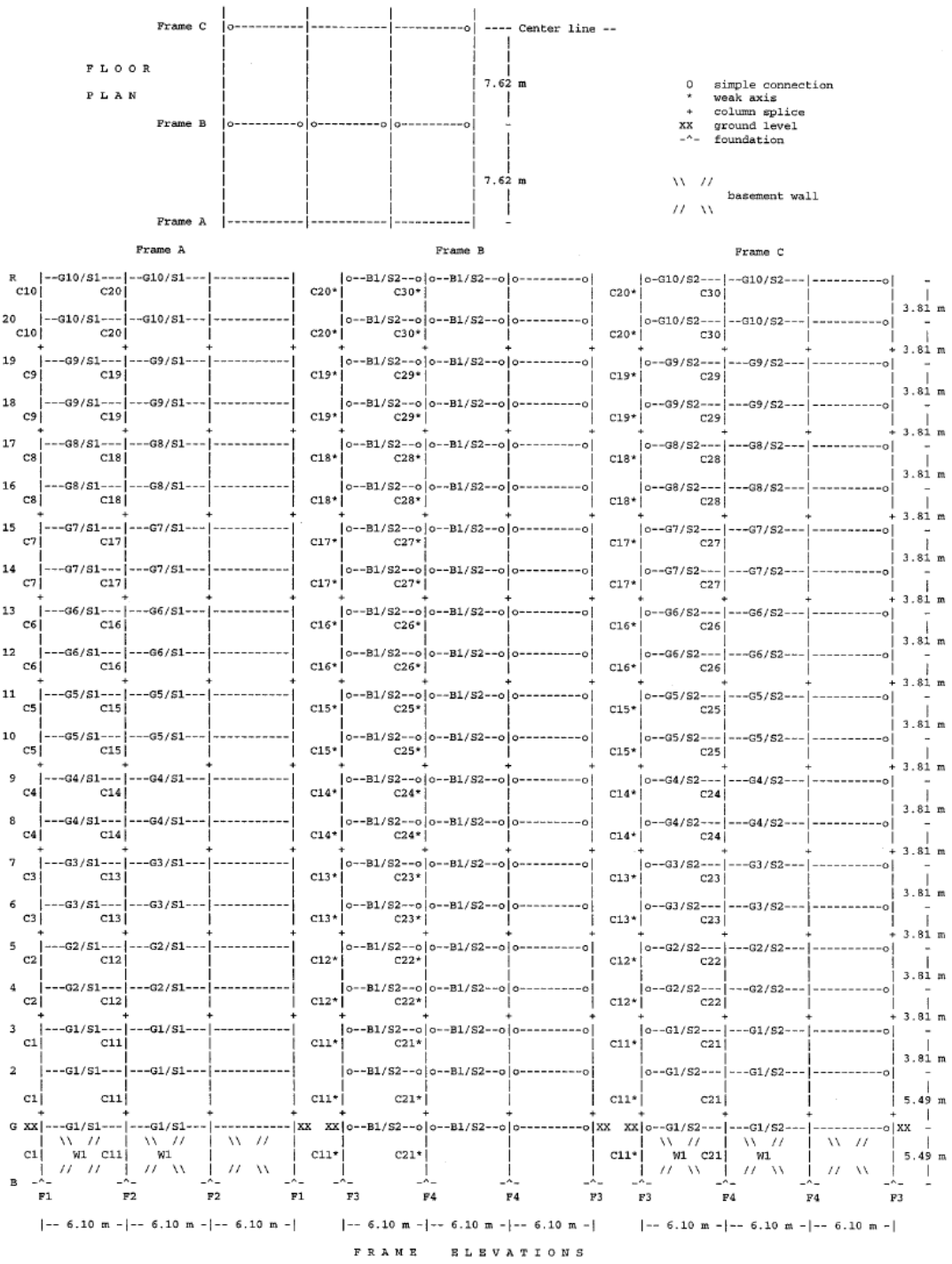

Figure 2.6. Floor plan and frame elevations of the 20-story building designed according to the Japanese building code (J20) (Hall, 1997).

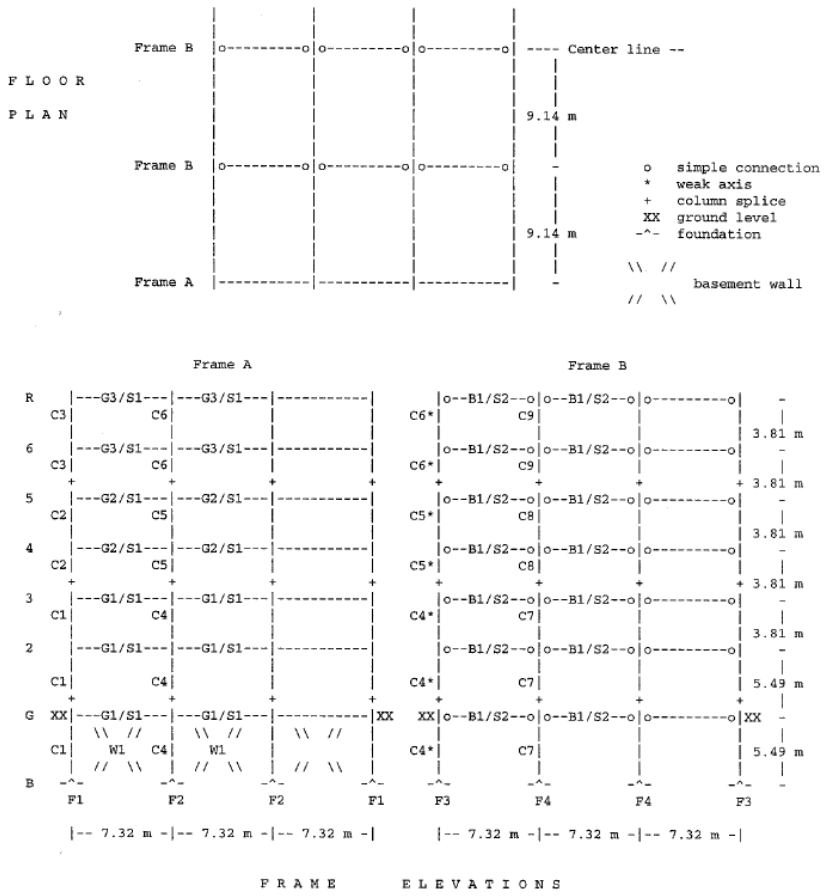

Figure 2.7. Floor plan and frame elevations of the 6-story building designed according to the UBC94 (U6) Reproduce from Hall (Hall, 1997).

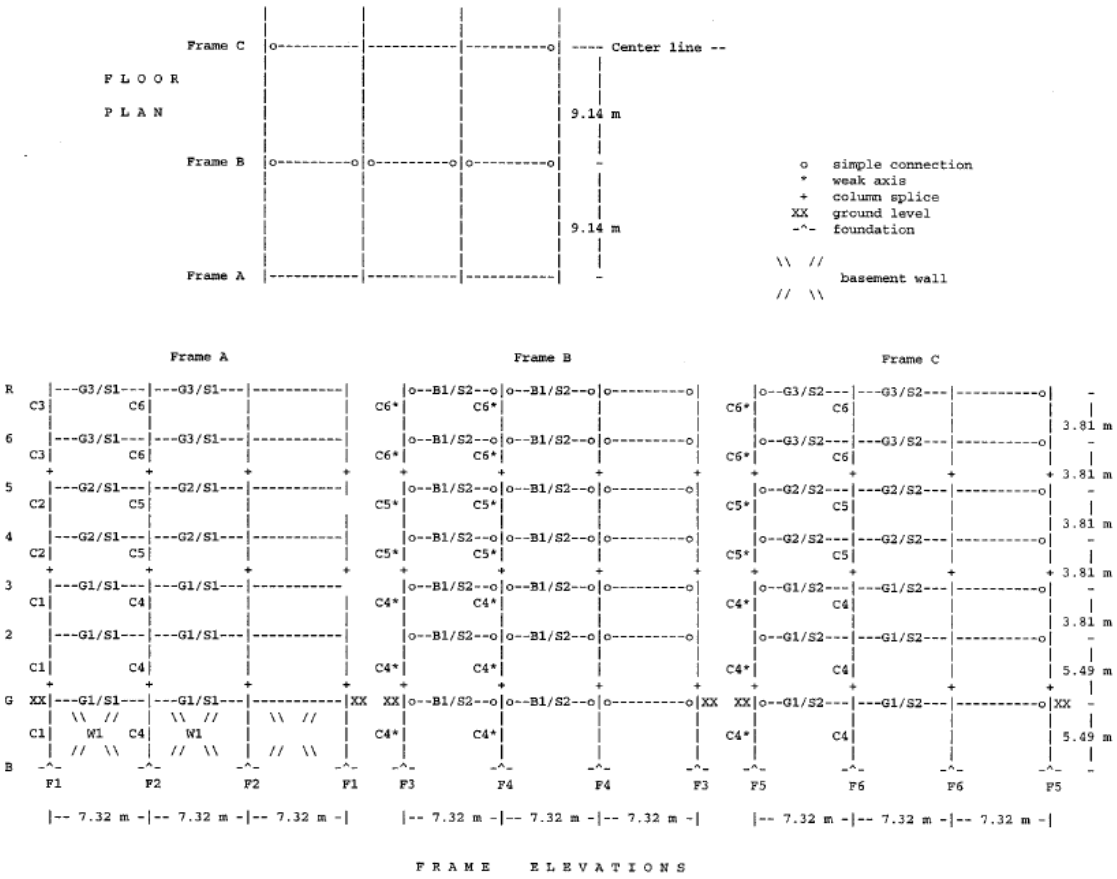

Figure 2.8. Floor plan and frame elevations of the 6-story building designed according to the Japanese building code (J6) (Hall, 1997).

Table 2.3. Characteristic values of the buildings

Building Type	U20B	U20P	J20B	J20P	U6B	U6P	J6B	J6P
Elastic Natural Period (in the narrow direction)	3.5 sec		3.05 sec		1.5 sec		1.17 sec	
Pushover Yield Strength %	4.9	9.5	8.2	12	9.5	17.0	20.1	31
Pushover Peak Strength %	6.6	10.5	8.3	14.6	16.8	22.8	24.5	39.7
Pushover Yield Displacement (cm)	30	65	35	65	10	20	12	24
Ductility	1.9	3.6	1.8	3.5	2.0	9.6	2.1	8.4

2.2.2 Pushover Analysis

To qualify the actual strength and ductility of buildings, pushover analysis is applied. Pushover curves relate the base shear strength which can be carried by structures (given as a percentage of the building weight) to the lateral roof displacement. To generate this curve, a building is subjected to a slow, ramped, horizontal ground acceleration that increases at the rate of 0.3g per minute. Stiffness, yield base shear, peak base shear and ductility of buildings can be obtained from pushover curves. The definitions of these parameters are illustrated in figure 2. 9 and their values are listed in table 2.3.

Hall (1997) contains a detail discussion about pushover analysis. Here, we compare the pushover curves for all the eight models in figure 2.10. Solid lines correspond to buildings with brittle welds whereas dashed lines correspond to buildings with perfect welds. From this figure, we can find that the 6-story buildings are stiffer and can carry much higher loads than the 20-story buildings. The ductility for the 6-story buildings is also much larger than the 20-story buildings because P-Delta effects are greater in high-rise buildings. As we already mentioned, the Japanese buildings are stiffer and stronger than the U.S. buildings. It is apparent that the presence of brittle welds could significantly reduce the pushover yield strength and ductility of the buildings.

2.2.3 Discussion

The models used in this study seem slightly out of date: designing according to pre-1995 codes and using yield stress = 42 ksi (Nowadays much stronger steels are used which have yield stress around 50 ksi). Recently, there were some concerns about the satisfaction of U20 to the drift limit of UBC94 and its reasonable representative of UBC-94 design. Hall and Krishnan (Oct. 2008) reran the analysis by different programs and contradicted these arguments. They showed that the U20 is an appropriate design under UBC94. Since there are numerous existing SMRF buildings built before the 1994 Northridge earthquake in

most seismic regions in the US, these models could be considered representative of the current building stock.

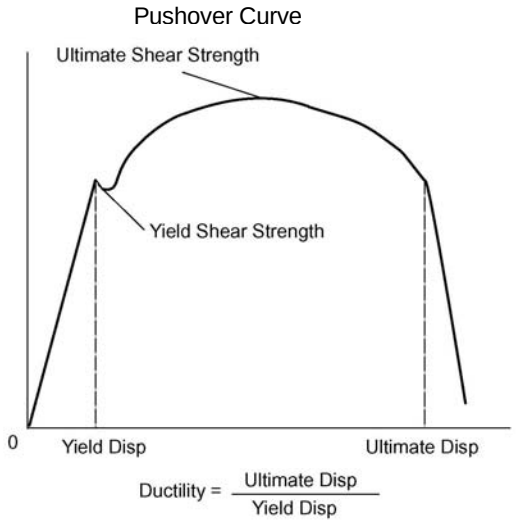

Figure 2.9. The definitions of ductility, yield strength and ultimate strength of a building on a pushover curve. Ultimate displacement is the place where pushover curve began to drop dramatically.

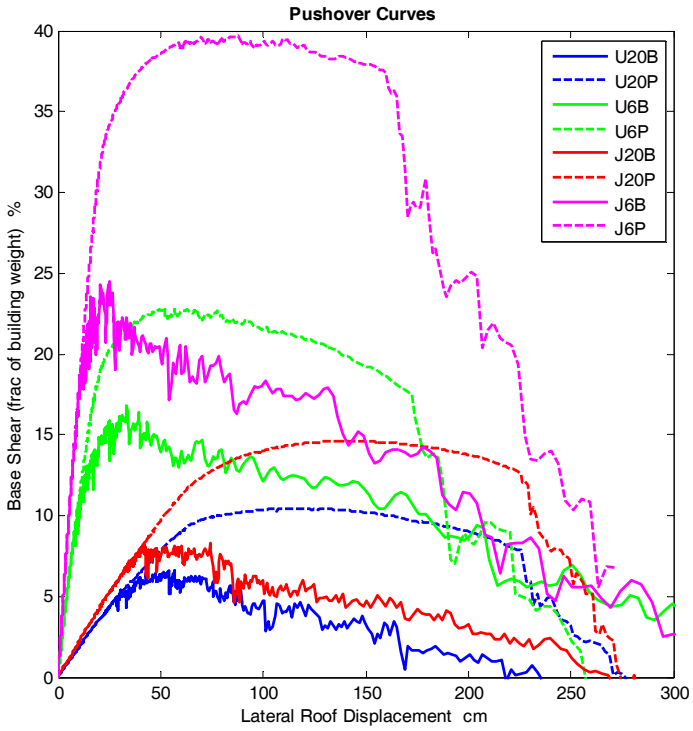

Figure 2.10. Pushover analysis of the 6- and 20-story steel moment frame buildings designed to the UBC94 and Japanese code with brittle welds and perfect welds.

Hall (1998) compared the building models used in this study to the UBC97 seismic provision. After the 1994 Northridge earthquake, there have been many improvements adopted in the building codes and construction practice. The main difference between UBC94 and UBC97 seismic design is that UBC97 uses near-source factors and requires lateral force resisting systems to resist larger earthquake force if located in a region close to active faults. The results show that J6 satisfies UBC97 and J20 satisfies only the near source factor less than or equal to 1.2 which corresponds to the location 10km from a seismic source with strong seismic activity.

If A572 steel (σ_y = 50 *ksi* and σ_u = 65 *ksi*) is used in our buildings, it also could increase the global strength of buildings. Figures 2.11 and 2.12 compare the pushover curves of the buildings using steel which has a yield stress σ_y = 42 *ksi* to those using steel with yield stress σ_y = 50 *ksi*. We can find that U20-50 is upper bounded by J20.

Above all, the current designed buildings are stronger than our building models, however, strengthening existing high-rise buildings is not an efficient method and in some ground motions, stronger and stiffer buildings perform even worse than more flexible buildings, which was discovered in section 5.5.3 and discussed in detail in section 6.5.3. Therefore, we still use σ_y = 42 *ksi* in this study for all the buildings unless stated otherwise.

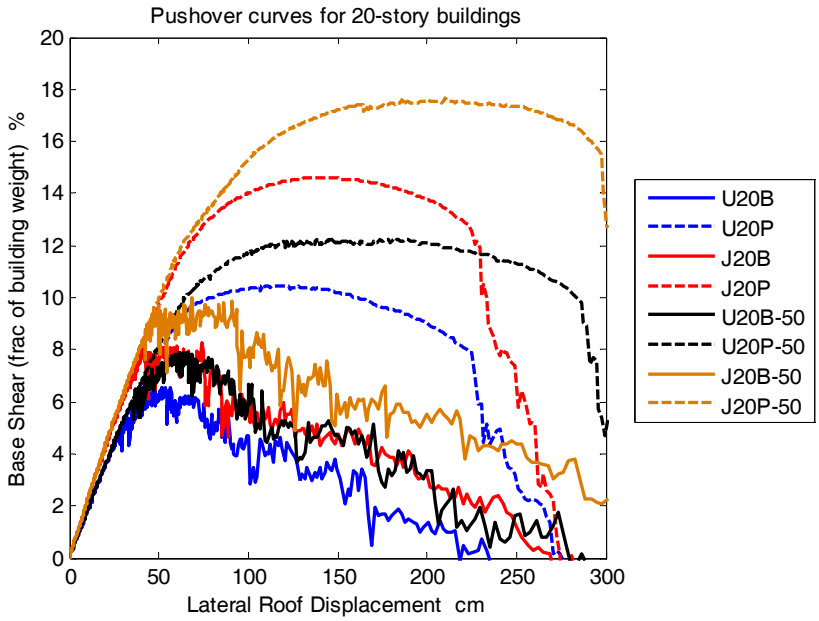

Figure 2.11. Comparison of pushover curves of the 20-story buildings using steel with yield stress σ_y = 42 ksi to those buildings using steel which has yield stress σ_y = 50 ksi.

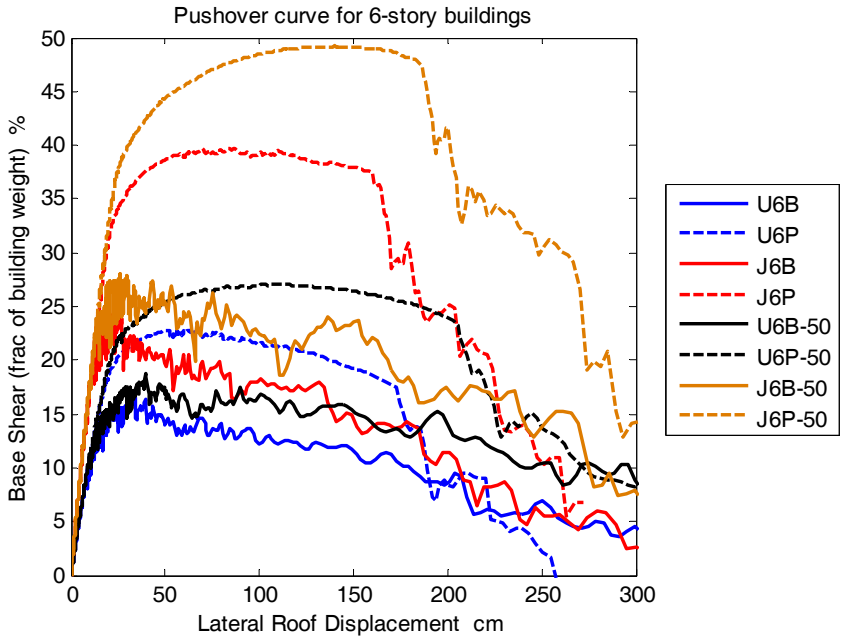

Figure 2.12. Comparison of pushover curves of the 6-story buildings using steel with yield stress σ_y = 42 ksi to those buildings using steel which has yield stress σ_y = 50 ksi.

CHAPTER 3

26 September 2003 Tokachi-Oki, Hokkaido, Earthquake M_w 8.1

The 2003 Tokachi-Oki earthquake M_w8.1 is the largest well-recorded earthquake till now and was recorded by various densely distributed seismic and GPS networks in Japan. It was the first time that large amplitude, long-period ground motions, which are characteristics of large subduction earthquakes, were densely recorded at many sites in Japan. The strong ground motions recorded at this event are good sources for us to study giant subduction earthquakes. In this chapter, we simulate the fully nonlinear responses of buildings mentioned in Chapter 2 from 276 strong motion stations located on Hokkaido Island. The results are analyzed and a new parameter called the "collapse factor" is introduced to describe the collapse safety margin of structures to a certain ground motion.

3.1 Introduction

On September 26, 2003 at 19:50 (GMT), a moment magnitude (M_w) 8.1 subduction earthquake occurred along the Kuril trench off Tokachi, Hokkaido, Japan. The hypocenter was at 41.78° N, 143.90° E, about 80 km east-southeast of Cape Erimo, at a depth of 27 km (USGS report). The Kuril trench is a highly active subduction zone where the Pacific plate is subducted toward N60°W beneath Hokkaido region at a rate of about 80 mm/year (Demets, Gordon *et al.*, 1990). Figure 2.1 gives the locations of the largest historic

earthquakes along this subduction interface during the past half a century (Yagi, 2004). By using teleseismic body waves, Yamanaka et al. (2003) estimated the main source parameters as follows: (Strike, dip, rake) = (230°, 20°, 109°), fault area is 90 × 70 km^2, the maximum slip is 5.8 m, the average slip is 2.6 m and the source duration is 40 sec. The geometry cross section of this region is shown in figure 4.4. The detailed structure of this region can be found in Iwasaki *et al*. (1989).

Despite the proximity of this large event to the island of Hokkaido, damage was relatively mild. There are numerous coastal towns in southeastern Hokkaido, but there are no large cities within the region of heaviest shaking. The short, stout buildings of Japanese coastal communities performed well in this long-period shaking. The most serious damage was due to sloshing in petroleum storage tanks located about 150 km west of Cape Erimo, which is the peninsula that juts out over the rupture surface (ABS Consulting Inc, 2003). This sloshing was undoubtedly caused by the large long-period ground motions generated by this event.

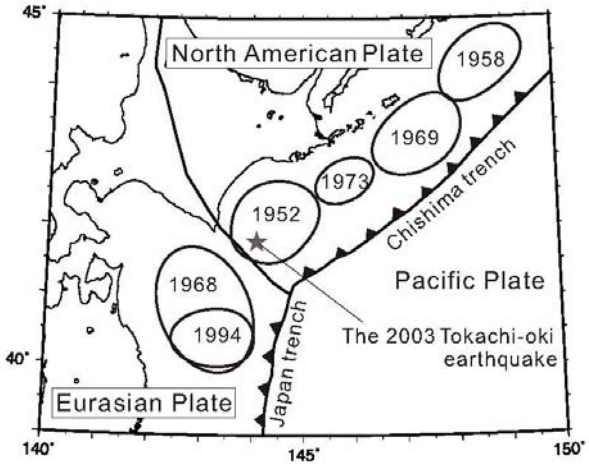

Figure 3.1. Historic large and giant earthquakes happened on Hokkaido region. The contours represent the source area for each event (Yagi, 2004). 1952 (Ms 8.2), 1958 (Ms 8.1), 1969 (Ms 7.8), and 1973 (Ms 7.4).

3.2 Recorded Strong Ground Motions and Site Condition on Hokkaido Island

The strong ground motions of 2003 Tokachi-Oki earthquake were recorded by various densely distributed seismic networks (K-Net, KiK-Net, H-Net etc) and geodetic networks in Japan. The raw data can be downloaded from the websites of Japanese National Research Institute for Earth Science and Disaster Prevention (NIED). Clinton (2004) contains a comprehensive description of these networks and their data. Both networks use K-NET95 accelerometers, with 144*dB* dynamic range and a clip of 2*g*. Frequency bandwidth is from about 20Hz to DC, so there is no need to remove instrument responses. Sampling frequency is 100 Hz for K-Net and 200 Hz for KiK-Net. In this chapter, we use records from 276 K-Net and KiK-Net stations located on Hokkaido Island (figure 3.2).

To show the ground motion intensity of this event, peak ground acceleration (PGA), velocity (PGV) and displacement (PGD) are calculated. It is unfeasible to recover the real ground displacements for all the stations in this event (discussed in page 33), so a zero-phase 4^{th}-order Butterworth filter at frequency 0.02 Hz is applied to all the records before these ground motion intensity measures are calculated. Pseudo spectral accelerations (PSA) for all the stations are also calculated at periods T=1.5 sec and 3.5 sec for 5% damping. These periods are about the natural periods of U6 and U20 respectively. PSA = $\omega^2|x(t)|_{max}$, where $|x(t)|_{max}$ is the maximum displacement of a mass in a one dimensional spring-mass system with a fixed natural period subjected to ground motion. The bigger values of the two horizontal components (EW and NS) are chosen as our ground motion intensities. Table 3.1 lists the maximum values and figures 3.2 to 3.3 show the distributions of these values.

This ground motion dataset shows the significant spatial variation of shaking on Hokkaido Island. Hatayama *et.al.,* (2007) carefully investigated the spatial variation of long period strong ground motions within the Yufutsu basin (figure 3.3) and concluded that the thickness of near-surface (<1 km) soft sediments rather than bedrock depth governs the spatial variation of amplitudes of the long period (7 to 8 second, natural period of oil storage tank). His study also showed that the Yufutsu basin not only amplified the ground

motion amplitude but also elongated the strong shaking from 20 sec to more than 100 sec (figure 2 in Hatayama *et.al*.).

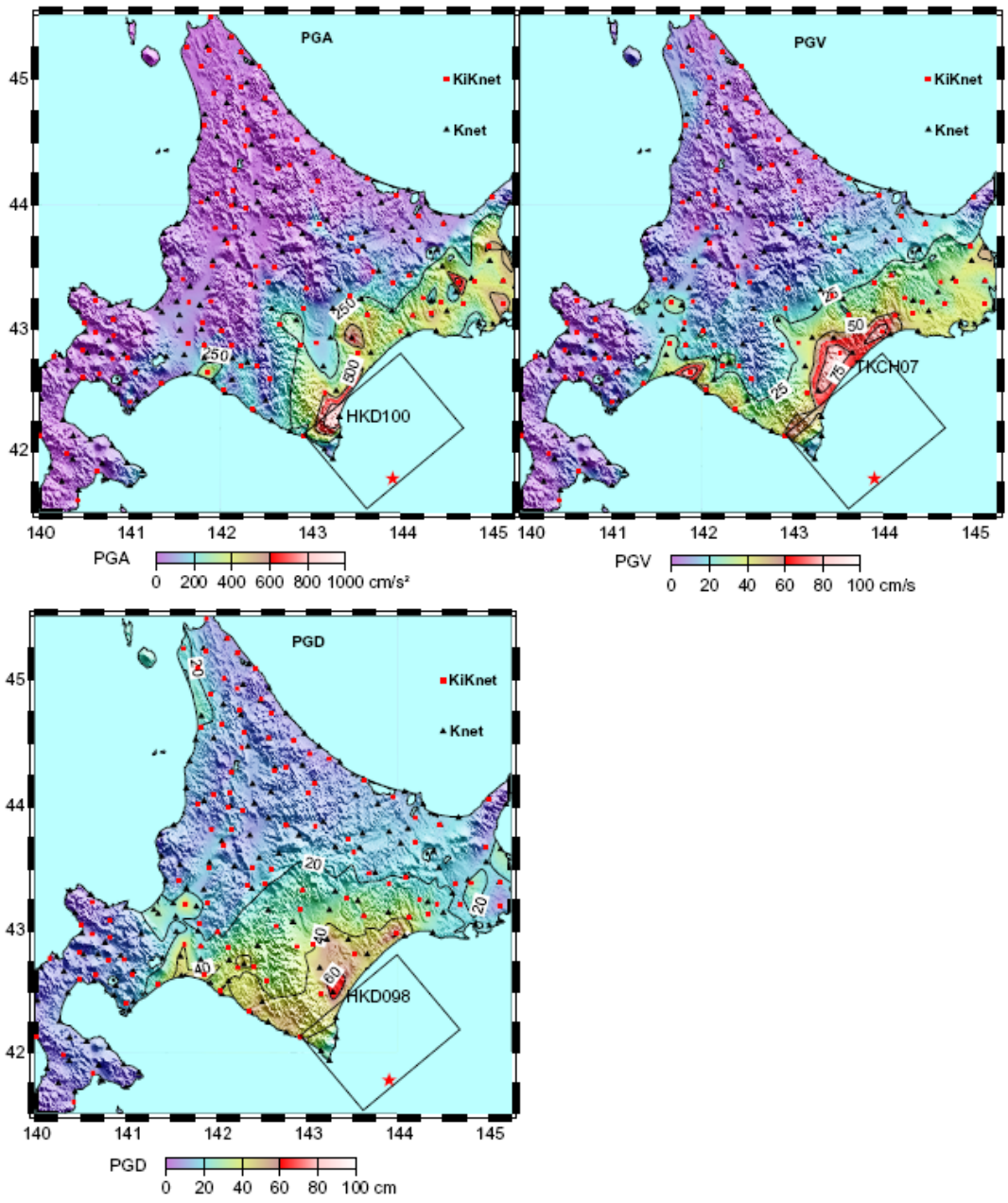

Figure 3.2. The distributions of PGA, PGV and PGD. Locations which have the largest values are labeled on maps. Zero-phase 4th-order Butterworth filters at frequency 0.02 Hz are applied. The largest PGA is 0.97g, the largest PGV is 0.96 m/s and the largest PGD is 0.6 m.

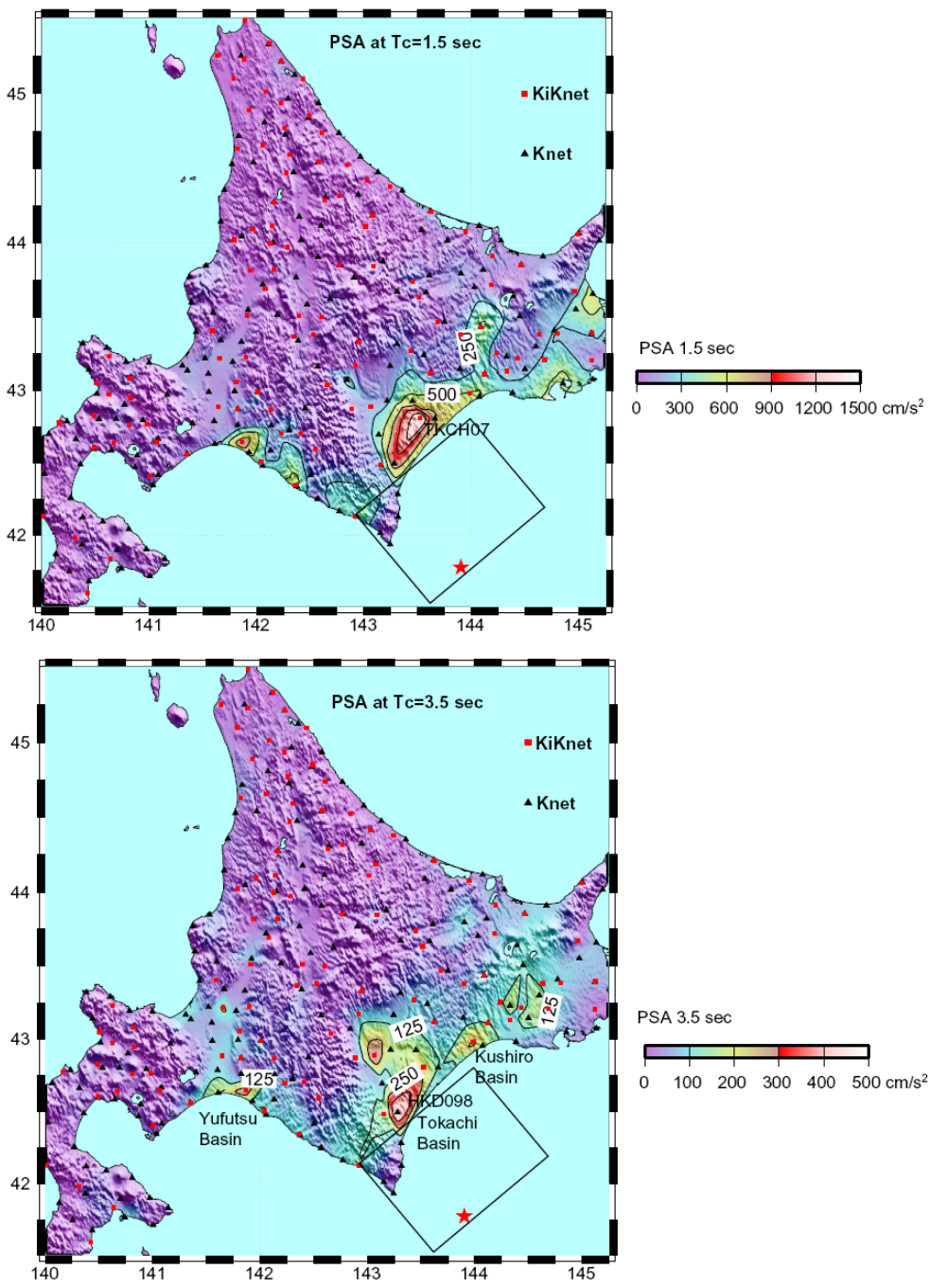

Figure 3.3. The distributions of pseudo spectral accelerations at periods of 1.5 sec (natural period of U6) and 3.5 sec (natural period of U20) for 5% damping. The largest $PSA_{1.5}$ is 1.4g and the largest $PSA_{3.5}$ is 0.45g. Comparing with PGA, PGV and PGD, the distribution of PSA is more consistent with the topography of Hokkaido Island at these long periods. Stations with larger PSA are concentrated at Tokachi Basin and Yufutsu Basin

Table 3.1 Maximum PGA, PGV, PGD, $PSA_{1.5}$ and $PSA_{3.5}$

	Maximum peak value	Location
Ground Acceleration	0.97 g	HKD100
Ground Velocity	96.6 cm/s	TKCH07
Ground Displacement	63.6 cm	HKD098
Pseudo Spectral Acceleration at 1.5 sec (natural period of U6) for 5% damping.	1.422 g	TKCH07
Pseudo Spectral Acceleration at 3.5 sec (natural period of U20) for 5% damping.	452 cm/s^2	HKD098

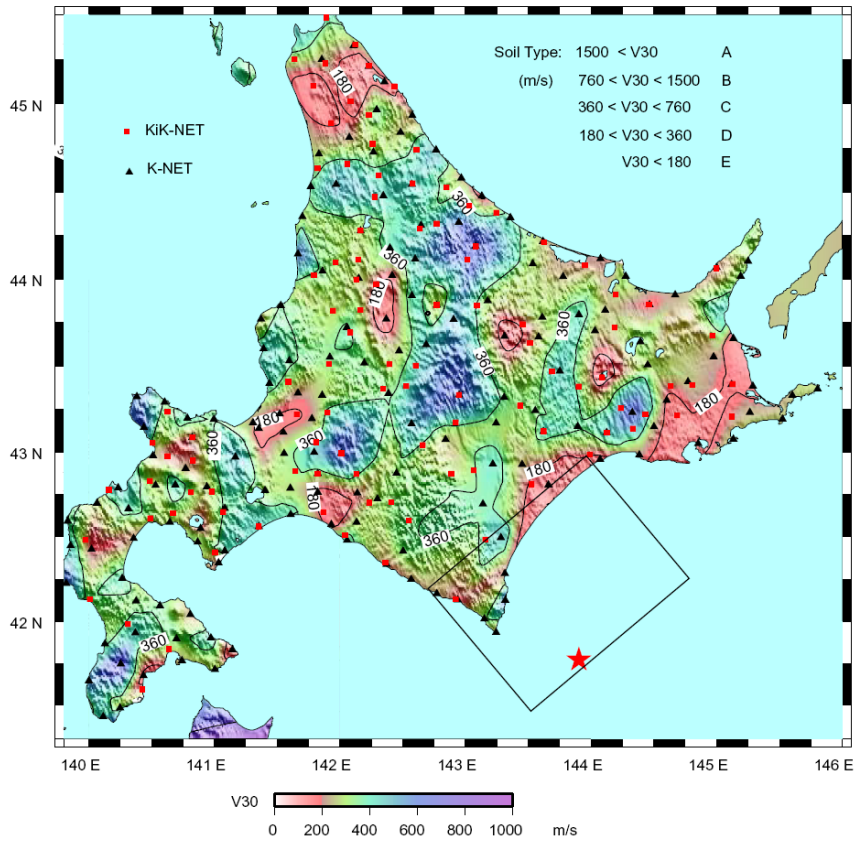

Figure 3.4. Contours of the average shear wave velocity in the upper 30 meters. The site classification criterion used in UBC97 and IBC is listed in the upper part of the figure. Soil type E (basin) is show in red colors. Soil type D is in green. Soil type C is in blue. Most stations are located at site C, D and E.

Engineers are used to describing local site condition in terms of V_s^{30}. It is the average shear-wave velocity in the upper 30 m (~100 ft) of the deposit. UBC97 and IBC both use this parameter as the primary basis to classify site categories. For each K-Net station, soil

condition has been investigated down to a depth of 10 to 20 meters. This information allows us to approximately estimate the V_s^{30} by assuming the velocity of the remaining deeper soil equals the deepest measured velocity. It should be noticed that this assumption would underestimate V_s^{30} and give a lower limit. The V_s^{30} is calculated from the following formula:

$$V_s^{30} = \frac{\sum_{i=1}^{n} d_i}{\sum_{i=1}^{n} \frac{d_i}{V_{si}}} \tag{3.1}$$

where V_{si} is the shear-wave velocity of the i^{th} soil layer and d_i is its thickness. The site classification criterion and the contour map of V_s^{30} can be found in figure 3.4. It could roughly capture the basin areas but some areas in Tokachi Basin are classified as soil class C. It indicates that V_s^{30} alone is not enough to represent the site conditions.

Although accelerometer K-NET95 is capable to capture the ground motion over a wide range of frequencies, sometimes even can provide reliable static displacements after the earthquake ceases, displacement time series obtained from double integration of acceleration recordings are often plagued with unrealistic baseline drifts and grow dramatically with time (most commonly as t^2). Many issues can induce this drift: instrument tilt, baseline offsets and other unknown sources of long-period noise. Researchers have also proposed numerous data processing techniques to eliminate the displacement drift (USGS data; Caltech EERL report 1974-1976; Iwan, Moser *et al.*, 1985; Boore, 2001; Zhu, 2003; Shakal, Huang *et al.*, 2004). Unfortunately, all of them require the specification of processing parameters that strongly affect the derived ground displacements. We developed a scheme (Chapter 7) to better estimate the broadband ground displacements by combining the seismic records with high-sample rate GPS records. This methodology is easy to implement and is consistent and robust for all stations. However, it requires colocated seismic and GPS stations. In this seismic event, only a few seismic stations have colocated GPS stations. Therefore, using Boore's method (Boore, 2001), we carefully ansalyzed each record in an attempt to recover the static ground displacement and show horizontal radial (parallel to the trench) ground displacements at

selected stations in figure 3.5. The largest displacement was about 1.5 m and occurred at station HKD098.

The accelerograms corrected only for preevent means are used in this study to simulate the response of buildings. Although acceleration is insensitive to data processing in most cases, it generates different responses for the same building model when processed by different correction schemes (Yang and Heaton, 2005). To avoid the potential artificial effects, we use raw accelerations (corrected for preevent means) as our input to Frame-2D.

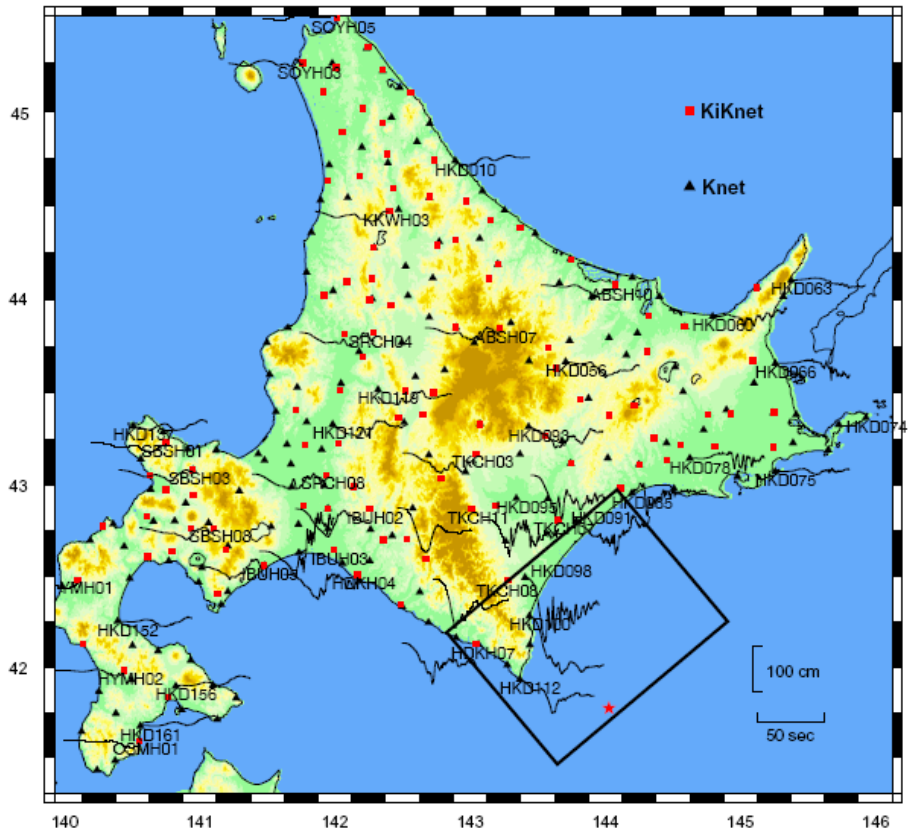

Figure 3.5. Locations of 276 K-Net (black triangle) and KiK-Net (red square) stations that recorded the 2003 Tokachi-Oki earthquake (M_w 8.1) on Hokkaido Island. The approximate surface projection of the rupture is given by the black rectangular box (Yagi, 2004). The radial components of ground displacements for selected stations are also shown. The red star is the epicenter of this event. The largest recorded displacement was 1.5 meters.

3.3 Nonlinear Performance of Buildings

Although short, stiff buildings performed well in this earthquake, an obvious question is raised by this event. How well would tall, flexible structures perform in these long-period ground motions? In order to answer this question, we simulated the responses of four tall buildings described in Chapter 2 (U20, J20 with brittle welds and perfect welds) using 276 ground motions recorded on Hokkaido Island. Their responses are compared against the low-rise U6 and J6 buildings, also described in Chapter 2. The results are presented in the form of contour maps.

In this study, we use the peak interstory drift ratio (IDR) as the main quantity to evaluate the performance of buildings. Other parameters such as roof displacement relative to the ground and percentage of fractured welds among all beam-to-column connections are also provided to assist the response evaluation. Interstory drift ratio is the relative horizontal displacement of adjacent floors divided by the story height. For steel moment frame type of structure which can be modeled by a shear beam, interstory drift ratio basically is the shear strain of one story. Roof displacement is defined as the relative horizontal deflection between roof and foundation. These definitions are graphically illustrated in figure 2.4. The responses of buildings located at 276 stations are illustrated on contour maps. Figure 3.6 to 3.9 map the peak interstory drift ratio in the U20, J20, U6, and J6 with brittle and perfect welds. All the peak values and the corresponding location are listed in table 3.2.

The peak IDR of U20B is 3.8% at station HKD098. This value is very close to collapse, which will be discussed in next section. Many stations along the coastal area have peak IDRs exceeding 1.5% and they have more than 15% connection welds fractured. It reflects the large deformation and yielding occurring in the buildings.

The contour maps show clearly that the strong ground shaking would affect 20-story buildings in a larger region than 6-story buildings. High-rise buildings in Yufutsu and Ishikari basin (shown in the bottle map in figure 3.3) would experience more deformation than low-rise buildings in these areas.

The contour maps also confirm that buildings with perfect welds perform much better than buildings with brittle welds. The regions with peak IDR exceeding 1.5 % is much smaller for 20P than 20B. This improvement is much higher than that getting from strengthening buildings (from the U.S. buildings to the Japanese buildings) especially for buildings with perfect welds. The collapse factor introduced in section 3.5 could confirm this argument in a quantitative way.

From these figures, we find that the roof displacements of buildings designed to the Japanese code are greater than these of the U.S. buildings although the peak IDR are smaller for J20/J6 than for U20/U6. The reason is that the higher yielding strength required by Japanese code results in stiffer building (as can be seen from pushover curves in figure 3.2), so the deformation is distributed more evenly to each story instead of localized in bottom or weak story. This also explains the same phenomena for buildings with brittle welds and perfect welds that larger maximum interstory drift ratios associated with smaller roof displacements.

Figures 3.16 to 3.17 combine the pushover curves with the histogram of maximum roof displacements for 20- and 6-story buildings respectively. They provide another way to show how many buildings would yield on Hokkaido during this event. It is easy to find that the existing brittle welds would cause buildings yielding in much more stations. Furthermore, in some stations, the amount of lateral force carried by structures with brittle welds begins to decrease and the damage caused is irreparable. The similarity between histograms of U20 and J20 also confirms that increasing the strength of building alone (from U to J) does not change the station distribution much. However, the 6-story buildings remain elastic in more stations than the 20-story buildings.

Figures 3.6 to 3.9 show that buildings located to the northeast and to the southwest (around IBUH03) suffered strong shaking even though they are almost 200 km away from the epicenter. The disaster investigation team from ABS Consulting Inc. also reported that in the area around station IBUH03, large petroleum storages tanks were serious damaged by sloshing (ABS Consulting Inc. report 2003). Another feature is that ground motions

directly above the rupture at Cape Erimo caused less simulated damage than stations located in a band just to the northwest. Comparing with contour map of V_s^{30} (figure 3.4), both of these facts are effects of the local site geology. The basin areas indicated by red color in figure 3.4 have apparent site amplification effects in figures 3.6 to 3.9.

In general, the whole coastal region would have been strongly shaken by the 2003 Tokachi-Oki earthquake if there had been high-rise buildings. Although none of the buildings collapsed in these simulations, the peak IDRs in some stations (eg. HKD098) were very close to collapse level. This indicates that if there existed a 20-story steel moment frame building of pre-Northridge earthquake type, it would have had very high potential of collapse. We will discuss this issue in more detail in section 3.5.

Table 3.2. Summary of response for each type of buildings

Building Type	Peak IDR %	Max RD cm	Fractured welds %
U20B	3.8	93	38
J20B	3.4	103	36
U20P	2.1	129	
J20P	2.5	144	
U6B	5.5	79	55
J6B	4.8	75	58
U6P	4.0	70	
J6P	2.8	49	

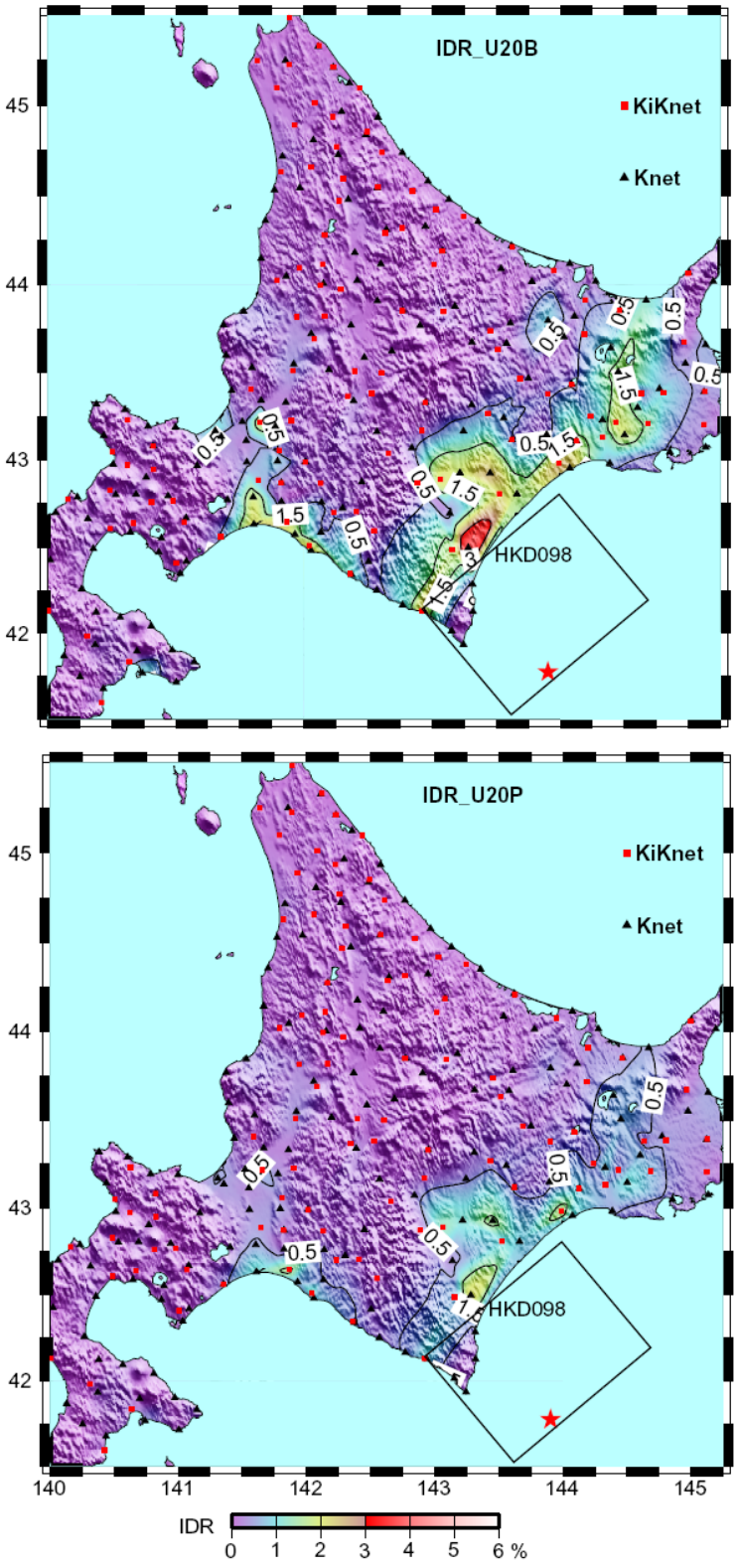

Figure 3.6. Peak interstory drift ratio (IDR in percent) for U20B and U20P. The maximum value is 3.8% and 2.1% respectively, and both occurred at station HKD098.

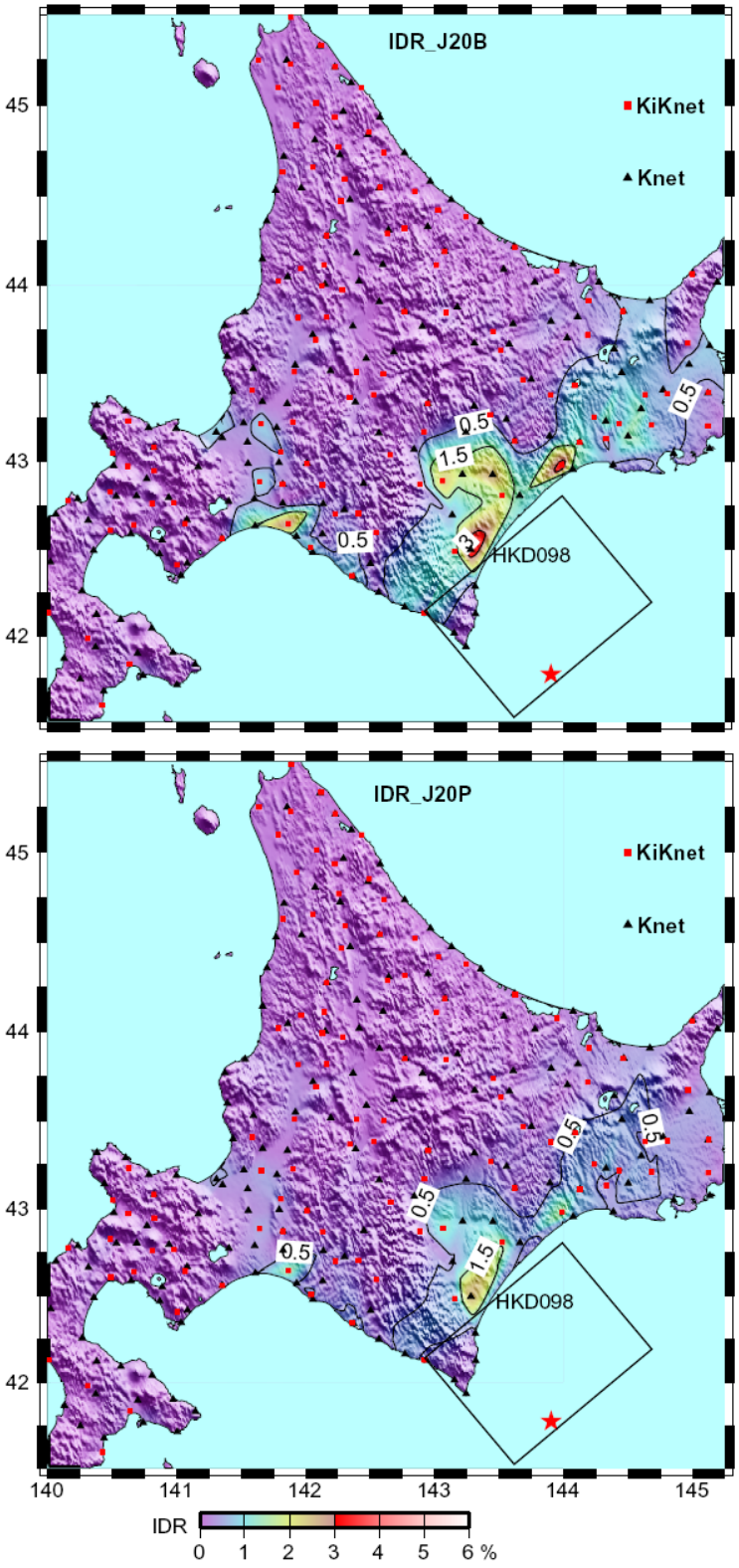

Figure 3.7. Peak interstory drift ratio (IDR in percent) for J20B and J20P. The maximum value is 3.4% and 2.5% respectively, and both occurred at station HKD098.

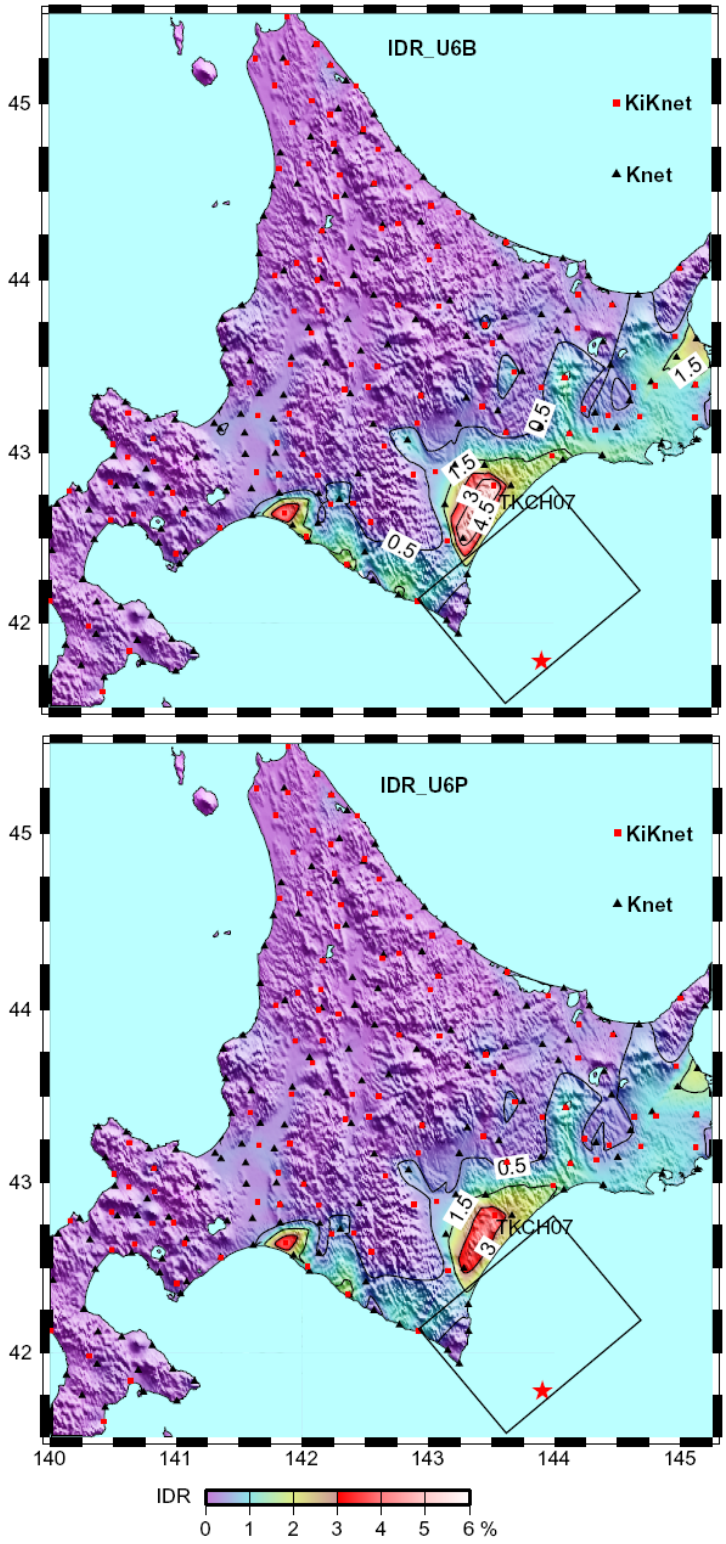

Figure 3.8. Peak interstory drift ratio (IDR in percent) for U6B and U6P. The maximum value is 5.5% and 4.0% respectively, and both occurred at station TKCH07.

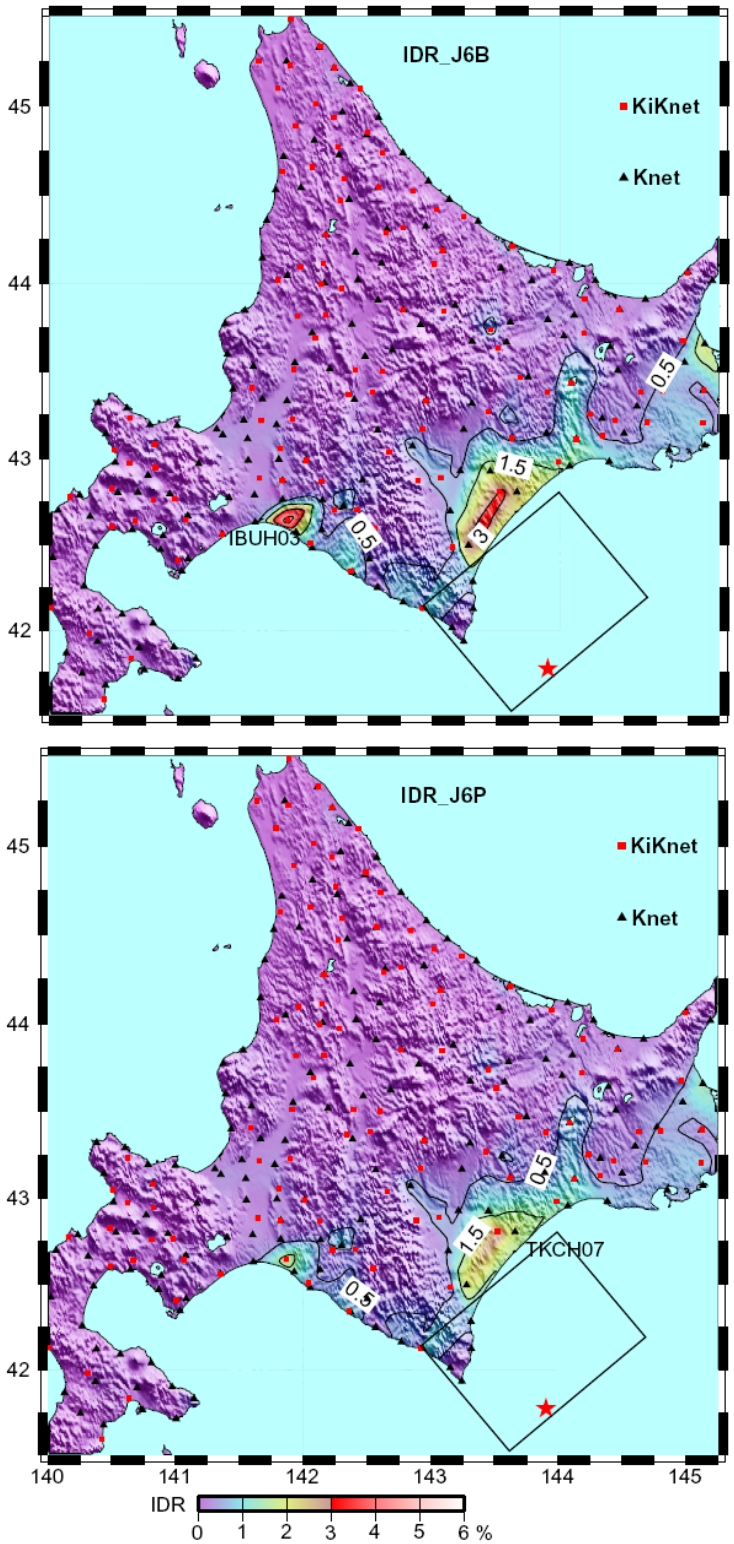

Figure 3.9. Peak interstory drift ratio (IDR in percent) for J6B and J6P. The maximum value is 4.8% at IBUH03 and 2.8% at TKCH07 respectively.

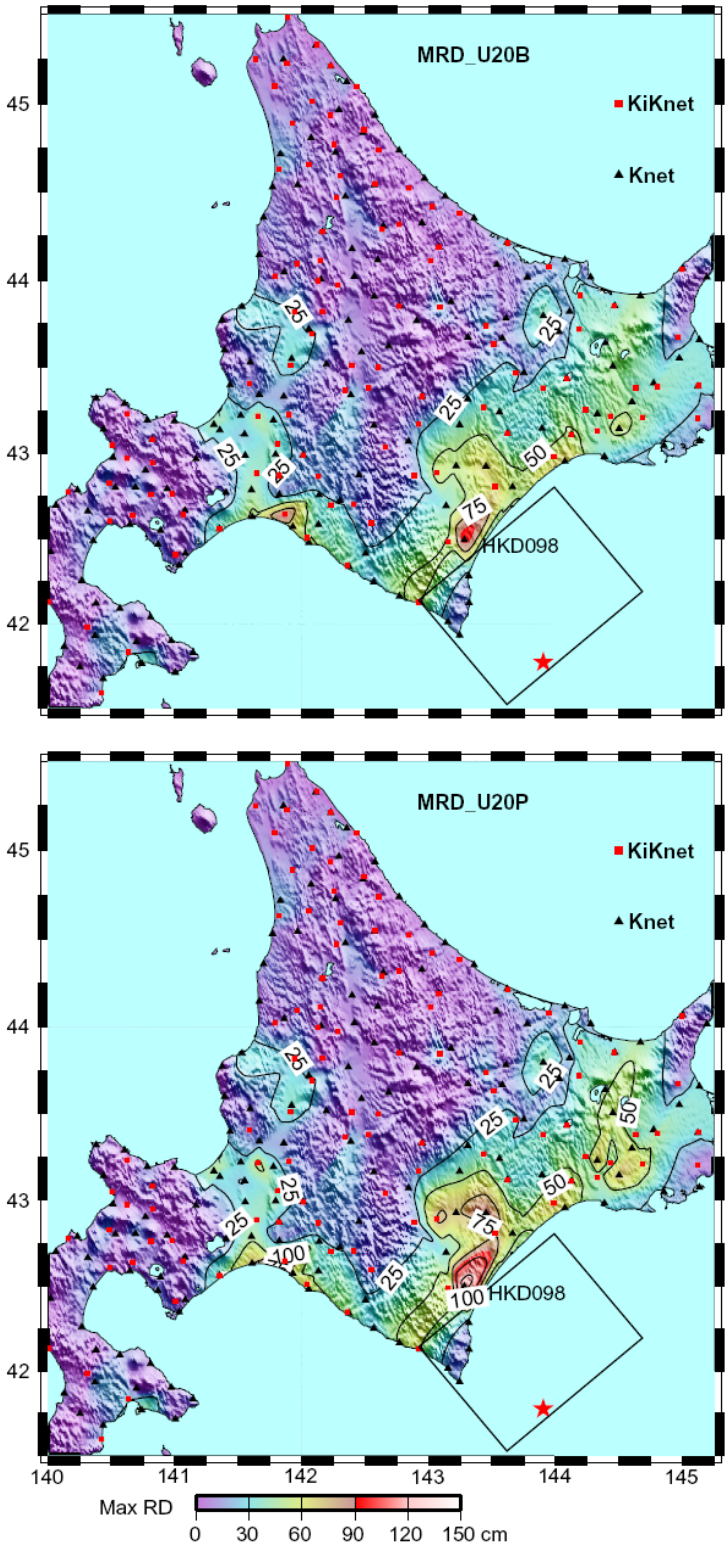

Figure 3.10. Maximum roof displacement for U20B and U20P. The maximum value is 93 cm and 129 cm respectively, and both occurred at station HKD098.

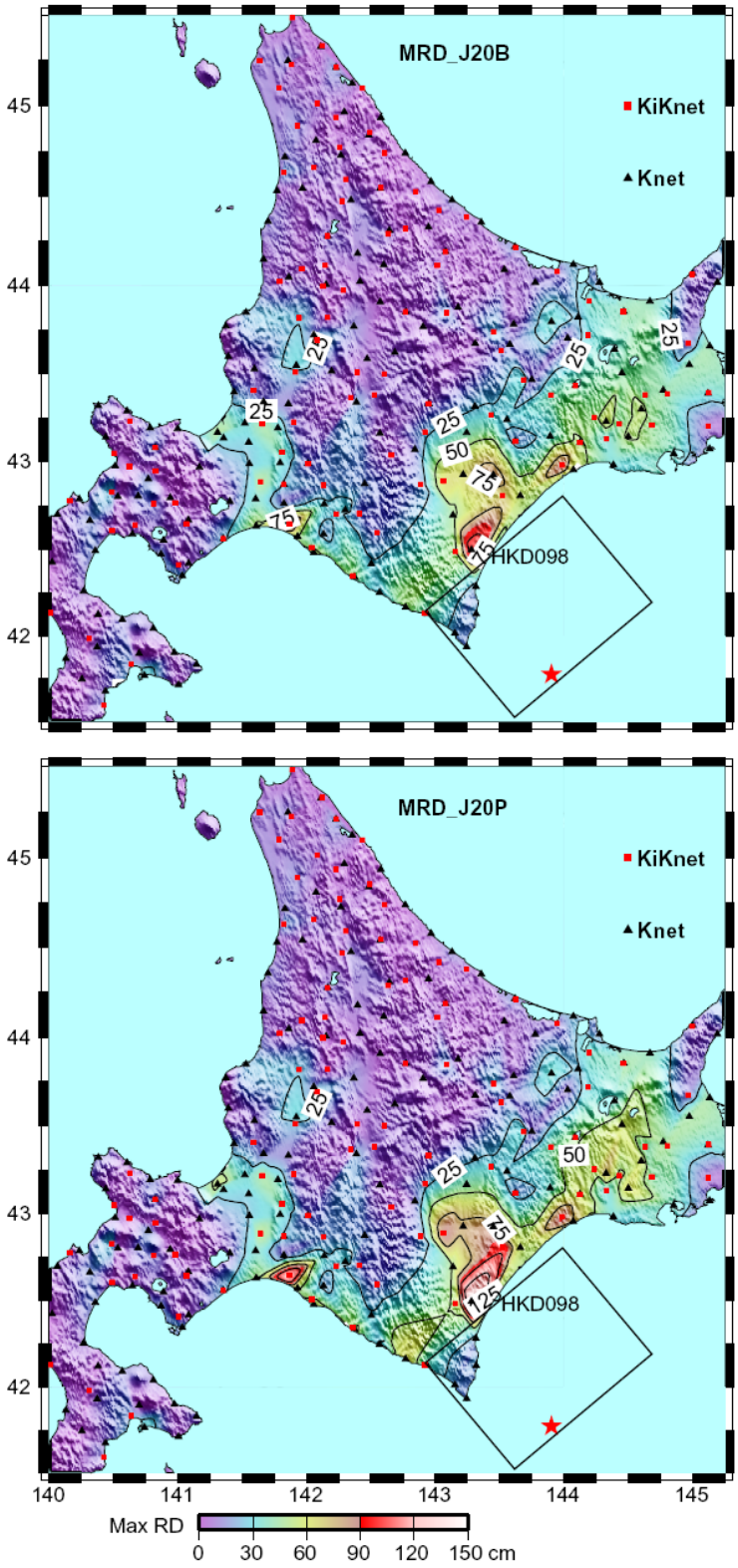

Figure 3.11. Maximum roof displacement for J20B and J20P. The maximum value is 103 cm and 144 cm respectively, and both occurred at station HKD098.

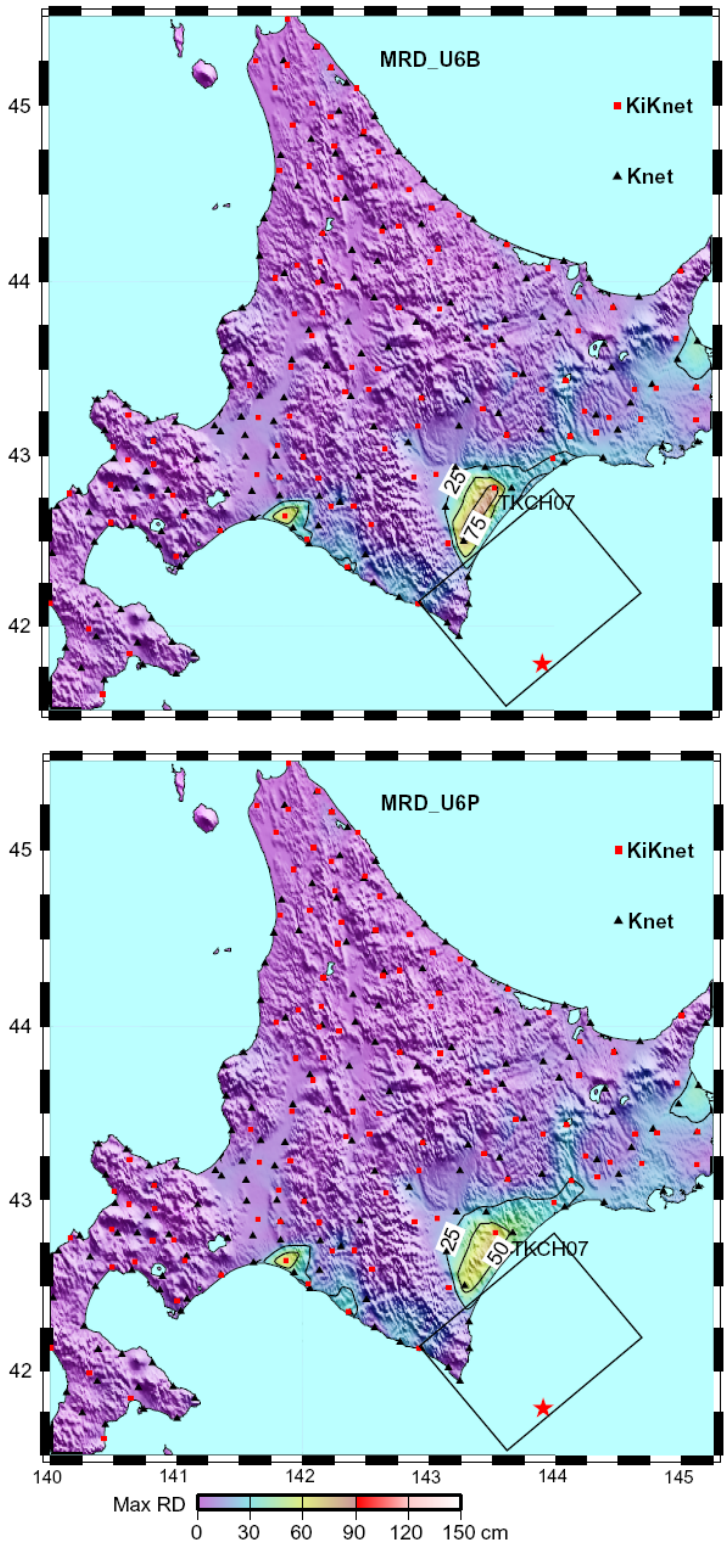

Figure 3.12. Maximum roof displacement for U6B and U6P. The maximum value is 79 cm and 70 cm respectively, and both occurred at station TKCH07.

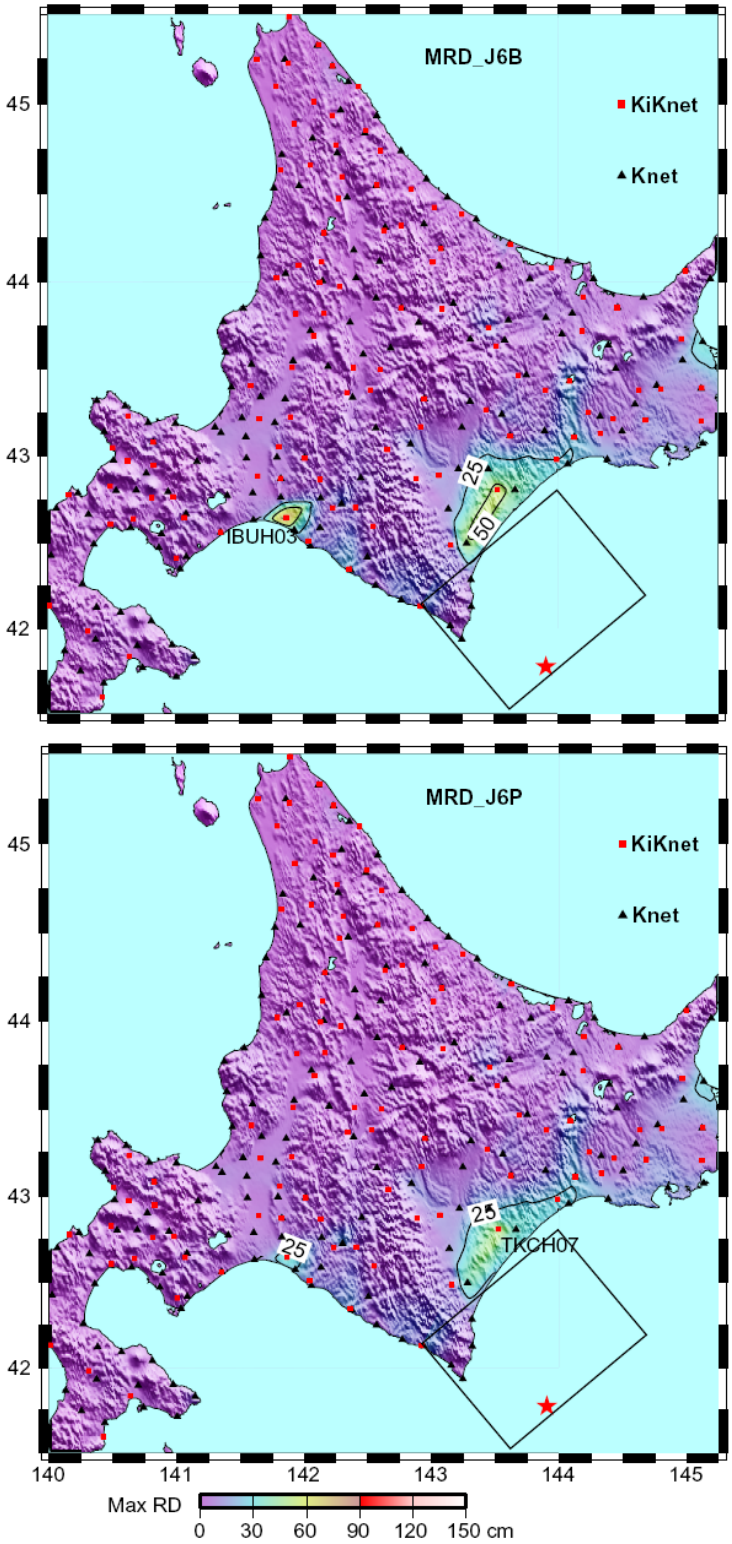

Figure 3.13. Maximum roof displacement for J6B and J6P. The maximum value is 75 cm at IBUH03 and 49 cm at TKCH07 respectively.

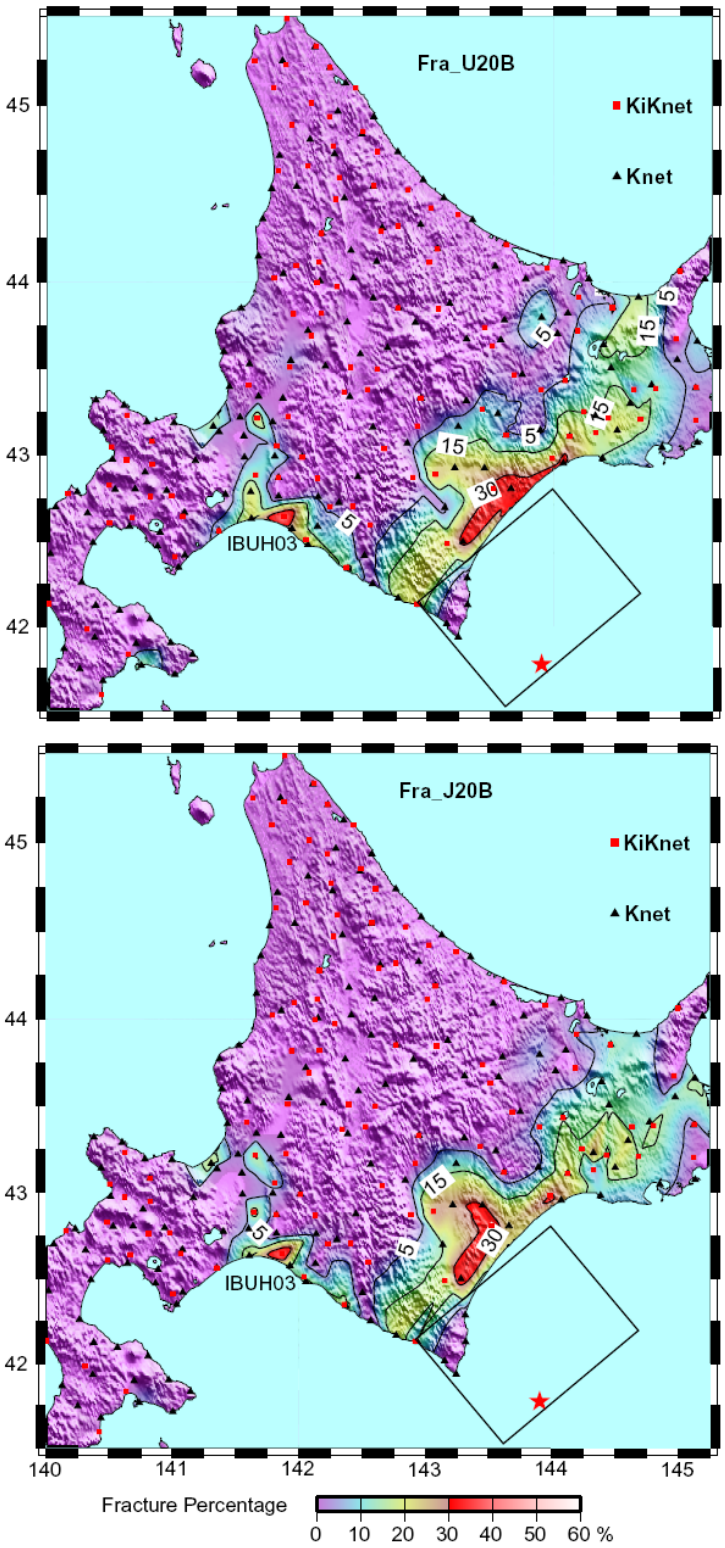

Figure 3.14. Percentage of the total welded moment-resisting connections that fractured for U20B and J20B. The maximum value is 38% and 36% respectively, and both occurred at station IBUH03.

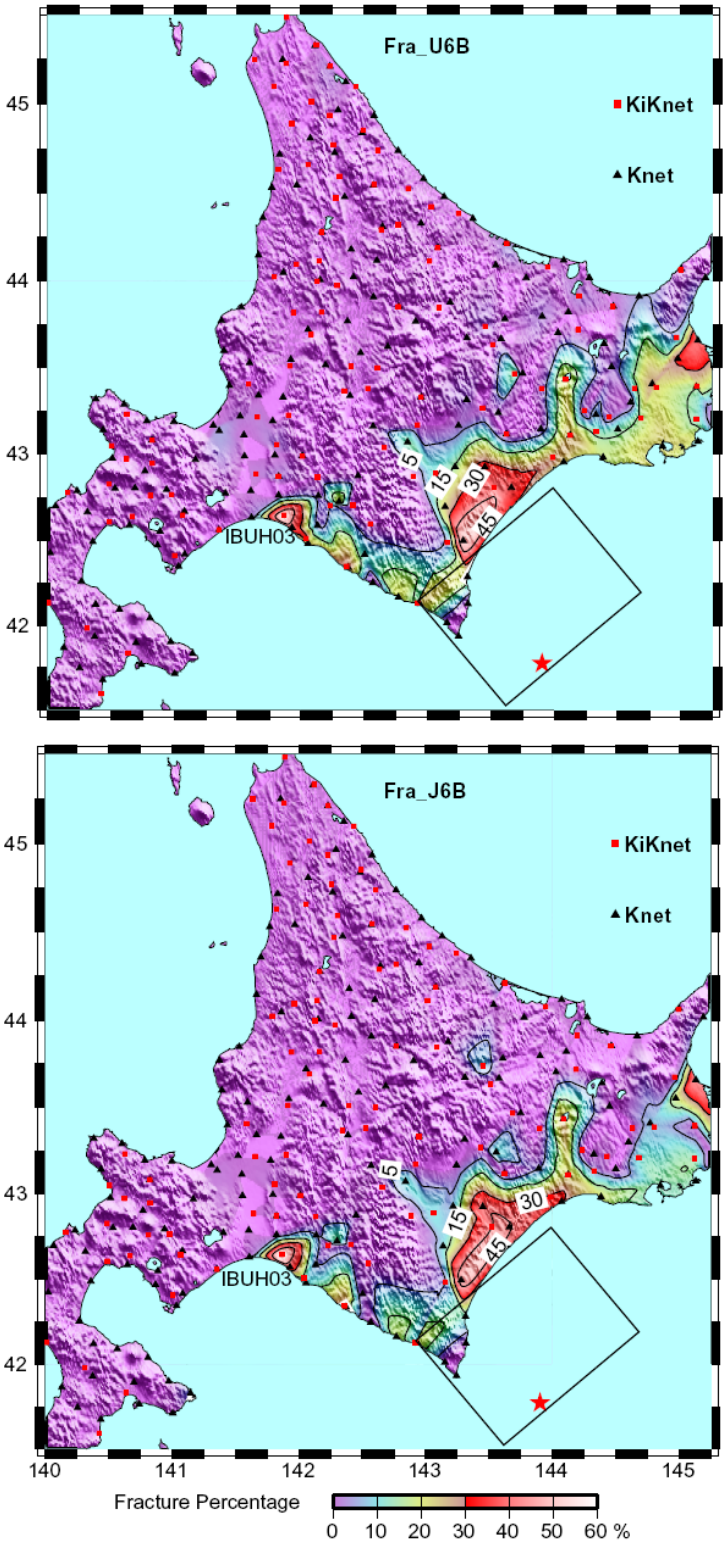

Figure 3.15. Percentage of the total welded moment-resisting connections that fractured for U6B and J6B. The maximum value is 55% and 58% respectively, and both occurred at station IBUH03.

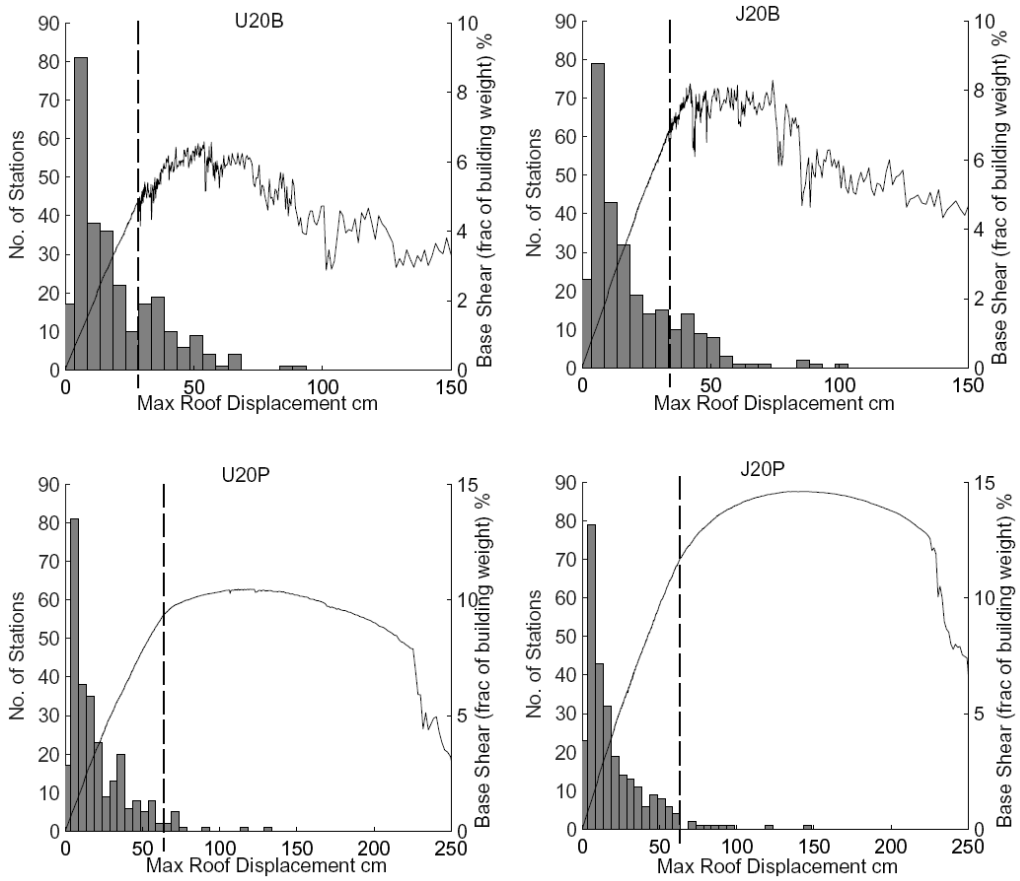

Figure 3.16. Combination of the pushover curves for 20-story buildings and the histogram of roof displacements to show the number of stations with elastic and inelastic performance. Left y-axis is the number of stations in terms of maximum roof displacements (MRD). Right y-axis is the base shear force in the buildings in terms of MRD. Dash lines indicate the onset of yielding. It is easy to find that the existing brittle welds cause more buildings yielding. Furthermore, in some stations, the amount of lateral force carried by structures with brittle welds begins to decrease and the damage caused is irreparable. Increasing the strength of buildings alone (from U20 to J20) does not change the station distribution much.

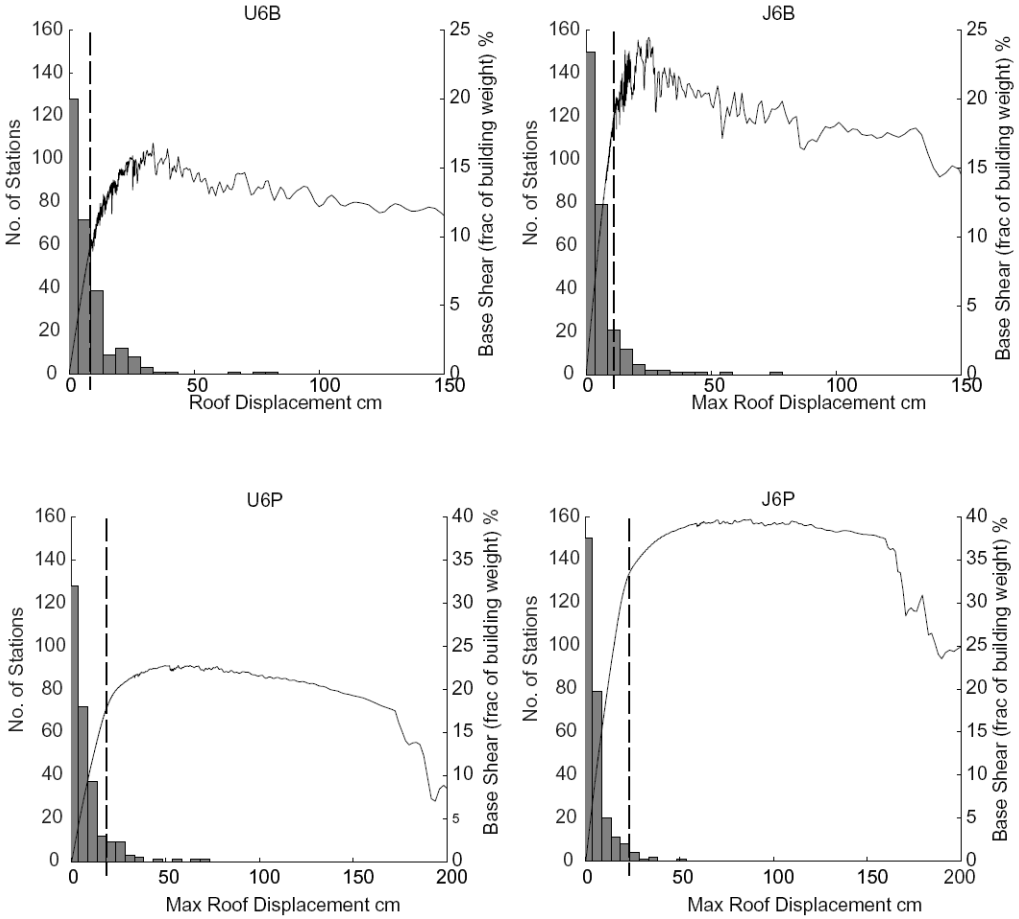

Figure 3.17. Combination of the pushover curves for 6-story buildings and station distribution for roof displacements to show the number of stations with elastic and inelastic performance. Left y-axis is the number of stations in terms of maximum roof displacements (MRD). Right y-axis is the base shear force in the buildings in terms of MRD. Dash lines indicate the onset of yielding. The same trend is found that existing brittle welds cause more buildings yielding. And increasing the strength alone (from U6 to J6) does not change the station distribution much. However, comparing with the 20-story buildings, the 6-story buildings remain elastic in more stations.

3.4 Relations Between Responses of Buildings and Ground Motions

The extensive simulations for all the recorded stations on Hokkaido Island discussed in the previous section not only give a detailed picture of regional performance of high-rise buildings in a quantitative manner, but also provide an opportunity to seek the correlations between the building responses and ground motion intensity measures. Although using scalar measures characterizing the shaking intensity of earthquakes are known to be

inadequate in predicting the response of buildings, nevertheless, they are widely used in many deductions, reasoning, conclusions and design because of their simplicity. Several intensity measures have been proposed such as PGA, PGV, PGD and response spectra but there is no consensus on the one that can best predict SMRF response. So it is important to choose the most appropriate single parameter to represent earthquake hazard.

Comparing the contour map of these parameters (figures 3.3 to 3.4) with contour maps of buildings' peak IDRs (figures 3.6 to 3.9) gives us a rough pattern. It is found that the distribution of response spectra is most similar to that of peak IDRs. On the other hand, the contour map of PGA gives a surprisingly bad match of peak IDRs. For example, station HKD100 has the highest PGA, but it is associated with relatively small deformation for 20-story buildings. With regard to PGD, the exact values are sensitive to data processing schemes. Therefore, among PGA, PGV and PGD, PGV is the best parameter to predict the performance of SMRF buildings.

To cement this argument, the peak IDRs as functions of ground motion intensity measures for U20 are compared in figure 3.18. All the data is separated roughly into linear (peak IDRs < 0.25%) and nonlinear cases (peak IDRs > 0.25%). In the linear range, the linear relationships of PSV to peak IDRs or PGV to peak IDRs are apparent and can be represented by a straight line, whereas there is a big scatter in terms of PGA to predict the performance of buildings. Although PSV fits the linear trend very well, it is worth to note that when buildings with brittle welds become nonlinear, their peak IDRs are larger than the value predicted by the trend line. This is reasonable because the response spectra method is based on a SDOF linear model analysis. Once buildings become inelastic, the stiffness of the structures would decrease and damage would localize at certain stories. So PSV can not accurately reflect the behavior of buildings with nonlinear effects. In other words, a single degree of freedom model no longer works in that case. On the other hand, PSV is good at predicting the response of buildings with perfect welds for both linear and nonlinear ranges. This could also be seen in figure 3.19 where peak IDRs for U20P increase relatively smoothly as PSV increases.

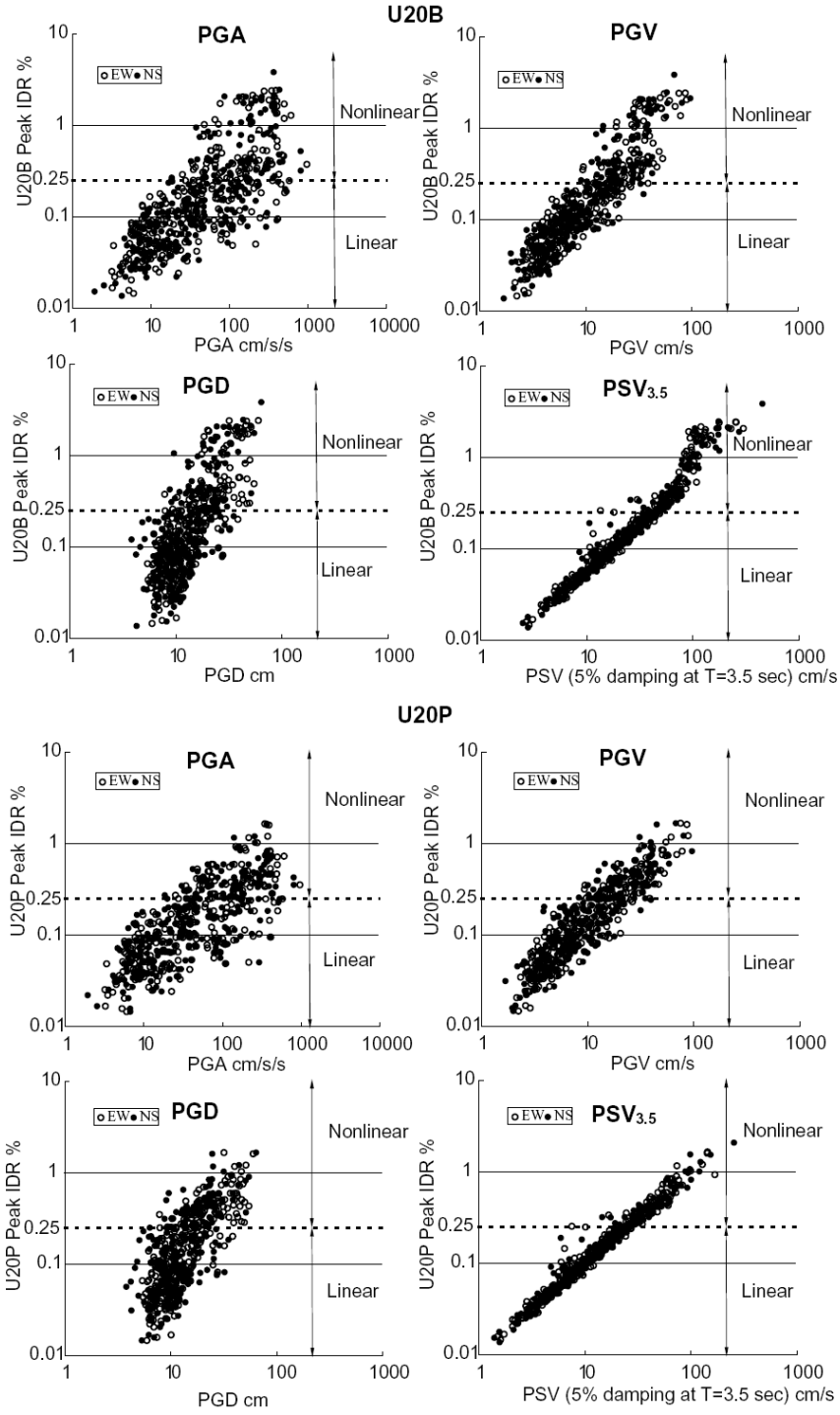

Figure 3.18. Relationships between peak IDRs of U20 and ground motion intensity measures: PGA, PGV, PGD and PSV. PSV = $\omega|x(t)|_{max}$, where $|x(t)|_{max}$ is the maximum displacement of a mass in a one dimensional spring-mass system with a fixed natural period subjected to ground motion. In linear range, the linear relationships of PSV to peak IDRs or PGV to peak IDRs are apparent and can be represented by a straight line, whereas there is a big scatter in terms of PGA to predict the performance of buildings.

3.5 Collapse Factor

It is difficult to use ground motion intensity to predict the nonlinear response of buildings with brittle welds. To illustrate this, a perfect elastic building model (U20E, U6E) was added to show purely linear response vs. nonlinear response of buildings with brittle and perfect welds. In the elastic model, the elements would never yield (achieved by using infinite yield stress but the same mass and stiffness). All three building models were subjected to ground motions which were obtained by multiplying the recorded ground acceleration by a sequence of constants. The response results of 20- and 6-story buildings at five stations are given in figures 3.19 and 3.20. The top x-axis shows the scalar multipliers for the ground motion and the bottom x-axis gives PSV of the scaled ground motion at natural period of the corresponding building. The linear relationship between PSV and peak IDRs is apparent for elastic models, however the peak IDRs of the brittle welds model are larger than the value predicted by PSV when peak IDRs exceed 0.25%. Furthermore, there is no apparent relationship between the response of elastic models to the response of brittle welds models. Notice that peak IDR in U20B does not monotonically increase as PSV increases at stations HKD105 and HKD117. Other stations have similar features. We can find that when the peak IDR approaches 4%, U20B is very close to collapse, whereas U20P has a larger collapse peak IDR. This means that the ductility of U20B is much smaller than U20P. The collapse peak IDR for U6B is larger than 6% because of the smaller P-Delta effects. The most interesting thing appears in figure 3.20. An station HKD105, when PSV reaches 250 cm/s, U6B collapses. However, when PSV increases to 300 cm/s, U6B does not collapse and its peak IDR is around 6%. This high degree of nonlinearity indicates that response spectra can not predict the performance of buildings when large deformations occur in the buildings. Time history analysis is necessary for design purposes.

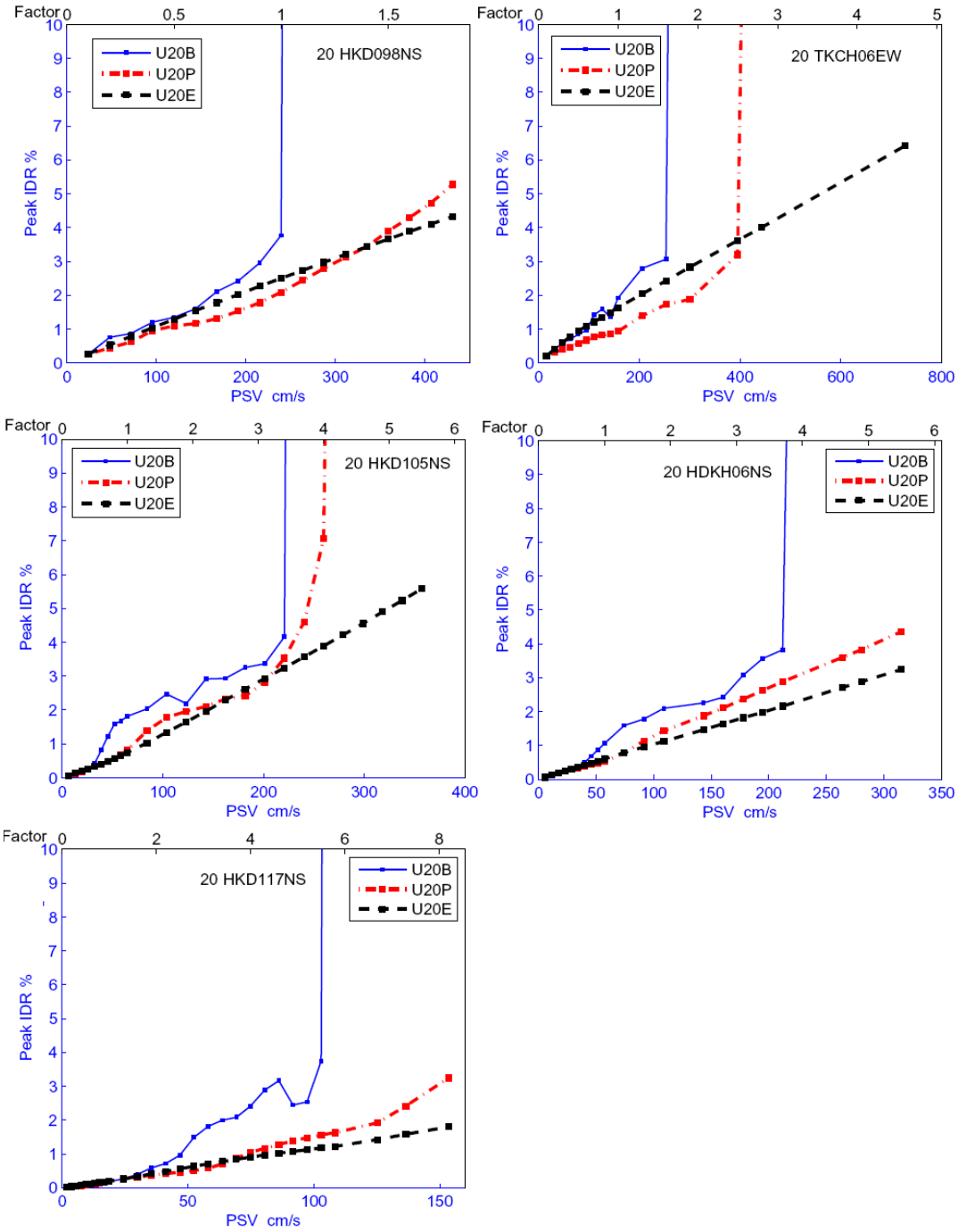

Figure 3.19. Relationships of pseudo spectral velocity (5% damped) to peak IDRs for 3 sets of 20-story building models (blue solid line is for U20 with brittle welds, red dash-dot line is for U20 with perfect welds and black dashed line is for elastic U20). The top x-axis shows the scalar multipliers for ground motions and the bottom x-axis gives the corresponding 5% damp 3.5 sec pseudo spectral velocity. It shows that when the peak IDR approaches 4%, U20B is very close to collapse, whereas U20P has a larger peak IDR when approaching collapse.

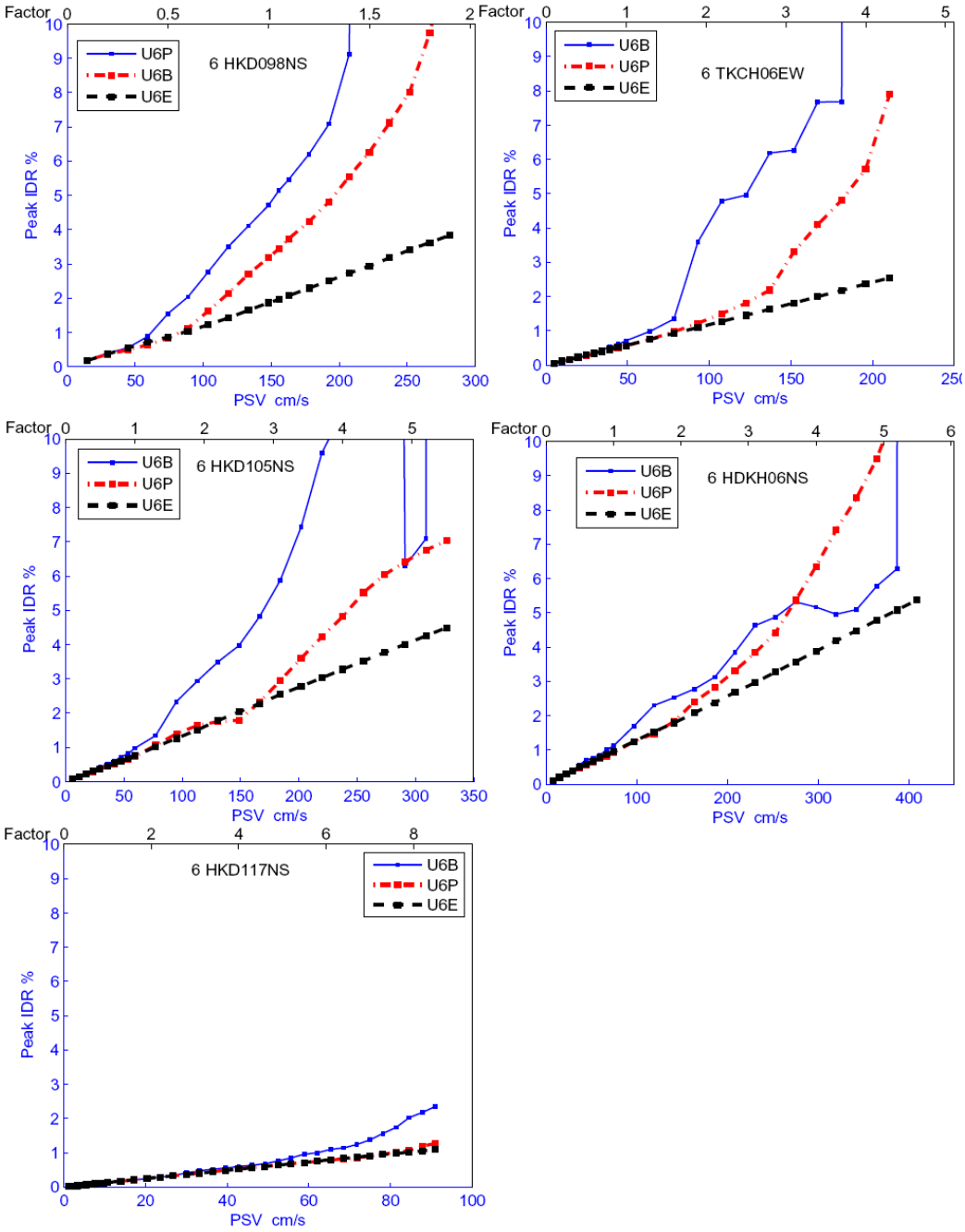

Figure 3.20. Relationships of pseudo spectral velocity (5% damped) to peak IDRs for 3 sets of 6-story building models (blue solid line is for U6 with brittle welds, red dash-dot line is for U6 with perfect welds and black dashed line is for elastic U6). The top x-axis shows the scalar multipliers for ground motions and the bottom x-axis gives the corresponding 5% damp 1.5 sec pseudo spectral velocity. The peak IDR for U6B approaching collapse is larger than 6% because of the smaller P-Delta effects

Extending the previous idea further, we use a parameter to quantify the collapse possibility of simulated buildings. We named it the “collapse factor” and it is defined to be the scalar multiplier of the recorded ground motion that is required to cause collapse of the model. That is, we simply multiplied the recorded ground motion by a constant and then re-ran the building simulation. When the multiplying constant was large enough to cause simulated collapse, then we called that multiplier the collapse factor. For example, collapse factor of U20B is 1.06 at HKD098 and 5.5 at HKD117 which can be figured out in figure 3.19. This parameter is good at describing the collapse safety margin of structures to a certain ground motion.

We map the collapse factors for U20B and J20B in figure 3.21. From this figure, we found that although no building shown simulated collapse, increasing the ground motion amplitude recorded at station HKD098 only by 6% caused collapse for U20B. This is well within the uncertainty of this type of calculation. Since Frame-2D does not consider local failure which is possible to occur along the column flanges once fracture developed in the beam-column joints, in reality, U20B has a high potential to collapse at station HKD098 in the Tokachi-Oki event. The contour maps of collapse factors for U20P and J20P are given in figure 3.22. As expected, buildings with perfect welds have larger collapse factors than buildings with brittle models. Some of the ground records are so small that they cause simulated collapse only when the collapse factors are very large. This is out of our interest. Collapse factors larger than 20 are not calculated in this study and these areas were covered by blue color in figures 3.21 and 3.22.

The contour maps of collapse factor indicate some interesting phenomena. In general, the contour maps of collapse factor (figures 3.21 and 3.22) have the same regional pattern as the contour maps of peak IDRs (figures 3.6 to 3.9). However, there are conspicuous discrepancies in some areas. For example, the peak IDRs for U20B at areas around station HKD016 (around 0.2%) are much smaller than the peak IDRs at areas around station HKD105 (around 1 to 2%). However the collapse factors are almost the same for these two areas (about 3.6). That means increasing the ground motions at these areas by the same

scale would cause collapse although buildings at areas around HKD105 was shaken much heavier than these at areas around HKD016. It might be due to the soft soil amplification caused by the Teshio basin underneath HKD016 (refer figure 3.4). Notice, the low collapse factor at station IKRH02 is also due to the local site amplification at Ishikari basin.

Figure 3.23 shows the collapse factor ratio between J20 and U20. In general, J20 is safer than U20 by a factor 1 to 1.4. However for station close to collapse (e.g. HKD098), the collapse factor of J20B is only 6% larger than that of U20B. This difference is much smaller than their strength difference (20%). In addition, for perfect welds models, the collapse factors of J20P are surprising smaller than these of U20P in some areas which were believed to experience strong shaking (covered by red color). In other words, when welds in the building do not fracture in violent shaking, the performance of stiffer and stronger Japanese buildings is not as good as that of relatively flexible and weak U.S. buildings. This demonstrates the crucial roles of connection welds played in the performance of buildings. It also shows that evaluating the advantages of stronger and stiffer high-rise buildings should be more done cautiously.

Figure 3.24 shows the collapse factor ratio between 20P and 20B. Again, the ratios corresponding to the collapse factor greater than 20 were not calculated and these areas were covered with white color. As expected, in most areas, 20P is safer than 20B by a factor of 1.2 to 2.0 which is larger than the ratio between J20 and U20. Therefore, fixing the welds is a more efficient way to increase the collapse factor than strengthening existing buildings.

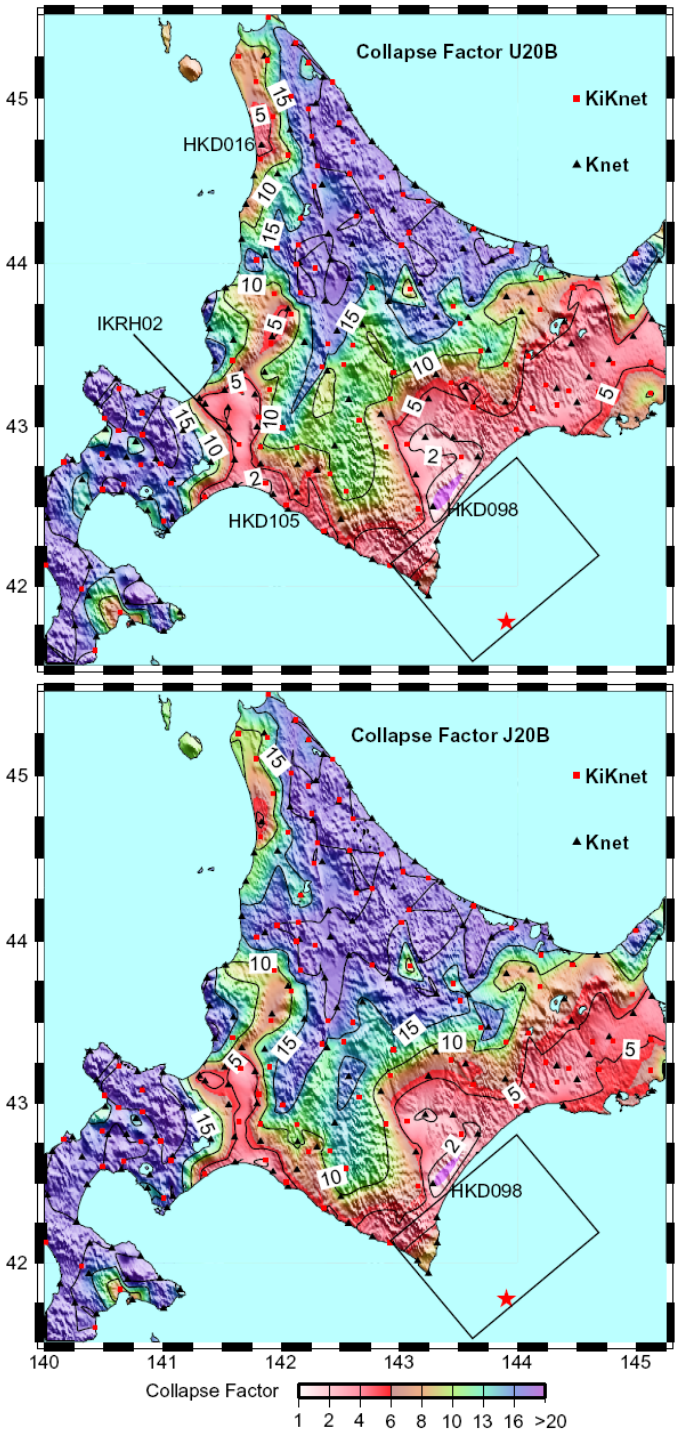

Figure 3.21. Contour maps of collapse factor for U20B and J20B. The minimum value is 1.06 and 1.125 respectively at station HKD098. This means that increasing the amplitude of HKD098 only by 6% (12.5%) caused simulated collapse of U20B (J20B). The collapse factor in purple areas is larger than 16. Their exact values are out of our interest.

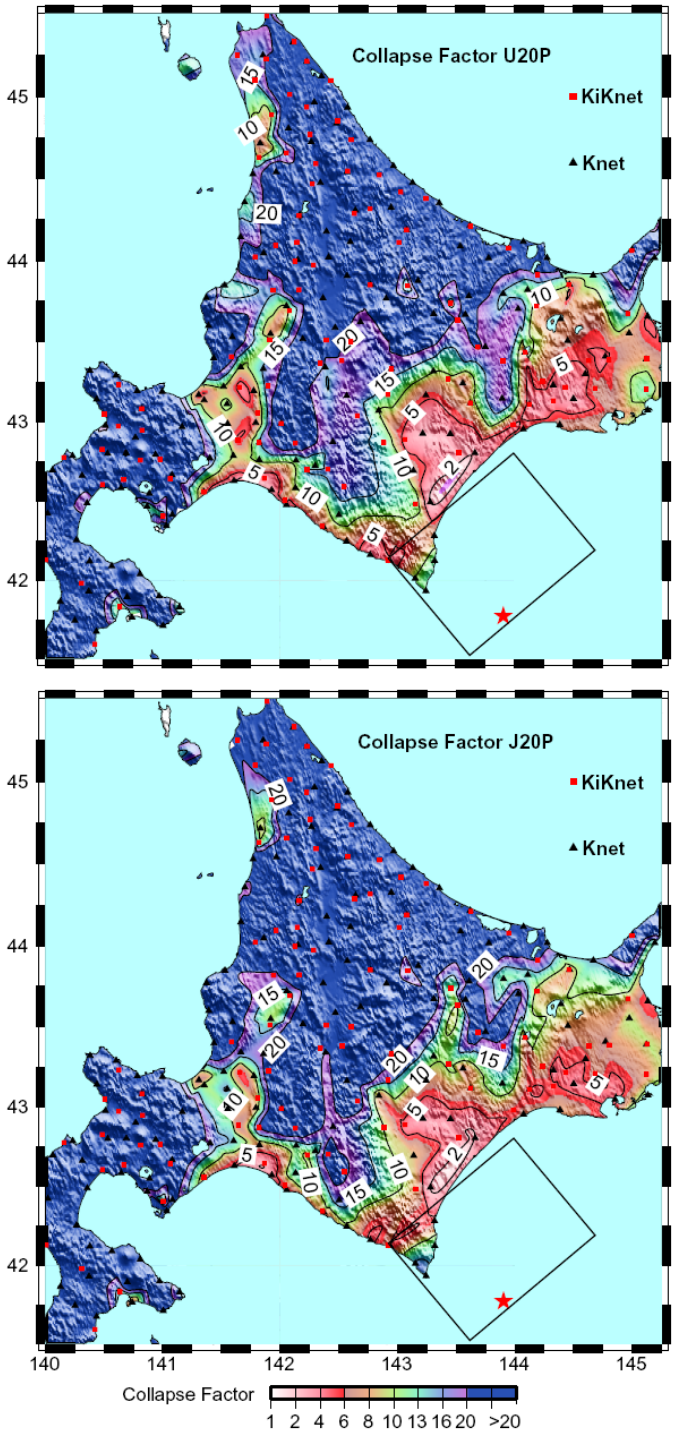

Figure 3.22. Contour maps of collapse factor for U20P and J20P. The minimum value is 1.98 at station HKD098 for both buildings. This means that doubling the amplitude of HKD098 caused simulated collapse of U20P (J20P). The collapse factor in blue areas is larger than 20. Their exact values are out of our interest.

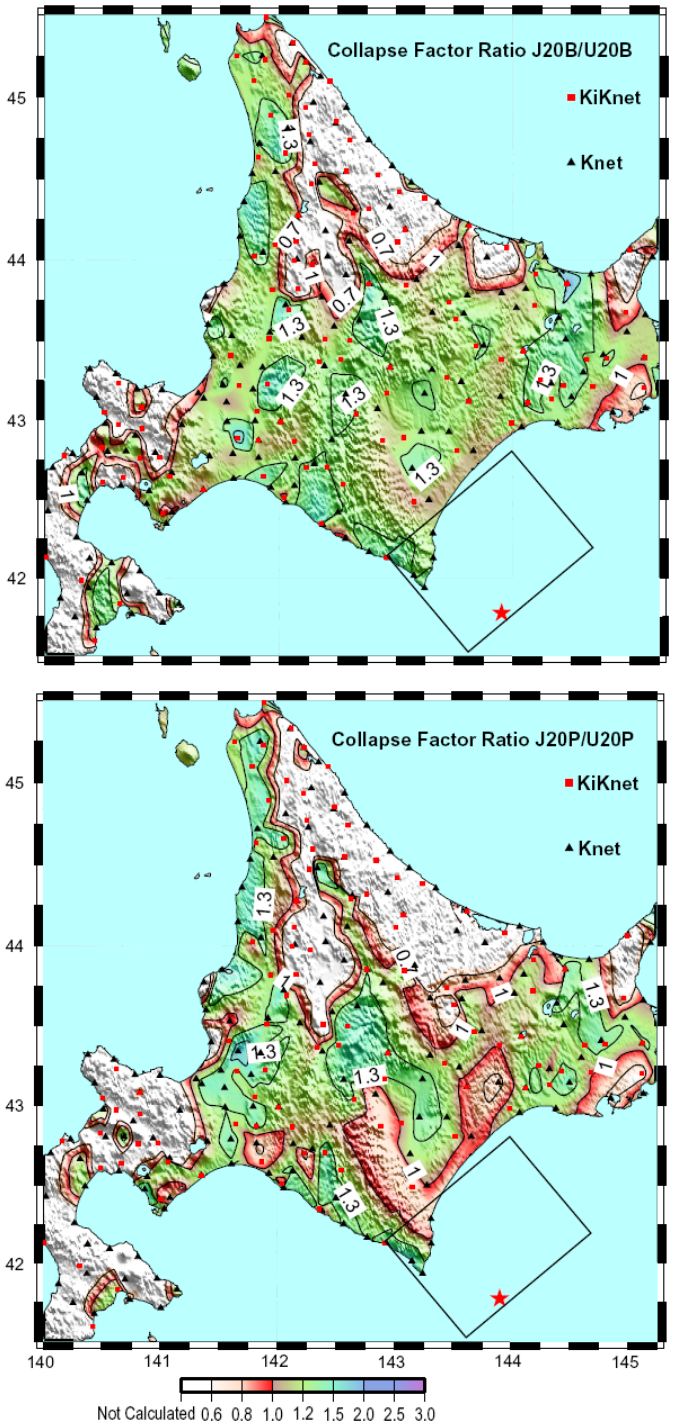

Figure 3.23. Contour maps of collapse factor ratio between J20 and U20. The ratios at white areas are not calculated because the exact collapse factor values are not available and out of our interest. In most areas, strengthening buildings increases the collapse factor. But comparing with figure 3.22, the increase is smaller. The advantage of stronger Japanese buildings is not apparent.

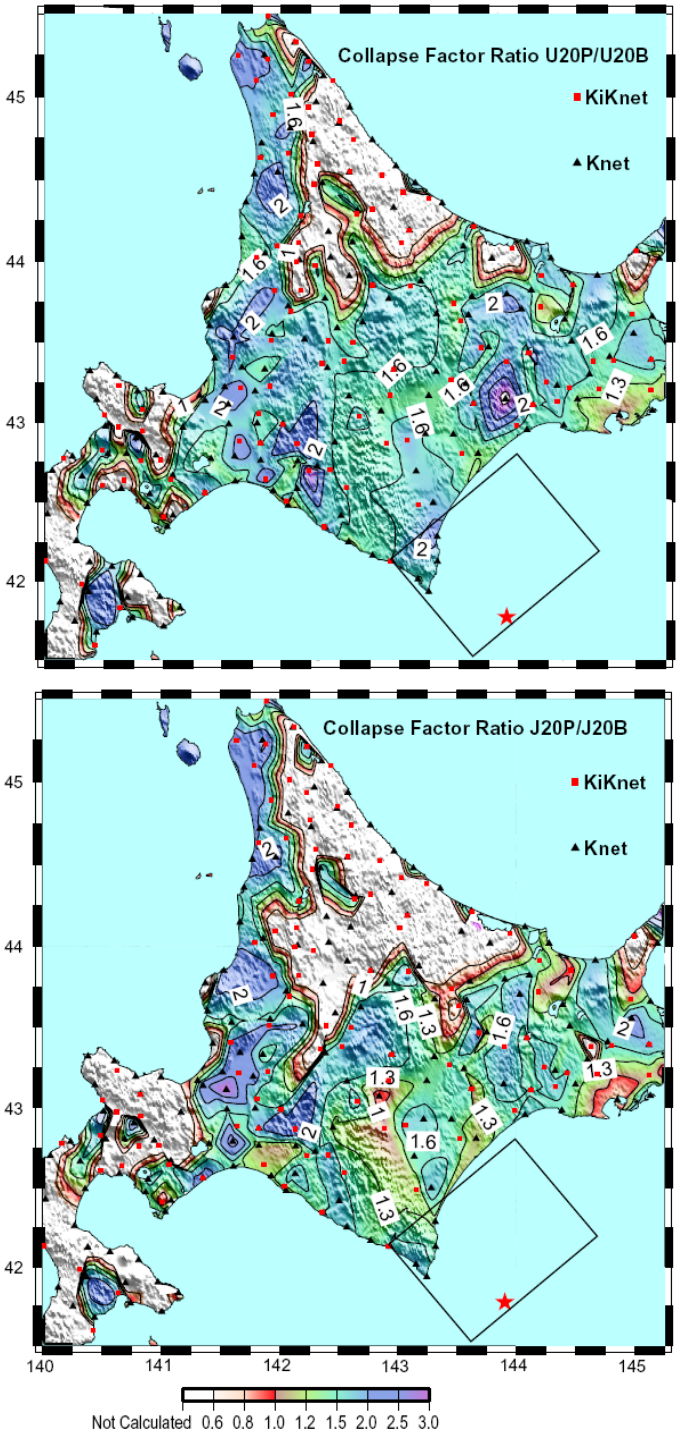

Figure 3.24. Contour maps of collapse factor ratio between 20P and 20B. The ratios at white areas are not calculated because the exact collapse factor values are not available and out of our interest. In most areas, fixing the welds increases the collapse factor.

CHAPTER 4

Empirical Green's Functions Method

Estimating the strong ground motions for great historic and future earthquakes is an active and challenging research topic because of the meager recorded data. These synthetic strong ground motions could provide insight to seismologists in understanding the special characteristics associated with great earthquakes. Additionally, they also provide guidance to earthquake engineers in designig flexible structures located in seismic regions with the potential for great earthquakes.

Current ground motion simulation techniques can be grouped into three main categories. The first one is fully theoretical modeling where the ground motion is numerically computed by the finite element method. In this approach, simulated waves are generate from a fault with proposed temporal and spatial slip time history, and propagated through a realistic 3-D earth structure model (Komatitsch, Liu *et al.*, 2004). The second category is empirical method. This method was originally proposed by Hartzell (1978). It uses recordings of small earthquakes as empirical Green's functions and convolves them with a source model. The third category is a combination of these two schemes individually processed at different frequency bandwidth (Heaton, Hall *et al.*, 1995).

Empirical Green's functions (EGF) method is more suitable to simulate the strong ground motions from great earthquakes than the theoretical method. In the fully theoretical method, researchers have to assume the spatial and temporal evolution of slip for each grid on the large fault. They also have to assume the rupture velocity for each subfault. Although some

progress has been made recently to understand the source parameters in giant earthquakes thanks to the Sumatra event, it is still far away to understand well the physics of the rupture process based on our current level of knowledge. For a giant earthquake, there are more than 10,000 subfaults according to the popularly used grid dimension (2 to 5 km). The little knowledge about giant earthquakes would cause large uncertainty in the resulting synthetics. This makes us not confident to accept the simulated results from more than 10,000 assumed spatio-temporal slip histories. Furthermore, the theoretical method also needs to assume the three-dimensional earth structures in shallow and deep part. The elastic structure of the real earth is very complex, with oddly shaped bodies of low velocity materials that can be of first order importance to wave propagation. It is hard to obtain this detailed information for a region more than 1000 km long. Last, but not the least, even if we obtain all the detailed information, the computation is too expensive for current supercomputers to solve the fully 3-dimensional dynamic continuum problems at most frequencies of engineering interest. On the other hand, the previous issues do not cause problems for the empirical Green's function method. In this method, the ground motions recorded in real earthquakes are used as Green's functions. If motions from a larger earthquake are chosen to be the EGFs, the heterogeneous caused by the slip variations in time and space are inherently included. Furthermore, if the waves from the smaller and larger events travel through similar seismic velocity structures in a similar manner, the unknown soil structures can be removed. Finally, the computation cost is much lower. Therefore, we choose the empirical Green's functions method to estimate strong ground motions for great subduction earthquakes.

In this chapter, I briefly discuss the empirical Green's function technique and show the self-similarity for the 2003 Tokachi-Oki and the 2004 Sumatra event. Tectonic settings of the Hokkaido, Sumatra and Cascadia subduction zones are compared. We show that it is reasonable to use records from the 2003 Tokachi-Oki earthquake as empirical Green's functions to generate the 2004 Sumatra earthquake, as well as simulate a hypothetical giant Cascadia earthquake.

4.1 Empirical Green's Functions Technique

Empirical Green's functions (EGF) method is based on the assumption that larger earthquakes can be considered to be a linear combination of smaller ones. It originally used aftershock records as empirical Green's functions (Hartzell, 1978) and later was generalized to use records from earthquakes with similar tectonic settings (Kanamori, 1979; Hartzell and Heaton, 1985; Heaton and Hartzell, 1989). A Brief discussion of this technique is provided in this section. A detailed deduction can be found in Appendix B of Heaton and Hartzell (1989).

The ground motion $U(t)$ (either teleseismic data or strong ground motion recordings) can be represented as a finite source model convolving with Green's functions, that is,

$$U(t) = \int_0^L \int_0^W \dot{D}(x,y,t) * G(x,y,t) dy dx \,, \tag{4.1}$$

where $D(x,y,t)$ is the dislocation time histories for the larger earthquake; $G(x,y,t)$ is the double-couple impulse response of the medium; L and W are length and width of the planar fault respectively. Modeling the earth as a linear system, $U(t)$ can be represented as a summation of the motions from subfaults,

$$U(t) = \sum_{i=1}^{l} \sum_{j=1}^{m} U_{ij}(t) = \sum_{i=1}^{l} \sum_{j=1}^{m} \int_{(i-1)\Delta L}^{i\Delta L} \int_{(j-1)\Delta W}^{j\Delta W} \dot{D}(x,y,t) * G(x,y,t) dy dx \,. \tag{4.2}$$

The ground motions $u_{ij}(t)$ from a smaller earthquake that ruptured the ij-th subfault would be given by

$$u_{ij}(t) = \int_{(i-1)\Delta L}^{i\Delta L} \int_{(j-1)\Delta W}^{j\Delta W} \dot{d}(x,y,t) * G(x,y,t) dy dx \,, \tag{4.3}$$

where $d(x,y,t)$ is the dislocation time histories for the smaller earthquake. Assume

$$D(x,y,t) = F_{ij}(t) * d_{ij}(x,y,t) \,, \tag{4.4}$$

$$F_{ij}(t) = \sum_{k=1}^{n} \delta(t - T_{ij} - \tau_k) \text{ and } \tau_k = (k - \chi_k)\frac{t_d}{n}, \tag{4.5}$$

where T_{ij} is the delay time for the rupture front to travel from the hypocenter to the ij-th subfault; τ_k is a simple distribution of times between zero and the dislocation rise time; t_d is the duration of the dislocation of the large event and χ_k is a uniform random number between 0 and 1. Combining all these equations together, we obtain

$$U(t) = \sum_{i=1}^{l}\sum_{j=1}^{m} F_{ij}(t) * u_{ij}(t) = \sum_{i=1}^{l}\sum_{j=1}^{m}\sum_{k=1}^{n} u_{ij}\left[t - T_{ij} - (k - \chi_k)\frac{t_d}{n}\right]. \tag{4.6}$$

That is, the ground motions $U(t)$ for a larger event is the summation of the empirical Green's functions $u_{ij}(t)$ recorded at smaller earthquakes. I use a schematic figure 4.1 to illustrate this method.

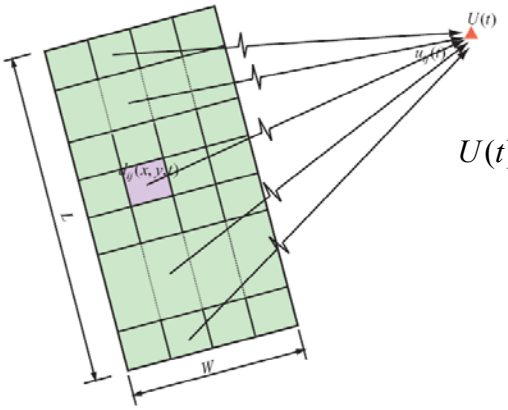

near field or far field station

$$U(t) = \sum_{i=1}^{l}\sum_{j=1}^{m} F_{ij}(t) * u_{ij}(t)$$

$$= \sum_{i=1}^{l}\sum_{j=1}^{m}\sum_{k=1}^{n} u_{ij}\left[t - T_{ij} - (k - \chi_k)\frac{t_d}{n}\right]$$

Figure 4.1. Illustration of empirical Green's function method. Red triangle represents a station and green rectangular represents the rupture fault for a large earthquake and purple rectangular is a subfault. The ground motion recorded at stations is a summation of subfaults motions convolving with a comb function with some time delays.

Once the framework is set up, the most difficult question left is how many empirical Green's functions (N=lmn) are needed to add together. Heaton and Hartzell (1989) proposed to use the short-period teleseismic waveforms as constraints to find this number N. One natural choice is that N equals the ratio of the seismic moments of the larger event M_0 to the smaller event M_0'. However, results in Section 5.3 imply that the predicted

teleseismic P-waves using this ratio are much larger than the corresponding recorded P-waves in most cases. Another choice is that N equals the ratio of the rupture surface areas of the larger event to the smaller event. As mentioned before, high-frequency motions from large earthquakes are of interest for engineers. Many researchers found that near-source high-frequency ground motions saturate as a function of magnitude (Kanamori and Jennings, 1978; Cua and Heaton, 2007). That is to say, they are independent of the amplitude of slip and are proportional to the rupture surface areas (Boatwright, 1982; Yamada, 2007). Our result in section 5.3 indicates that this ratio did a good job to match the recorded teleseismic P-waves. A third choice is proposed by Joyner and Boore (1986) in order to make empirical Green's function techniques consisting with Brune's (1970) ω^{-2} spectral scaling law. They summed $N^{4/3}$ records and scaled the final results by $N^{-1/3}$. However, the synthetic motions simulated by this method led to underestimates of the teleseismic P-waves (refer to section 5.3). Although Brune's spectral scaling law is very popular, there are still some debates about its constant spectral slope ω^{-2} (Hartzell and Heaton, 1985). Finally, the ratio of rupture areas is chosen in this study to determine the total number of the summed Green's functions.

4.2 Choosing Records From the 2003 Tokachi-Oki Earthquake (M_w 8.1) as Empirical Green's Functions

The empirical Green's function technique basically is an extrapolation from smaller earthquakes to larger earthquakes. To get reasonable results, this extrapolation should be kept as small as possible. It is ideal for two events to be self-similar. Although it is a hard problem to determine whether two events are self-similar with each other, we know that larger subduction earthquakes have much higher possibility than smaller earthquakes to be self-similar with great subduction earthquakes. Hartzell and Heaton (1988) found that the self-similarity failed for large earthquakes ($M_w > 8¼$) to smaller one ($M_w < 8¼$). Therefore, it is better to choose an earthquake as large as possible to be the EGF to simulate a giant earthquake. Furthermore, if a M_w 6 earthquake was chosen to simulate a M_w 9 earthquake,

we would need more than 30,000 EGFs based on seismic moment ratio and 400 EGFs based on rupture size ratio. There is a large variation in N and in the final results compared with using a M_w 8 earthquake to simulate a M_w 9 earthquake which needs 20 to 50 EGF.

The 2003 Tokachi-Oki earthquake is the largest well recorded earthquake. It provides an adequate set of records to use as Green's functions and needs the least extrapolation by the EGF method. The response spectra of teleseismic P-waves are similar for the Tokachi-Oki event with the Sumatra event. In figure 4.2 and 4.3, we compare the smoothed teleseismic P-wave Fourier amplitude spectra for all the large shallow subduction earthquakes ($M_w \geq$ 7.6) that occurred from 1990 to 2007; 22 events are considered. Figure 4.2 plots acceleration spectra to focus on comparing the short period components whereas figure 4.3 plots displacement spectra to focus on comparing the long period components. For each event, the smoothed Fourier spectrum is the average of all the recorded teleseismic P-waves corrected to a distance at 60^o and the frequency band is 0.0033 to 9 Hz. Although the slopes are different from one to another, it is clear to see that the slopes of the Sumatra and the Tokachi-Oki events are very similar with each other. It provides insight to the similarity between the Tokachi-Oki event and the Sumatra event.

In order to get reasonable results from empirical Green's function method, two events should also have similar wave propagation paths. In other words, impulse response of the medium $G(x,y,t)$ in equation (4.1) should be the same for two events. The subduction zone where the 2003 Tokachi-Oki Earthquake occurred shares many similar characteristic with the Sumatra and Cascadia subduction zones. Figure 4.4 displays the cross sections of these three subduction zones. The references used to plot these cross sections are: Iwasaki et al. (1989); Katsumata et al. (2003); Subarya et al. (2006); Fisher et al. (2005). The interfaces of one plate subducting beneath the other are all gently sloping. The similarity is especially high for subduction zones with a potential for giant earthquakes such as Sumatra and Cascadia. In these subduction zones, the trench is followed by an outer-arc ridge, an outer-arc basin, a trench-parallel strike-slip fault system and volcanoes. Although the Hokkaido subduction zone is slightly different from the other two zones, to date the 2003 Tokachi-

Oki event is the best earthquake we can find to provide empirical Green's functions. In figure 4.4, we also provide the extents of sources for hypothetical Cascadia earthquake with different rupture faults (wide and narrow) which are introduced in Chapter 6.

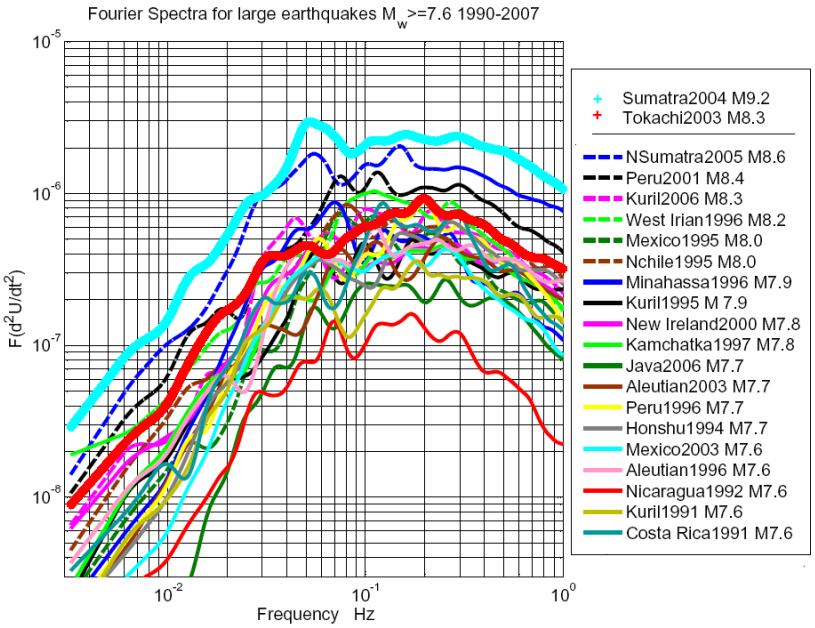

Figure 4.2 Smoothed teleseismic P-wave Fourier acceleration spectra for large shallow subduction earthquakes ($M_w \geq 7.6$) occurred in 1990 to 2007. The 2004 Sumatra and 2003 Tokachi-Oki events are represented by blue and red lines respectively. Although the slopes are different from one to another, the slopes of the Sumatra and the Tokachi-Oki events are very similar with each other. It provides insight to the similarity between that 2003 Tokachi-Oki event and the 2004 Sumatra event.

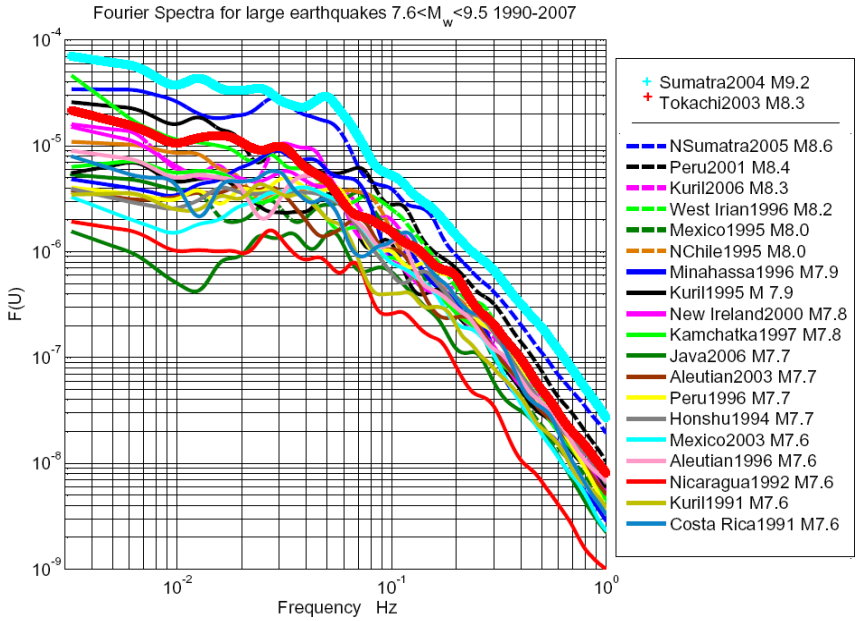

Figure 4.3. Smoothed teleseismic P-wave Fourier displacement spectra for large shallow subduction earthquakes ($M_w \geq 7.6$) occurred in 1990 to 2007.

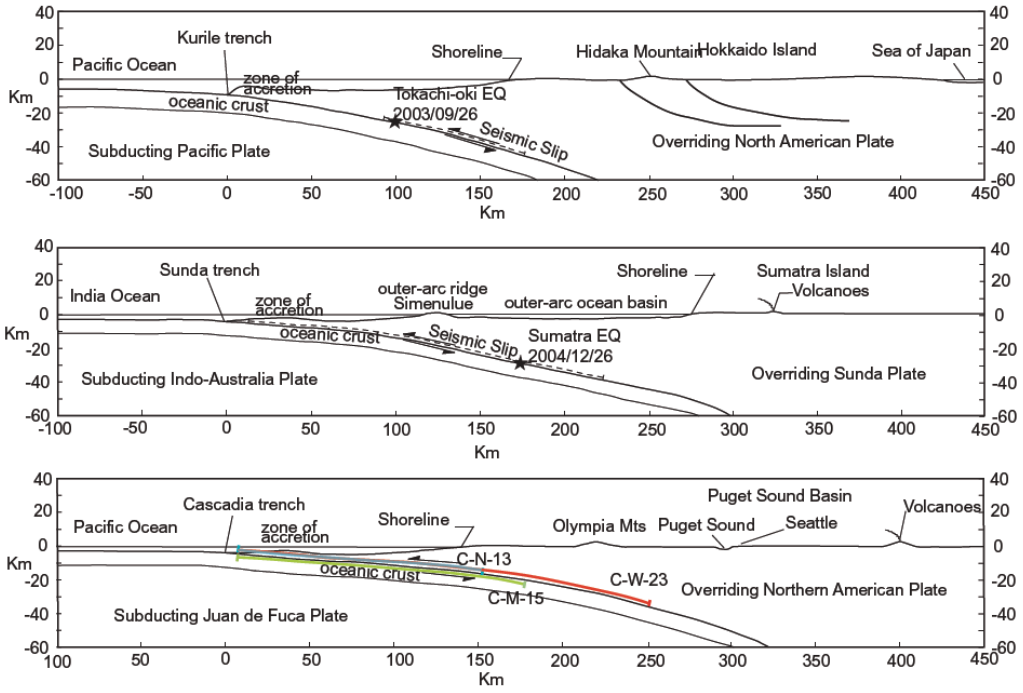

Figure 4.4. Cross sections of the approximate geometry of the rupture surfaces. The top panel is for of Hokkaido subduction zone, the middle panel is for Sumatra subduction zone and the bottom panel is for Cascadia subduction zone. There is no depth exaggeration used to plot these cross sections. The blue, green and red lines in the bottom figure represent the wide, middle and narrow rupture models used in Chapter 6 respectively. The tectonic settings of these subduction zones are very similar with others.

CHAPTER 5

December 2004 Sumatra-Andaman, Indonesia, Earthquake M_w 9.2

The 2004 Sumatra-Andaman earthquake (M_w 9.2) is the third largest earthquake since the installation of seismometers. It generated more than 0.2 million people dead or missing and one million people displaced. Although much of the damage was caused by the accompanying tsunami, it is still not clear how much of the damage was associated with strong ground shaking. Unfortunately, there are no seismic records on scale at close distances. The nearest station recording this event was the PPI station of the JISNET network which is about 650 km from the epicenter (Sørensen, Atakan *et al.*, 2007). On the other hand, the teleseismic data of this event was recorded globally by substantial high-quality broadband seismometers and we know much more information about this event than any other historic giant earthquakes (M_w > 9.0). Since the rupture size of this earthquake is at the same scale to the event that we expect in the Cascadia area, it provides a good source model for that scenario event.

In this chapter, I briefly introduce the 2004 Sumatra-Andaman earthquake. Then the strong ground motions from two rupture models (wide and narrow rupture width) for two site conditions (rock and soil) are estimated by empirical Green's functions method. Nonlinear dynamic responses of 20- and 6-story steel moment-frame buildings are simulated for this event.

5.1 Introduction

The 2004 Sumatra-Andaman earthquake ruptured the Sunda Trench subduction zone along which the Indo-Australian plates are subducted northeastward beneath the Sunda shelf at a convergence rate 45 to 60 mm/year (Menke, Abend *et al.*, 2006). The hypocenter was at latitude 3.3^{o}N, longitude 96.0^{o}E, at a depth of 28 km (Harvard CMT). The rupture length of this event was initially estimated to 400 km and later modified to 1200 to 1300 km (Sieh, 2005). Most researchers agree that rupture occurred in two broad phases. The rupture velocity was 2.8 km/s for the southern 500 to 600 km of the rupture and lasted 200 seconds. It reduced to 2.1 km/s for the northern part of the rupture fault (Menke, Abend *et al.*, 2006). The source duration was more than 480 seconds. The estimates of seismic moment varied from 3.95×10^{22} to 1.17×10^{23} Nm for different researchers using different data sets and assumptions. Kanamori (2006) gave an explanation about the difference. The estimates of average slip along the fault also varied from 5 to 10 m because of the complexity of this event.

5.2 Rupture Fault Models

Like the variability in estimating seismic moment, the rupture model sizes proposed by different investigators are different. The rupture length is estimated to be 1300 to 1600 km (Lay, Kanamori *et al.*, 2005; Subarya, Chlieh *et al.*, 2006). For the rupture width, Lay *et. al.* (2005) proposed that it is around 240 km along the northwestern Sumatra and 160 to 170 km along the Nicobar and Andaman Islands. However, Subarya *et. al*. (2006) estimated that the rupture width is less than 150 km and Ammon *et. al.* (2005) proposed 240 km all along the rupture length. Choosing a geometric rupture model is a primary aspect in empirical Green's function scheme. So, in this chapter, we use two geometric rupture faults with different widths as our simulation basis because we found that the final strong motion predictions are sensitive to the width instead of length of the rupture fault.

Figure 5.1 gives the geometry of the rupture faults used in our empirical Green's function method. The first geometric model is named S-Wide where "S" represents the Sumatra event and "Wide" represents that the width of rupture fault is wider. It has a rupture width 250 km in the first segment (south part of the fault) and reduces to 200 km in the second segment (north part of the fault). The second geometric model is named S-Narrow where "Narrow" represents the narrower width rupture fault. It has a rupture width 175 at the first segment and 200 km at the second one. The rupture size of the 2003 Tokachi-Oki earthquake which is used to tile the Sumatra rupture fault is around 130 ×100 km^2. Because there are some overlaps in the tiling, the average fault width of the Tokachi event is about 85 km, a value similar with Yamanaka's model (2003). The subfaults in the adjacent rows are staggered to reduce the artificial pattern in the simulated results.

As for how many Green's functions should be summed together, we propose three criteria to determine *N*. The first one is based on the seismic moment ratio of larger and smaller events. The second one is based on the ratio of the rupture fault size. The last one is based on the Joyner and Boore's method (1986) as mentioned in Chapter 4. It is easy to figure out from figure 5.1 that rupture size ratio is 24 for wide models and 20 for narrow models. Therefore, each subfault would rupture only once if *N* was determined from the rupture size ratio. However, if *N* was determined from the moment ratio, each subfault would rupture at least three times since the seismic moment ratio is about 50 to 70 for Sumatra event to Tokachi event. Although there is a big variation in estimated seismic moments, we can calculate the seismic moment ratio with respect to the rupture size ratio in another way. Since it is well known that $M_o=\mu SD$, assuming μ is the same for two events, $\frac{M_{oS}}{M_{oT}} = \frac{S_S}{S_T}\frac{D_S}{D_T}$, that is the seismic moment ratio is the product of the rupture size ratio with the average slip ratio. The average slip is 2.6 m for the Tokachi event and 5 to 10 m for the Sumatra events. If we choose the median value, then $\frac{M_{oS}}{M_{oT}} = 3 \times \frac{S_S}{S_T}$ that is, N=72 for wide models and 60 for narrow models. Recall from Chapter 4, if we use Joyner and Boore's method, we should sum $N^{4/3}$ records and reduce the amplitude by $N^{1/3}$.

Considering all these possibilities, we propose eight models to predict teleseismic data. Their source parameters are listed in table 5.1. There are two segments along the fault with different strike, dip and rupture velocity values. And the source parameters within each segment are assumed the same. Recommended models can be chosen to best match the observed recordings. Slightly change of strike, dip and rupture velocities have much smaller effects to the final results than the number change of EGFs.

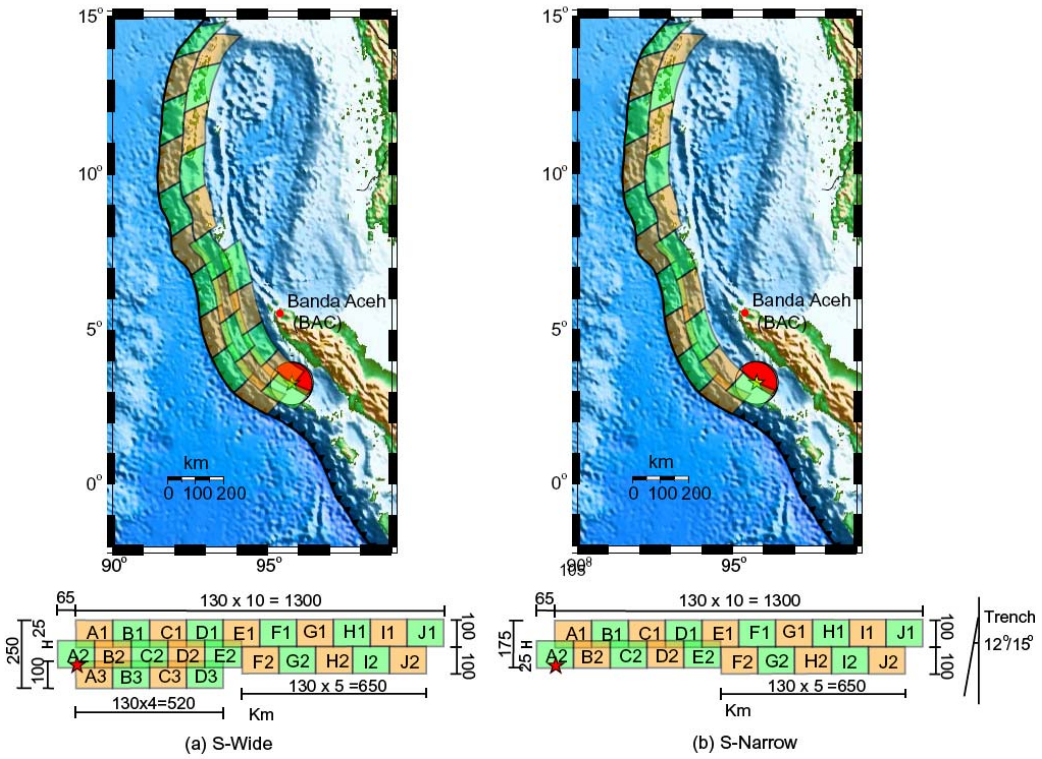

Figure 5.1. Geometries of the rupture fault models used to simulate the 2004 Sumatra-Andaman earthquake. Red star represents the hypocenter of this event. Red dot represents observe station at Banda Aceh (BAC) where strong ground motions would be estimated. Each box represents a subfault whose response is simulated by summing the ground motion from the 2003 Tokachi-Oki earthquake. Letters in each box denotes the name for each subfault. The size of each subfault is 130 × 100 km^2. Left figure (a) shows S-Wide models which have wide fault width. Right figure (b) shows S-Narrow models which have narrow fault width.

Table 5.1. Parameters for each model

Model Code	Strike	Dip	No. of added EGF	No. of rupture	Rupture Vel (km/s)	L (km)	W (km)	m*	n*
S-Wide-24	315º /** 342º	12º / 15º	24	1	2.8 / 2.5	650 / 650	250 / 200	5/5	3 / 2
S-Narrow-20			20				175 / 200		2
S-Wide-72			72	3			250 / 200		3 / 2
S-Narrow-60			60				175 / 200		2
S-Wide-24-JB			72				250 / 200		3 / 2
S-Narrow-20-JB			60				175 / 200		2
S-Wide-72-JB			288	12			250 / 200		3 / 2
S-Narrow-60-JB			240				175 / 200		2

*m is the number of subfaults along the fault length; n is the number of subfaults along the fault width;
** The parameters for two segments are separated by '/'.

5.3 Teleseismic P-wave Simulation

Teleseismic P-waves simulated from EGF technique provide an important constraint on the model parameters of our strong ground motion models. Recorded teleseismic P-waves from the 2003 Tokachi-Oki earthquake are used as EGFs to simulate the teleseismic P-waves at about 60 degrees in the 2004 Sumatra earthquake. All the teleseismic time histories were downloaded from the website of IRIS (Incorporated Research Institutions for Seismology). Their sampling frequency is 20 Hz. To avoid nyquist side effect and to remove very long period motions which are out of our interest, a Butterworth filter at a period band of 0.11 to 300 sec is applied to all the records. Figure 5.2 illustrates the locations and recordings of all stations between 30 to 90 degrees for Tokachi and Sumatra events. Figure 5.3 and 5.4 order these waveforms by distance for easy comparison.

Recordings from station YSS (Δ=60.5^o) in Sumatra event (circled in the bottom of figure 5.2) is our simulation target since its location is far away from nodes as you can see from figure 5.2. Recordings from four stations KBS (Δ=55.9^o), KEV (Δ=59.3^o), ABKT (Δ=63.0^o) and OBN (Δ=65.1^o) in Tokachi event are chosen to constitute our EGFs teleseismic database (circled in the top of figure 5.2). All of these stations are far away from nodes and close to simulated distance 60^o. This database requires the smallest

spherical spreading correction and avoids the final results depending on a single record. Figure 5.5 plots their waveforms. Comparing with other stations around 60^o (e.g., CTAO, WRAB) shown in Figure 5.3, it is clear to see that these four recordings have similar waveform shapes and their amplitudes are at the same scale. Each Green's function was assigned a code to represent its recorded station. These codes are listed in the left column in figure 5.5.

Eight source models listed in table 5.1 are simulated. These models are grouped into two cases: wide and narrow models. Their Green's functions are randomly distributed and the sets that used in our simulation are shown in figure 5.6. Different distributions only slightly change the resulted peak amplitudes and the discrepancy can be ignored.

The simulated results from eight models at distance 60^o are compared in figure 5.7. The records from station YSS are all plotted in the last row in each panel. The peak value is listed on the top left for each trace. By comparing the peak values, we find that waveforms generated by Model S-Wide-72 and S-Narrow-60 which are based on the seismic moment ratio overestimate the observed waveforms. On the other hand, Model S-Wide-24-JB and S-Narrow-20-JB which apply Joyner and Boore's method to the rupture size ratio underestimate the observed waveforms. Model S-Wide-72-JB and S-Narrow-60-JB which apply Joyner and Boore's method to the seismic moment ratio could well estimate accelerations; however they underestimate the velocities and displacements which are more important than accelerations in teleseismic signals. If the whole envelopes of the waves are compared, S-Wide-24 and S-Narrow-20 give the best fit. Smoothed Fourier spectra of teleseismic P-waveforms from different models and records at station YSS ($\Delta = 60.5^o$) in Sumatra event are compared in figure 5.8. Overall, Model S-Wide-24 and S-Narrow-20 which are based on the rupture size ratio give comparable results to the recorded P-waves in terms of velocities and displacements although overestimate the accelerations. From these comparisons, we conclude that the total Green's functions number N is best determined by the rupture size ratio.

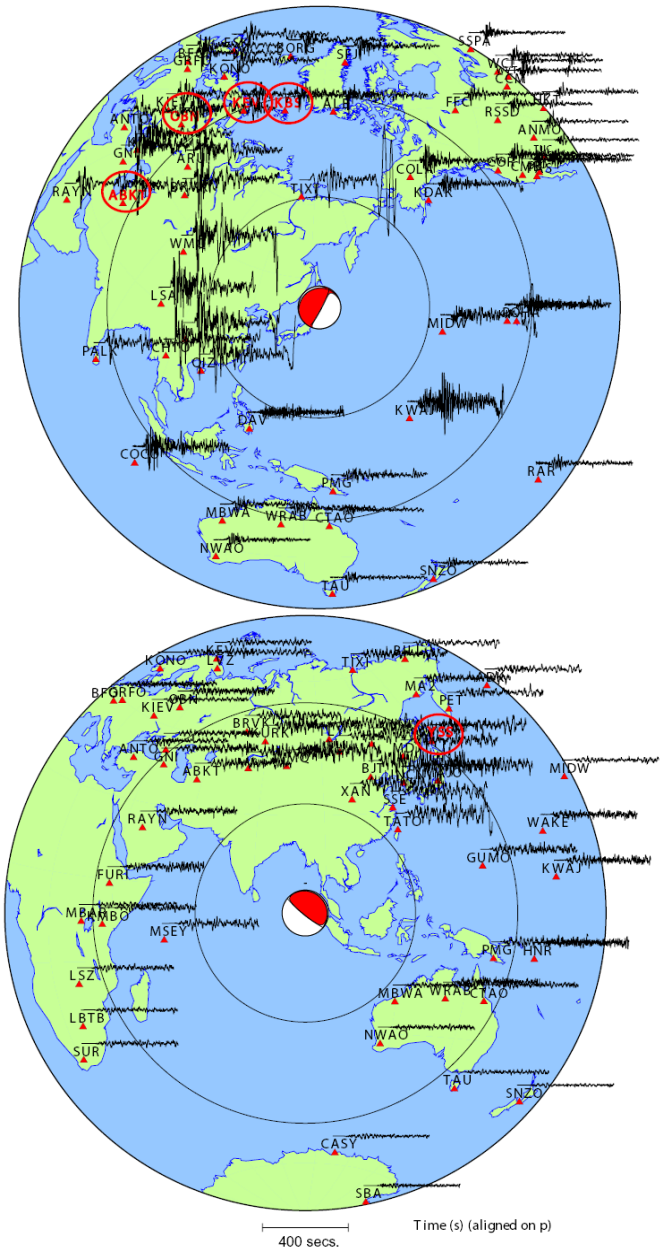

Figure 5.2. Locations of Global Seismograph Network stations (Δ= 30º to 90º) which had recorded teleseismic data from the 2003 Tokachi-Oki earthquake (top) and the 2004 Sumatra-Andaman earthquake (bottom). Teleseismic P-wave seismograms are shown for each station and focal mechanisms of these events are also shown. The amplitude scale is different for two events in order to show them clearly. Four stations whose records are used as EGFs are circled by red ellipses in the top figure. The station YSS whose record is used to compare with predicted motions is also circled in the bottom figure. Notice that their relative azimuths with event strikes are similar for two events.

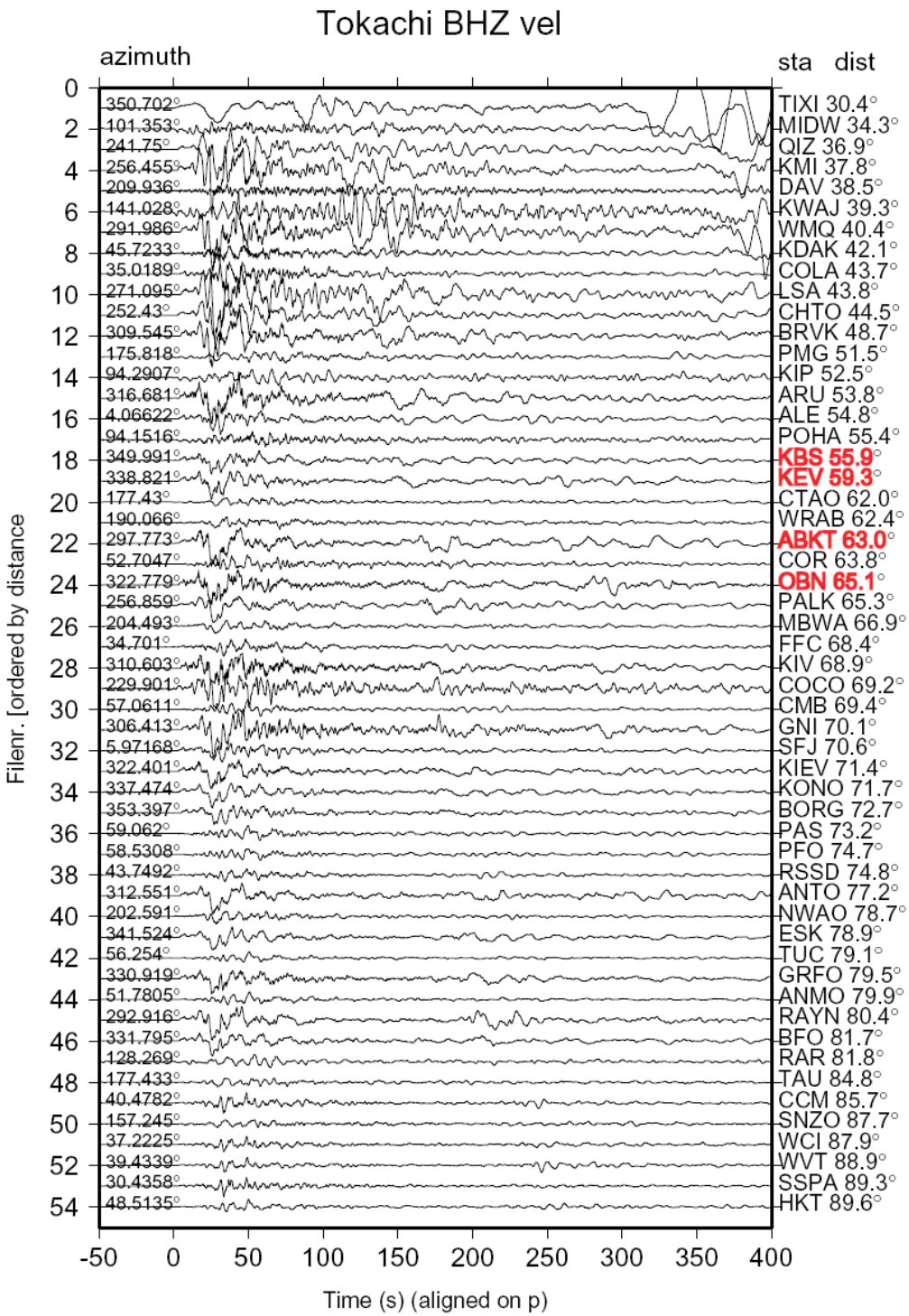

Figure 5.3. Teleseismic P-wave seismograms recorded at Global Seismograph Network stations (Δ = 30º to 90º) from the 2003 Tokachi-Oki earthquake. They are ordered by distance. Four stations whose seismograms are used as our empirical Green's functions are labeled in red.

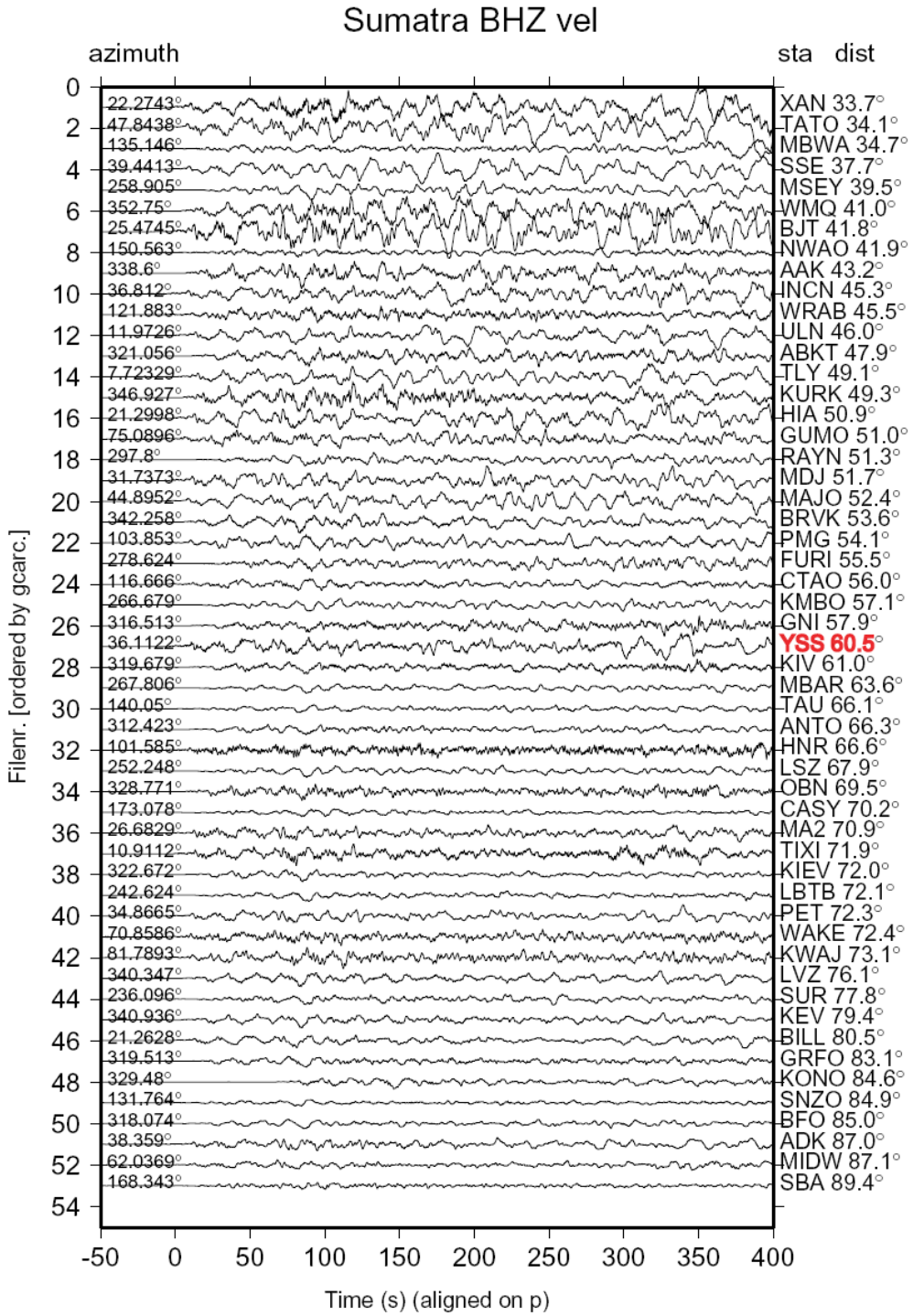

Figure 5.4. Teleseismic P-wave seismograms recorded at Global Seismograph Network stations (Δ = 30º to 90º) from the 2004 Sumatra-Andaman earthquake. They are ordered by distance. Station YSS whose seismograms are used to compare with our simulation is labeled in red.

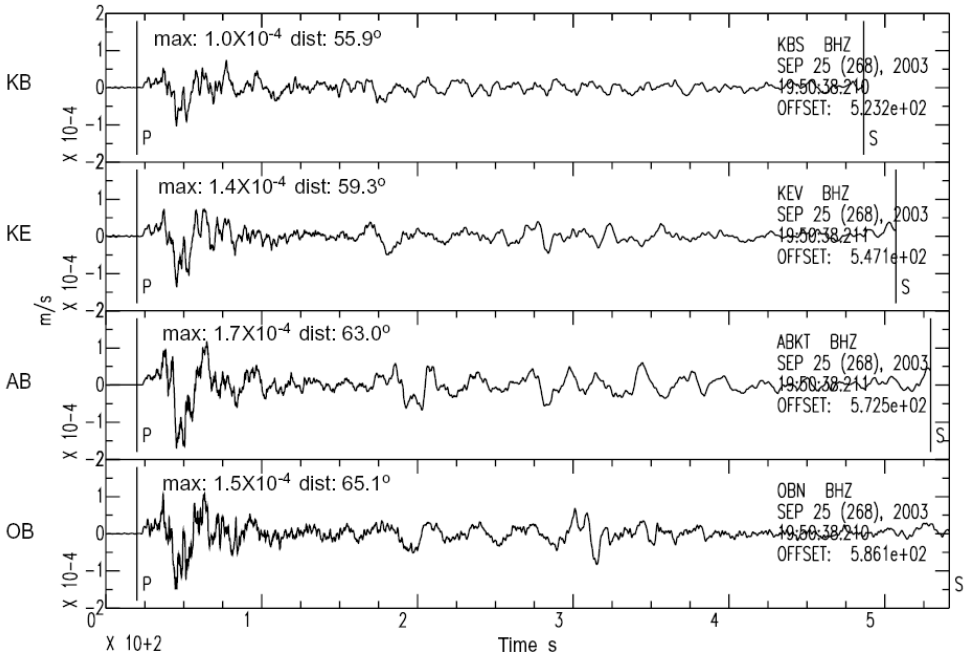

Figure 5.5. Four teleseismic P-wave seismograms recorded at the 2003 Tokachi-Oki earthquake used as empirical Green's functions to simulate the 2004 Sumatra earthquake. Notice that their waveforms are very similar with each other, only with slightly different amplitudes.

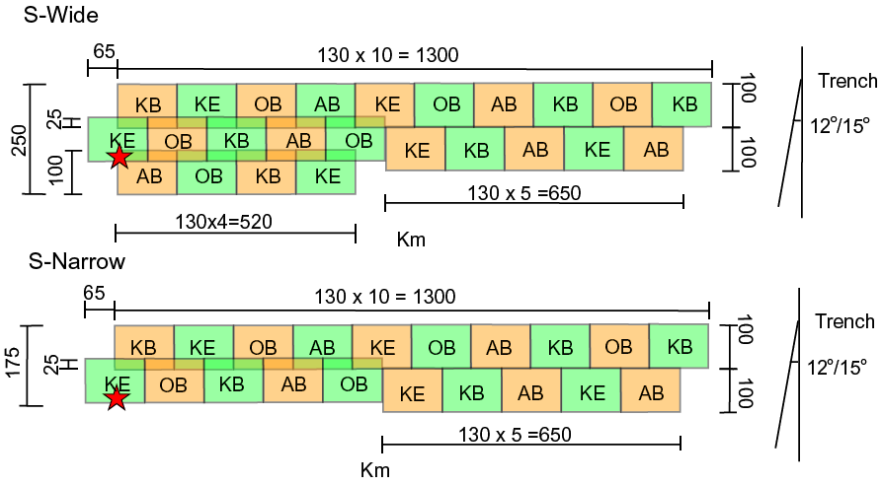

Figure 5.6. Distributions of empirical Green's functions used to simulate teleseismic P-waves from 2004 Sumatra earthquake. Each box represents a subfault. Letters in the box refer to figure 5.5 and designate which records from the 2003 Tokachi-Oki event are used as Green's functions. These records are chosen randomly from the four stations. Difference choices would only slightly affect the resulted peak amplitudes. Star represents the hypocenter of Sumatra event. The top figure is for rupture model with wide width and the bottom figure is for rupture model with narrow width.

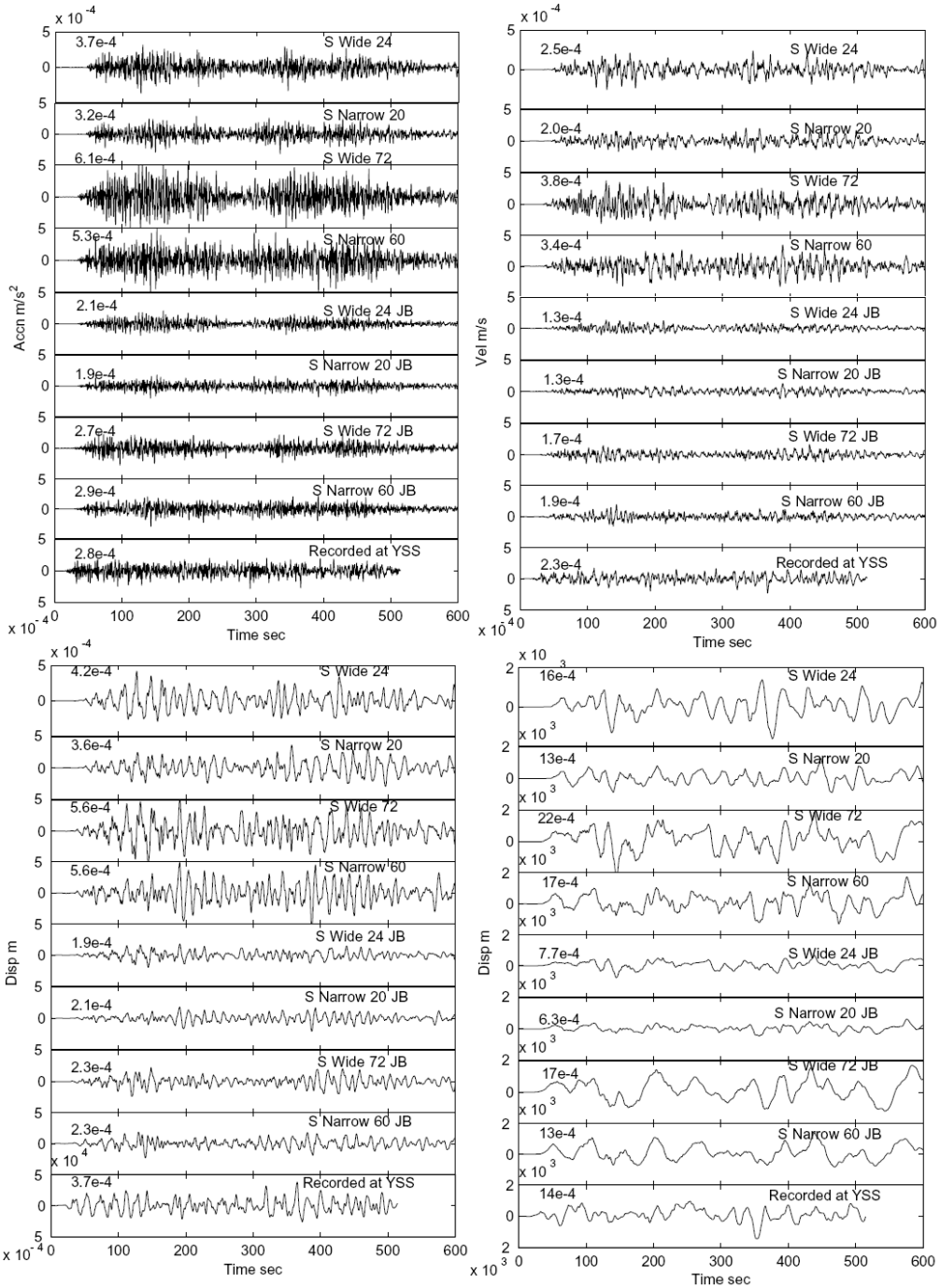

Figure 5.7. Comparison of simulate teleseismic P-waveforms at distance 60^{o} from eight models with observed recordings at station YSS (Δ = 60.5º) in Sumatra event. Accelerations are shown at top left, velocities are shown at top right and displacements are shown at bottom left. These data are highpassed at 0.05 Hz. Displacements without filters are listed at the bottom right. Maximum value for each waveform is shown on the left. Detailed parameters for each model can be found in table 5.1. Green's functions distributions for these models are shown in figure 5.6.

As to which one is preferred between S-Wide-24 and S-Narrow-20, teleseismic P-wave could not provide enough information to decide. Although we found that in strong ground motion simulation, results are very sensitive to the rupture width, simulating teleseismic P-waves could not give a constraint on how much down dip a fault would rupture. Based on our current understanding on the physical of earthquake, we could not decide either. Therefore, considering the similarity with the records as well as the simplicity of method, we choose both S-Wide-24 and S-Narrow-20 as our rupture fault models for simulating teleseismic and strong ground motions waves.

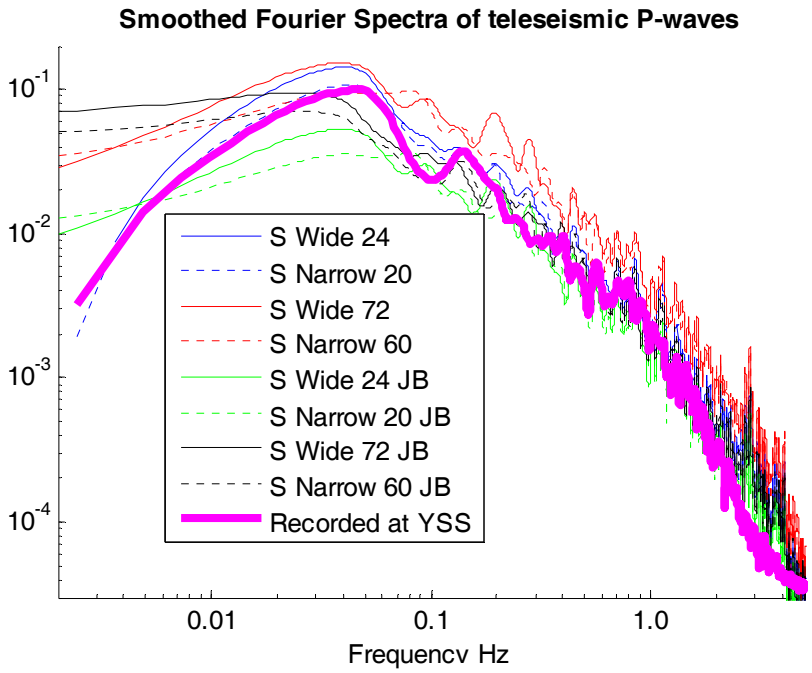

Figure 5.8. Comparison of smoothed Fourier spectra of teleseismic P-waveforms from different models and records at station YSS (Δ = 60.5º) in Sumatra event.

5.4 Strong Ground Motion Simulation

5.4.1 Choosing Empirical Green's Functions

Rupture model S-Wide-24 and S-Narrow-20 are used to simulate strong ground motions at Banda Aceh (BAC). For doing this, we need to choose appropriate records from Tokachi-

Oki event as a Green's function for each subfault in our models. In principle, the Green's functions were chosen such that the difference in distance between that required by the model geometry and that at which they were observed is smaller than a range, say 10 km. According to this criterion, there are several stations with scatted amplitudes within that distance range, because K-Net and KiK-Net are densely deployed at Hokkaido Island. This fact can be clearly found from figure 5.9 which relates peak ground velocities with the central distances (from the station to the center of the fault) for all the stations.

These qualified signals were recorded at stations with different site conditions. Generally speaking, signals recorded at soil sites are more sensitive to the local geology condition and have large spatial variations. On the other hand, site effects are much smaller for signals recorded at bedrock sites. Therefore, it is ideal to use Tokachi-Oki rock records to simulate Sumatra rock synthetics and then amplify the synthetics based on the local site condition in Banda Aceh area. However, to date, there have been few studies on local soil structure in Sumatra area. The site amplification information is not available for us. In order to consider the shaking on soil sites in Banda Aceh, we directly use soil records in Tokachi event as our EGFs to simulate strong motions. Although processing excludes the site condition of Banda Aceh completely, it could shed some insight on motions at soil sites.

To classify rock and soil sites, we can use the parameter V_s^{30} introduced in section 3.2. Soil type B and C belong to rock sites whereas type D and E belong to soil sites. Recall that there are no soil structure investigations for KiK-Net, site conditions are unknown for KiK-Net stations. This fact limited our main source of Green's functions to K-Net. Figure 5.9 shows the attenuation trends for rock K-Net stations, soil K-Net stations and KiK-Net stations. We use a simplest attenuation relationship which has the form $log\ (PGV) = a - b\ log(R)$ to address the amplitude difference for rock and soil site conditions, where R is the distance from the center of the fault to the station. As expected, soil sites generally give stronger shaking than rock sites. Site condition is not classified for KiK-Net stations, so the slope of its trend (b =1.4 to1.5) is slightly different from that of the K-Net stations (b =1.9

to 2.0). We noticed that PGV is much smaller than that predicted by the trend when station is close to the fault ($R \approx 50$ to 70km).

In the following, rock synthetics are simulated using rock record which has a median PGV for a given central distance as an EGF for the corresponding subfault. At the same time, soil synthetics are estimated using soil record which has a median PGV for a given central distance as an EGF for the corresponding subfault. The important parameters of the record chosen for each subfault as EGF are listed in table 5.2. To estimate ground motions at regions rather than Banda Aceh, all these EGFs should be chosen correspondingly to achieve the smallest scaling and best results.

Recall from Chapter 3 that signals recorded at KiK-Net station IBUH03 in Yufutsu basin contain a lot of long period motions (large petroleum storages tanks were serious damaged in this region). Its PGV is 90 cm/s, substantially larger than the median PGV (around 20 cm/s) for that central distance. Although this record seems like an extreme case, we are interest in the results from which this record was included in our EGF data base. Soil-L model which uses IBUH03 recording as an alternative EGF choice for subfault D2 (others are the same as Soil model) is considered for comparison. In the model name, L represents long-period motions.

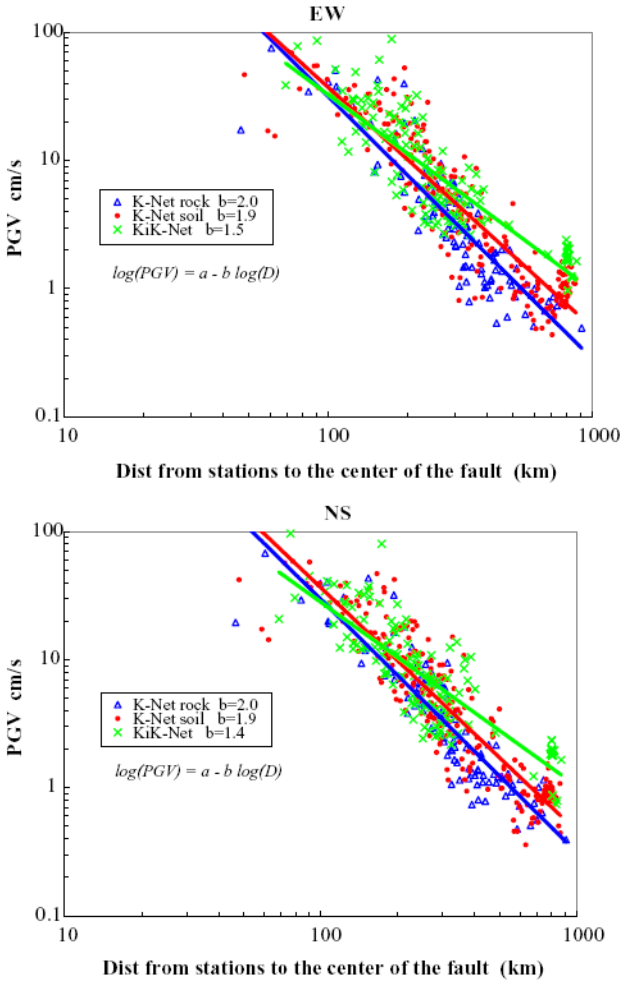

Figure 5.9. Peak ground velocities versus distance from stations to the center of the fault. K-Net stations at rock sites are represented by blue triangles, K-Net stations at soil sites are represented by red circles and KiK-Net stations are green crosses. Their linear trends for loglog scale are represented by corresponding colored solid lines. Notice that the site condition is unknown for KiK-Net stations, so the slope of its trend (b =1.4~1.5) is slightly different from that of the K-Net stations (b =1.9~2.0). These figures are useful for choosing maximum, median or minimum empirical Green's functions for a certain distance. The top figure is for east-west component and the bottom figure is for north-south component.

Table 5.2. Strong ground motions chosen to be empirical Green's functions to simulate notions at Banda Aceh (BAC) in the 2004 Sumatra earthquake.

Subfault Code	Dist (km)	Rock Model				Soil Model (Soil-L Model*)			
		Sta Name	Dist (km)	PGA cm/s/s	PGV cm/s	Sta Name	Dist (km)	PGA cm/s/s	PGV cm/s
A1	309	HKD175	298	27.1	6.8	AOM025	307	23.0	7.8
A2	297	HKD047	292	20.8	4.6	AOM020	298	30.3	7.2
A3	226	HKD041	234	45.1	6.9	HKD127	221	104.9	17.7
B1	259	HKD131	257	82.4	6.2	HKD052	260	47.7	15.4
B2	218	HKD124	231	49.5	20.2	HKD127	221	104.9	17.7
B3	130	HKD096	128	200.1	30.5	HKD077	136	407.4	40.3
C1	233	HKD124	231	49.5	20.2	HKD053	226	100.4	12.7
C2	172	HKD083	163	192.9	29.3	HKD079	175	188.3	28.1
C3	119	HKD096	128	200.1	30.5	HKD085	131	277.8	53.4
D1	281	HKD177	281	25.3	6.9	HKD156	280	33.9	3.7
D2	204	HKD101	195	45.8	8.1	HKD072 (IBUH03)	197 (206)	293.8 (374.9)	19.8 (89.6)
D3	224	HKD041	234	45.1	6.9	HKD127	221	104.9	17.7
E1	386	IWT015	390	6.6	0.9	AKT005	382	9.6	5.1
E2	316	IWT017	316	16.3	1.0	HKD143	322	20.5	6.0
F1	524	MYG016	512	4.3	0.8	FKS001	512	9.4	0.7
F2	449	MYG009	459	4.3	0.8	MYG006	443	12.3	2.2
G1	657	TCG006	690	3.7	0.7	TCG005	658	3.2	0.9
G2	591	FKSH13	610	3.8	0.2	FKS024	593	5.9	1.0
H1	787	NGNH27	777	0.6	0.4	CHB014	782	3.6	0.8
H2	718	TCG012	713	3.7	1.2	IBR011	716	5.0	1.2
I1	911	SZOH34	887	0.6	0.2	SZOH39	903	0.5	0.2
I2	848	YMNH10	855	0.4	0.2	NGNH21	849	0.5	0.2
J1	1016	SZOH34	887	0.6	0.2	SZOH39	903	0.5	0.2
J2	957	SZOH34	887	0.6	0.2	SZOH39	903	0.5	0.2

*using station in the blanket as an empirical Green's function. It is for Soil-L model, where L represents long period records.

5.4.2 Results and Discussion

Considering different rupture fault widths and site conditions, there are totally six models simulated. They are S-Wide-24 Rock; S-Narrow-20 Rock; S-Wide-24 Soil; S-Narrow-20 Soil; S-Wide-24 Soil-L and S-Narrow-20 Soil-L. Their simulated accelerations, velocities, displacements and response spectra (with 5% damping) at station BAC are compared in

Figure 5.10 to 5.13. And peak amplitudes are compared in figure 5.14. All of these synthetics are highpassed at 0.075 Hz (~13.3 sec) to avoid unstable displacements.

We estimate that PGA is around 0.15 to 0.25 g in rock site at Banda Aceh. It is consistent with the damages caused by strong shaking in that area (Somerville, Thio *et al.*, 2005). PGA at soil sites is estimated to be 0.3 to 0.4 g which is about 1.5 to 2 times larger than that in rock site. Estimated PGV in rock site is around 30 to 40 cm/s. This is smaller than PGV ≈ 80 cm/s which is estimated from the empirical relations between PGV and intensity (Sørensen, Atakan *et al.*, 2007). On the other hand, PGV estimated from Soil-L model is in that range. But it should be pointed out that this relationship was achieved from California earthquake database whose signals were mostly recorded at moderate to large crustal earthquakes. From our simulation, the amplification in low-frequency components from Rock model to Soil model is relatively small (smaller difference of PGV between rock and soil model). It may be caused by the underestimation of V_s^{30} as discussed in section 3.2. In fact, the so called soil sites are firmer than the real soil sites.

Response spectra in figure 5.13 provide frequency distributions of the ground shaking. The peaks occur at period 1 to 3 seconds for all the models. And the Soil-L model has a striking peak at 2 sec due to records at IBUH03.

By comparing these waveforms, we found that the soil site synthetics have longer duration than the rock site synthetics and Soil-L models give the longest shakings. The strong shaking duration is about 150 sec in rock sites and is more than 200 sec in soil sites. It is also similar to the value estimated by Sørensen (2007).

Motions estimated from wide rupture width models (S-Wide) generally are stronger than these from narrow rupture width models (S-Narrow). However, this is not true for Soil-L models because the velocity from one EGF (record of IBUH03 included in both wide and narrow models) significantly larger than EGFs at other subfaults.

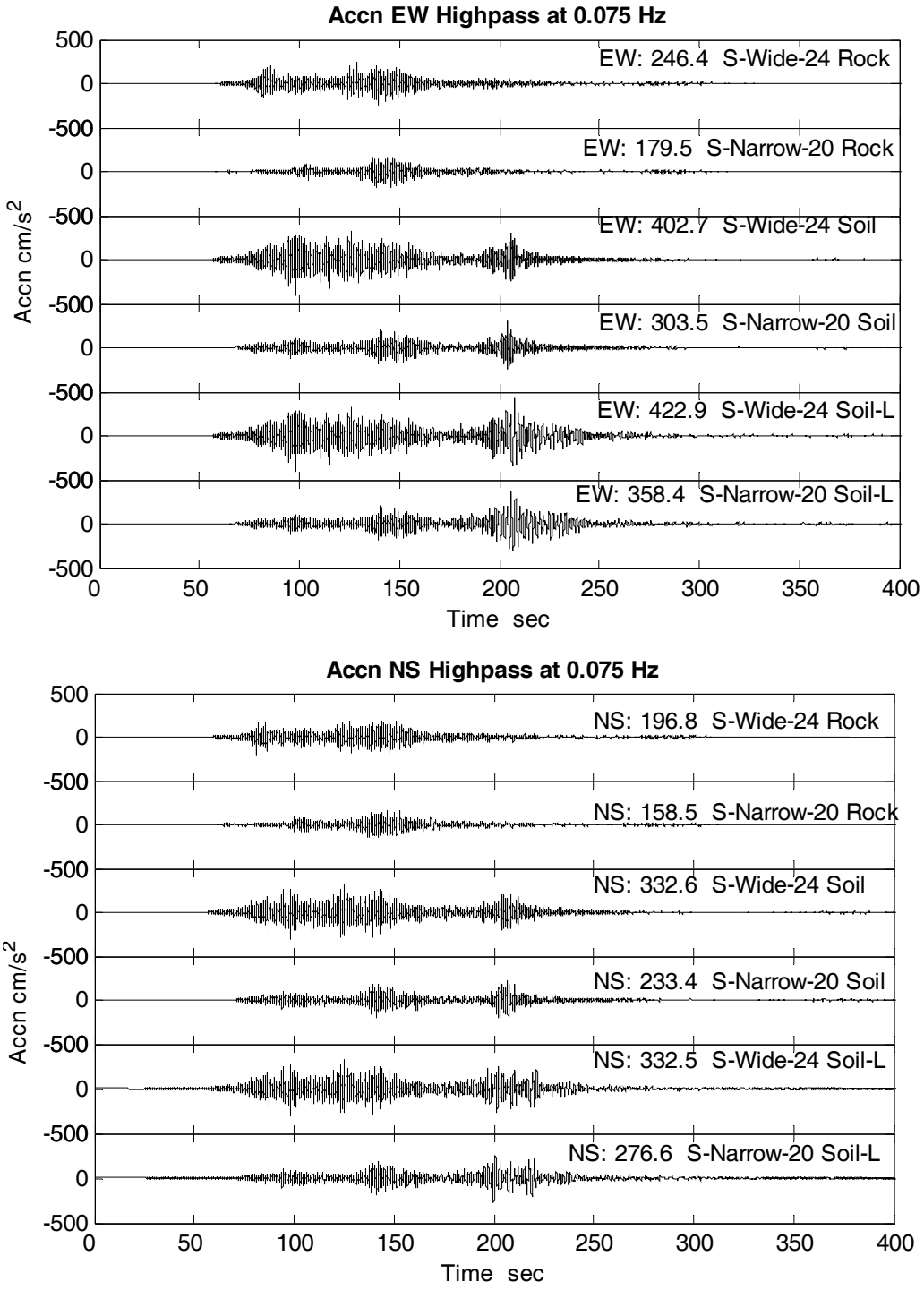

Figure 5.10. Simulated accelerations for six models in BAC. A highpass filter at 0.075 Hz is applied. Maximum value for each waveform is shown in front of the model name. The top figure is for east-west component and the bottom figure is for north-south component.

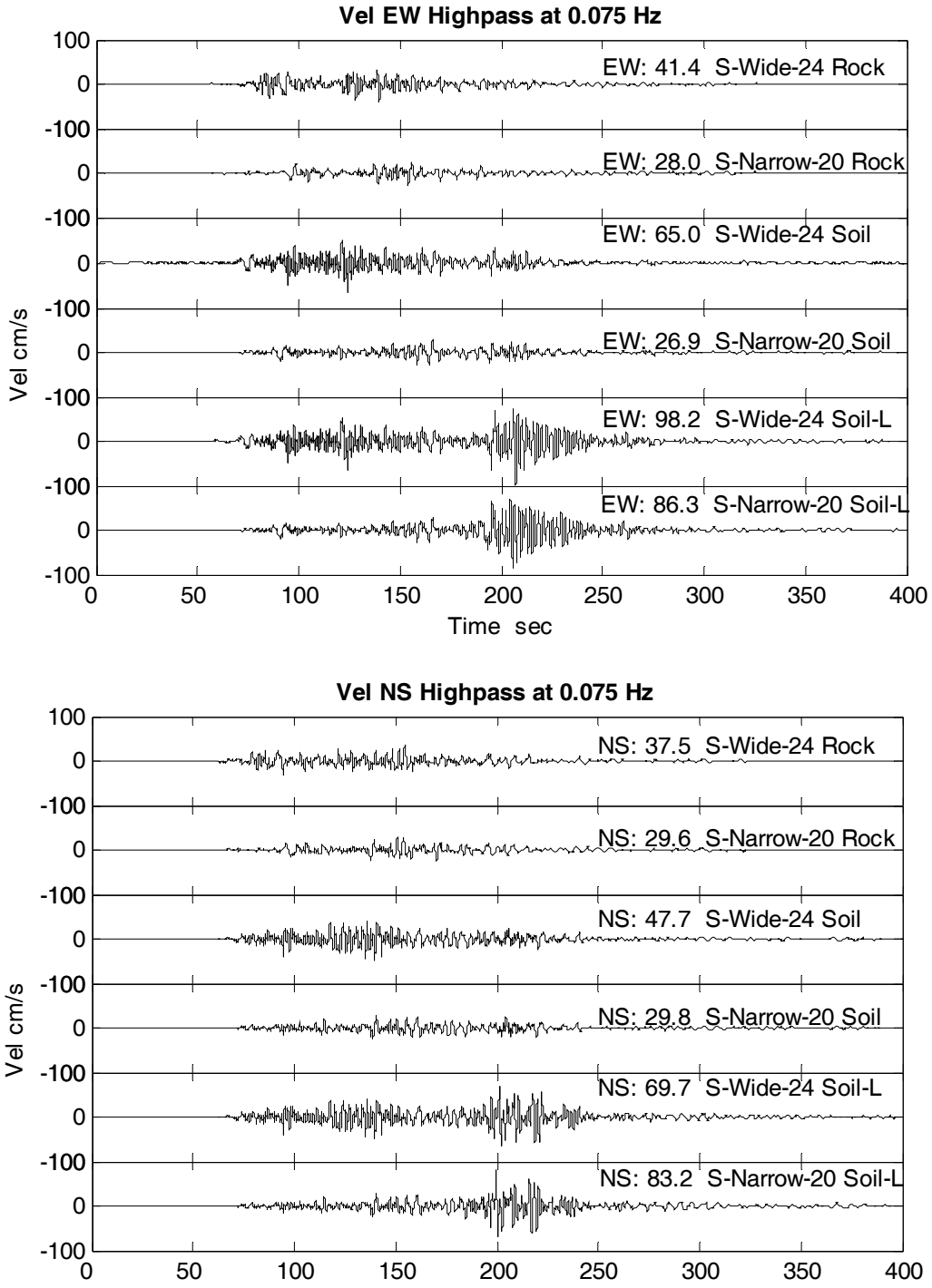

Figure 5.11. Simulated velocities for six models in BAC. A highpass filter at 0.075 Hz is applied. Maximum value for each waveform is shown in front of the model name. The top figure is for east-west component and the bottom figure is for north-south component.

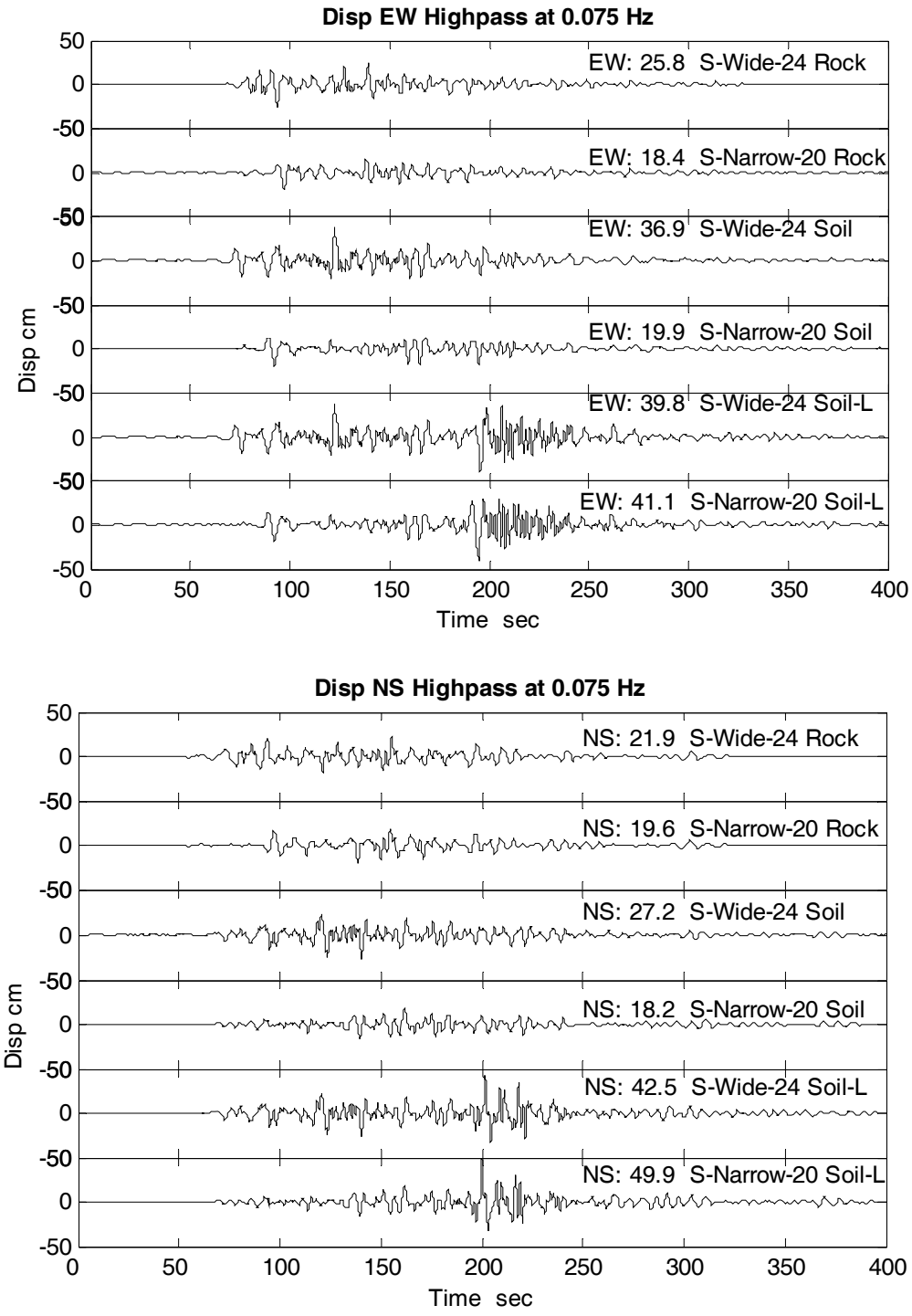

Figure 5.12. Simulated displacements for six models in BAC. A highpass filter at 0.075 Hz is applied. Maximum value for each waveform is shown in front of the model name. The top figure is for east-west component and the bottom figure is for north-south component.

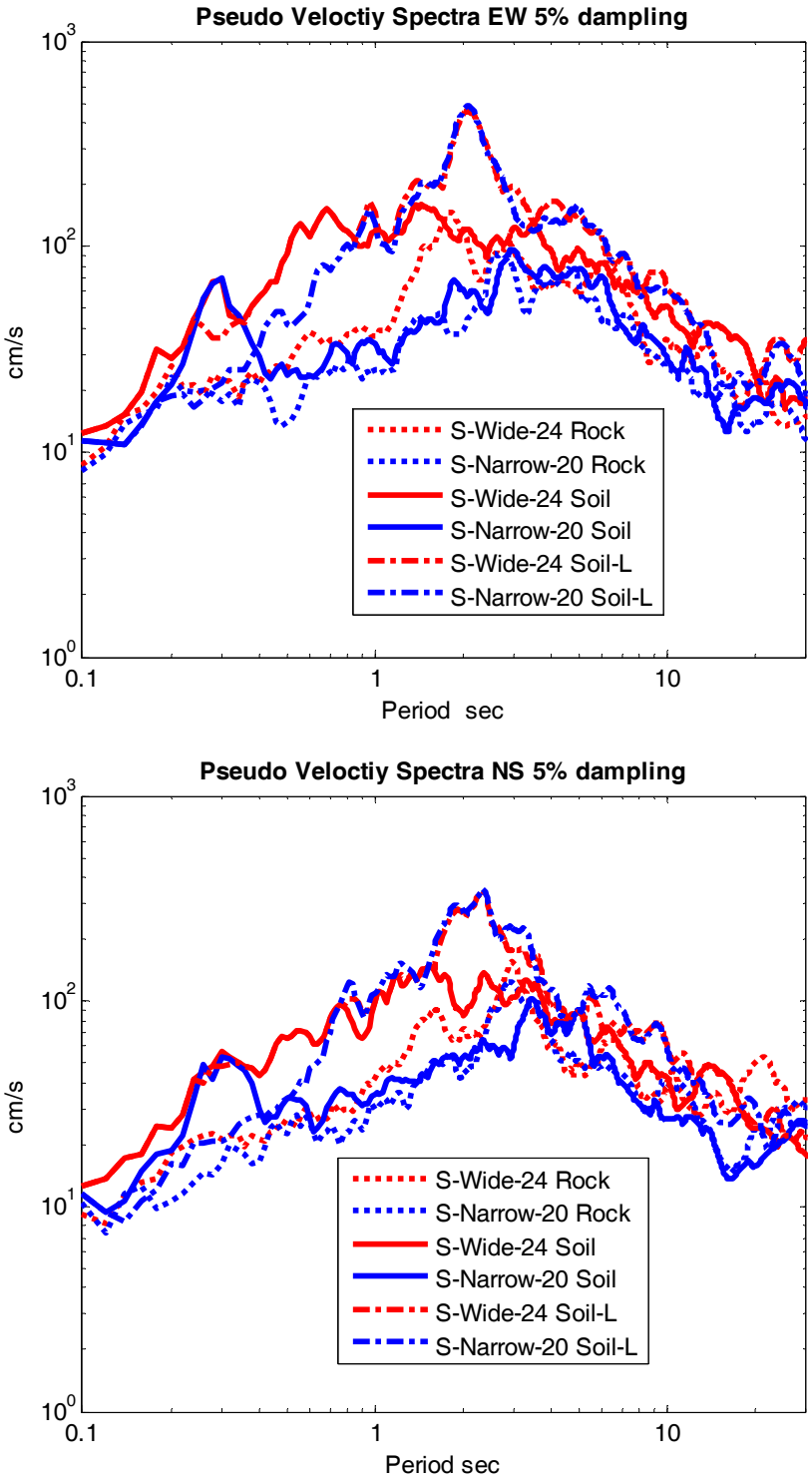

Figure 5.13. Pseudo velocity spectra for simulated data with 5% damping. The top figure is for east-west component and the bottom figure is for north-south component.

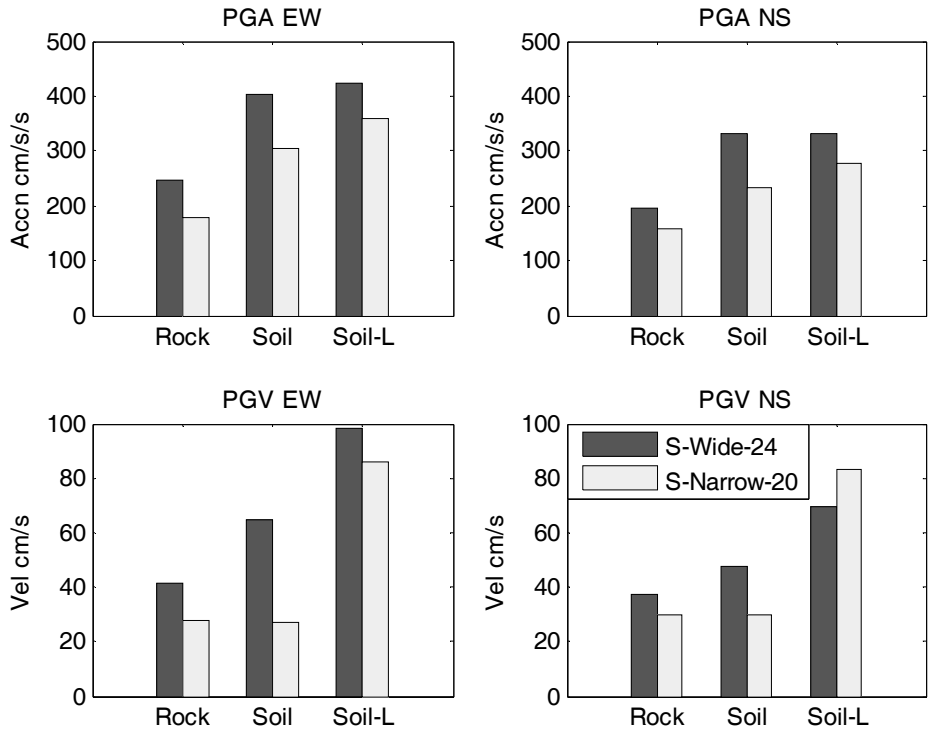

Figure 5.14. Comparing PGA and PGV for different models. The left column is for east-west component and the right column is for north-south component.

In our strong motion simulation, results are sensitive to some parameters in the modeling. The first one is the number of subfaults close to the observation point. Since the central distances (from center of subfaults to station BAC) are extremely large for subfaults such as I1 and J1 in the far north end of rupture fault, their corresponding EGFs are very small and contribute little to the final waveforms. The final results are contributed mainly by EGFs from nearby subfaults such as A3, B3 and C2. Therefore, rupture width is far more important than rupture length to affect results. If the fault rupture extended down dip further, the subfaults were closer to the observation point, larger EGFs would be chosen for these subfaults. Overall, these facts all indicate the importance of choosing empirical Green's functions. Choosing different sets of Green's function would generate waveforms with different peak ground motions. In this chapter, we choose median records as our EGFs and in Chapter 6 we choose maximum, median and minimum records as EGFs separately to consider the large uncertainty associated with the hypothetical Cascadia earthquake.

5.5 Nonlinear Performance of Buildings

All of the strong ground motions obtained from above models are used to simulate the nonlinear responses of 20- and 6-story buildings as discussed in Chapter 2. As mentioned in section 3.3, we retrieve peak interstory drift ratio (IDR %) and maximum roof displacements (MRD cm) to get an insight to the performance of buildings. Their values are exhibited in table 5.3 and figure 5.15.

Table 5.3. PGA and PGV of simulated strong ground motions at station BAC and performance of 20- and 6-story buildings shaken by these motions

Model Name		Rock				Soil				Soil-L			
		S-Wide-24		S-Narrow-20		S-Wide-24		S-Narrow-20		S-Wide-24		S-Narrow-20	
Direction		EW	NS	EW	NS	EW	NS	EW	NS	EW	NS	EW	NS
PGA cm/s^2		246	197	180	159	403	333	304	233	423	333	358	277
PGV cm/s		41.4	37.5	28.0	29.6	65.0	47.7	26.9	29.8	98.2	69.7	86.3	83.2
U20B	MRD	43.5	51.9	42.0	46.9	74.4	52.7	46.5	45.5	77.7	72.0	68.6	72.3
	IDR	1.2	1.0	0.9	0.9	2.1	1.3	1.1	1.4	2.4	2.2	1.7	2.1
U20P	MRD	52.0	57.9	53.9	64.4	71.3	68.5	55.5	59.3	120	81.1	108	106
	IDR	0.6	0.6	0.5	0.7	1.3	0.8	0.6	0.7	1.9	0.9	1.6	1.3
J20B	MRD	47.3	52.0	36.8	56.9	71.2	57.3	51.5	53.7	71.2	72.4	66.5	75.9
	IDR	1.2	0.9	0.6	1.2	2.4	1.5	1.0	1.2	2.3	2.1	2.1	2.1
J20P	MRD	63.6	74.8	40.0	67.7	82.2	72.9	65.7	58.6	106	128	81.4	135
	IDR	0.6	0.7	0.4	0.7	1.0	0.9	0.7	0.6	1.6	1.5	1.0	1.8
U6B	MRD	29.9	18.3	11.6	13.2	26.8	34.9	13.9	11.9	79.6	88.6	54.7	73.2
	IDR	2.1	1.1	0.7	0.8	1.6	2.4	0.9	0.7	4.8	5.1	3.7	4.3
U6P	MRD	26.6	20.2	11.5	12.8	26.4	30.0	12.6	13.4	59.4	62.4	59.1	75.5
	IDR	1.5	1.0	0.6	0.6	1.5	1.7	0.6	0.6	3.6	3.6	3.6	4.4
J6B	MRD	14.3	11.7	5.8	8.2	30.5	28.0	7.1	9.6	68.2	54.5	66.1	56.2
	IDR	0.7	0.5	0.3	0.3	1.9	1.6	0.3	0.4	4.3	3.4	4.2	3.5
J6P	MRD	11.3	11.2	5.8	8.2	28.9	28.5	7.1	9.7	31.2	28.4	29.8	33.4
	IDR	0.5	0.5	0.3	0.3	1.7	1.5	0.3	0.4	1.7	1.5	1.6	1.7

MRD represents Maximum Roof Displacements (cm). IDR represents peak interstory drift ratio (%).
Yellow cells denote buildings experienced large deformation and damaged.

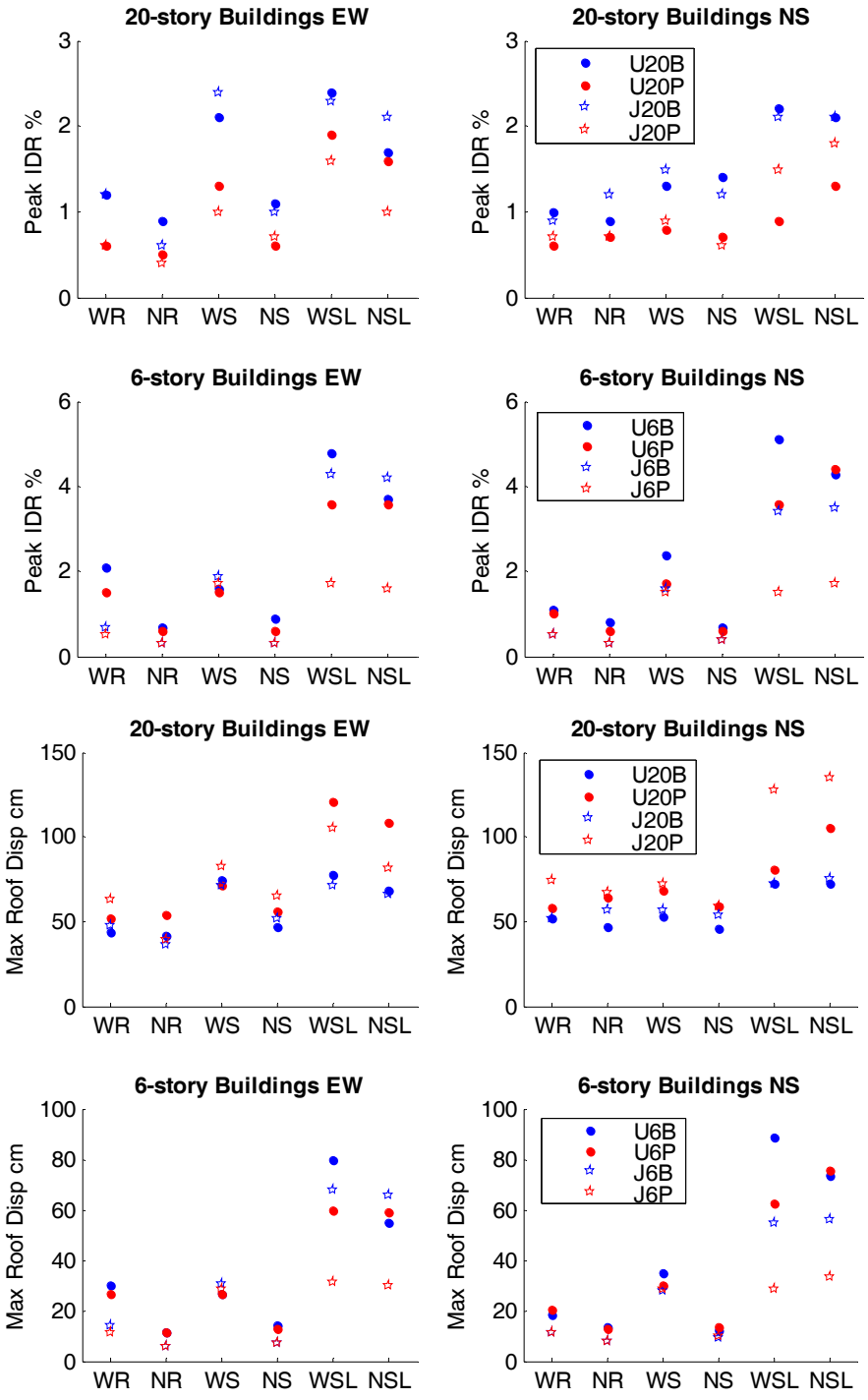

Figure 5.15. Peak interstory drift ratio (top) and maximum roof displacements (bottom) of 20- and 6-story buildings at rock and soil sites for wide and narrow models. x-axis lists the model names. Since space is limited, we abbreviate wide model as W, narrow model as N, rock model as R, soil model as S and soil model with long period motions as SL.

For 20-story buildings, the peak IDR is less than 1% for rock model and is around 2% for soil model. Comparing with their performance in Tokachi-Oki event (Chapter 3), these values would have caused buildings yielding but no collapse. The conclusion is similar for 6-story buildings. It should be pointed out that our soil model may underestimate the site amplification since not much site condition information available in Sumatra area. The roof displacement time histories from U20B are plotted in figures 5.16 to 5.17 as an example. We find that motions from rupture down dip further (S-Wide model) would have caused U20B large permanent deformation with peak IDR above 2%. Detailed discussions are presented later according to different models.

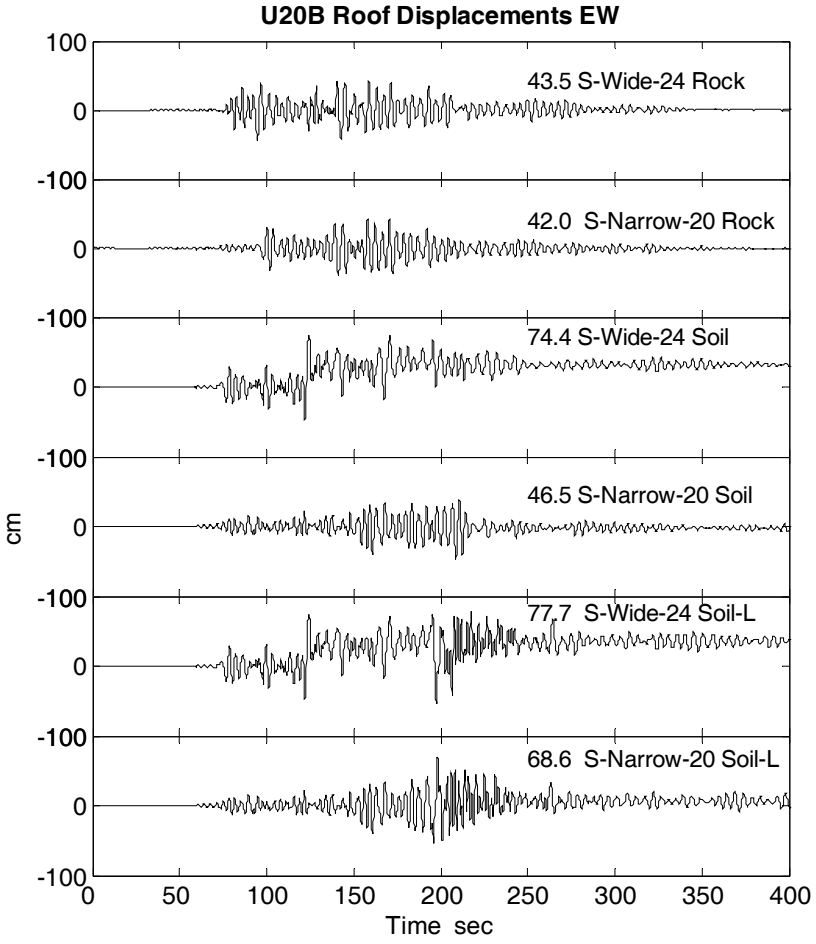

Figure 5.16. Roof displacement time histories for U20B for 6 models in east-west component. The maximum value is shown on the top right of each trace. Large permanent roof displacement (around 0.5 m) occurs for U20B in Model S-Wide at soil sites. It indicates lot of damage occurred along U20B.

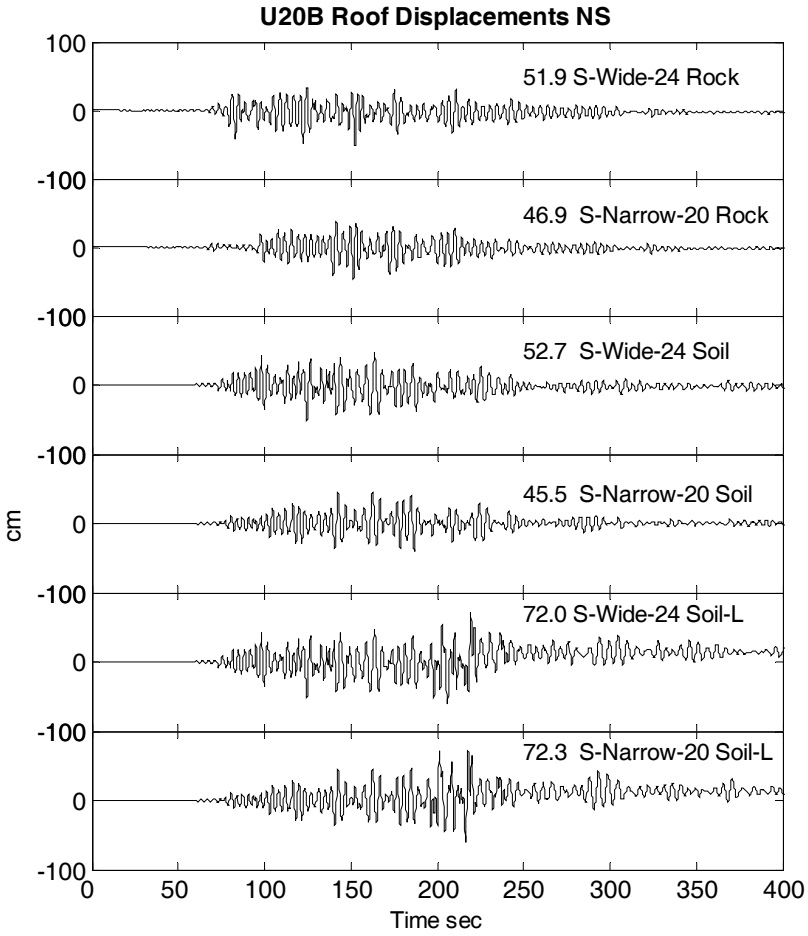

Figure 5.17. Roof displacement time histories for U20B for 6 models in north-south component. The maximum value is shown on the top right of each trace. Permanent roof displacement is around 0.25 m for U20B in Model S-Wide Soil-L.

5.5.1 20-Story vs. 6-Story Buildings

From table 5.3 and figure 5.15, it is clear to find that 6-story buildings have larger peak IDRs than 20-story buildings. However, they are much stronger than 20-story buildings as discussed from pushover curves in section 2.2. The peak IDR for 6-story buildings closing to collapse is much larger than that for 20-story buildings because of less P-Delta effects and larger lateral force-resisting capacity. Therefore, directly comparing peak IDRs for the two types of buildings is meaningless.

More attention should be paid to the much larger deformations of 6-story buildings in Soil-L model. It is induced by a striking response spectrum peak at 2 sec for Soil-L model (figure 5.13) when IBUH03 record is included in EGF database. This peak is close to the natural period of U6 which is about 1.5 sec. J6P has a natural period of 1.15 sec which is at the down hill of this peak, so its performance is much better than U6. Although J6B has the same natural period with J6P, its performance is much worse than J6P with larger deformation and more damage in strong motions. It is due to the greater nonlinearity associated with welds fracturing and the building's natural period increases during the shaking. Therefore, its performance can not be predicted obviously from response spectra. It confirms the conclusion drawn in section 3.4.

5.5.2 Buildings with Brittle Welds vs. Perfect Welds

Table 5.3 and figure 5.15 also provide performance comparison between buildings with brittle welds and with perfect welds. The peak IDRs of buildings with perfect welds are significantly smaller than these of buildings with welds which are prone to facture. This decrease of peak IDRs is significant larger than the decrease from Japanese buildings to U.S. buildings, as we will discuss further in the next section. On the other hand, 20-story buildings with perfect welds (20P) have larger maximum roof displacements (MRD) than buildings with brittle welds (20B). This opposite trend discloses that once the high-rise buildings yield under strong shaking, the deformation distribution patterns are different for buildings with different welds condition. 20B concentrates deformation on weak floors whereas 20P tries to extend the deformation to the whole buildings more evenly. To illustrate it more clearly, the peak IDRs distributions along the height of the buildings are shown in figure 5.16 for U20B, U20P and U20E for one strong record. U20E refers to the building in which material nonlinearity is removed. As a result, it would never yield as mentioned in section 3.4. Different from U20P and U20E whose peak IDRs change smoothly above the 3rd floor, the peak IDR for U20B drops significantly from the 8th floor to the 10th floor as shown in the figure. Most deformations are concentrated in story 6 to 8 of U20B. For low-rise buildings, this concentration is not so significant. As we can see

from the pushover curves in figure 2.10, 20P has larger yielding displacements than 20B. Therefore larger MRD in 20P does not imply that its performance is poor compared to 20B.

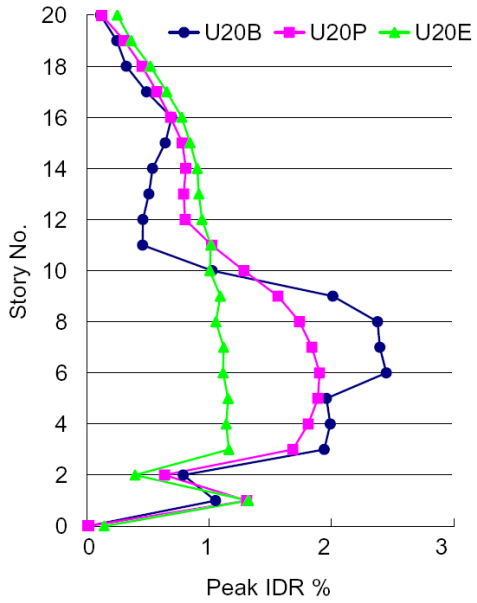

Figure 5.18. Distribution of peak IDRs along the height for U20 with brittle welds, perfect welds and elastic elements (never yield at in strong shaking as discussed in section 3.4). Curve marked with blue circles is for buildings with brittle welds. Curve marked with pink squares is for buildings with perfect welds. Curve marked with green triangles is for elastic buildings which are designed to be never yields in strong shaking. Unlike U20P and U20E whose peak IDRs change smoothly above the 3rd floor, peak IDRs for U20B drop significantly from the 8th story to the 10th story.

5.5.3 Stiffer vs. More Flexible Buildings

From table 5.3 and figure 5.15, we find that stiffer, stronger 20-story buildings which are designed according to Japanese building code (J20) do not perform as well as we expect. It is surprising that in some models, J20 had greater damage than those designed according to UBC94 (U20). For example, in Model S-Wide-24 Soil, J20B has larger peak IDR than U20B although J20P has smaller peak IDR than U20P. The roof displacement time histories for these building models are compared at figure 5.17. They also confirm that the advantage of J20 over U20 is not universally suitable for all the ground motions. This phenomenon appears not only for Soil model, but also for Rock model and Soil-L model.

Comparing with significant deformation reduction from retrofitting the fracture-prone welds as discussed in the pervious section, increasing the strength capacity and stiffness are not as efficient as fixing welds in this type of earthquakes.

For low-rise buildings, the advantage of J6 to U6 is striking. Table 5.3 and figure 5.15 show that 6-story Japanese buildings with perfect welds (J6P) have much smaller deformation either in terms of peak IDR or in terms of MRD. It may imply that strengthening buildings is a powerful way to improve the earthquake resistance for low-rise buildings.

5.5.4 Responses of Buildings for Different Site Conditions

As expected, the deformation of all type of buildings at soil site is generally larger than that at rock site especially when IBUH03 record with large PGV is used as an EGF. Since the response spectrum of records at IBUH03 has a peak at 2 sec (close to the natural period of 6-story buildings), motions from Model Soil-L could shake 6-story building more violently than motions from other site condition.

Because the soil condition is unknown for the Sumatra area, soil synthetics in this study depend completely on the stations recording Tokachi-Oki event. Therefore, it should be more cautious to explain the simulated results for soil sites in the Sumatra event.

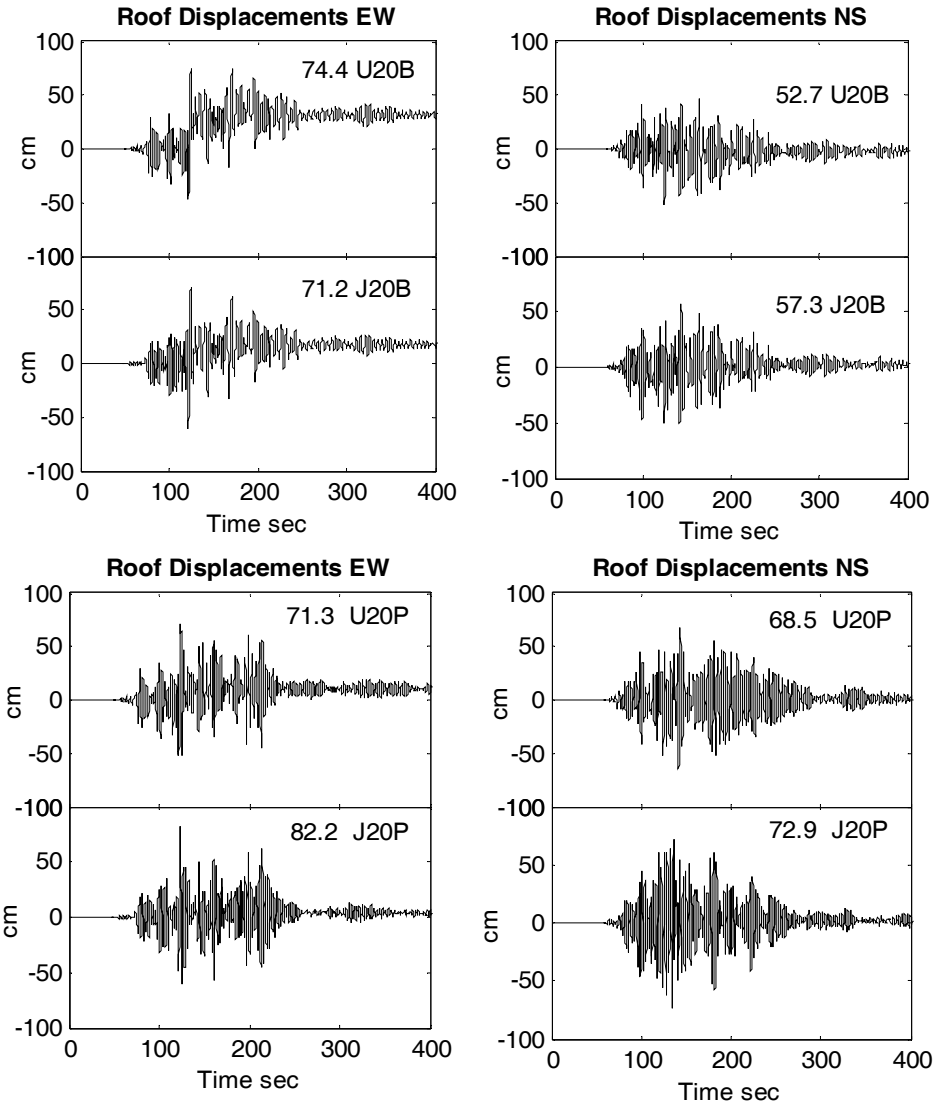

Figure 5.19. Comparing roof displacements between flexible U20 and stiff stronger J20 in Model S-Wide-24 Soil. In this case, many J20 give larger roof displacements than U20 although in some other cases, J20 could give smaller roof displacements than U20. The MRD value is listed on the top right for each trace. The advantage of stiffer high-rise buildings to flexible buildings can not be found here.

5.5.5 Comments on Long Duration Effects

Although our simulation did not show the collapse of building in this event, it is hard to conclude the none-collapsing for the real high-rise steel moment-frame buildings which have more deterioration mechanisms than our model. Recall in section 2.1.5, our FEM

building model did not consider any local buckling in the elements. This limitation may not be significant for moderate crustal earthquakes (such as the 1994 Northridge earthquake and 1995 Kobe earthquake) whose durations are around 10 to 30 seconds. However, for giant subduction earthquakes strong shaking duration is very long. Our simulation presents more than 3 minutes strong shaking in BAC for the Sumatra event (section 5.4.2) and more than 5 minutes strong shaking in the Seattle basin for the Cascadia (section 6.4.2). Their contribution could not be ignored. Because once structural damage is initiated, it tends to progressively worsen as the number of large-amplitude cycles increases, for longer shaking, more damage will accumulate.

For low-rise buildings, the advantage of J6 to U6 is striking. Table 5.3 and figure 5.15 show that 6-story Japanese buildings with perfect welds (J6P) have much smaller deformation either in terms of peak IDR or in terms of MRD. This tells us that strengthening buildings is a powerful way to improve the earthquake resistance for low-rise buildings.

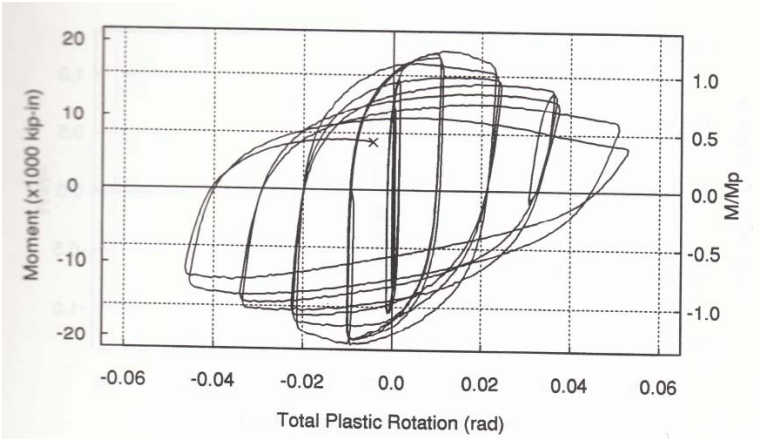

Figure 5.20. An example of hysteresis loop obtained from the SAC experiment Test No. UCSD-3R (SAC 1996). This is a steel specimen of beam with local flange buckling occurred.

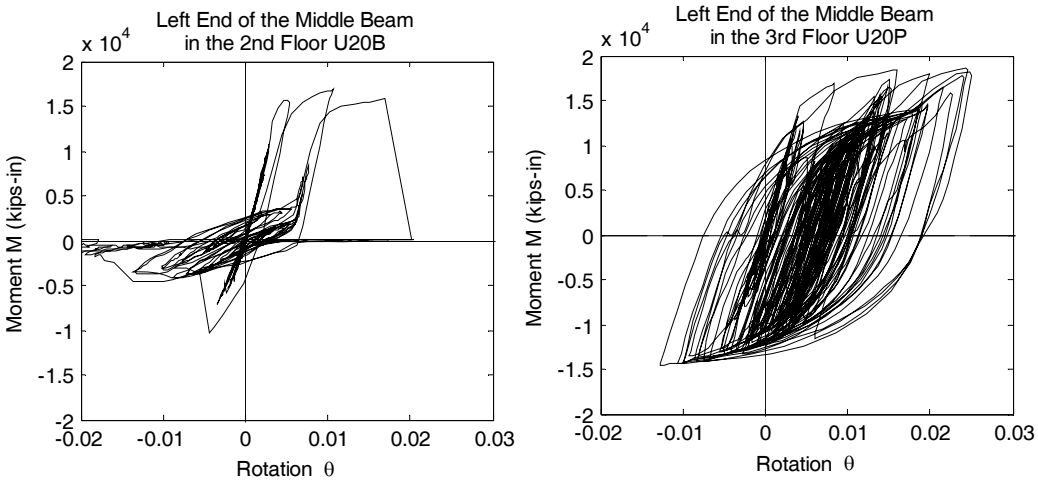

Figure 5.21. Examples of moment-rotation response (hysteresis loop) in an end of a beam to the simulated ground motions. The left figure is for U20B. Since some fibers fractured duration the shaking, resisting moment decreased suddenly. The right figure is for U20P. Since local buckling is not considered in this model, stiffness and yielding strength are kept constant after so many cycles. There is no degradation mechanism involved in the figure.

Figure 5.20 shows an example of a hysteresis loop for a beam obtained from the SAC test with Test No. UCSD-3R (SAC 1996). This is a typical loop for the specimen with local flange buckling and web distortion but no welds fracture occurring during the test. Its yielding strength and stiffness were reduced as cyclic loading continued. For comparison, figure 5.21 gives examples of strength-deformation response (i.e. hysteresis loop) of beams for building model U20B and U20P to our simulated ground motion. The figure shows clearly that there is no other degradation mechanisms involved in U20P during this long shaking. Our simulation shows that buildings are heavily yielded during shaking but continue to sway back and forth for the remaining one to two minutes (and three to four minutes for the Cascadia event in section 6.4.2.). If more deterioration mechanisms are considered in our model, the yield stress and stiffness of elements would decrease gradually after plastic hinges are formed. With so many cycles after yielding, the roof displacements may not be as stable as we show in figures 5.16, 5.17, 5.19 for 20-story buildings with perfect welds. And the real high-rise buildings would have performed significantly worse than our simulation.

This long duration also bring out the possibility of the stress decreasing because of the temperature raise. As we know, most of the energy generated by plastic deformation of a material would transfer to the heat if there is no other energy exchange in the system. The shaking from earthquake happens too quickly to allow heat transition. The heat could concentrate on the connections and increase the steel temperature locally. To obtain the amount of temperature increase, we need to first calculate the plastic energy generated duration the shaking. The amount of plastic energy can be classified as the area under the stress-strain diagram up to a specified strain. This can be roughly expressed as:

$$\Delta E(t) = \iiint_{V,\tau=0\to t} \sigma(\tau) d\varepsilon(\tau) dV d\tau \tag{5.1}$$

At the same time, energy can be represented as the following equation in terms of temperature change,

$$\Delta E = mC\Delta T = \rho VC\Delta T \,, \tag{5.2}$$

where C is the heat capacity of steel. So the temperature change can be roughly calculated as

$$\Delta T = \frac{\iiint_{V,\tau=0\to t} \sigma(\tau) d\varepsilon(\tau) dV d\tau}{\rho VC} \,. \tag{5.3}$$

Using this simplified method, we get that the temperature increase is no more than 100ºC after 200 seconds strong shaking. It does not reach the threshold which would reduce steel yield stress. However, it provides an idea to include deterioration mechanism in terms of energy in FEM model. Detailed description and applications are beyond the scope of this thesis and can be regarded as future work.

CHAPTER 6

The Scenario Cascadia Subduction Earthquake M_w 9.2

Researchers have found that Cascadia subduction zone generated a giant earthquake (M_w >9.0) three hundred years ago and has a potential to generate another one in the future (Atwater, 1987; Heaton and Hartzell, 1987). The strong ground motions from this type of earthquake will shake the inland cities such as Seattle, Portland and Vancouver where more than 900 modern high-rise buildings exist. These modern designs have never been examined by such large earthquakes except the 1985 Michoacan earthquake (M8.2) where many 10- to 20-story modern designed buildings collapsed in Mexico city which is 400 km away from epicenter (Anderson, Bodin P. *et al.*, 1986; Hall and Beck, 1986). To understand the performance of high-rise buildings under this scenario earthquake is of great importance for earthquake engineers as well as residence in these areas.

In this chapter, the scenario Cascadia subduction earthquake is assumed to have the similar source model as the 2004 Sumatra earthquake. Based on this assumption, we apply empirical Green's function method to estimate the strong ground motions in the city of Seattle. We calculate the Settle basin amplification and simulate the responses of 20- and 6-story steel moment frame buildings in this expecting event.

6.1 Introduction

The Cascadia subduction zone is a very long sloping fault that stretches from Brooks Peninsula on Vancouver Island to Cape Mendocino in northern California. The recognition of great earthquakes associated with Cascadia subduction zone began in the early 1980s. Heaton and Kanamori (1984) firstly proposed this idea although scientists had long assumed that there is no great-earthquake potential in the Cascadia area. This argument spurred a lot of debate until Atwater (1987) found geologic evidence of an great subduction earthquake occurred 300 years ago. This earthquake also explained the mysterious tsunami documented in Japanese historic literatures (Atwater, Satoko *et al.*, 2005) and in native Indian legend (Heaton and Snavely, 1985). For a detailed historic story, reader can refer Nance's book: On Shaky Ground (Nance, 1988). Nowadays, researchers have achieved consensus that a giant earthquake (M_w >9.0) has rupture the Cascadia subduction zone in 1700 from northern California to British Columbia and would return in the future.

More than half of the 900 existing high-rise buildings in the Cascadia area were constructed before the great-subduction earthquake threat was reflected in the seismic design code in 1997 (Atwater, Satoko *et al.*, 2005). Even for the newly constructed high-rise buildings, the local crustal earthquakes instead of the subduction earthquakes control the design (White and Ventura, 2004). In this study, we focus on Seattle because there are lots of site investigation results available (Frankel, Carver *et al.*, 2002; Pratt, Brocher *et al.*, 2003) in this area. Although this great subduction earthquake would occur offshore and be more than 250 km away from city of Seattle, long-period waves would attenuate slowly and may get trapped and significantly amplified in the Seattle basin. A series of SHIPS investigations were conducted (Pratt, Brocher *et al.*, 2003; Pratt, 2006) and Pratt found that the amplifications of 0.3 to 0.8 Hz seismic waves can be as large as a factor of 6 to 8 in the Seattle basin. Many engineers do not realize this and frame the Seattle seismic building codes similar to California seismic building codes although they are threatened by very different types of earthquakes. Therefore, numerical simulation of building's response is necessary to quantify the seriousness of this issue. Figure 6.1 shows an example of the

modern high-rise buildings in downtown Seattle. Its unusual appearance in the foot base may not be a good lateral force-resisting system for seismic purpose. If a future giant subduction earthquake occurs in weekday, the collapse of these high-rise buildings would generate a large death toll.

Figure 6.1. Rainer Tower in downtown Seattle. It is a 40-story building constructed at 1977.

6.2 Rupture Fault Models

The Cascadia subduction zone separates the Juan de Fuca and North America plates where the Juan de Fuca plate is subducted beneath the North American plate along this 1300 km long zone at a convergence rate of 3 to 4 cm/year. Figure 4.4 has shown the cross section of geometry of this subduction zone. The Cascadia subduction zone shares many characteristics with other subduction zones such as southern Chile where giant subduction earthquakes have occurred (Heaton and Hartzell, 1987). A magnitude 9 earthquake would occur if the whole subduction zone ruptured. Therefore, we use the source model from the 2004 Sumatra-Andaman earthquake to estimate the hypothetical Cascadia subduction earthquake.

In this study, three rupture models with different widths were proposed (figure 6.2). It is found in Chapter 5 that the results are sensitive to the rupture width, considering different widths cases would include this uncertainty in our modeling. The wider model extends beyond the Olympic Mountain with a maximum rupture width 250 km. It is the same as the wide model used in the Sumatra event. The Olympic Mountain can be regarded as an outer-arc ridge. Its counterpart in the 2004 Sumatra event is the Simenulue Island. The narrow model has a maximum rupture width 150 km and rupture extends to the coastline. This coastline is approximately along the hinge line where rupture fault ends in elastic rupture modeling. The intermediate model has a maximum rupture width 175 km. It extends more inland than the narrow model but has not reached the Olympic Mountain.

The number of EGFs summing up together for each model is determined from the rupture size ratio as recommend in Chapter 5. The wide model has 23 subfaults; the median model has 15 subfaults and the narrow model has 13 subfaults. Each subfault ruptures once. Their geometries are shown in figure 6.2. Notice that the overlap areas increase in narrow model in order to better fit the shape of the Cascadia subduction zone. And the rupture length is around 1200 km. Source parameters are listed in table 6.1. Again, results are not sensitive to the slight changes of strike, dip, fault length and rupture velocity.

Table 6.1. Parameters for each model

Model Code	Strike	Dip	No. of added EGF	No. of rupture	Rupture Vel (km/s)	L (km)	W (km)	m*	n*
C-Wide-23	310º / ** 0º	8º	23	1	2.5 / 2.8	390 / 780	175 ~ 250	3 / 6	2 ~ 3
C-Med-15			15				100 ~ 175		
C-Narrow-13			13				100 ~ 150		

*m is the number of subfaults along the fault length; n is the number of subfaults along the fault width;
** The parameters for two segments are separated by '/'.

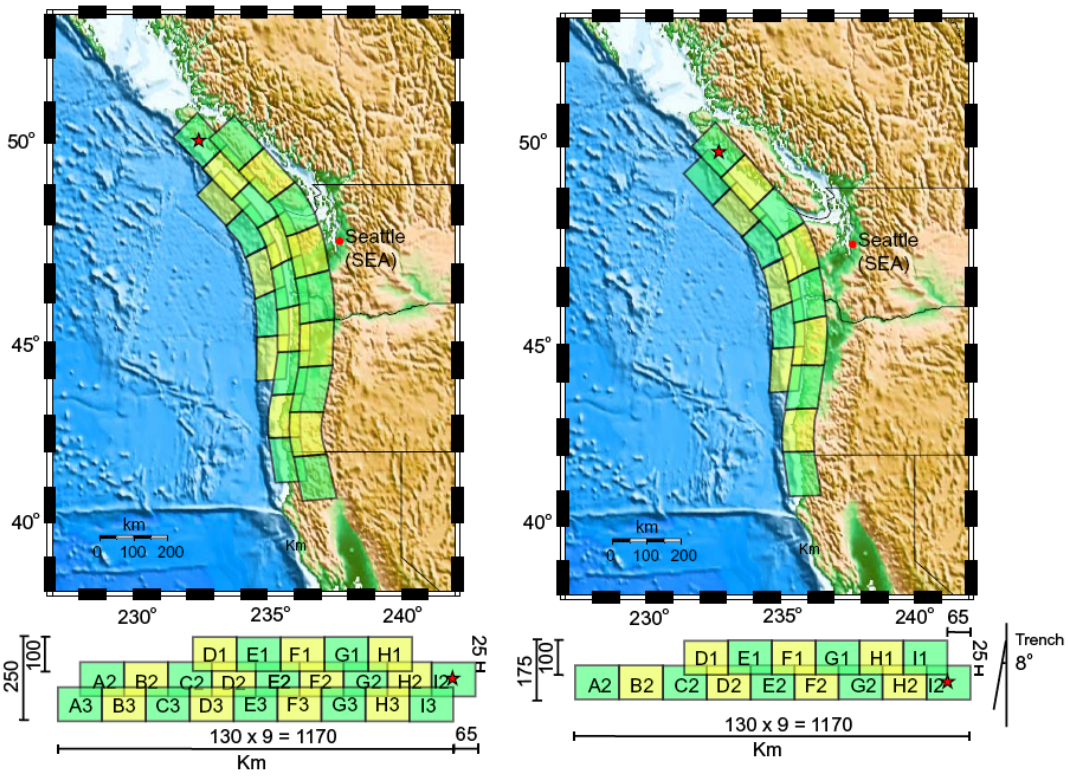

(a) C-Wide-23

(b) C-Med-15

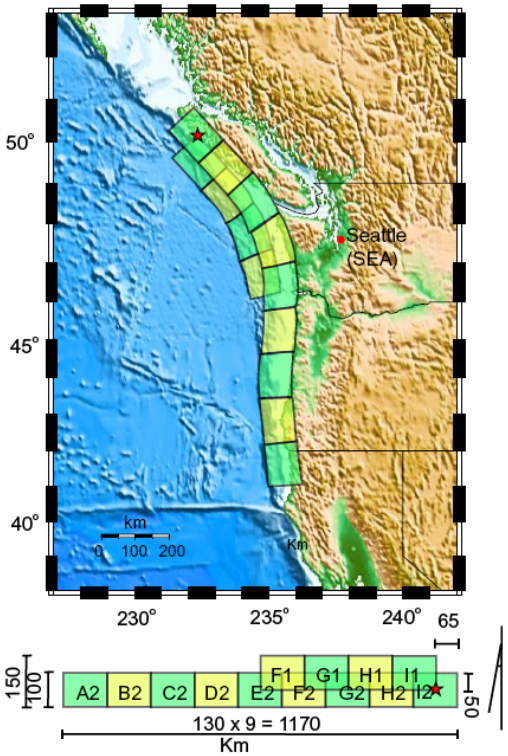

(c) C-Narrow-13

Figure 6.2. Geometry of rupture fault models used to simulate the Scenario Cascadia Earthquake M_w9.2. Red star represents the hypocenter of this event. Red dot represents the location where strong ground motions would be simulated. Each box represents a subfault whose response is simulated by the ground motions recorded corresponding station from the 2003 Tokachi-Oki earthquake. Letters in each box denote the subfault code. (a) shows the wide rupture width model. (b) shows the median rupture width model. (c) shows the narrow rupture width model.

6.3 Teleseismic P-wave Simulations

Teleseismic P-waves are simulated for the above three models using four records from Tokachi-Oki event as our empirical Green's functions. These four records are shown in Figure 5.5 and the method is completely the same as that discussed in section 5.3. Distribution of EGFs is randomly assigned to the subfaults and the sets that used in our simulation are shown in figure 6.3. Difference choices would only slightly affect the resulted peak amplitudes.

The simulated teleseismic P-waveforms at distance 60° are exhibited in figure 6.4. Signals recorded at station YSS in the Sumatra event are compared with our simulation. It indicates that estimated velocities and displacements are slightly smaller than the observed data for all the three models but in the same scale. And the estimated accelerations are similar with recordings. However, if the envelopes are compared, we found that model C-Wide-23 gives a best estimation.

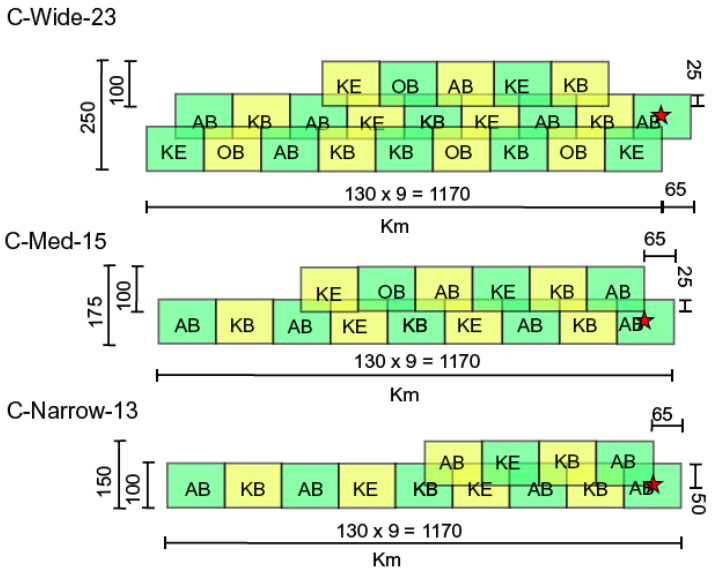

Figure 6.3. Distribution of empirical Green's functions used to simulate teleseismic P-waves from the expected Cascadia earthquake. Each box represents a subfault. Letters in the box refer to figure 5.5 and designate which records from the 2003 Tokachi-Oki event are used as Green's functions. These records are chosen randomly from the four stations. Difference choices would only slightly affect the resulted peak amplitudes. Star represents the hypocenter of the Cascadia event. The top figure is for rupture model with wide width; the middle figure is for rupture model with intermediate width and the bottom figure is for rupture model with narrow width.

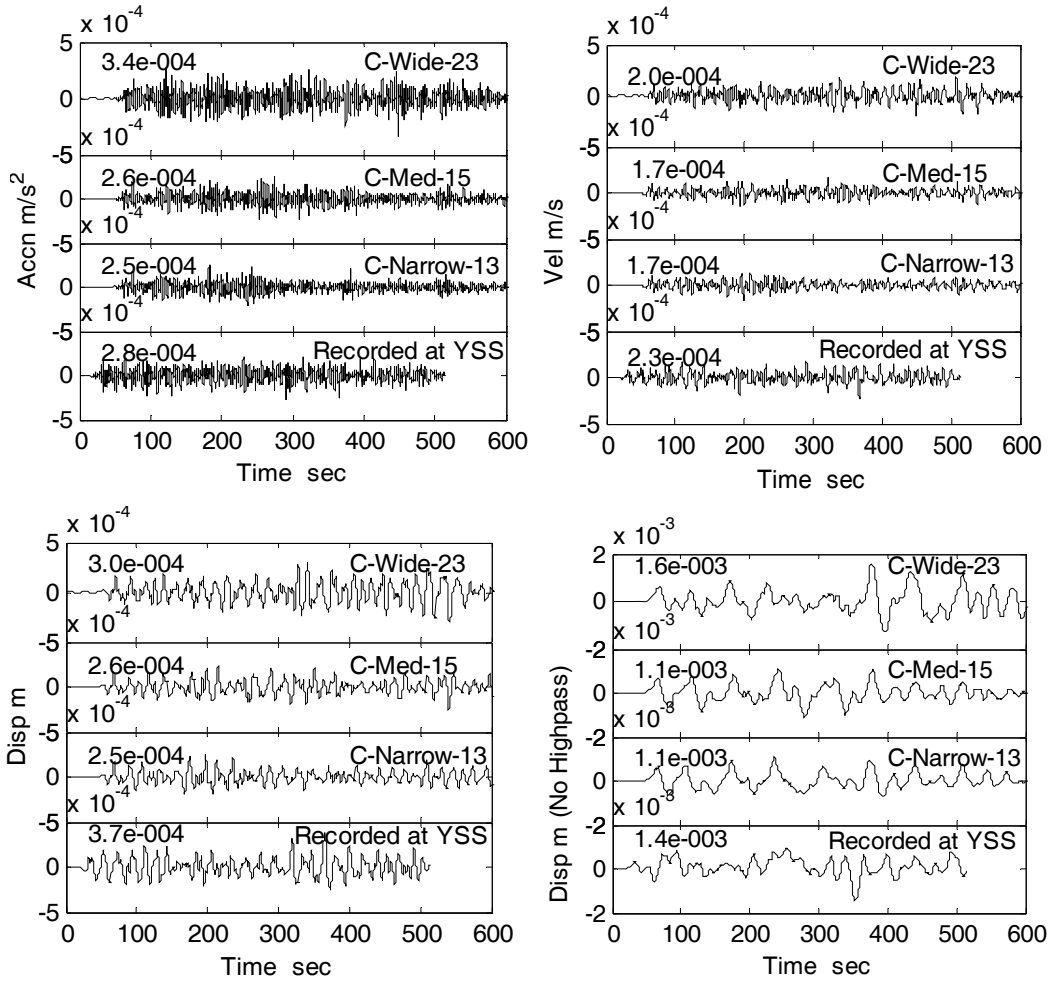

Figure 6.4. Comparison of simulate teleseismic P-waveforms at distance 60º from three models with observed recordings at station YSS (Δ = 60.5º) in the Sumatra event. Accelerations are shown in the top left, velocities are shown in the top right and displacements are shown in the bottom left. Data is highpassed at 0.05 Hz. Displacements without filters are listed in the bottom right. Maximum value for each waveform is shown on the left. Detailed parameters for each model can be found in table 6.1. The distributions of Green's functions for these models are shown in figure 6.3.

6.4 Strong Ground Motion Simulations

6.4.1 Rock Sites

As discussed in section 5.4.1, we use strong ground motion recordings from the 2003 Tokachi-Oki event as the database for EGFs. The same as before, we first simulate the synthetics at rock site in Seattle (station SEA) using data recorded at rock sites. Classification of rock sites and soil sites were discussed in section 5.4.1. For each subfault, there are several records within that central distance range and they are suitable to be an EGF. Unlike the Sumatra event, this future giant Cascadia subduction earthquake has a larger uncertainty. Three sets of EGFs are chosen for each subfault to consider this uncertainty. If a record which gives the maximum PGV is chosen as an EGF for that subfault, we call this model Max Model. If a record which gives the median PGV is chosen as a Green's function, we call this model Med Model. If a record which gives the minimum PGV is chosen as a Green's function, we call this model Min Model. Table 6.2 lists the records chosen for each subfault in these three models. The reason to use PGV as a choosing criterion is that buildings' response can be better predicted by PGV than PGA and PGD which is discussed in section 3.4.

Considering different rupture fault widths and different EGF sets, there are nine models simulated in total. They are C-Wide-23 Max; C-Med-15 Max; C-Narrow-13 Max; C-Wide-23 Med; C-Med-15 Med; C-Narrow-13 Med; C-Wide-23 Min; C-Med-15 Min and C-Narrow-13 Min, where "C" represents the Cascadia event. The simulated accelerations, velocities, displacements and response spectra (with 5% damping) at station SEA are compared in figures 6.5 to 6.8, respectively. All of these synthetics are highpassed at 0.075 Hz (13.3 sec) to avoid displacements drift and be consistent with reliable frequency range of the transfer functions representing the Seattle basin amplification. This would be discussed in more detail in the next section.

Table 6.2. Strong ground motions chosen to be empirical Green's functions to simulate motions of the scenario Cascadian earthquake experienced at rock sites in Seattle (SEA).

Subfault Code		Dist (km)	Max Model			Med Model			Min Model		
			Sta Name	PGA cm/s/s	PGV cm/s	Sta Name	PGA cm/s/s	PGV cm/s	Sta Name	PGA cm/s/s	PGV cm/s
C-W-23	A2	665.6	FKS014	2.5	0.7	FKS014	2.5	0.7	FKS014	2.5	0.7
	A3	708.6	IBR006	6.5	1.0	IBR006	6.5	1.0	IBR006	6.5	1.0
	B2	536.6	MYG016	4.3	1.3	MYG016	4.3	1.3	MYG016	4.3	1.3
	B3	576.3	FKS007	5.1	0.9	FKS007	5.1	0.9	FKS007	5.1	0.9
	C2	406.8	IWT015	6.7	1.4	IWT015	6.7	1.4	IWT015	6.7	1.4
	C3	438.1	MYG003	10.9	1.0	MYG003	10.9	1.0	MYG003	10.9	1.0
	D1	388.6	IWT025	6.5	1.3	IWT025	6.5	1.3	IWT025	6.5	1.3
	D2	283.0	HKD020	7.6	6.8	HKD020	7.6	6.8	AOM022	26.1	2.8
	D3	303.9	HKD017	9.7	9.5	HKD018	9.4	6.1	HKD170	6.4	2.3
	E1	277.5	HKD020	7.6	6.8	HKD020	7.6	6.8	AOM022	26.1	2.8
	E2	185.1	HKD129	86.7	39.8	HKD124	50.2	19.7	HKD035	14.1	7.0
	E3	176.1	HKD054	54.0	16.2	HKD054	54.0	16.2	HKD041	45.0	8.0
	F1	224.2	HKD117	27.6	12.5	HKD131	81.9	7.7	AOM004	26.2	3.8
	F2	164.1	HKD105	141.6	43.3	HKD123	34.2	14.5	HKD038	192.0	12.5
	F3	94.4	HKD084	353.8	50.7	HKD095	192.5	41.0	HKD096	200.3	34.5
	G1	246.7	HKD176	47.2	9.3	AOM008	55.6	7.6	AOM009	35.4	4.6
	G2	247.1	HKD176	47.2	9.3	AOM008	55.6	7.6	AOM009	35.4	4.6
	G3	152.4	HKD105	141.6	43.3	HKD088	162.9	19.6	HKD101	47.0	11.8
	H1	340.2	AOM018	11.1	4.5	AOM029	11.8	2.6	IWT016	15.1	1.6
	H2	357.2	AOM018	11.1	4.5	AOM029	11.8	2.6	IWT016	15.1	1.6
	H3	269.6	HKD022	34.2	10.1	HKD146	27.5	8.0	AOM002	22.8	2.9
	I2	468.4	MYG011	29.5	1.3	MYG011	29.5	1.3	MYG011	29.5	1.3
	I3	384.9	AKT021	3.6	1.3	AKT021	3.6	1.3	AKT021	3.6	1.3
C-M-15	A2	699.2	IBR006	6.5	1.0	IBR006	6.5	1.0	IBR006	6.5	1.0
	B2	568.8	FKS005	6.8	1.1	FKS005	6.8	1.1	FKS005	6.8	1.1
	C2	437.8	MYG003	10.9	1.0	MYG003	10.9	1.0	MYG003	10.9	1.0
	D1	409.2	IWT015	6.7	1.4	IWT015	6.7	1.4	IWT015	6.7	1.4
	D2	305.6	HKD017	9.7	9.5	HKD018	9.4	6.1	HKD170	6.4	2.3
	E1	295.0	HKD169	29.6	6.8	HKD169	29.6	6.8	AOM028	28.4	3.8
	E2	192.8	HKD129	86.7	39.8	HKD124	50.2	19.7	HKD035	14.1	7.0
	F1	225.8	HKD117	27.6	12.5	HKD131	81.9	7.7	AOM004	26.2	3.8
	F2	152.9	HKD105	141.6	43.3	HKD088	162.9	19.6	HKD101	47.0	11.8
	G1	237.3	HKD176	47.2	9.3	HKD177	25.2	7.9	HKD031	11.9	5.5
	G2	224.5	HKD117	27.6	12.5	HKD131	81.9	7.7	AOM004	26.2	3.8
	H1	326.6	HKD171	6.7	2.9	HKD171	6.7	2.9	HKD171	6.7	2.9
	H2	333.6	HKD171	6.7	2.9	HKD171	6.7	2.9	HKD171	6.7	2.9
	I1	432.4	MYG002	22.5	1.3	MYG002	22.5	1.3	MYG002	22.5	1.3
	I2	446.8	MYG003	10.9	1.0	MYG003	10.9	1.0	MYG003	10.9	1.0
C-N-13	A2	686.8	TCG006	3.7	0.8	TCG006	3.7	0.8	TCG006	3.7	0.8
	B2	562.4	FKS005	6.8	1.1	FKS005	6.8	1.1	FKS005	6.8	1.1
	C2	436.4	MYG003	10.9	1.0	MYG003	10.9	1.0	MYG003	10.9	1.0
	D2	314.0	HKD017	9.7	9.5	HKD018	9.4	6.1	HKD170	6.4	2.3
	E2	217.2	HKD130	58.0	20.6	HKD117	27.6	12.5	AOM004	26.2	3.8
	F1	247.2	HKD176	47.2	9.3	AOM008	55.6	7.6	AOM009	35.4	4.6
	F2	187.4	HKD129	86.7	39.8	HKD124	50.2	19.7	HKD035	14.1	7.0
	G1	254.3	HKD175	27.2	9.2	HKD030	11.6	6.7	HKD045	10.0	4.0
	G2	259.7	HKD022	34.2	10.1	HKD175	27.2	9.2	HKD045	10.0	4.0
	H1	333.9	HKD171	6.7	2.9	HKD171	6.7	2.9	HKD171	6.7	2.9
	H2	367.0	AKT003	8.1	3.9	AKT003	8.1	3.9	AKT003	8.1	3.9
	I1	434.7	MYG002	22.5	1.3	MYG002	22.5	1.3	MYG002	22.5	1.3
	I2	481.3	YMT002	3.2	2.1	YMT002	3.2	2.1	YMT002	3.2	2.1

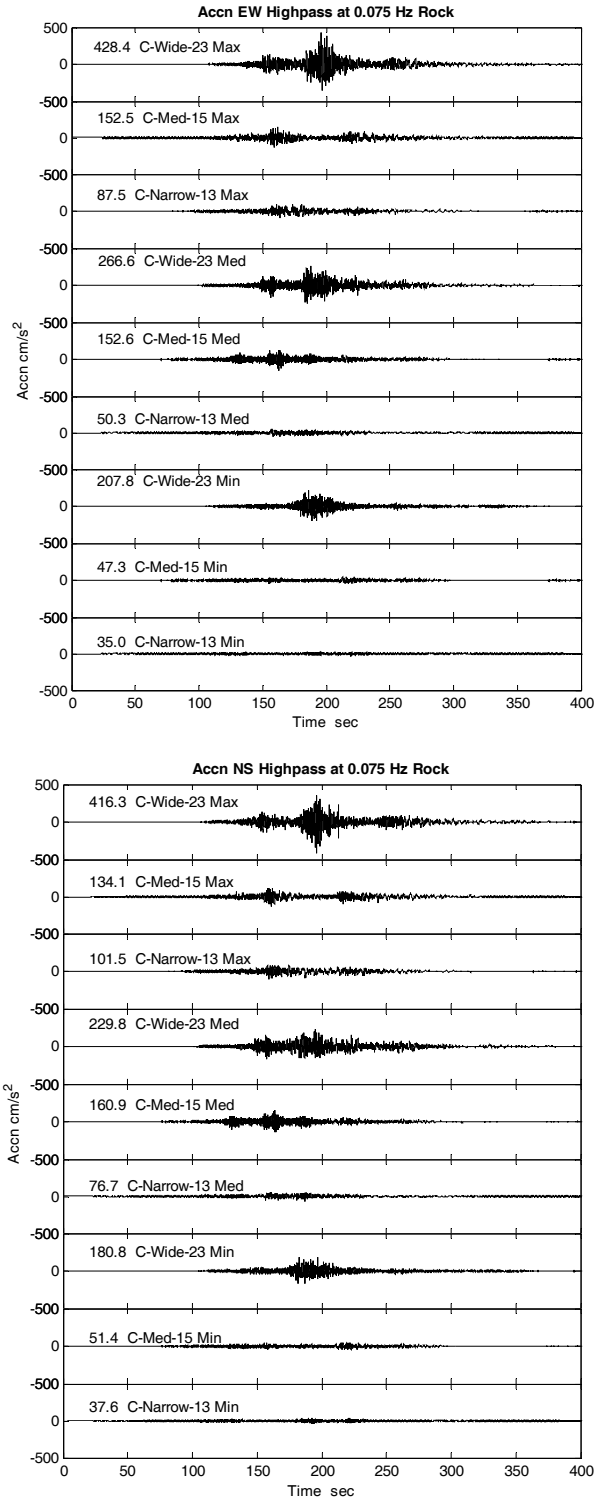

Figure 6.5. Simulated accelerations for nine models at rock sites in SEA. A highpass filter at 0.075 Hz is applied. Maximum value for each trace is shown in the front of the model name. Top figure is for east-west component and bottom figure is for north-south component.

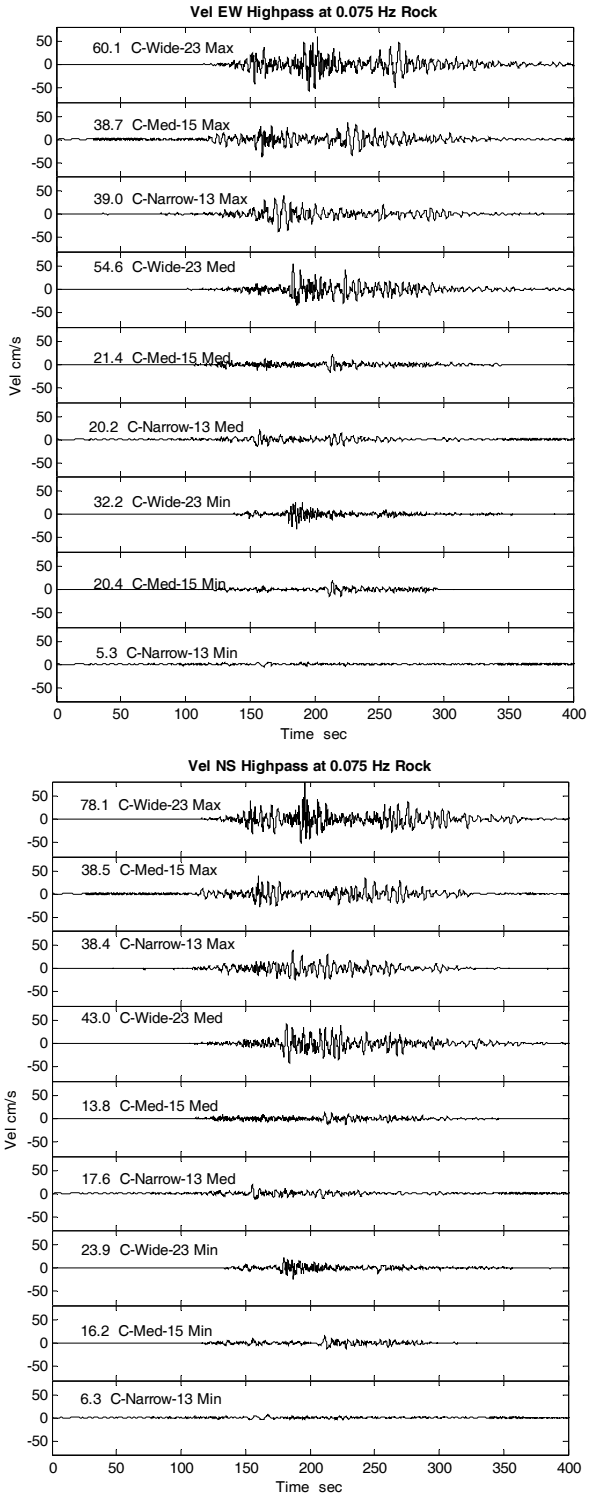

Figure 6.6. Simulated velocities for nine models at rock sites in SEA. A highpass filter at 0.075 Hz is applied. Maximum value for each trace is shown in the front of the model name. Top figure is for east-west component and bottom figure is for north-south component.

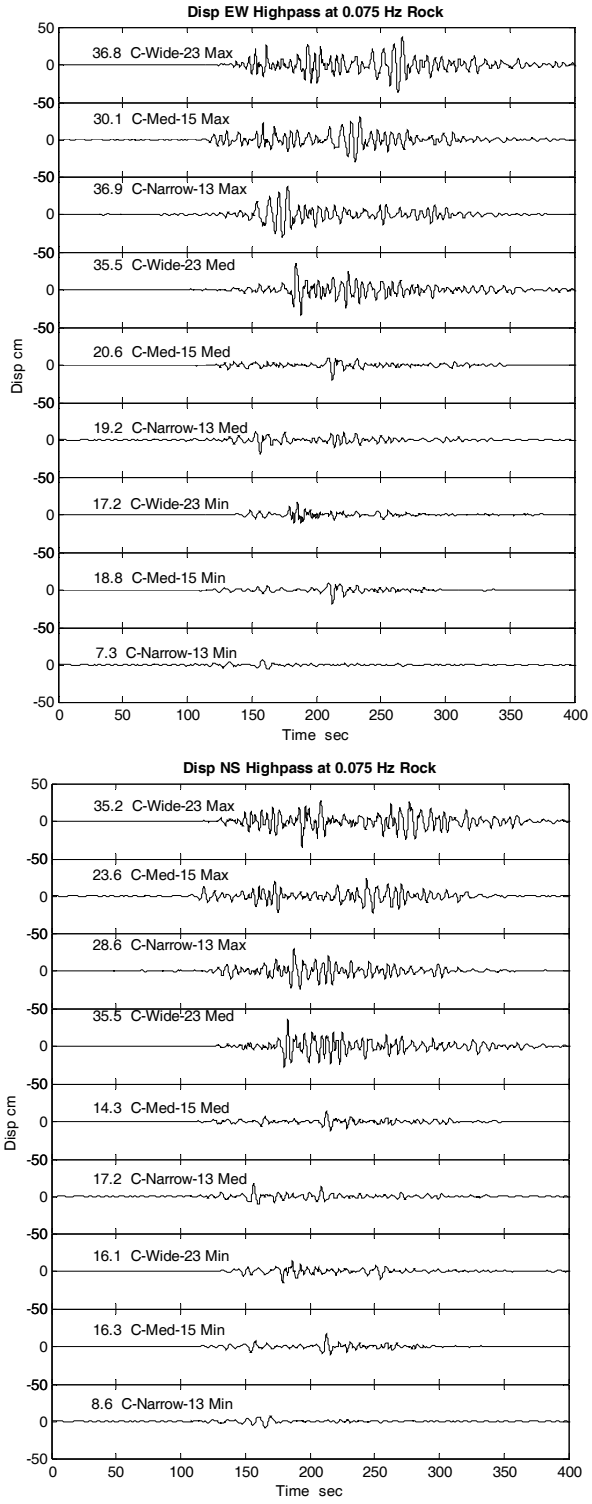

Figure 6.7. Simulated displacements for nine models at rock sites in SEA. A highpass filter at 0.075 Hz is applied. Maximum value for each trace is shown in the front of the model name. Top figure is for east-west component and bottom figure is for north-south component.

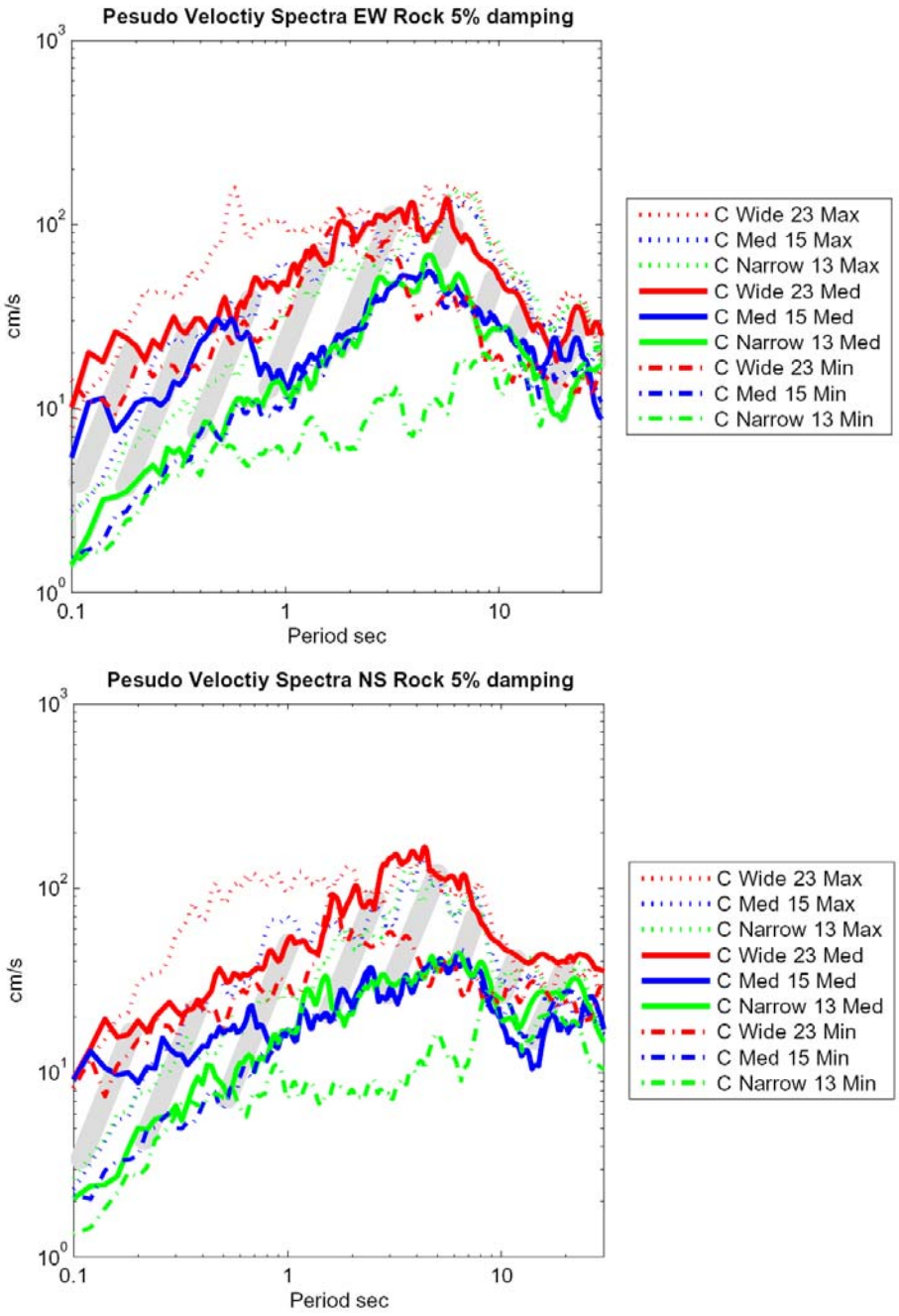

Figure 6.8. Pseudo spectral velocities for simulated data at rock sites in SEA with 5% damping. The top figure is for east-west component and the bottom figure is for north-south component. If two extreme cases (C-Wide-24 Max and C-Narrow-13 Min) are excluded, the pseudo spectral velocity are concentrated on a belt (shaded by grey lines) where C-Wide-23 Med gives the upper limit and C-Narrow-13 Med gives the bottom limit. The peaks appear at 2 to 5 sec. Red lines are for wide models, blue lines are for median models and green lines are for narrow models.

Large variation can be found in the results. Since there are so many unknowns, it is hard to determine which one is the best. However, from statistical point of view, two extreme cases: Model C-Wide-24 Max which gives very large results and Model C-Narrow-13 Min which gives very small results, could be excluded. After this exclusion, the pseudo spectral velocity are concentrated on a belt in figure 6.8 where C-Wide-23 Med gives the upper limit and C-Narrow-13 Med gives the lower limit. Therefore, we can focus more attention on models using median PGV.

If Med Model is considered, the estimated PGA is around 0.25 g for wide model, 0.15 g for median model and 0.05 g for narrow model. The estimated PGV is around 50 cm/s for wide model and 20 cm/s for median and narrow model. The same as before, wide models give larger values than narrow models. These values are comparable to the results from Sumatra event. Pseudo spectral velocity has a peak around 2 to 5 sec.

6.4.2 Site Amplification

The city of Seattle is located in Puget Sound. This region is home to the majority of Washington State citizens. Beneath the sound, there are three major sedimentary basins: Everett, Seattle and Tacoma. The deepest and most studied is the Seattle basin which is 70 km by 30 km, 7 to 9 km deep (Johnson, Potter *et al.*, 1994; Pratt, Johnson *et al.*, 1997; Brocher, Parsons *et al.*, 2001). Portions of the city of Seattle are also underlain by artificial fill created by hydraulically sluicing dirt from downtown hills onto the nearby tide flats (Galster and LaPrade, 1991). V_s^{30} is investigated to be 140 to 680 m/sec in Seattle (Williams, Stephenson *et al.*, 1999).

Recently, many researchers have found the large seismic amplifications in the Seattle region. Analysis of arrivals from local Nisqually earthquake M6.8 (Frankel, Carver *et al.*, 2002), regional Denali earthquake M_w7.9 (Barberopoulou, Qamar *et al.*, 2004) and teleseismic Chi-Chi earthquake M_w7.6 (Pratt, Brocher *et al.*, 2003) all indicated that the Seattle basin amplifies seismic waves with peak amplifications in the 0.2 to 0.5 Hz range.

Forward computer models also predict the amplification of low-frequency seismic waves (Frankel and Stephenson, 2000; Pitarka, Graves *et al.*, 2004). At higher frequency ranges, the effects are variable but most sites show decreasing amplification with increasing frequency (Pratt, Brocher *et al.*, 2003).

Fortunately, Seattle area has considerable more information of site condition than the Sumatra region. In this study, we use teleseismic S-waves collected by the SHIPS02 (the 2002 Seismic Hazard Investigation of Puget Sound) study to estimate the transfer function of the Seattle basin. Frequency domain analysis has been widely used to reveal site amplification because it could clearly show the amplification factor for a certain frequency range. However, it disregards the phase information and could not disclose the longer duration caused by basin effects that is crucial for building's response. To overcome these disadvantages, we propose a time domain analysis. In this empirical analysis, the main target is to achieve a transfer function which transfers rock records to basin records. This method is based on an assumption that the site response is linear. Most nonlinearity of site response is generated by shallow soil structure and would deamplify the high-frequency motions. However, for long-period motions (<1 Hz), the nonlinearity can be ignored and linear assumption is reasonable. Therefore, we can extrapolate site amplification derived from weak motions to site amplification for strong motions.

6.4.2.1 Data

The SHIPS project consisted of a series of studies designed specifically to help characterize the seismic hazard in the region. In SHIPS02, 85 seismometers were installed throughout the central Puget Lowland to record ground motions between January and May, 2002 (Pratt, 2006). Four teleseismic earthquakes with magnitude 7.1 to 7.5 were recorded with clear S-wave arrivals (table 2 in Pratt's paper 2006). The sites were classified into 5 sets based on the underlying geologic structures and shallow deposits. Teleseismic S-waves (with duration = 100 sec) from bedrock sites and the Seattle basin sites are used in our analysis.

6.4.2.2 Method

The purpose of our method is to find transfer functions which satisfy,

$$Rock(t) * G(t) = Basin(t), \tag{6.1}$$

where *Rock*(*t*) is a teleseismic S-waves recorded at bedrock site, *Basin*(*t*) is a teleseismic S-waves recorded at the Seattle basin site and *G*(*t*) is a transfer function. A band-pass filter at 0.075 to 1 Hz is applied to all *Rock*(*t*) and *Basin*(*t*) recorded at SHIPS02 experiment. Amplifications for high-frequency (>1 Hz) motions is not considered because of the large varied amplification ratio and nonlinearity associated with the site response. Very low-frequency (< 0.1 Hz) signals are not reliable because of the low signal-to-noise ratio for 2 Hz sensor used in SHIPS02 experiment (Pratt, 2006). Therefore, we define the frequency band 0.075 to 1 Hz in our calculation.

G(*t*) can be deconvolved in frequency domain by $\hat{G}(\omega) = \frac{Basin(\omega)}{\hat{R}ock(\omega)}$. However, exact deconvolution would contaminate important characteristics of transfer functions by recovering the noises. Therefore, this inversion problem is widely solved by linear least squares methods in time domain. The j^{th} component of *Basin*(*t*) can be written as,

$$b_j = (r * g)_j = \sum_{k=1}^{N} r_k g_{j-k} \tag{6.2}$$

where r_j is the j^{th} component of *Rock*(*t*) and g_j is the j^{th} component of *G*(*t*); *N* is the total length of the signal. In order to remove the end effects, we pad *N* zeros at the beginning of the rock and basin recordings. The matrix form of this equation can be written as,

$$\begin{bmatrix} r_1 & r_n & r_{n-1} & \cdots & \cdots & r_2 \\ r_2 & r_1 & r_n & \cdots & \cdots & r_3 \\ r_3 & r_2 & r_1 & \cdots & \cdots & r_4 \\ \vdots & \vdots & \vdots & \cdots & \cdots & \vdots \\ \vdots & \vdots & \vdots & \cdots & \cdots & \vdots \\ r_n & r_{n-1} & r_{n-2} & \cdots & \cdots & r_1 \end{bmatrix} \begin{bmatrix} g_1 \\ g_2 \\ g_3 \\ \vdots \\ \vdots \\ g_n \end{bmatrix} \cong \begin{bmatrix} b_1 \\ b_2 \\ b_3 \\ \vdots \\ \vdots \\ b_n \end{bmatrix}, \tag{6.3}$$

where $n=2N$ because of the zero padding. This matrix form can be denoted as $Ax \cong b$ where x is deconvolved by least squares methods. In general, the solution is unstable because A is an ill-conditioned matrix that means a small change in the data results in a large change in the solution. This problem can be stabilized by appending linear stability constraints generated through singular value decomposition. That is,

$$\left[\frac{A}{\lambda F}\right]x \cong \left[\frac{b}{\lambda d}\right]. \tag{6.4}$$

Decompose singular values of A as $A = USV^T$ where U and V are orthogonal matrices, S is the diagonal matrix of singular values and T indicates the transpose of the matrix. Then $F=VHV^T$ and $d = 0$, where

$$H = \begin{cases} H_{ii} = 0 & i \le k \\ H_{ii} = 1 & i > k \\ H_{ij} = 0 & i \ne j \end{cases}. \tag{6.5}$$

This stability constraint is basically a highpass filter to the singular values of A matrix. For a detailed description, readers can refer to Olson and Apsel (1982). We choose k = 150 for the 1000×1000 matrix H in this study. Final results are not sensitive to k changing from 100 to 300. $\lambda(t)$ is a weight function. To concentrate the main components of transfer function at the beginning, we use an exponential decay function for the first 90 sec in weight function and set $\lambda(t>90) = 0$.

6.4.2.3 Results

A transfer function can be obtained from each pair of rock and basin records. Figure 6.9 shows an example. Once a transfer function is determined, it can be convolved with the rock synthetics to predict the strong ground motions in basin sites. The results vary when using transfer functions obtained from different pairs of rock basin sets. To simplify our method in a statistical way, the transfer function which could give a median PGV of basin

synthetics is chosen as our standard transfer function to represent the Seattle basin effects. Figure 6.9 shows this representative transfer function.

The representative transfer function convolves with strong ground motions simulated at rock sites to estimate the motions in the Seattle basin. Figure 6.10 shows the Fourier spectra of the rock synthetics, transfer function and basin synthetics. We assume that there is no amplification in high-frequency range. So the frequency components larger than 1 Hz are set to be 1 for the transfer function. Figure 6.11 shows the time histories of the rock and basin synthetics. It can be found that the amplification is much more significant for velocities than for accelerations. This is reasonable because amplification in high-frequency components is not considered here. As we expected, the transfer function not only amplifies the amplitude of rock motions by 2.5 to 6 times but also significantly elongates the duration of strong shakings by 150 to 200 sec.

Figures 6.12 to 6.15 plot the simulated strong ground accelerations, velocities, displacements and pseudo spectral velocity with 5% damping at the Seattle basin in SEA for nine models discussed in the previous section. The same as the results for rock sites, there is a substantial variation for motions generated from different models. North-south direction has stronger motions than east-west directions because of the large transfer function in north-south direction. Excluding two extreme cases (C-Wide-23 Max and C-Narrow-13 Min), PGA is estimated around 0.1 to 0.4 g for east-west direction and 0.2 to 0.6 g for north-south direction. PGV is around 50 to 120 cm/s for east-west direction and 80 to 300 cm/s for north-south direction. PGD is around 30 to 100 cm for east-west direction and 50 to 150 cm for north-south direction. The variable range is about 3 times. The pseudo spectral velocities show peaks at 1, 3 and 8 sec for east-west direction and 2 to 6 sec for north-south direction. Figure 6.16 compares the simulated PGA and PGV for nine models at rock sites and at the Seattle basin at station SEA.

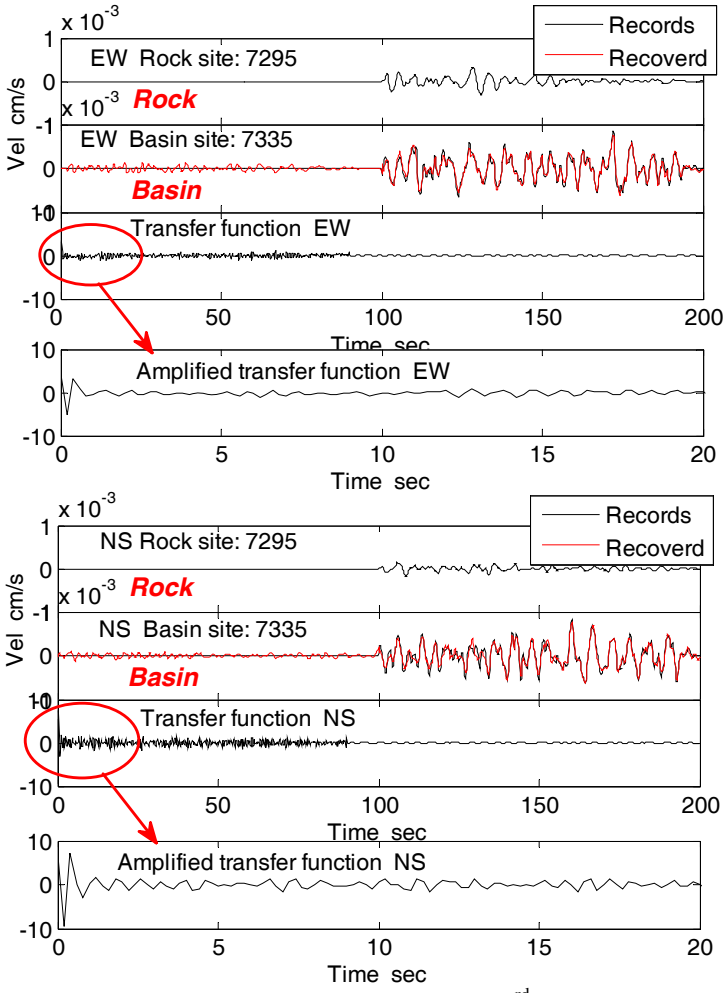

Figure 6.9. Resulting transfer functions time history (the 3rd trace) deconvolved teleseismic S-waves recorded in rock site 7295 (the 1st trace) from basin site 7335 (the 2nd trace) in the 2002 Taiwan M7.1 earthquake. This transfer function is chosen to represent the Seattle basin effects since it results median basin motion PGV. It is shown in large scale in the 4th trace. The top figure is for east-west component and the bottom figure is for north-south component. Station names are listed in table 1 in Pratt's paper (2006).

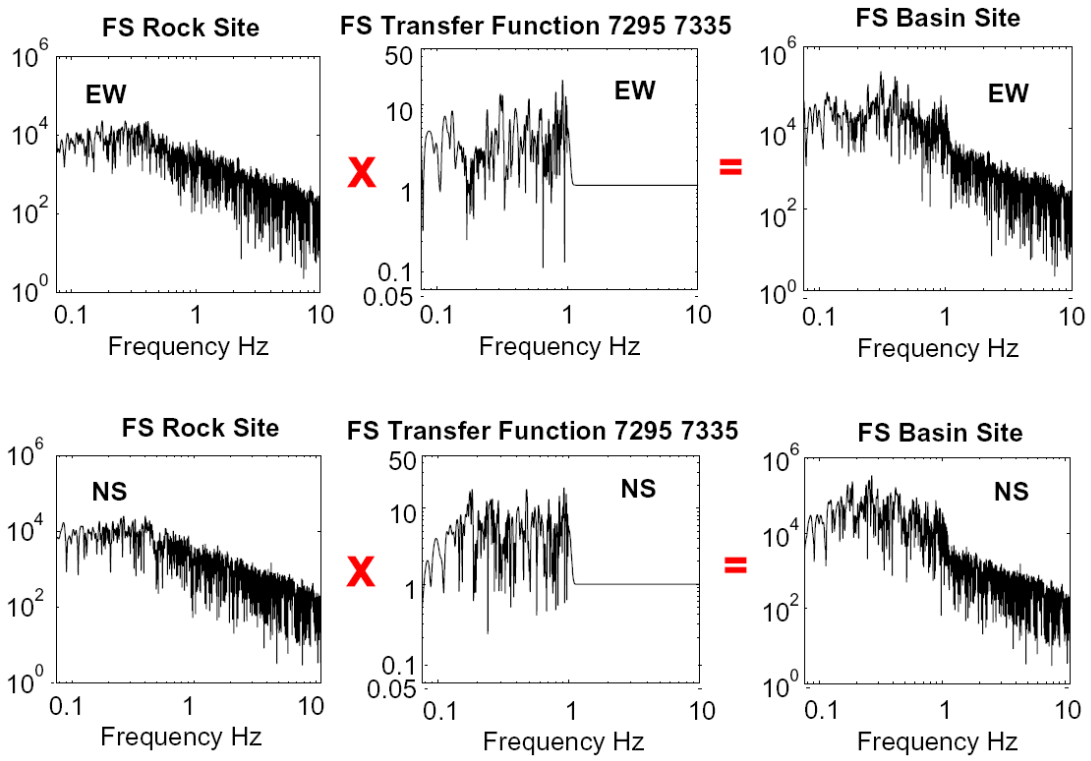

Figure 6.10. Convolve transfer function (middle column) with simulated ground motions at rock sites (left column) to get motions at basin sites (right column) in frequency domain. For transfer function, frequency larger than 1 Hz is set to be 1. This assumes that there is no amplification in high-frequency range. The top figure is for east-west component and the bottom figure is for north-south component.

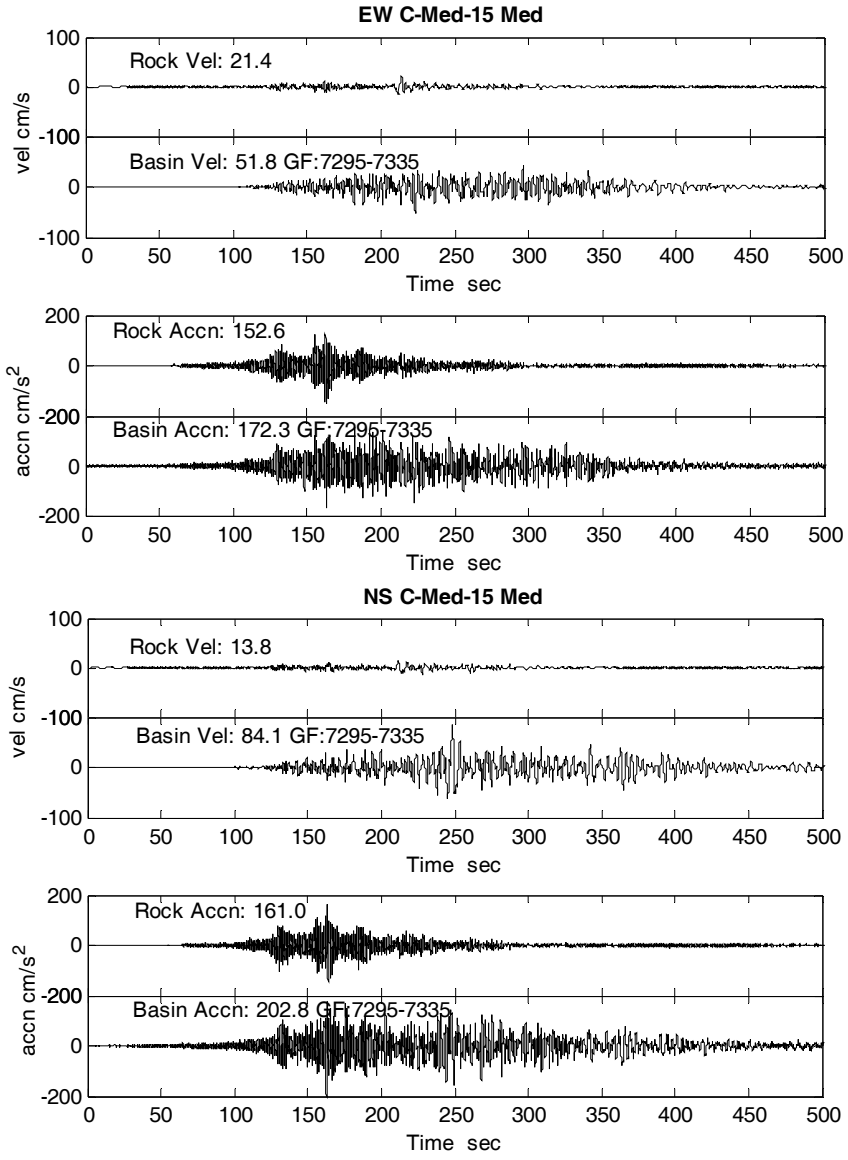

Figure 6.11. A pair of simulated velocities and accelerations in rock sites and basin sites. The representative transfer function is used to amplify rock motions. The top figure is for east-west component and the bottom figure is for north-south component. Maximum values are shown in the top left for each signals. The amplification is much more significant for velocities than for accelerations. NS component has larger amplification than EW component. The transfer function not only amplifies the amplitude of rock motions but also significantly elongates the duration of strong shakings.

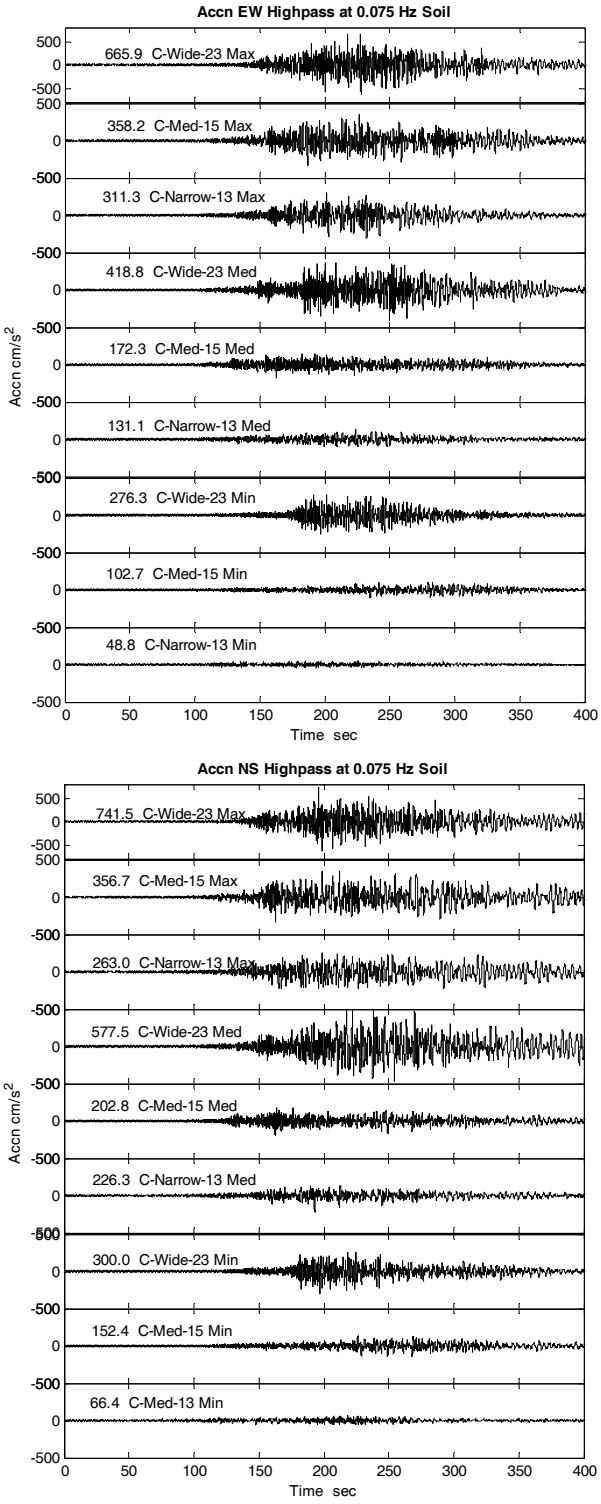

Figure 6.12. Simulated accelerations for nine models at the Seattle basin. A highpass filter at 0.075 Hz is applied. Maximum value for each waveform is shown in front of the model name. Top figure is for east-west component and bottom figure is for north-south component.

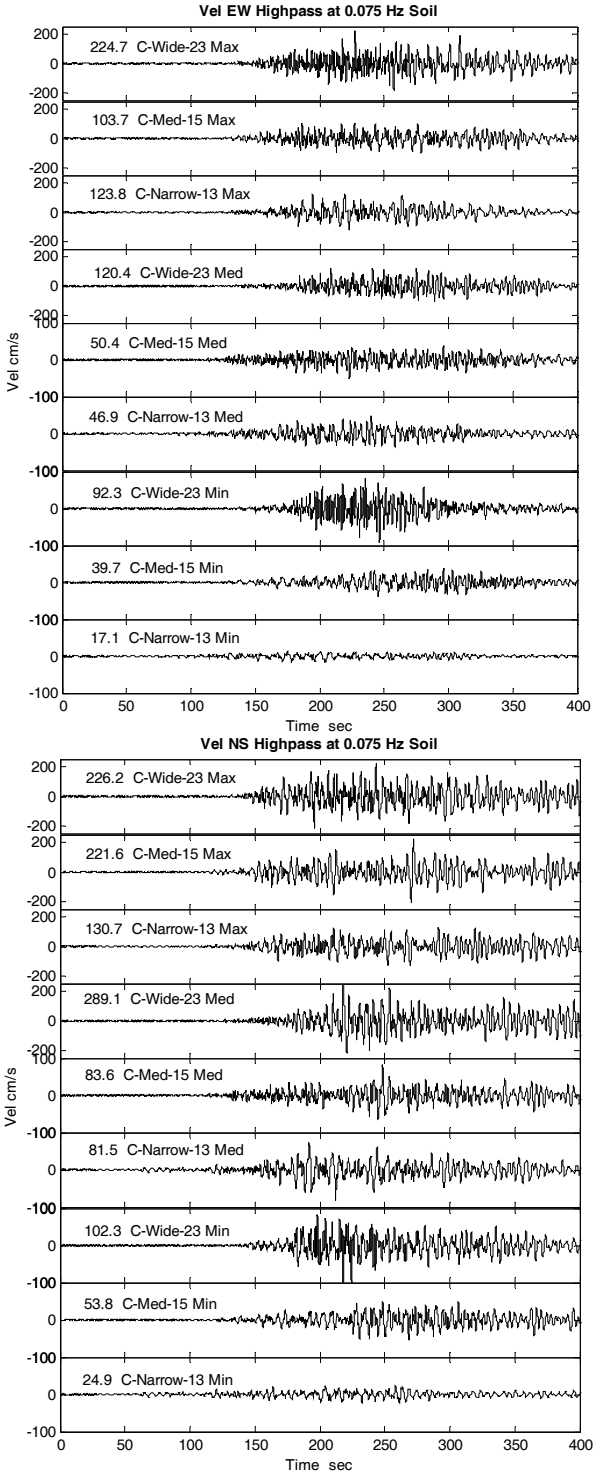

Figure 6.13. Simulated velocities for nine models at the Seattle basin. A highpass filter at 0.075 Hz is applied. Maximum value for each trace is shown in the front of the model name. Top figure is for east-west component and bottom figure is for north-south component. Notice the different y-axis scales for the top 4 and bottom 5 traces.

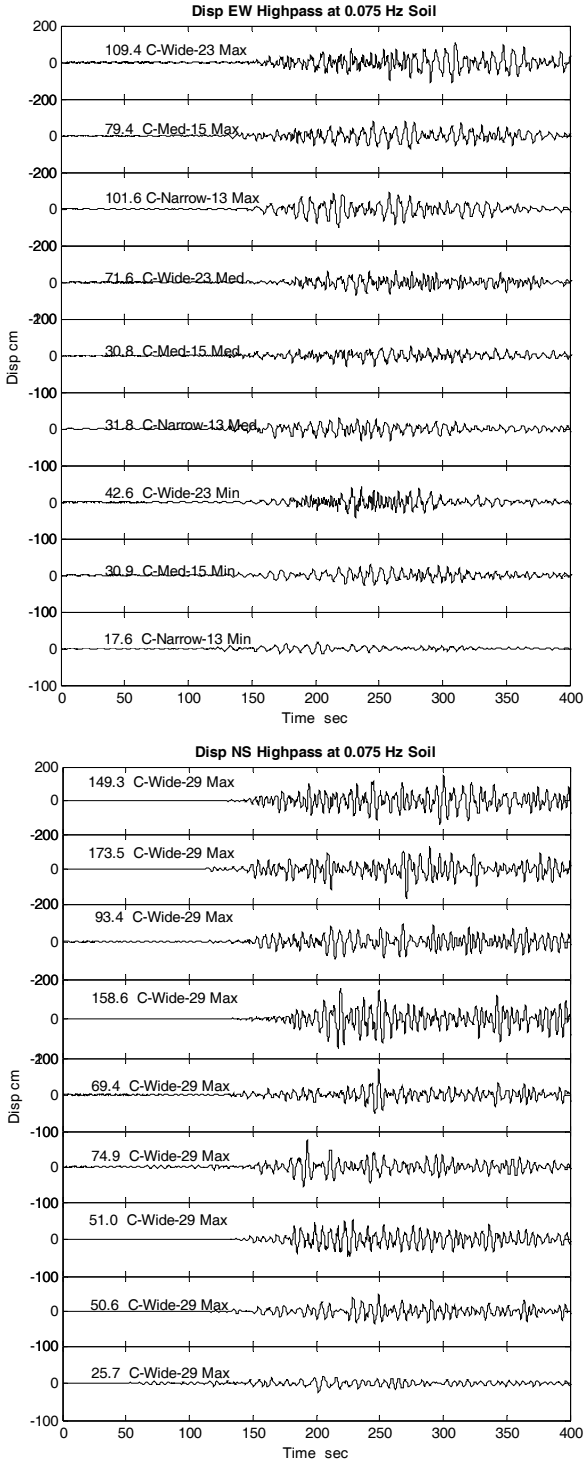

Figure 6.14. Simulated displacements for nine models at the Seattle basin. A highpass filter at 0.075 Hz is applied. Maximum value for each trace is shown in the front of the model name. Top figure is for east-west component and bottom figure is for north-south component. Notice the different y-axis scales for the top 4 and bottom 5 traces.

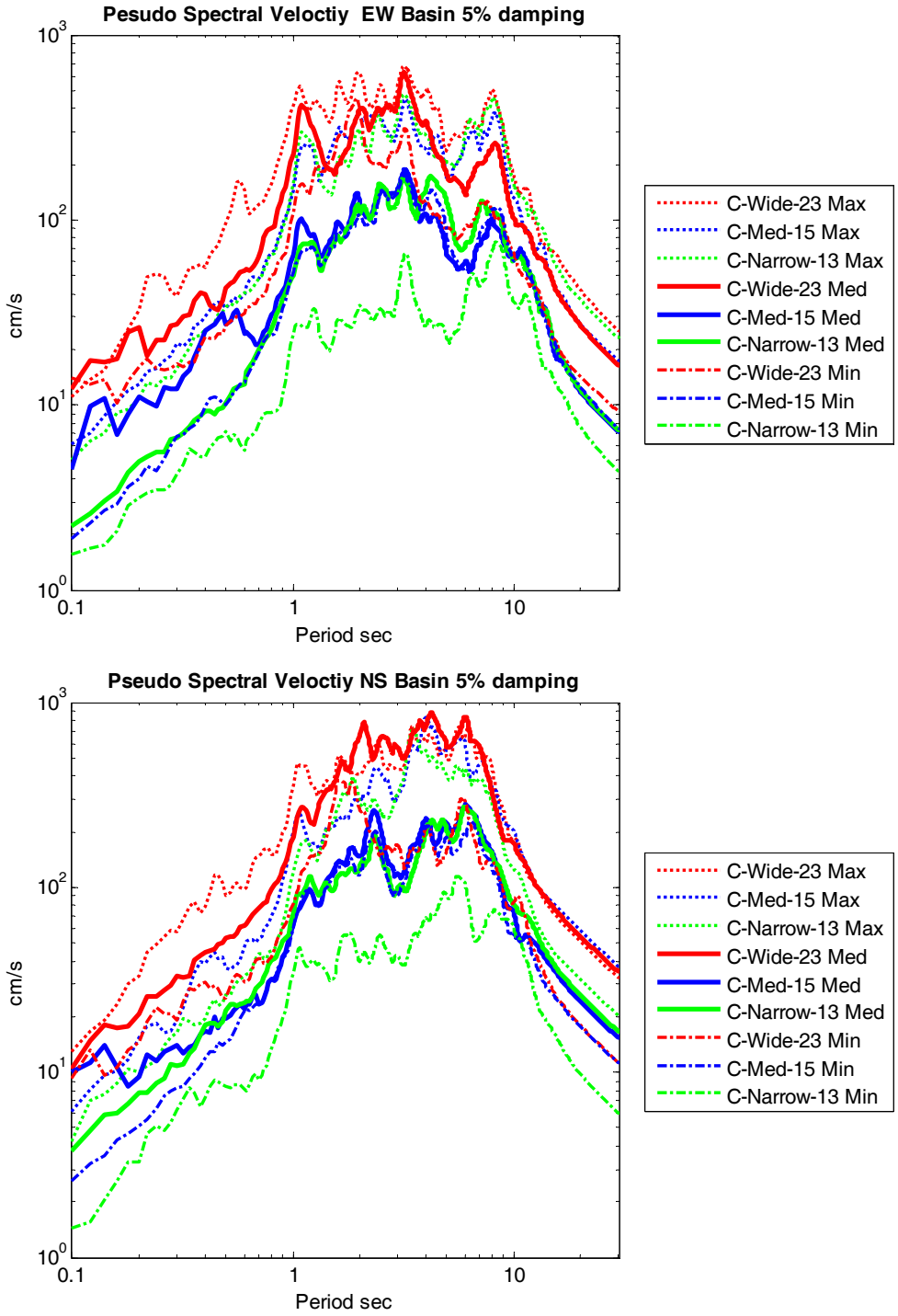

Figure 6.15. Pseudo spectral velocities for simulated data at the Settle basin with 5% damping. The top figure is for east-west component and the bottom figure is for north-south component. Excluding two extreme cases (C-Wide-23 Max and C-Narrow-13 Min), Pseudo spectral velocities are mostly concentrated in a belt limited by Med Models (soiled lines). Red lines are for wide models, blue lines are for median models and green lines are for narrow models.

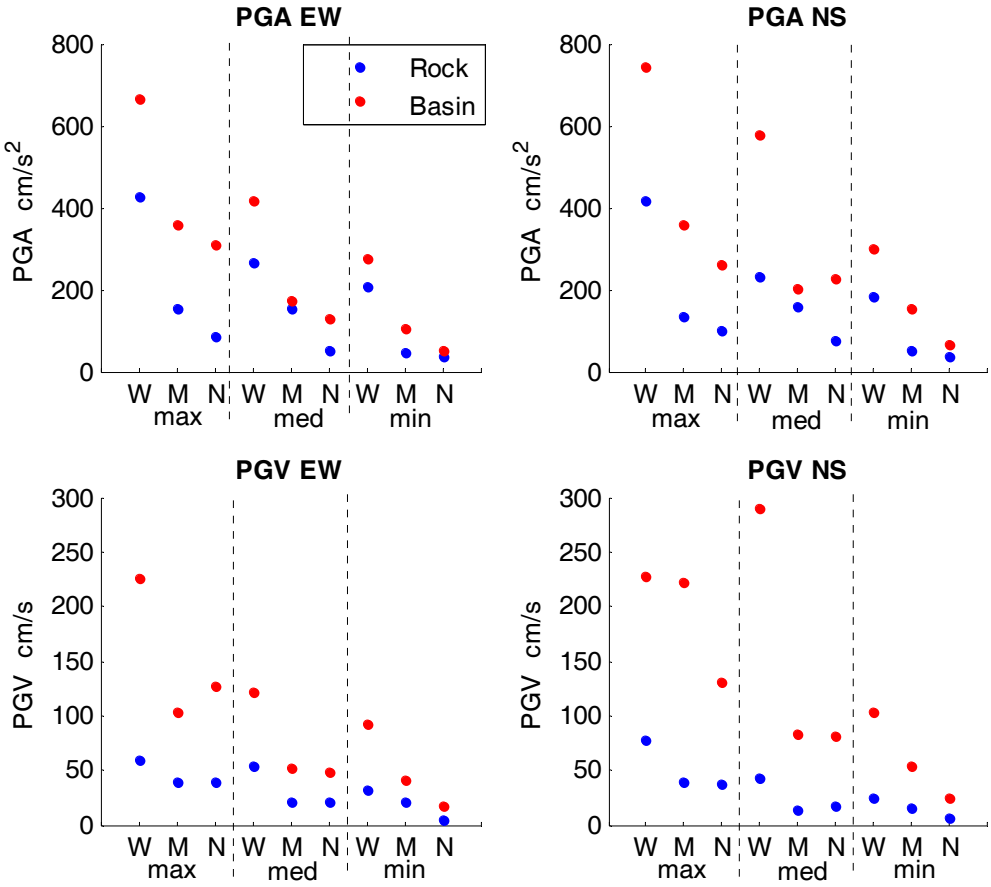

Figure 6.16. Comparing simulated PGA and PGV for nine models at rock sites and at the Seattle basin at station SEA. The left column is for east-west component and the right column is for north-south component.

6.5 Nonlinear Performance of Buildings

All of the strong ground motions obtained from rock sites and basin sites in nine models are used to simulate the nonlinear responses of 20- and 6-story buildings as discussed in Chapter 2. As before, we list peak interstory drift ration (IDR %) in table 6.3 to get an insight to the performance of buildings. From these results, we find that many buildings collapse in basin sites although their performances are acceptable for safety purpose in rock sites. Since there is a large variation in the results, we focus more attention on Med Model. Figure 6.17 compares the peak IDRs and MRDs for different models. We would discuss in more detail in the following for different types of buildings.

Table 6.3. PGA and PGV of simulated strong ground motions at station SEA and performance of 20- and 6- story buildings shaken by these motions.

Model Name		Rock						Basin					
		C-Wide-23		C-Med-15		C-Narrow-13		C-Wide-23		C-Med-15		C-Narrow-13	
Direction		EW	NS	EW	NS	EW	NS	EW	NS	EW	NS	EW	NS
PGA cm/s^2	max	428	416	153	134	88	102	666	742	358	357	311	263
	med	267	230	153	161	50	77	419	578	172	203	131	226
	min	208	181	47	51	35	38	276	300	103	152	49	66
PGV cm/s	max	60	78	39	39	39	38	227	227	103	222	127	131
	med	55	43	21	14	20	18	121	290	52	84	48	82
	min	32	24	20	16	5	6	92	103	41	54	18	25
U20B IDR (%)	max	3.0	2.3	2.1	2.6	2.0	2.0	CO	CO	CO	CO	CO	CO
	med	1.6	2.3	0.6	0.4	0.6	0.4	CO	CO	1.5	CO	2.3	CO
	min	0.6	0.7	0.7	0.4	0.1	0.1	2.1	CO	2.1	CO	0.5	1.3
U20P IDR (%)	max	1.0	1.2	0.6	1.0	0.8	1.4	CO	CO	3.0	CO	CO	CO
	med	1.4	1.8	0.4	0.3	0.4	0.3	CO	CO	1.2	2.4	1.2	2.9
	min	0.4	0.5	0.4	0.3	0.1	0.1	1.5	1.7	1.0	2.2	0.4	0.6
J20B IDR (%)	max	2.8	2.1	1.1	2.2	0.9	2.5	CO	CO	CO	CO	CO	CO
	med	2.3	2.6	0.4	0.3	0.5	0.3	CO	CO	1.9	CO	2.1	4.4
	min	0.9	0.5	0.4	0.2	0.1	0.1	1.6	CO	2.4	4.3	0.7	0.3
J20P IDR (%)	max	1.0	1.1	0.5	0.5	0.5	0.7	CO	CO	CO	6.2	5.0	CO
	med	1.0	1.2	0.4	0.3	0.4	0.3	4.2	CO	1.1	1.2	1.0	0.9
	min	0.5	0.4	0.4	0.2	0.1	0.1	1.9	1.2	1.1	1.0	0.5	0.3
U6B IDR (%)	max	1.8	2.0	1.3	1.1	0.9	0.7	CO	CO	CO	CO	CO	CO
	med	1.6	1.2	0.3	0.2	0.2	0.4	CO	CO	2.1	3.5	1.7	3.5
	min	1.5	1.0	0.2	0.3	0.1	0.1	3.9	4.7	1.3	3.4	0.3	0.6
U6P IDR (%)	max	1.6	2.1	1.0	0.8	0.8	0.5	CO	CO	CO	CO	4.7	CO
	med	1.0	1.0	0.3	0.2	0.2	0.4	CO	CO	1.3	1.9	1.1	1.8
	min	1.1	0.9	0.2	0.3	0.1	0.1	4.6	4.7	1.2	1.8	0.3	0.5
J6B IDR (%)	max	1.1	1.5	0.7	0.5	0.4	0.3	CO	CO	CO	CO	5.4	CO
	med	0.8	0.6	0.2	0.2	0.1	0.2	CO	CO	0.8	1.9	0.6	1.9
	min	0.6	0.3	0.1	0.2	0.1	0.1	3.9	3.5	0.7	2.0	0.3	0.4
J6P IDR (%)	max	0.9	1.4	0.6	0.5	0.4	0.3	CO	CO	3.1	3.8	2.3	2.4
	med	0.6	0.5	0.2	0.2	0.1	0.2	2.4	CO	0.8	0.8	0.7	1.2
	min	0.5	0.3	0.1	0.2	0.1	0.1	2.4	2.4	0.7	1.1	0.3	0.4

Red cells with CO represent that buildings collapse in those cases. Organge cells denote large peak IDRs. In these cases, buildings are severely damaged and close to. Yellow cells denote the cases associated with large deformation and damaged Results from Med Model are shown in blue and emphasized by grey background. Results from Max Model are shown in black and results from Min Model are shown in purple.

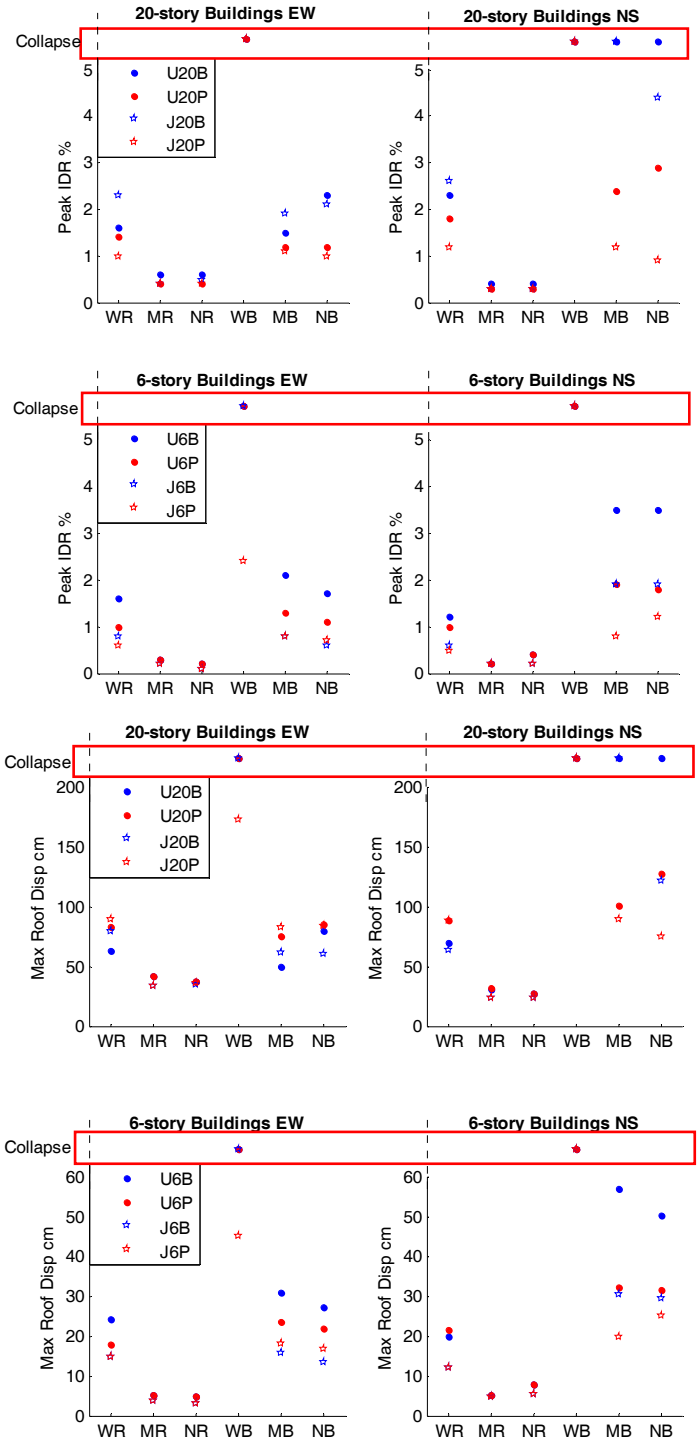

Figure 6.17. Peak interstory drift ratio (top) and maximum roof displacements (bottom) of 20- and 6- story buildings at rock and basin sites for Med Models. X-axis lists the model names. Due to the limited space, we abbreviate wide model as W, median model as M, narrow model as N, rock model as R, basin model as B. We put all the collapsed cases in red rectangular boxes.

6.5.1 20-Story vs. 6-Story Buildings

6-story buildings perform much better than 20-story buildings. Most of them have smaller IDRs than 20-story buildings although their strength capacities are much larger than 20-story buildings. 6-story buildings located in Seattle basin would collapse for wide model, while they are strong enough to avoid collapse for all the other models. The performance of J6P is strikingly better than U6P or J6B. The building is mostly in linear range when shaken by rock motions and has much smaller IDRs when shaken by basin motions from median width and narrow width models.

6.5.2 Buildings with Brittle Welds vs. Perfect Welds

Table 6.3 and figure 6.17 provide response comparison between buildings with brittle welds and with perfect welds. Perfect welds in buildings could largely reduce the peak IDR and, prevent buildings collapse in certain cases. Figure 6.18 directly compare the performances of U20 with two type welds in Med Model. Due to the small deformations in east-west direction, there is no large difference for the performance of buildings with brittle and perfect weld. However, in north-south direction, all U20B collapse in basin sites whereas U20P do not collapse in med and narrow models. Comparing with strengthening and stiffening high-rise buildings, fixing brittle welds is a more efficient way to increase the capacity of buildings especially for high-rise buildings.

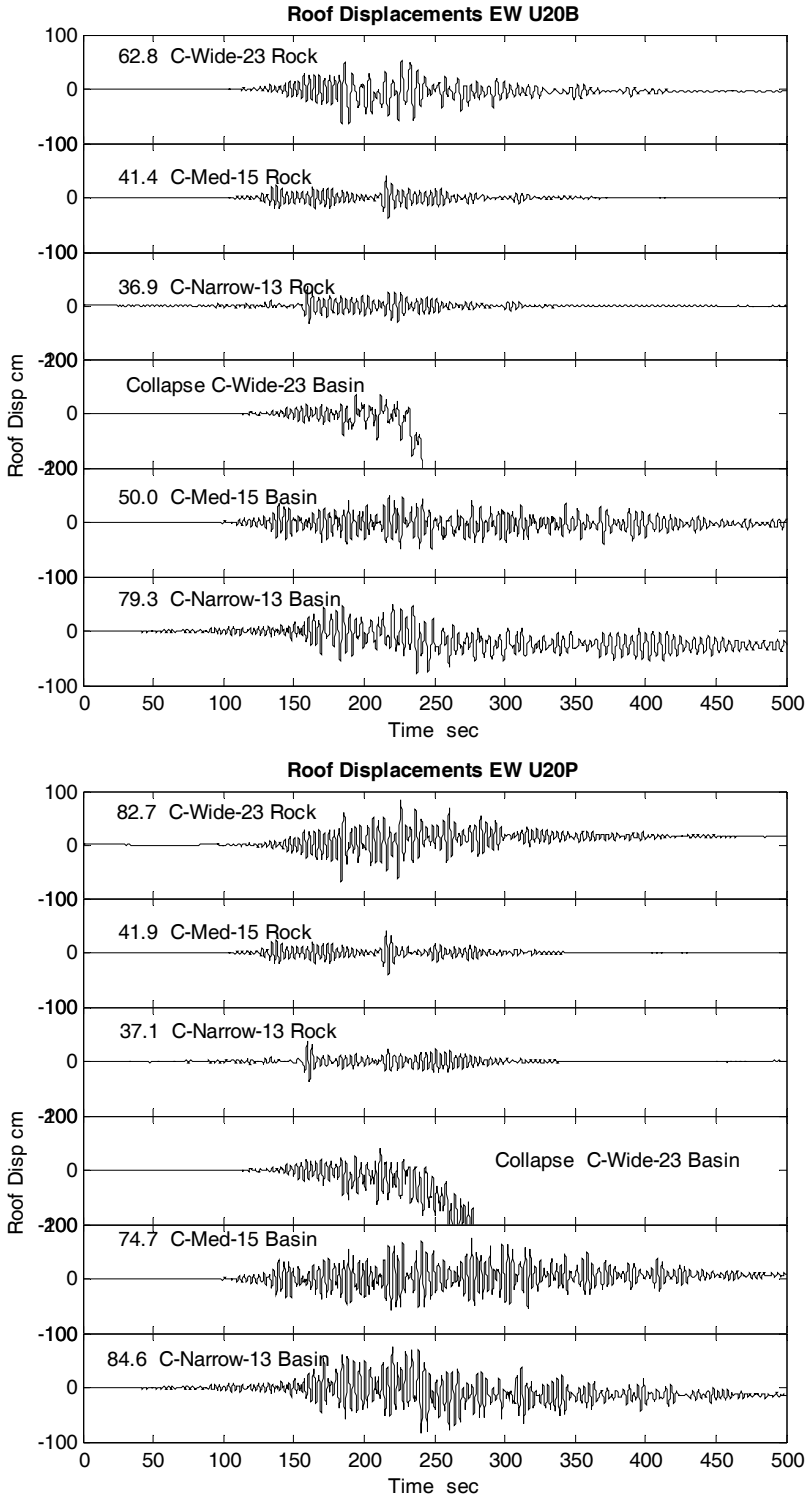

Figure 6.18. Compare roof displacement time histories for U20B and U20P to six Med Models in east-west component. The maximum value is shown on the top right of each trace. In this direction, there is not much difference for buildings with brittle welds and perfect welds because of the small deformations.

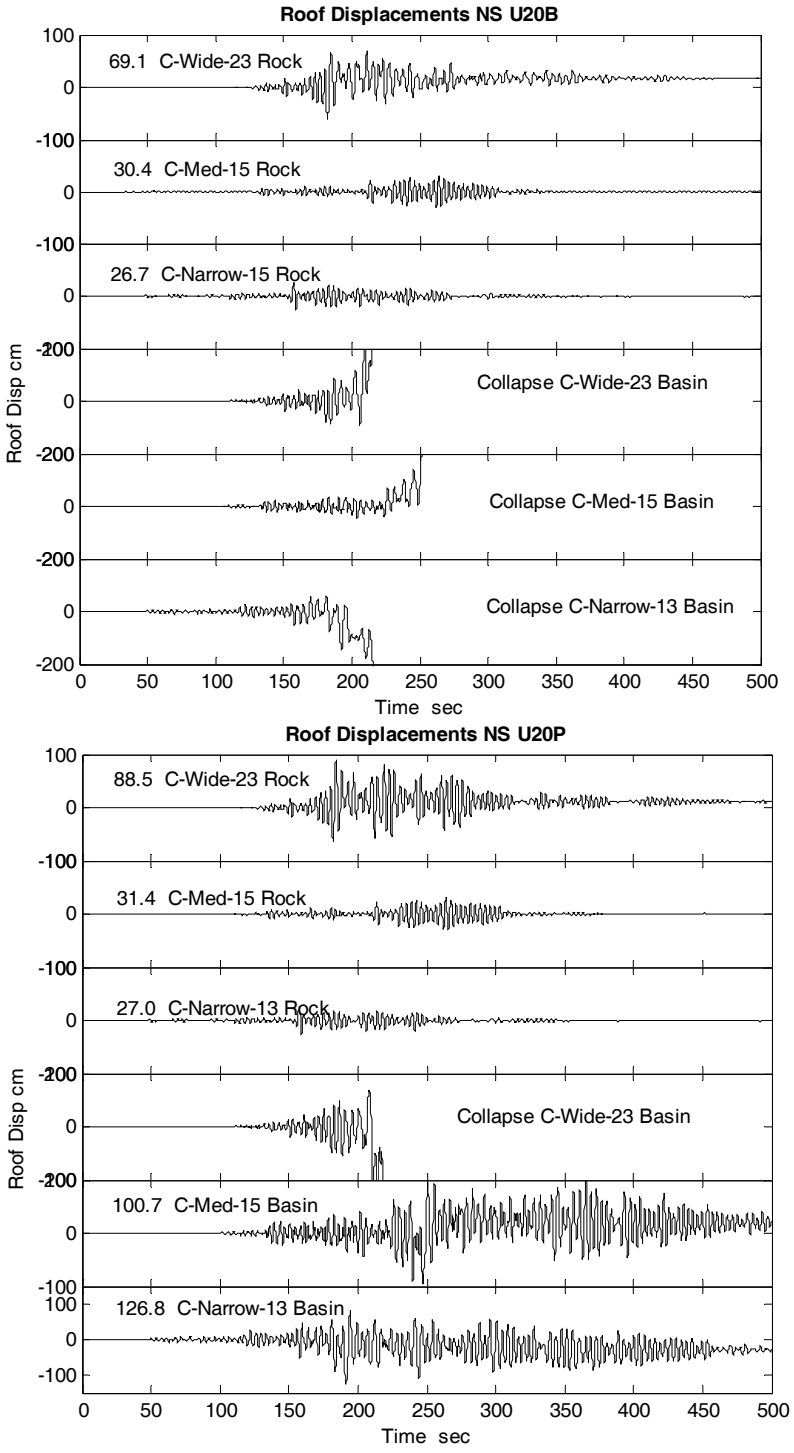

Figure 6.19. Compare roof displacement time histories for U20B and U20P to six Med Models in north-south component. The maximum value is shown on the top right of each trace. In this direction, motions in basin sites cause all U20B collapse whereas did not cause U20P collapse in med and narrow models.

6.5.3 Stiffer vs. More Flexible Buildings

From table 6.3 and figure 6.17, we find that the performance of stiffer stronger Japanese high-rise buildings especially with perfect welds have smaller IDRs than corresponding more flexible U.S. Buildings. This statement seems conflict with the results we obtained from the Sumatra event where there is no evidence of advantage of J20 over U20. To explain this conflict, we need to refer the frequency contents of the ground motions. Recall that the natural period of U20 is about 3.5 sec and natural period of J20 is about 3.15 sec. Pseudo spectral velocity for Sumatra event (figure 5.12) has a peak around 2 sec for Soil-L model. So $PSV_{3.5}$ is smaller than $PSV_{3.15}$ especially in the north-south direction. This explains the better performance of flexible buildings to stiffer buildings. In the Cascadia event, pseudo spectral velocity (figures 6.8 and 6.15) has several local peaks and it causes P$SV_{3.5}$ larger than $PSV_{3.15}$ for many cases. This explains the worse performance of flexible buildings than stiffer buildings.

Olsen (2008) used thousand of synthetics from several scenario earthquakes in Los Angeles and San Francisco to simulate the response of J20 and U20. Based on her simulation, it was found that U20 have 1-4 times larger collapse possibility than J20. However, most of these synthetics have a frequency upper limit of 0.5 Hz. The signal information from 0 to 2 sec is missing. So the response spectrum with peak around 2 sec shown in records from IBUH03 would not be reflected in these synthetics. Therefore, in general, a stiffer high-strength Japanese building performs better than a more flexible lower-strength U.S. building. However, in some cases, it is not true. Overall, it is really hard to determine whether stiffer or flexible high-rise buildings are better. The real performance of buildings depends largely on the frequency content of the strong ground motions.

The frequency content in the ground motions also explains why J6P has the best performance in our simulation. Recall the natural period of U6 is about 1.5 sec and J6 is about 1.17 sec. In the pseudo spectral velocity of all our models, $PSV_{1.17}$ is always smaller than $PSV_{1.5}$. According to the nearly linear relationship between PSV and peak IDR for

buildings with perfect welds (figure 3.18), it is not surprise to find that J6P has smaller deformation that U6P.

6.5.4 Responses of Buildings for Different Site Conditions

Table 6.3 and figure 6.17 also show that the Seattle basin amplification is significant. It not only amplifies the amplitude of ground motion by 2.5 to 5 times but also elongate the shaking duration by 150 to 200 sec. At rock sites, high-rise buildings were shaken for about 2 minutes while at basin sites, the shaking would last more than 5 minutes.

At basin sites, simulated collapse occurs for all types of buildings when ground motions are estimated from wide model. Large yielding occurs for 20-story buildings when motions are estimated from median and narrow model. The long duration would make the local bucking critical after plastic hinges developed which is the case in many of our simulations. This would make the real performance of high-rise buildings in Seattle even worse than our simulation as we have discussed in section 5.5.5.

6.5.5 Response of Buildings to Motions from Different Fault Width Models

If the rupture extended beyond the Olympic Mountain, our simulation shows that 20- and 6-story buildings in the Seattle basin area would mostly collapse. If the rupture extended to the coastline, our simulation shows that the buildings with brittle welds would collapse and the buildings with perfect welds would be heavily yielded. However if hysterics and local bucking considered, these more than 4 minutes strong shaking could probably collapse these buildings.

CHAPTER 7

Determining Broadband Displacements by Combining Inertial Seismic Records and High-Sample Rate GPS Records

In this chapter, we develop a new data processing methodology based on the data recorded from colocated inertial seismic and high-frequency GPS stations, and apply this method to recordings from the 2003 Tokachi-Oki earthquake (M_w 8.1) to recover accurate strong ground motion displacements. This method saves significant time and reduces sensitivity to the choice of processing parameters.

7.1 Introduction

Accurate measurement of coseismic near-source ground displacement time histories is of great importance. These displacement time histories are often very diagnostic in the inversion of seismic data to derive source rupture models. Furthermore, they can also be important to understand the deformations of flexible buildings that experience large nonlinear deformations. Unfortunately, derivation of ground displacement from the analysis of inertial seismograms always results in ground motions that diverge with time. The dashed lines shown in figure 7.1 are the horizontal displacements derived from double integration of accelerograms (corrected for preevent means) recorded at K-Net station HKD084 during the 2003 Tokachi-Oki earthquake. These integrated accelerograms

compare poorly with 1 Hz GPS observations of ground motion recorded at nearby stations. Unfortunately the divergent displacement records are typical. The problem is that a recorded accelerogram $a_s(t)$, actually consists of

$$a_s(t) = \ddot{u}(t) + g\sin\left(\frac{\partial u_z(t)}{\partial x}\right) + \varepsilon_s(t) \ , \tag{7.1}$$

where $u(t)$ is the true displacement, $g\sin\left(\frac{\partial u_z(t)}{\partial x}\right)$ is the gravitational acceleration caused by tilting of the seismometer (this term drops out for vertical components), and $\varepsilon_s(t)$ is error introduced by the seismometer and digitizer. Even though significant progress has been made in reducing $\varepsilon_s(t)$, the tilting term is an independent degree of freedom that cannot be removed from this problem unless there is an independent data stream, such as inertial rotation or GPS displacement data (Clinton, 2004).

In the mean time, researchers have also proposed numerous data processing techniques to eliminate the displacement drifts caused by the tilting and instrumental errors as we mentioned in section 3.2 (USGS data; Caltech EERL report 1974-1976; Iwan, Moser *et al.*, 1985; Boore, 2001; Zhu, 2003; Shakal, Huang *et al.*, 2004). Unfortunately, all of these correction approaches require the specification of processing parameters that strongly affect the derived ground displacements. While approximate knowledge of the static displacement (typically from geodetic data) can help to constrain these processing techniques, it can be time consuming to employ trial and error to discover the processing parameters that produce the desired ground displacements from processing the seismic data.

In this chapter, we develop a new data processing methodology based on colocated inertial seismic and high-frequency GPS stations, and apply this method to recordings from the 2003 Tokachi-Oki earthquake (M_w 8.1) to recover accurate strong ground motion displacements. This method saves significant time and reduces sensitivity to the choice of processing parameters.

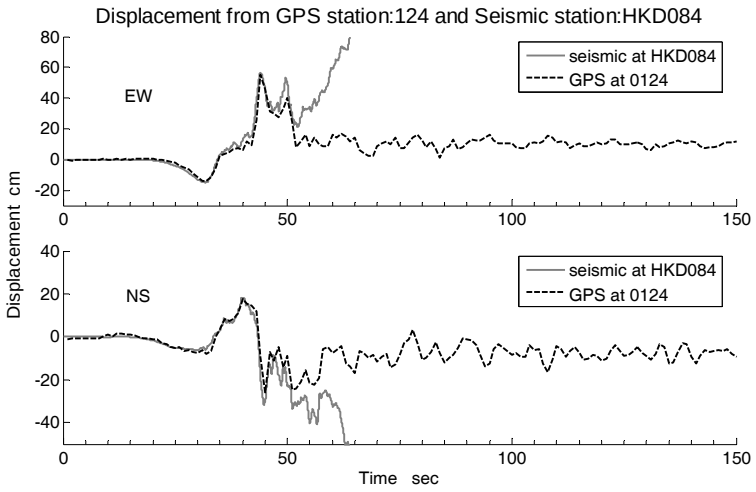

Figure 7.1. Horizontal displacements from GPS station 124 (solid line) and double-integrated seismic station HKD084 (dashed line) during the 2003 Tokachi-Oki earthquake. These two stations are very close to each other (about 1 km apart). The recording frequency is 100 Hz for seismic data and 1 Hz for GPS data.

7.2 Correction Scheme

7.2.1 Seismic Data

If we doubly integrate equation (7.1) and assume that the tilt is small, we obtain

$$u(t) = \iint_t a(\tau)d\tau - \int_0^t \int_0^t \left[g\left(\frac{\partial u_z(t)}{\partial x} \right) + \varepsilon_s(t) \right] d\tau \,. \tag{7.2}$$

In most existing correction schemes, it is assumed that there are discrete steps in the baseline of recorded acceleration. That is, it is assumed that

$$g\left(\frac{\partial u_z(t)}{\partial x} \right) + \varepsilon_s(t) \approx \sum_{i=1}^{n} b_i H(t - t_i) \,, \tag{7.3}$$

where $H(t)$ is a Heaviside step function, b_i is the amplitude of the i^{th} step, and t_i is the time at which it occurs. In practice, usually only one step and sometimes two steps are

considered. Unfortunately, it is extremely difficult to determine the starting time of steps, not to mention that real baseline offsets could be far more complex than the sum of several Heaviside functions. If we substitute equation (7.3) into equation (7.2), we find that

$$u(t) = \iint_t a(\tau) d\tau - \sum_{i=1}^{n} b_i (t - t_i)^2 H(t - t_i) . \tag{7.4}$$

Or in other words, current correction schemes are equivalent to adding one or two parabolas to the displacement time series. Since each parabolic correction has a Fourier amplitude spectrum that scales as f^{-3}, these baseline corrections have very little effect at high frequencies. That is, these shifts predominantly contaminate the long-period parts of waveforms; short-period waveforms are relatively immune from these baseline issues.

7.2.2 GPS Data

Traditionally, GPS receivers have been used to record slow movements of the Earth that develop over days and years (Segall and Davis, 1997). In these studies, one position is estimated for each site over a 24-hour period. Time series of these positions can then be used to study plate tectonics and plate boundary processes. The primary usage of GPS in earthquake studies has been the calculation of "static" offsets. By comparing the 24-hour average position of a receiver before and after an earthquake, permanent ground deformation can be inferred. In previous baseline correction approaches, the permanent displacement measured by GPS has been used as a valuable constraint to find the inversion parameters (Boore, 2001).

Recently, it has been shown that GPS receivers operating at high sample rates (1 Hz) can be used to measure seismic waves associated with large earthquakes (Ji, Larson *et al.*, 2003; Larson, Bodin *et al.*, 2003; Larson, Bilich *et al.*, 2006). These GPS positions are intrinsically different from data collected with traditional seismic instruments. Noise levels on a seismic observable are related to the type of seismometer and its local environment.

In contrast, the GPS observable is not position; it is the measurement of distance between a GPS satellite transmitter and a ground antenna. The GPS position estimates or displacements of interest to seismologists are computed in a least-squares analysis of GPS distance observations from four or more satellites and two or more receivers[1]. The major error sources that must be addressed in GPS least squares analysis are satellite and receiver positions, satellite and receiver clocks, and atmospheric delays. Because the range observations are biased by an unknown number of integer cycles, phase ambiguity terms are also estimated for each satellite-receiver pair. While the orbits are very precisely determined, they are not without error, and this impacts how well receiver positions can be determined. Another critical issue for high-rate GPS studies is the geometry of the GPS constellation. While the precision of a 24-hour average position has only a slight dependence on geometry, initial high-rate GPS studies in Alaska showed that the east component of displacement was much better determined than the north component (Larson, Bodin *et al.*, 2003). Both horizontal components are more precisely determined than the vertical component, by a factor of 2 to 3.

Evaluating the noise levels in high-rate GPS time series is an area of active research (Langbein and Bock, 2004; Genrich and Bock, 2006; Larson, Bilich *et al.*, 2006). Most studies find the short periods (0.1-10 sec) are characterized by white noise; longer period noise falls off as *1/f*. Bilich (2006) has shown that the white part of the error spectrum depends critically on the receiver manufacturer. For the Tokachi-Oki dataset, these values are 0.4 and 1.7 mm for east and north components; for San Simeon (Ji, Larson *et al.*, 2003), a different receiver was used and the high-frequency precisions (0.2 and 0.4 mm) were much better.

Some of the long period errors can be removed by modified sidereal filtering (Choi, Bilich *et al.*, 2004). Because the GPS constellation repeats its orientation in space approximately

[1] It is possible to compute the position of a single GPS receiver if one has access to very accurate high-rate estimates of each satellite's clock behavior (Zumberge et al. 1997). In practice, these are not available and thus measurements from two or more receivers are needed to remove the effect of the satellite clocks.

every sidereal day (one day minus 246 sec), some of the geometry related systematic errors such as multipath, which generally have periods of 100-500 seconds, can be modeled using empirical corrections (Larson, Bilich *et al.*, 2006). Amplitude spectra of the east-west component of 100 seconds preevent noise from GPS receiver 0124 is shown in figure 7.2. For the high-rate GPS data recorded during the Tokachi-Oki earthquake, a standard deviation calculated from the 500 seconds before the earthquake yielded precisions of 4.5, 8.4, and 15.3 mm in the east, north, and vertical components (Miyazaki, Larson *et al.*, 2004).

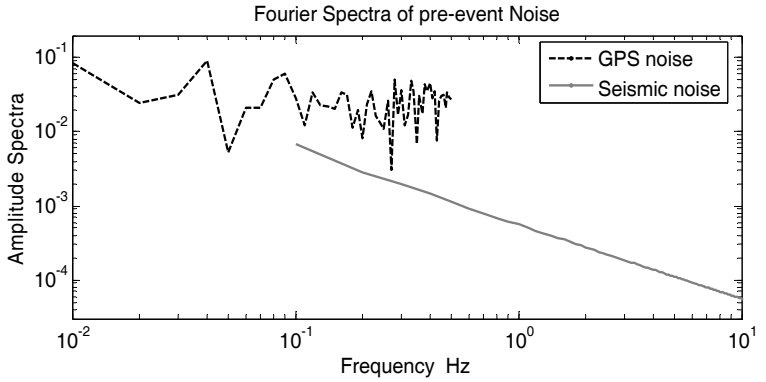

Figure 7.2. Amplitude spectra of east-west preevent noise at GPS station 0124 and K-Net station HKD084 recordings. 100 and 10 seconds preevent signals are chosen for 0124 and HKD084 respectively.

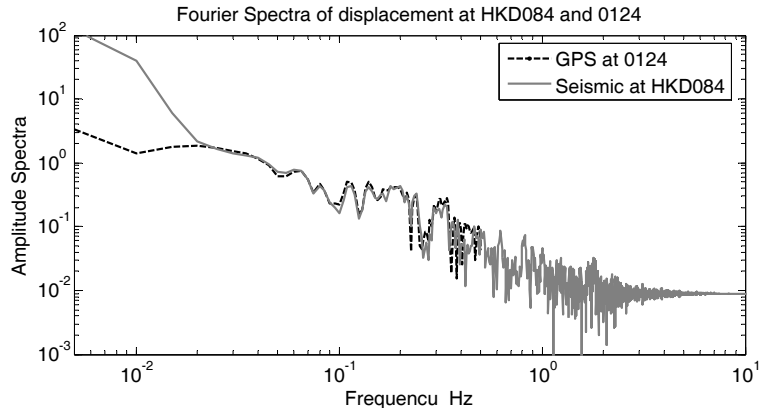

Figure 7.3. Amplitude spectra of displacements. Dashed line is for 200 seconds east-west data recorded at GPS receiver 0124. Solid grey line is for 200 seconds double integration of east-west accelerograms at K-Net HKD084. All the displacements time series are tapered by Chebyshev window at 80 sec to 200 sec to make sure that the signals are periodic function for Fourier transformation.

Figure 7.2 also shows the 10 seconds preevent noise spectrum from the K-Net seismic station HKD084. In this earthquake, the preevent signal recorded by event-triggered accelerometers is less than 15 seconds, so we can not find the seismic noise larger than 0.1 Hz. However, we clearly discover that noise is much lower for the inertial seismometers than for GPS receivers at high-frequency band. Although, this view of the seismometer noise is somewhat deceptive in that it does not include any baseline shifts that are introduced in large amplitude shaking from several sources, including tilting from soil compaction and unknown instrumental effects, the f^{-3} scales for their spectra will not largely increase the seismic noise at high frequency band.

7.2.3 Correction Scheme

From the above discussion, we know that seismic data has high-quality at high frequency band whereas high-sample rate GPS data has high-quality at long period up to static frequency. Fourier amplitude spectra for displacement obtained from GPS receiver 0124 and accelerometer at HKD084 is shown at figure 7.3. It clearly shows the complementary advantages of high-sample rate GPS data and seismic data. These motivated us to develop a procedure for processing data in a manner that can make the best use of their individual advantages.

The purpose of this method is to extract the displacement trend from the double-integrated accelerogram recordings. The procedure can be summarized by the following equation:

$$u_B(t) = f_{LP}(t) * \left[\iint_t a_s(\tau) d\tau - D_G(t) \right], \tag{7.5}$$

where, $u_B(t)$ is the displacement trend produced by accelerogram baseline offset. $D_G(t)$ is the GPS displacement time series, and $f_{LP}(t)$ is low-pass filter. In this study, we use zero-phase 4th-order Butterworth filters. After we find $u_B(t)$, the final strong ground accelerations, velocities and displacements can be calculated as:

$$u_{processed}(t) = \iint_t a_s(\tau)d\tau - u_B(t) \tag{7.6}$$

$$\dot{u}_{processed}(t) = \iint_t a_s(\tau)d\tau - \frac{d}{dt}(u_B(t)) \tag{7.7}$$

$$\ddot{u}_{processed}(t) = a_s(t) - \frac{d^2}{dt^2}(u_B(t)). \tag{7.8}$$

All the above steps are processed at time domain and $u_B(t)$ is the final output for each site. It is extremely difficult to recover the displacements from frequency domain constituting by that of GPS data at low-frequency band and that of seismic data at high-frequency band. The reason is that Fourier transformation is only valid for periodic functions, so the displacement time series obtained by frequency domain analysis are distorted from the real ground displacement with permanent deformation. In other words, Fourier domain analysis does not have the capacity to recover the static residual displacements.

In this method, the only parameter that needs to be determined by user is the corner frequency of the low-pass filter. In our Matlab package CIT_GFD, we provided a way to define this corner frequency: the frequency where accelerogram began to diverge from GPS recordings in low-frequency band. In other words, when exceeding this frequency, accelerogram can no longer provide high-quality data. To elaborate the reason underlying this setting, we can express equation (7.5) in another way:

$$u_B(t) = f_{LP}(t) * \left[\iint_t a_s(\tau)d\tau - D_G(t) \right]$$

$$= [1 - f_{HP}(t)] * \iint_t a_s(\tau)d\tau - f_{LP}(t) * D_G(t) \quad \text{where, } f_{LP}(t) = 1 - f_{HP}(t)$$

$$= \iint_t a_s(\tau)d\tau - \left[f_{HP}(t) * \iint_t a_s(\tau)d\tau + f_{LP}(t) * D_G(t) \right]. \tag{7.9}$$

Equation (7.9) shows that the displacement trend is identical to the residual when processed data is subtracted from the seismic displacement. And the processed data is high-frequency part of seismic data plus low-frequency part of GPS recordings. The corner frequency is the place to separate high-frequency part from low-frequency part, where seismic data is used in the former and GPS data is used in the latter. For example, in figure 7.3, seismic data from HKD084 is poor at frequency smaller than 0.02 Hz, whereas GPS data from 0124 is poor at frequency larger than 0.2 Hz. Since in high-frequency region, data quality from seismic instruments is much higher than that from GPS receiver, it is better to exhaust use seismic data. So we set 0.02 Hz as the corner frequency for this site. In fact, the final processed displacements are not sensitive to the corner frequency (see figure 7.4). Although the shapes of derived baseline offsets of accelerogram change, the noise/signal ratios are too small to be important for building design.

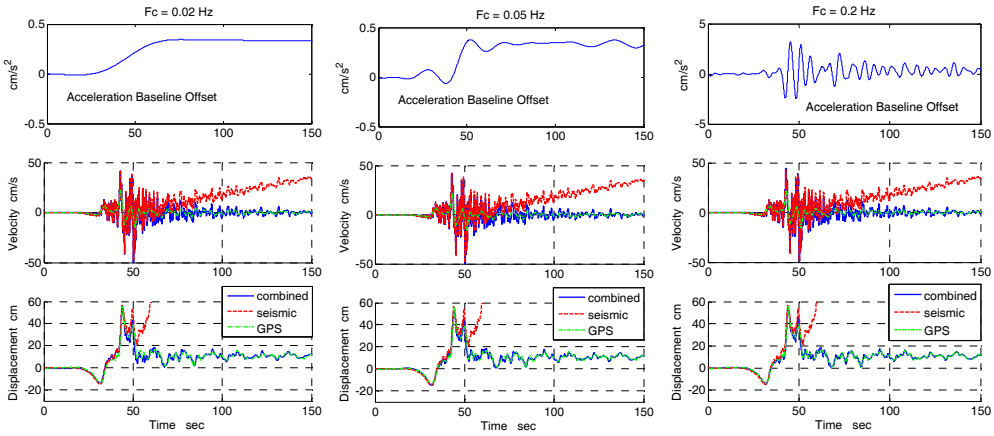

(a) (b) (c)

Figure 7.4. Derived acceleration baseline offsets and the final velocities and displacements results processed by different corner frequencies. Corner frequency is 0.02 Hz at case (a), 0.05 at case (b) and 0.2 Hz at case (c). The blue lines at the last two rows represent final results. Notice that corner frequencies do not affect the final processed velocities and displacements. Although the shapes of baseline offsets differ, if you choose reasonable smaller corner frequency (smaller than 0.1 Hz), we can capture the approximate shape of the baseline offsets.

To qualify this method, $a_s(t)$ and $D_G(t)$ should be collected from colocated seismic and GPS station pair. For the Tokachi-Oki earthquake 2003, there are no exactly colocated station pairs, so the requirement has been relaxed to station pairs very close to each other. In general, the long-period ground deformations are not sensitive to the small distance changes; therefore the difference of two long-period ground displacements recorded at stations very closed to each other is very small. This can be seen from figure 7.1. In this example, the displacements collected from the seismic station HKD084 (43.1116N, 144.1269E) and GPS station 124 (43.1206N, 144.1265E) are compared. These two instruments are approximately 1 km apart; the difference between the two displacements in the first 40 seconds is so small that we can regard these two stations as a colocated station pair.

7.3 Error Analysis

In this section, we use a known displacement history to demonstrate whether this method has the ability to recover an accurate measure of ground displacement. By doing this, we arbitrarily choose a stable ground displacement and assume that it is accurate (the first column in figure 7.5). First, we perturb it with acceleration baseline offsets (the second column in figure 7.5) to generate a typical-looking seismic recording (solid lines in the third column in figure 7.5). Secondly we resample the original ground displacement to 1 Hz (the first column in figure 7.6) and perturb it with randomly recorded GPS noise (the second column in figure 7.6) to generate a typical-looking GPS recording (solid lines in the third column in figure 7.6). Finally, we processed these artificial recordings by CIT_GFD program. The corner frequency chosen by the program is 0.02 Hz. Figure 7.7 (a) compare the program derived acceleration baseline offset with the real added acceleration baseline offset. The corresponding velocities are show in figure 7.7 (b). The displacement error caused by this method is shown in solid line in figure 7.7 (c). As expected, in long-period region, the processing error is mainly caused by the filter applying to the GPS noise, while it is caused by the filter applying to the jumps in the added acceleration baseline offset.

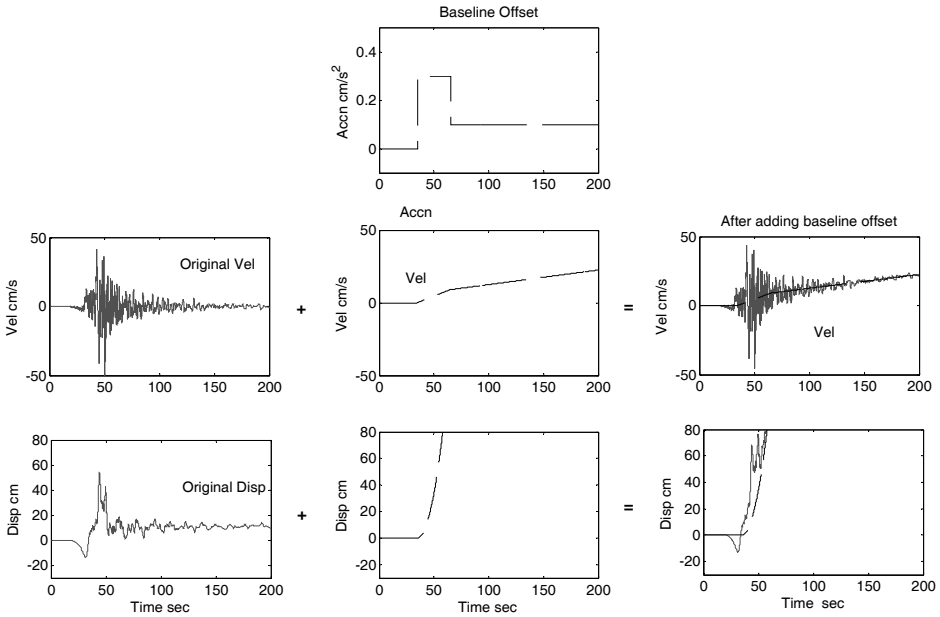

Figure 7.5. Baseline offset (dot-dash lines in the second columns,) is added to the original data (the first column, with reasonable displacement) to generate typical seismic recordings (solid lines in the third column). The first row is acceleration. Since the baseline offset is extremely small, it is not necessary to plot the original and disturbed acceleration. The second row shows velocity and the third row shows displacement. In this example, we use a two-step Heaviside function. One step occurs at 40 sec and the other occurs at 65 sec.

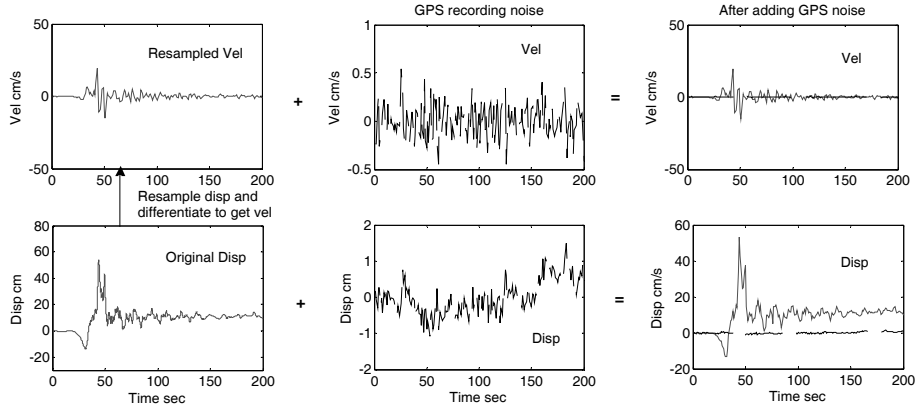

Figure 7.6. GPS noise (the dash lines in the second column,) is added to the original displacement data (the first column) to make typical GPS recordings (the solid lines in the third column). The first row gives velocity and the second row shows the displacement.

The errors also depend on the corner frequency. Figure 7.8 shows the processing errors using corner frequency at 0.05 Hz and 0.2 Hz. Obviously, when corner frequency equals 0.2 Hz, the derived acceleration baseline offset can not capture the pulse shape of the added baseline shift at all. Although the displacement error is not large, the acceleration error is

increased dramatically which is critical for structural design. When corner frequency equals 0.05 Hz, the derived acceleration baseline shift can almost capture the shape of the added baseline offset, and displacement error is relatively smaller. This is because the time difference of the two consecutive step functions is 30 sec, which is close to this corner period. However, in real recordings, since we do not know time interval or even the numbers of time intervals, it is better to choose a longer corner period.

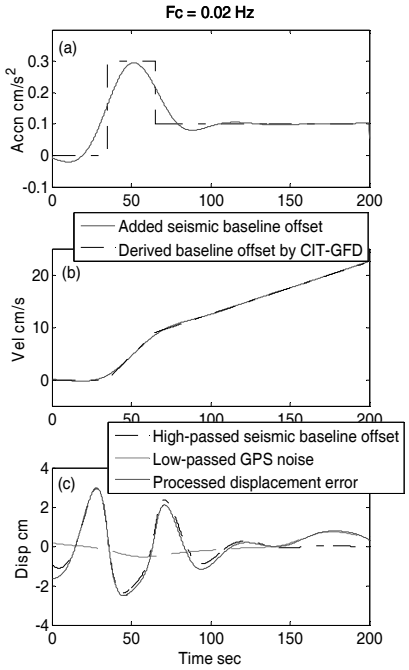

Figure 7.7. Processing error using corner frequency equals 0.02 Hz. (a) Comparing the acceleration baseline offset derived by CIT-GFD (solid line) and the added acceleration baseline offset. (b) The derived and added velocity caused by acceleration baseline offset. (c) The difference between the processed displacement and the original displacement (solid line). This error is caused by the high-passed filter to baseline offset (dot-dash line) and the low-passed filter to the GPS noise (grey dash line).

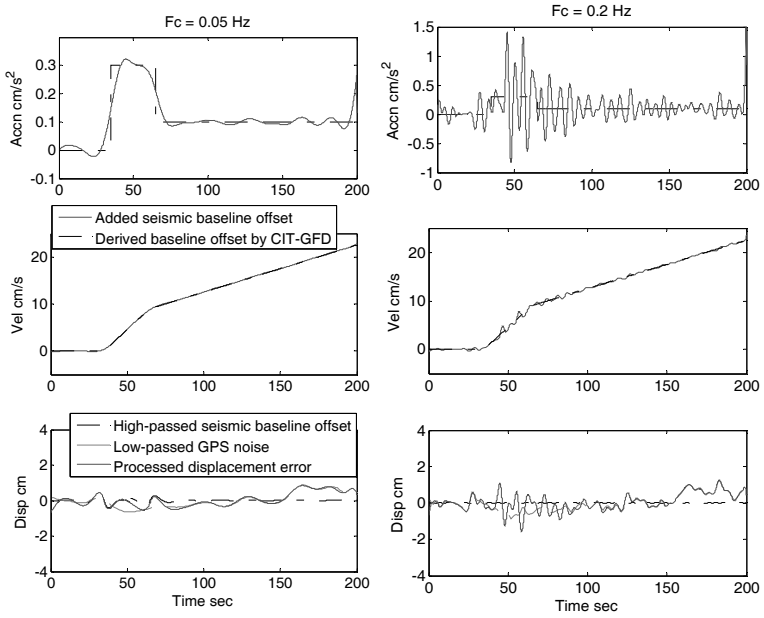

(a)

Figure 7.8. The acceleration baseline offsets and displacement error derived by different corner frequencies. Corner frequency equals 0.05 Hz at column (a) and equals 0.02 Hz at column (b).

7.4 Results

To demonstrate the implementation of this method we use data from the 2003 Tokachi-Oki earthquake M_w 8.1. This earthquake is far and away the largest event recorded by an extensive strong motion network. It also recorded continuous high-frequency GPS data at many receivers (Miyazaki, Larson *et al.*, 2004). Indeed, it is the most suitable database to exhibit the benefits of this methodology.

All the colocated seismic and GPS (without power failure) station pairs are shown in figure 7.9. Figure 7.11 lists the derived baseline offsets and corrected ground velocities and displacements for seismic station HKD095 and GPS station 521. East-west, south-north and vertical components are given individually. Corner frequencies chosen by the program are listed in figures. Figure 7.12 and 7.13 give another example for station HKD129 and GPS station 136. Notice the seismic recording at east-west direction provided a relatively stable displacement, so the corner frequency used in this direction is extremely small which

means a majority of seismic data contributes to the corrected result. More results for other colocated pairs can be found at the following link: http://www.ecf.caltech.edu/~jingy/HULDresults.htm.

These figures illustrate that the final velocities are almost the same as velocities integrated from strong motion accelerations whereas they are not quite similar with velocities differentiated from geodetic displacements. This is reasonable because velocities include much more frequency components higher than 1 Hz which can not be captured by recent GPS receivers. These figures also indicate that the final displacements are similar with geodetic displacements in envelops; meanwhile they follow the short periodic waveforms in seismic displacements. The overall indicates that we successfully recovered the real coseismic ground motions.

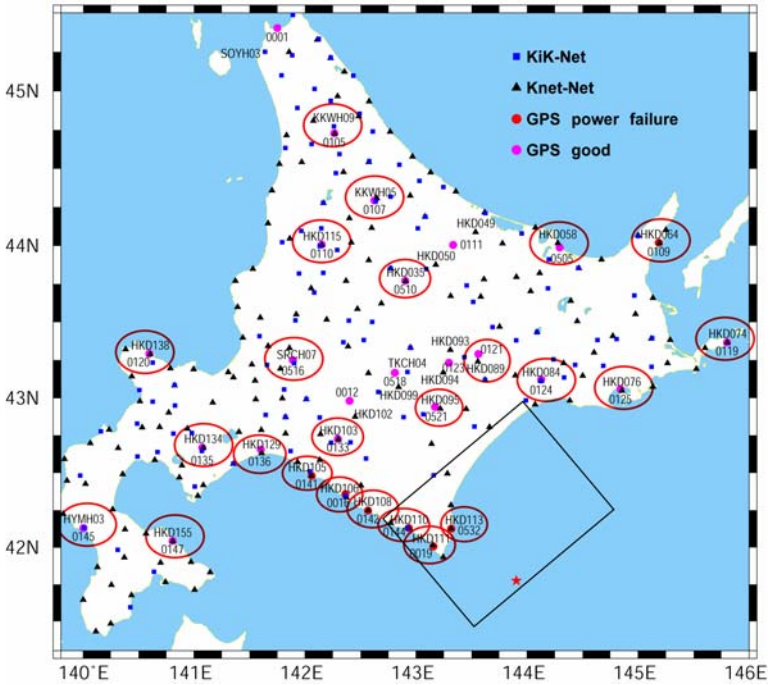

Figure 7.9. Distribution of colocated seismic and GPS station pairs on Hokkaido. The solid red dots represent high-frequency GPS stations which suffered telemetry power failure during the 2003 Tokachi-Oki earthquake. The solid pink dots recovered the entire event. The triangles and squares represent seismic network K-Net and KiK-Net respectively. Open red ellipses are used to group the colocated seismic and GPS station pairs.

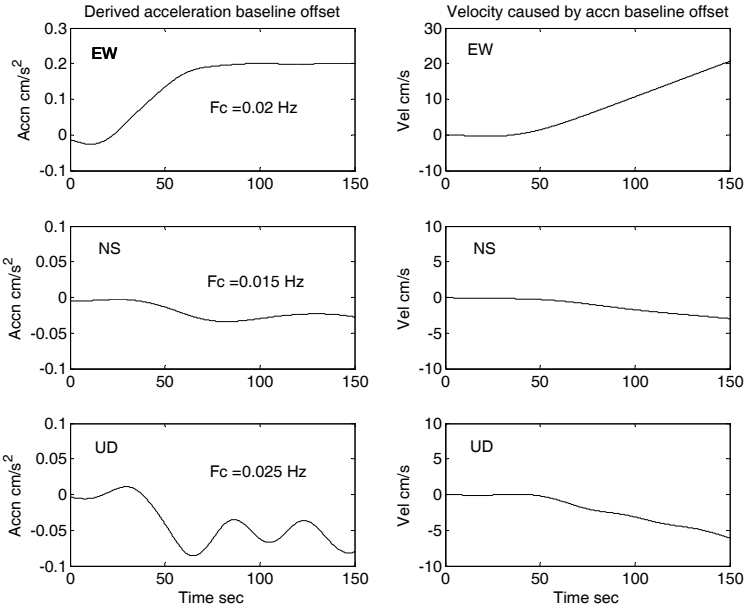

Figure 7.10. Derived baseline offsets from GPS station 521 and K-Net station HKD095. These two stations are about 4 km away from each other. They are about 150 km from the epicenter.

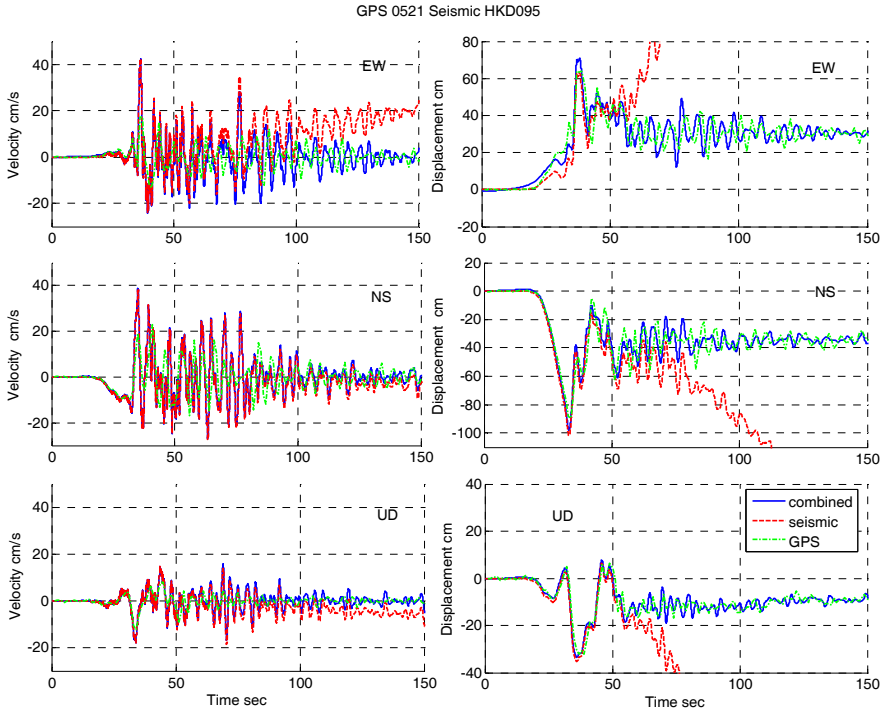

Figure 7.11. Original and corrected velocities (left panel) and displacements (right panel) from GPS station 521 and K-Net station HKD095. The red dashed lines represent seismic time series, the green dash dotted lines represent GPS time series and the solid blue lines are the results processed by our correction scheme.

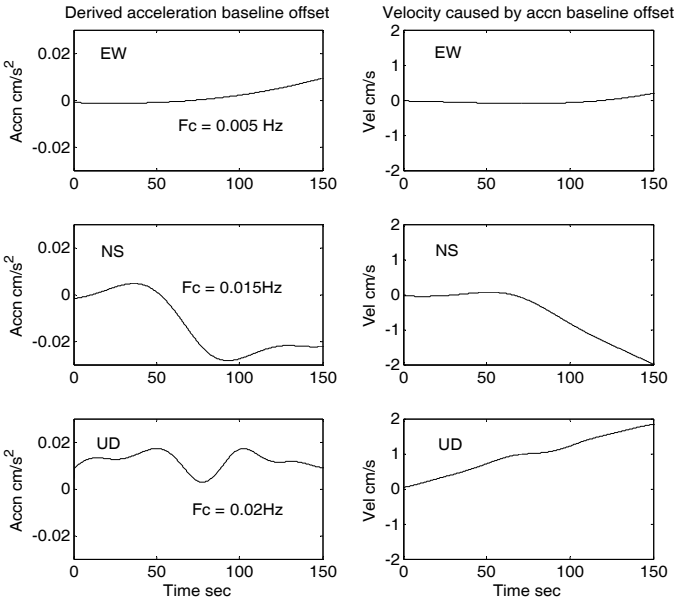

Figure 7.12. Derived baseline offsets from GPS station 136 and K-Net station HKD129. These two stations are about 2.7 km away from each other. They are about 225 km from the epicenter.

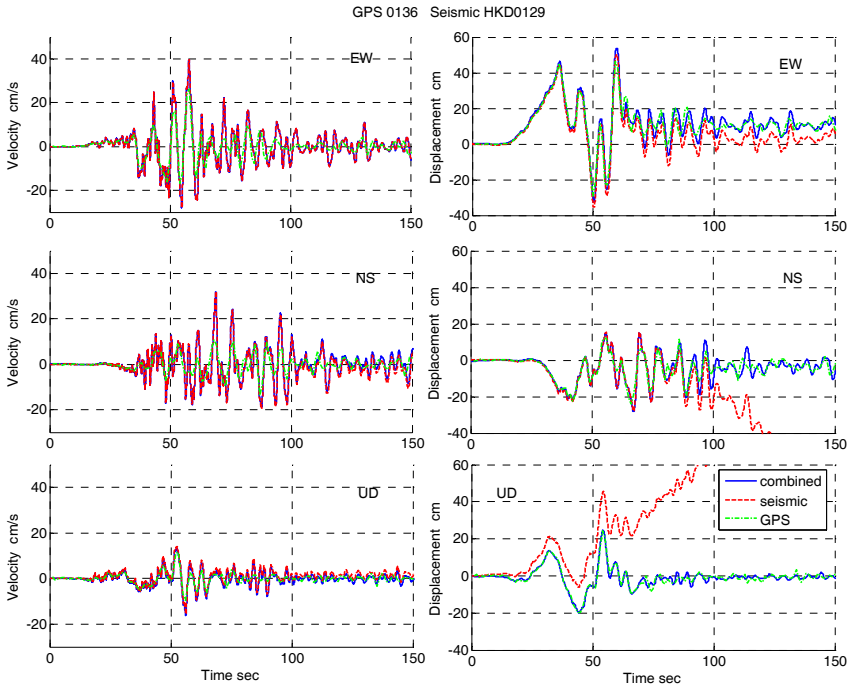

Figure 7.13: Original and corrected velocities (left panel) and displacements (right panel) from GPS station 136 and K-Net station HKD129.

7.5 Conclusions

By introducing high-frequency GPS data, our study provides a new way to recover strong ground displacements. It is essentially a combination of seismic and geodetic data recorded at the same place, fully employed the advantages of each type of data. This method is easy to implement and is consistent and robust for all stations. As long as colocated data are available, results can be generated within seconds. Choice of corner frequencies of the filters is the only thing that needs to be determined. Fortunately, the final results are not sensitive to this parameter. The Matlab package CIT-GFD provided a way to find the corner frequency which is the place where seismic data begins to diverge from GPS data in frequency domain. No other human judgments are needed. In addition, this method is more general in that it can deal with the case where acceleration baseline offsets cannot be simplified as one- or two-step Heaviside functions. Given the promise of this new method, we recommend that high-frequency GPS receivers be collocated at seismic stations in the future.

CHAPTER 8

Concluding Remarks

8.1 Summary of Research

This study is essentially in two parts. One part is simulating strong ground motions from giant subduction earthquakes and the other is simulating the nonlinear performance of steel moment-resisting frame buildings subjected to these synthetics. It combines the conventional work done by seismologists and earthquake engineers.

The strong motions recordings from the 2003 Tokachi-Oki earthquake were first studied. They show significant spatial variation of shaking on Hokkaido Island. The contour maps of peak interstory drift ratios demonstrate that the 20- and 6-story flexible steel moment-resisting frame buildings designed according to both 1994 Uniform Building Code and 1987 Japanese building code would have been strongly excited throughout the coastal region, with the potential for collapses at some locations. Among all the ground motion intensity measures, the response spectrum best predicts the performance of buildings. However, it fails when large deformations occur in the buildings. A collapse factor was introduced to describe the collapse safety margin of buildings. It reveals that although Japanese buildings are 20% to 30% stronger than U.S. buildings, their capacity to resist collapse does not proportionally increase.

After this comprehensively study of Tokachi-Oki event, their records constitute the database of empirical Green's functions to simulate the strong motions for the 2004 Sumatra-Andaman earthquake and a scenario Cascadia earthquake. The Cascadia earthquake is assumed to have the same source model as the Sumatra event. Synthetics from rupture models with different width and from observation stations with different site conditions were estimated. The empirical Green's function method is able to simulate the broadband waves and does not have any limits for the frequency range. The basin site amplification is represented by a transfer function obtained through deconvolving rock records from basin records. Although there is a large variation in the results, all the synthetics have very long shaking duration. The nonlinear performance of 20- and 6-story SMRF buildings excited by these synthetics is estimated. The simulations show that the 20-story buildings in Banda Aceh would have yielded in the Sumatra event while the 20-story buildings in Seattle basin would collapse in the Cascadia event.

8.2 Conclusions

- The first numerical simulation of the response of flexible steel buildings in Seattle due to a giant Cascadia subduction earthquake. Although there is a large uncertainty for the strong motions synthetics caused by the site amplification, rupture models and choice of empirical Green's functions, the simulated waveforms are consistent with available data and current knowledge. Uncertainty also exits in the finite-element method building models. It can be caused by unmodeled local buckling during long duration shaking and caused by unknown weaknesses that have not been discovered yet in buildings. Since the effects from some uncertainties may cancel with each other to some degree, we can conclude based on our simulations that the high-rise buildings in the Seattle basin designed according to California building code may not survive in the expected giant Cascadia subduction earthquake

- The site condition is of particular importance to the simulated ground motions in Seattle. Site amplification from the Seattle basin is significant. The PGV (peak ground

velocity) of Seattle basin synthetics can be 6 times larger than the PGV of rock synthetics in the scenario Cascadia event although the amplification for PGA is not so obvious. The importance of basin amplification is also demonstrated in the Tokachi-Oki event. The Yufutsu basin which is located more than 200 km away from the epicenter amplifies the long period motions large enough so that we could expect irreparable damage for 20-story buildings.

- All the synthetics from giant subduction earthquakes, especially at the basin sites, exhibit very long duration strong shaking. The duration can be as long as 5 minutes in the Seattle basin. These motions are strong enough to cause large lateral deformation and to develop plastic hinges; the long duration would lead to an accumulation of such damages. With so many cycles after yielding, the stress and stiffness degradation would be extremely significant. Since Frame-2D used a degradation model which did not include effects from local flange buckling, our building simulations should be considered to give a low estimate. It would be valuable to include local flange buckling and web distortion into Frame-2D in the future.

- The down-dip limit of rupture significantly affects the resulting synthetics. Although simulated teleseismic P-waves are similar for models with wide, median and narrow rupture width, the strong ground motions simulated from a wide model can be 2.5 to 4 times larger than those simulated from a narrow model. However, based on our current knowledge, there is no unique solution of the rupture models. More scenarios should be considered to include this large uncertainty.

- Any high-rise buildings in the coastal regions would have been strongly shaken in the 2003 Tokachi-Oki earthquake. Although none of the buildings collapsed in our simulations, some of the 20-story buildings were very close to collapsing (at some stations, increasing the ground motion amplitude by 6% would cause simulated collapse for 20-story U.S. building with brittle welds, and increasing 12.5% would cause 20-story U.S buildings with perfect welds collapse.).

- The fracture of welds in the connections of beams and columns dramatically reduces the strength and ductility of buildings. Brittle welds induce the concentrated deformation at some stories in the buildings. The increased nonlinearity effects make prediction of structural performance much more difficult by using just ground motion intensities. Existing weak stories also give rise to high collapse potential for high-rise buildings under P-Delta effects. Therefore fixing brittle welds is an efficient way to enhance the lateral force resisting capacity of existing steel buildings.

- Strengthening buildings has much less impact on the seismic design than fixing the welds in the connections. In general, a stiffer high-strength Japanese building performs better than a more flexible lower-strength U.S. building. However, in some cases, the opposite occurs. In the Tokachi-Oki earthquake, we found that 20-story Japanese buildings with perfect welds perform worse than 20-story U.S. buildings with perfect welds in areas suffering very strong shaking. This also happened in our Sumatra simulation. These different behaviors are caused by the different frequency content of the input ground motions. For example, when excited by a record from station IBUH03 which has a response spectrum peak around 2 sec, flexible high-rise buildings perform better than stiffer buildings. Overall, it is really hard to determine whether stiffer or flexible high-rise buildings are better. But we do know that strengthen high-rise buildings is less efficient for seismic design than fixing brittle welds.

8.3 Future Directions

- The long duration scenario shows a great demand of including stiffness and strength degradation into the hysteretic behavior of our FEM model. It can be included by modeling buckling or by establishing a failure criterion that is related to energy (personal communication with Professor Chia-Ming Uang).

- In this study, our focus area is Seattle. However, there are several other big cities along the Cascadia subduction zone, such as Portland and Vancouver, which have many

flexible structures. In the future, strong ground motions and the nonlinear performance of high-rise buildings in these cities are worthwhile simulating if we have more information about their site conditions.

- More realizations with different sets of empirical Green's functions, basin transfer functions, location of hypocenter and rupture directions should be considered in the future. A reasonable result could be found through a statistical model based on many different cases.

References

Aagaard, B.T., T.M. Brocher, et al. (2008). Ground-motion modeling of the 1906 San Francisco earthquake, part II: Ground-motion estimates for the 1906 earthquake and scenario events. *Bulletin of the Seismological Society of America* **98**, 1012-1046.

ABS Consulting Inc (2003). The September 26, 2003 Tokachi-oki earthquake http://www.absconsulting.com/resources/Catastrophe_Reports/Hokkaido%20EQ_FIN.pdf,. **last accessed Oct. 2008**.

Agnew, D.C. (2002). History of Seismology. In: *International Handbook of Earthquake and Engineering Seismology*. eds. W. H. Lee, H. Kanamori, P. C. Jennings and C. Kisslinger), **Part A**. Academic Press.

American Institute of Steel Construction Manual of Steel Construction (AISC) (2005). Load and resistance factor design. Chicago.

Ammon, C.J., C. Ji, et al. (2005). Rupture process of the 2004 Sumatra-Andaman earthquake. *Science* **308**, 1133-1139.

Anderson, J.G., Bodin P., et al. (1986). Strong ground motion from the Michoacan, Mexico, Earthquake. *Science* **233**, 1043-1049.

Atwater, B.F. (1987). Evidence for great holocene earthquakes along the outer coast of Washington-State. *Science* **236**, 942-944.

Atwater, B.F., M.-R. Satoko, et al. (2005). The Orphan Tsunami of 1700: Japanese Clues to a Parent Earthquake in North America. University of Washington Press, Seattle WA.

Barberopoulou, A., A. Qamar, et al. (2004). Local amplification of seismic waves from the Denali Earthquake and damaging seiches in Lake Union, Seattle, Washington. *Geophysical Research Letters* **31**.

Beck, J.L. and J.F. Hall (1986). Factors contributing to the catastrophe in Mexico-city during the earthquake of September 19, 1985. *Geophysical Research Letters* **13**, 593-596.

Bilich, A. (2006) *Improving the precision and accuracy of geodetic GPS: Applications to multipath and seismology*. University of Colorado.

Boatwright, J. (1982). A dynamic-model for far-field acceleration. *Bulletin of the Seismological Society of America* **72**, 1049-1068.

Bolt, B.A. and N.A. Abrahamson (2002). Estimation of strong seismic ground motions. In: *International Handbook of Earthquake and Engineering Seismology*. **81B**. Academic Press.

Boore, D.M. (2001). Effect of baseline corrections on displacements and response spectra for several recordings of the 1999 Chi-Chi, Taiwan, earthquake. *Bulletin of the Seismological Society of America* **91**, 1199-1211.

Brocher, T.M., T. Parsons, et al. (2001). Upper crustal structure in Puget Lowland, Washington: Results from the 1998 Seismic Hazards Investigation in Puget Sound. *Journal of Geophysical Research-Solid Earth* **106**, 13541-13564.

Brune, J.N. (1970). Tectonic stress and spectra of seismic shear waves from earthquakes. *Journal of Geophysical Research* **75**, 4997-5009.

Challa, V.R.M. and J.F. Hall (1994). Earthquake collapse analysis of steel frames. *Earthquake Engineering & Structural Dynamics* **23**, 1199-1218.

Choi, K., A. Bilich, et al. (2004). Modified Sidereal Filtering: Implications for High-Rate GPS Positioning. *Geophys. Research Letter* **31**.

Clinton, J.F. (2004) *Modern digital seismology-instrumentation, and small amplitude studies in the engineering World*. Ph. D., California Institute of Technology.

Cua, G. and T. Heaton (2007). The Virtual Seismologist (VS) method: a Bayesian approach to earthquake early warning, in Seismic early warning. eds. Gasparini, P., Manfredi, G. and Zschau, J.), **pp 85-132**. Springer Heidelberg.

Demets, C., R.G. Gordon, et al. (1990). Current plate motions. *Geophysical Journal International* **101**, 425-478.

Earthquake Engineering Research Laboratory (Caltech EERL) (1974-1976). Analyses of Strong Motion Earthquake Accelerograms. ***Technical Report series*** **EERL:1974-1976**. California Institute of Technology, Pasadena.

FEMA-354 (2000). A Policy Guide to Steel Moment-Frame Construction. Federal Emergency Management Agency, USA.

FEMA (1995). Interim Guidelines: Evaluation, Repair, Modification and Design of Welded Steel Moment Frame Structures. **FEMA 267**, Washington DC.

Fisher, M.A., R.D. Hyndman, et al. (2005). Crustal Structure and Earthquake Hazards of the Subduction Zone in Southwestern British Columbia and Western Washington. **Professional Paper 1661-C**. U.S. Geological Survey.

Frankel, A.D., D.L. Carver, et al. (2002). Nonlinear and linear site response and basin effects in Seattle for the M 6.8 Nisqually, Washington, earthquake. *Bulletin of the Seismological Society of America* **92**, 2090-2109.

Frankel, A.D. and W. Stephenson (2000). Three-dimensional simulations of ground motions in the seattle region for earthquakes in the Seattle fault zone. *Bulletin of the Seismological Society of America* **90**, 1251-1267.

Galster, R.W. and W.T. LaPrade (1991). Geology of Seattle, Washington, United States of American. *Bull. Assoc. Eng. Geol* **28**, 235-302.

Genrich, J.F. and Y. Bock (2006). Instantaneous geodetic positioning with 10-50 Hz GPS measurements: Noise characteristics and implications for monitoring networks. *J. Geophys. Res* **111**.

Gupta, A. and H. Krawinkler (2000). Dynamic P-delta effects for flexible inelastic steel structures. *Journal of Structural Engineering-Asce* **126**, 145-154.

Hall, J., T. Heaton, et al. (1995). Near-source ground motions and its effects on flexible buildings. *Earthquake Spectra* **11**, 569-605.

Hall, J.F. (1995). Parameter study of the response of moment-resisting steel frame buildings to near-source ground motions. **EERL-95-08**. *California Institute of Technology*, Pasadena.

Hall, J.F. (1997). Seismic Response of Steel Frame Buildings to Near-Source Ground Motions. **EERL-97-05**. *California Institute of Technology*, Pasadena.

Hall, J.F. (1998). Seismic response of steel frame buildings to near-source ground motions. *Earthquake Engineering & Structural Dynamics* **27**, 1445-1464.

Hall, J.F. (2002). Finite Element Analysis in Earthquake Engineering. In: *International Handbook of Earthquake and Engineering Seismology*. **81B**. Academic Press.

Hall, J.F. and J.L. Beck (1986). Structural damage in Mexico-City. *Geophysical Research Letters* **13**, 589-592.

Hall, J.F. and V.R.M. Challa (1995). Beam-column modeling. *Journal of Engineering Mechanics-Asce* **121**, 1284-1291.

Hartzell, S., A. Leeds, et al. (2002). Simulation of broadband ground motion including nonlinear soil effects for a magnitude 6.5 earthquake on the Seattle fault, Seattle, Washington. *Bulletin of the Seismological Society of America* **92**, 831-853.

Hartzell, S.H. (1978). Earthquake aftershocks as Green's functions. *Geophysical Research Letters* **5**, 1-4.

Hartzell, S.H. and T.H. Heaton (1985). Teleseismic time functions for large, shallow subduction zone earthquakes. *Bulletin of the Seismological Society of America* **75**, 965-1004.

Hartzell, S.H. and T.H. Heaton (1988). Failure of self-similarity for large (Mw greater-than 8 1/4) earthquakes. *Bulletin of the Seismological Society of America* **78**, 478-488.

Hatayama, K., T. Kanno, et al. (2007). Control factors of spatial variation of long-period strong ground motions in the Yufutsu sedimentary basin, Hokkaido, during the M-w 8.0 2003 Tokachi-oki, Japan, earthquake. *Bulletin of the Seismological Society of America* **97**, 1308-1323.

Heaton, T.H., J.F. Hall, et al. (1995). Response of highrise and base-isolated buildings to a hypothetical M(w)7.0 blind thrust earthquake. *Science* **267**, 206-211.

Heaton, T.H. and S.H. Hartzell (1987). Earthquake hazards on the Cascadia subduction zone. *Science* **236**, 162-168.

Heaton, T.H. and S.H. Hartzell (1989). Estimation of strong ground motions from hypothetical earthquakes on the Cascadia subduction zone, Pacific Northwest. *Pure and Applied Geophysics* **129**, 131-201.

Heaton, T.H. and H. Kanamori (1984). Seismic potential associated with subduction in the northwestern United States. *Bulletin of the Seismological Society of America* **74**, 933-941.

Heaton, T.H. and P.D. Snavely (1985). Possible tsunami along the northwestern coast of the United States inferred from Indian traditions. *Bulletin of the Seismological Society of America* **75**, 1455-1460.

Himmelwright, A.L.A. (1906). *The San Francisco Earthquake and Fire: A Brief History of of the Disaster: A Presentation of Facts and Resulting Phenomena, with Special Reference to the Efficiency of Building Materials: Lessons of the Disaster.*, The Roebling Construction Company, New York.

International Association of Earthquake Engineering (1992). Earthquake Resistant Design Method for Buildings. In: *Earthquake Resistant Regulations A Word List -1992*. **Chapter 23 Part 2** 23-55 to 23-71, Tokyo, Japan.

International Conference of Building Officials (1994). Uniform Building Code. Whitter CA.

Iwan, W.D., M.A. Moser, et al. (1985). Some observations on strong-motion earthquake measurement using a digital accelerograph. *Bulletin of the Seismological Society of America* **75**, 1225-1246.

Iwasaki, T., H. Shiobara, et al. (1989). A detailed subduction structure in the Kuril trench deduced from ocean bottom seismographic refraction studies. *Tectonophysics* **165**, 315-336.

Japanese Architectural Standard Specification (JASS) (1996). Structural Steelwork Specification for Building Construction. Architectural Institute of Japan.

Ji, C., K.M. Larson, et al. (2003). Slip history of the 2003 San Simeon Earthquake constrained by combining 1-Hz GPS, strong motion, and teleseismic data. *Geophys. Res. Lett.* **31**.

Johnson, S.Y., C.J. Potter, et al. (1994). Origin and evolution of the Seattle fault and Seattle basin, Washington. *Geology* **22**, 71-74.

Joyner, W.B. and D.M. Boore (1986). On Simulating Large Earthquakes by Green's-function Addition of Smaller Earthquakes. In: *Proceedings of the 5th Maurice Ewing Symposium on Earthquake Source Mechanics*. **pp 269-274**. AGU.

Kanamori, H. (1977). The energy release in great earthquakes. *J. Geophys. Res* **82**, 2981-2988.

Kanamori, H. (1979). Semiempirical approach to prediction of long-period ground motions from great earthquakes. *Bulletin of the Seismological Society of America* **69**, 1645-1670.

Kanamori, H. (2006). Seismological aspects of the December 2004 great Sumatra-Andaman earthquake. *Earthquake Spectra* **22**, S1-S12.

Kanamori, H. and P.C. Jennings (1978). Determination of local magnitude, Ml, from strong-motion accelerograms. *Bulletin of the Seismological Society of America* **68**, 471-485.

Katsumata, K., N. Wada, et al. (2003). Newly imaged shape of the deep seismic zone within the subducting Pacific plate beneath the Hokkaido corner, Japan-Kurile arc-arc junction. *Journal of Geophysical Research-Solid Earth* **108**.

Komatitsch, D., Q.Y. Liu, et al. (2004). Simulations of ground motion in the Los Angeles basin based upon the spectral-element method. *Bulletin of the Seismological Society of America* **94**, 187-206.

Krishnan, S. (2003). Three-Dimensional Nonlinear Analysis of Tall Irregular Steel Buildings Subject to Strong Ground Motion. **EERL-2003-01**. *California Institute of Technology*, Pasadena.

Krishnan, S., C. Ji, et al. (2006). Case studies of damage to tall steel moment-frame buildings in southern California during large San Andreas earthquakes. *Bull. Seism. Soc. Am, 96* **4A**, 1523-1537.

Langbein, J. and Y. Bock (2004). High-rate real-time GPS network at Parkfield: Utility for detecting fault slip and seismic displacements. *Geophys. Res. Lett.* **31**.

Larson, K., A. Bilich, et al. (2006). Reducing the effects of multipath in high-rate GPS analysis I: evaluation of modified sidereal filtering. *submitted to J. Geophys. Res*, available at <http://spot.colorado.edu/~kristine/publications.html>.

Larson, K.M., P. Bodin, et al. (2003). Using 1-Hz GPS data to measure deformations caused by the Denali fault earthquake. *Science* **300**, 1421-1424.

Lay, T., H. Kanamori, et al. (2005). The great Sumatra-Andaman earthquake of 26 December 2004. *Science* **308**, 1127-1133.

Mavroeidis, G.P., B. Zhang, et al. (2008). Estimation of strong ground motion from the great 1964 Mw 9.2 Prince William Sound, Alaska, earthquake. *Bulletin of the Seismological Society of America* **98**, 2303-2324.

Menke, W., H. Abend, et al. (2006). Review of the source characteristics of the Great Sumatra-Andaman Islands earthquake of 2004. *Surveys in Geophysics* **27**, 603-613.

Miyazaki, S., K. Larson, et al. (2004). Modeling the rupture process of the 2003 Tokachi-Oki earthquake using 1-Hz GPS data. *Geophys. Res. Lett.* **31**.

Nance, J.J. (1988). *On Shaky Ground: An Invitation to Disaster*, William Morrow and Company Inc, New York.

Olsen, A.H. (2008) *Steel Moment-Resisting Frame Responses in Simulated Strong Ground Motions: or How I Learned to Stop Worrying and Love the Big One*. Ph. D., California Institute of Technology.

Olsen, A.H., B.T. Aagaard, et al. (2008). Long-period building response to earthquakes in the San Francisco Bay Area. *Bulletin of the Seismological Society of America* **98**, 1047-1065.

Olsen, K.B., S.M. Day, et al. (2006). Strong shaking in Los Angeles expected from southern San Andreas earthquake. *Geophysical Research Letters* **33**.

Olsen, K.B., W.J. Stephenson, et al. (2008). 3D crustal structure and long-period ground motions from a M9.0 megathrust earthquake in the Pacific Northwest region. *Journal of Seismology* **12**, 145-159.

Olson, A.H. and R.J. Apsel (1982). Finite faults and inverse-theory with applications to the 1979 Imperial-Valley earthquake. *Bulletin of the Seismological Society of America* **72**, 1969-2001.

Pitarka, A., R. Graves, et al. (2004). Validation of a 3D velocity model of the Puget Sound region based on modeling ground motion from the 28 February 2001 Nisqually earthquake. *Bulletin of the Seismological Society of America* **94**, 1670-1689.

Plafker, G. (1965). Tectonic deformation associated with the 1964 Alaska earthquake. *Science* **148**, 1675-1687.

Pratt, T.L. (2006). Basin effects and site response over large sedimentary basins: Insights from the Puget Lowland, Washington State. *Bulletin of the Seismological Society of America* **submitted**.

Pratt, T.L., T.M. Brocher, et al. (2003). Amplification of seismic waves by the Seattle basin, Washington State. *Bulletin of the Seismological Society of America* **93**, 533-545.

Pratt, T.L., S. Johnson, et al. (1997). Seismic reflection images beneath Puget sound, western Washington state: The puget lowland thrust sheet hypothesis. *Journal of Geophysical Research-Solid Earth* **102**, 27469-27489.

Rosenblueth, E. and R. Meli (1986). The 1985 earthquake: causes and effects in Mexico City. In: *Concrete International*. 23-24. American Concrete Institute, Detroit, Michigan.

SAC Joint Venture (1996). Experimental Investigations of Beam-Column Subassemblages. **SAC-96-01, Part I and Part II**. SAC Joint Venture, Sacramento, CA.

Saikia, C.K. and P.G. Somerville (1997). Simulated hard-rock motions in Saint Louis, Missouri, from large New Madrid earthquakes (M(w)>=6.5). *Bulletin of the Seismological Society of America* **87**, 123-139.

Sato, T., R.W. Graves, et al. (1999). Three-dimensional finite-difference simulations of long-period strong motions in the Tokyo metropolitan area during the 1990 Odawara earthquake (M-J 5.1) and the great 1923 Kanto earthquake (M-S 8.2) in Japan. *Bulletin of the Seismological Society of America* **89**, 579-607.

Segall, P. and J. Davis (1997). GPS applications for geodynamics and Earthquake studies. *Ann. Rev. Earth Planet. Sci* **25**, 301-336.

Shakal, A.F., M.J. Huang, et al. (2004). CSMIP Strong motion data processing. In: *Proc. Invitational Workshop on Strong Motion Record Processing*. COSMOS, Richmond, CA.

Sieh, K. (2005). Aceh-Andaman earthquake - What happened and what's next? *Nature* **434**, 573-574.

Somerville, P.G., H.K. Thio, et al. (2005). Ground Motions of the Sumatra Earthquakes of 2004 and 2005. In: *SMIP05 Seminar Proceedings*. Los Angeles, California.

Sørensen, M.B., K. Atakan, et al. (2007). Simulated strong ground motions for the great M 9.3 Sumatra-Andaman earthquake of 26 December 2004. *Bulletin of the Seismological Society of America* **97**, S139-S151.

Steinbrugge, K.V., E.E. Schader, et al. (1971). San Fernando earthquake. In: *Technical Report*. Pacific Fire Rating Bureau, San Francisco CA.

Subarya, C., M. Chlieh, et al. (2006). Plate-boundary deformation associated with the great Sumatra-Andaman earthquake. *Nature* **440**, 46-51.

Takeo, M. and H. Kanamori (1997). Simulation of long-period ground motion near a large earthquake. *Bulletin of the Seismological Society of America* **87**, 140-156.

USGS data data processing http://nsmp.wr.usgs.gov/processing.html. **last accessed Oct. 2008**.

Villaverde, R. (2007). Methods to assess the seismic collapse capacity of building structures: State of the art. *Journal of Structural Engineering-Asce* **133**, 57-66.

White, T. and C.E. Ventura (2004). Ground motion sensitivity of a Vancouver-style high rise. *Canadian Journal of Civil Engineering* **31**, 292-307.

Williams, R.A., W.J. Stephenson, et al. (1999). Surface Seismic Measurements of Near-Surface P- and S-Wave Seismic Velocities at earthquake Recording Stations, Seattle, Washington. *Earthquake Spectra* **15**, 565-584.

Yagi, Y. (2004). Source rupture process of the 2003 Tokachi-oki earthquake determined by joint inversion of teleseismic body wave and strong ground motion data. *Earth Planets and Space* **56**, 311-316.

Yamada, M. (2007) *Early Warning for Earthquakes with Large Rupture Dimension*. Ph. D., California Institute of Technology.

Yamanaka, Y. and M. Kikuchi (2003). Source process of the recurrent Tokachi-oki earthquake on September 26, 2003, inferred from teleseismic body waves. *Earth Planets and Space* **55**, E21-E24.

Yanev, P.I., Gillengerten J.D., et al. (1991). *The performance of steel buildings in past earthquakes*, The American Iron and Steel Institute.

Yang, J. and T. Heaton (2005). The Importance of true ground displacement to nonlinear response of high-rise buildings. Poster for SSA annual meeting, Reno, Nevada.

Zhu, L.P. (2003). Recovering permanent displacements from seismic records of the June 9, 1994 Bolivia deep earthquake. *Geophysical Research Letters* **30**.

Zumberge, J.F., M.B. Heflin, et al. (1997). Precise point positioning for the efficient and robust analysis of GPS data from large networks. *J. Geophys. Res* **102**, 5005-5017.